

UNIVERSITY OF SOUTHAMPTON

**REPETITIVE STRUCTURES:
Eigenanalysis, Continuum Beam Modelling
and Pre-Twisted Form**

BY

YONG ZHANG
B.Eng, M.Eng

A THESIS SUBMITTED FOR THE DEGREE OF
DOCTOR OF PHILOSOPHY

COMPUTATIONAL ENGINEERING AND DESIGN GROUP
SCHOOL OF ENGINEERING SCIENCES

MARCH 2003

To my wife

ZHENG WANG

UNIVERSITY OF SOUTHAMPTON

ABSTRACT

FACULTY OF ENGINEERING AND APPLIED SCIENCE

SCHOOL OF ENGINEERING SCIENCES

Doctor of Philosophy

REPETITIVE STRUCTURES:

Eigenanalysis, Continuum Beam Modelling and Pre-Twisted Form

by Yong Zhang

Eigenanalysis is applied to three major types of repetitive structures: rigid-jointed, asymmetric, and pre-twisted.

For a 2-D rigid-jointed repetitive structure, the general idea of the *State Variable Transfer Matrix Method* is presented. This provides not only an exposition of the approach, but also justification for the treatment of rigid-jointed structures as pin-jointed.

For an asymmetric repetitive structure, a *generalised eigenproblem* is developed due to the non-existence of the conventional transfer matrix. Analysis of a 3-D *NASA* truss reveals couplings of tension-torsion, and bending-shear, and the equivalent continuum beam properties are determined. To fully understand these coupling effects, a 2-D planar asymmetric framework representing a single face of the 3-D truss is also analysed. Further, the continuum beam dynamic theories for the tension-torsion and bending-shear couplings are derived through the application of Hamilton's principle, and natural frequency predictions of the 3-D *NASA* truss are compared with those from FEM.

For a pre-twisted repetitive structure with uniform pre-twist rate, the Floquet system is transformed into an autonomous system by introducing a local coordinate system to define the transfer matrix, prior to eigenanalysis. For the multiple complex unity eigenvalues, near diagonal Jordan decompositions are employed to determine the simplest eigen- and principal vectors. Equivalent continuum properties including coupling coefficients are determined. The tension-torsion coupling agrees with established pre-twisted beam theory, but the bending and shear vectors cannot be fully explained according to existing approximate bending theory for pre-twisted structures. An in-depth study of tension-torsion coupling, both static and dynamic, is presented for structures with pre-twist angles per cell over the range of 0° to 180°. Variations of the equivalent continuum properties are also evaluated over this range.

Moreover, an alternative analytical approach is developed for the continuum modelling of a symmetric repetitive structure, based on minimisation of potential energy of a single cell.

CONTENTS

ABSTRACT	i
CONTENTS	ii
LIST OF TABLES	vi
LIST OF FIGURES	vii
ACKNOWLEDGEMENT	xiii
NOTATIONS	xiv
CHAPTER 1 INTRODUCTION	1.1
1.1 REVIEW OF PREVIOUS STUDY OF REPETITIVE STRUCTURES	1.6
1.2 REVIEW ON THE PREVIOUS STUDY OF PRE- TWISTED STRUCTURES	1.8
1.3 LAYOUT OF THE DISSERTATION	1.13
CHAPTER 2 EIGENANALYSIS OF RIGID-JOINTED REPETITIVE STRUCTURE	2.1
2.1 INTRODUCTION	2.1
2.2 TRANSFER MATRIX FORMULATION	2.1
2.3 EIGENANALYSIS	2.6
2.4 EQUIVALENT CONTINUUM PROPERTIES	2.15
APPENDIX 2 TRANSFORMATION MATRIX AND JORDAN CANONICAL FORM OF 2D RIGID-JOINTED FRAMEWORK, FIGURE 2.1	2.22

CHAPTER 3 AN ALTERNATIVE APPROACH FOR DETERMINATION OF EQUIVALENT CONTINUUM PROPERTIES	3.1
3.1 INTRODUCTION	3.1
3.2 EXAMPLE STRUCTURE	3.1
3.3 EXACT EQUIVALENT CONTINUUM PROPERTIES OF THE EXAMPLE STRUCTURE	3.2
3.4 ANALYTICAL EXPRESSIONS FOR THE EQUIVALENT CONTINUUM PROPERTIES OF A MORE GENERALLY DEFINED FRAMEWORK	3.6
APPENDIX 3 STIFFNESS MATRIX OF 2D PIN-JOINTED FRAMEWORK	3.9
CHAPTER 4 EIGENANALYSIS OF AN ASYMMETRIC REPETITIVE STRUCTURE	4.1
4.1 INTRODUCTION	4.1
4.2 GENERALISED EIGENVALUE PROBLEM	4.3
4.3 SIMPLE 2-D PLANAR ASYMMETRIC FRAMEWORK	4.5
4.3.1 Equivalent Continuum Properties and Coupling Coefficients	4.6
4.4 THE 3-D ASYMMETRIC <i>NASA</i> TRUSS	4.15
4.4.1 Equivalent Continuum Properties and Coupling Coefficients	4.16
4.4.2 Coupling Behaviour	4.30
APPENDIX 4.A TRANSMISSION MATRIX OF A SINGLE-FACE CELL OF THE 3-D SATELLITE TRUSS, FIGURE 4.2	4.33
APPENDIX 4.B TRANSMISSION MATRIX FOR THE 3-D PIN-JOINTED ASYMMETRIC FRAMEWORK, FIGURE 4.3	4.34
APPENDIX 4.C STIFFNESS MATRIX OF THE SINGLE FACE OF THE 3-D SATELLITE TRUSS, FIGURE 4.2	4.36

APPENDIX 4.D TENSION AND TORSION PAIRS FOR THE 3-D ASYMMETRIC PIN-JOINTED FRAMEWORK, FIGURE 4.3	4.37
CHAPTER 5 DYNAMIC ANALYSIS OF A REPETITIVE STRUCTURE	5.1
5.1 INTRODUCTION	5.1
5.2 MASS AND MOMENT OF INERTIA PER UNIT LENGTH	5.2
5.3 CONTINUUM DYNAMIC THEORY	5.2
5.3.1 Dynamic Equations	5.2
5.3.2 Solution of the Dynamic Equations	5.4
5.4 COMPARISON OF NATURAL FREQUENCY PREDICTIONS	5.10
APPENDIX 5 DERIVATION OF MATRIX $\mathbf{F}(\omega)$	5.15
CHAPTER 6 EIGENANALYSIS OF PRE-TWISTED REPETITIVE STRUCTURES	6.1
6.1 INTRODUCTION	6.1
6.2 EXAMPLE AND THEORY	6.1
6.2.1 Transfer Matrix	6.2
6.2.2 Floquet Theory	6.7
6.2.3 Eigenanalysis	6.9
6.2.4 Equivalent Continuum Properties	6.14
APPENDIX 6.A TRANSFORMATION MATRIX AND JORDAN CANONICAL FORM FOR 3D PIN-JOINTED PRE-TWISTED FRAMEWORK, FIGURE 6.2	6.30
APPENDIX 6.B TWO <i>PURE</i> SHEAR VECTORS FOR THE PIN-JOINTED PRE-TWISTED FRAMEWORK, FIGURE 6.2	6.35

CHAPTER 7 TENSION-TORSION COUPLING OF PRE-TWISTED REPETITIVE STRUCTURES	7.1
7.1 INTRODUCTION	7.1
7.2 VIBRATION ANALYSIS FOR PRE-TWIST ANGLE OF 22.5° PER CELL	7.3
7.3 EQUIVALENT CONTINUUM PROPERTIES FOR ANGLES OF PRE-TWIST OVER THE RANGE 0° TO 180°	7.4
7.4 VIBRATION ANALYSIS OVER THE RANGE 0° TO 180°	7.14
CHAPTER 8 CONCLUSIONS AND RECOMMENDATIONS	8.1
REFERENCES	R.1
BIBLIOGRAPHY	B.1

LIST OF TABLES

Table 2.1	Effect of jointing on eigenvalues	2.7
Table 2.2	Effect of jointing on equivalent continuum properties	2.20
Table 4.1	Deformation produced by arbitrary loads T , Q_p , M and Q	4.13
Table 5.1	Comparison of natural frequencies (Hz) in bending according to ANSYS and present method; free-free and fixed-fixed beam, $L = 10.284$ m (30 cells)	5.10
Table 5.2	Comparison of natural frequencies (Hz) in bending according to ANSYS and present method; free-free and fixed-fixed beam, $L = 3.428$ m (10 cells)	5.11
Table 5.3	Comparison of natural frequencies (Hz) in torsion and extension according to ANSYS and present method; free-free and fixed-fixed beam, $L = 10.284$ m (30 cells)	5.12
Table 5.4	Comparison of natural frequencies (Hz) in torsion and extension according to ANSYS and present method; free-free and fixed-fixed beam, $L = 3.428$ m (10 cells)	5.13
Table 5.5	Comparison of natural frequencies (Hz) in torsion and extension according to ANSYS and present method; cantilever beam	5.13
Table 7.1	Comparison of natural frequencies (Hz) in torsion and extension according to ANSYS and present method; free-free and cantilever beam, $L = 10.284$ m (30 cells)	7.2
Table 7.2	Comparison of natural frequencies (Hz) in torsion and extension according to ANSYS and present method; free-free and fixed-fixed beam, $L = 3.428$ m (10 cells)	7.3

LIST OF FIGURES

Figure 2.1	Rigid-jointed planar framework; the length of the truss is equal to the number of the cells, L .	2.2
Figure 2.2	Single (j^{th}) cell of framework in Figure 2.1; (a) and (b) show positive joint force and moment according to transfer matrix and FEA conventions, respectively.	2.2
Figure 2.3	Nodal forces and moments for left-hand decay modes; displacements not shown.	2.8
Figure 2.4	Coupling of eigenvector $\mathbf{V}(:,13)$ for rigid body displacement in the x -direction, with principal vector $\mathbf{V}(:,14)$ for tension; here and later, dotted lines show initial cell configuration.	2.15
Figure 2.5	Coupling of eigenvector $\mathbf{V}(:,15)$ for rigid body displacement in the y -direction, with principal vector $\mathbf{V}(:,16)$ for rigid body rotation; y -components of displacements on the left-hand side are negligible.	2.17
Figure 2.6	Coupling of principal vector $\mathbf{V}(:,16)$ for rigid body rotation, with principal vector $\mathbf{V}(:,17)$ for pure bending.	2.18
Figure 2.7	Coupling of principal vector $\mathbf{V}(:,18)$ for shearing force and left-hand bending moment, with principal vector $\mathbf{V}(:,17)$ for pure bending.	2.19
Figure 2.8.	Decomposition of the displacements in the x -direction from Figure 2.7: (a) shear angle due to the shearing force; (b) bending curvature due to the left-hand bending moment.	2.20
Figure 3.1	Single cell loaded in tension; dotted lines show initial cell configuration.	3.2
Figure 3.2	Single cell loaded in pure bending.	3.3
Figure 3.3	Single cell subject to shear and bending moment.	3.5
Figure 4.1	A ten cell 3-D pin-jointed satellite truss with equilateral triangular cross-section.	4.1
Figure 4.2	A 2-D planar asymmetric framework with typical cell.	4.2

Figure 4.3 Two consecutive cells, j^{th} and $(j+1)^{\text{th}}$, of the framework shown in Figure 4.1. 4.3

Figure 4.4 A 2-D planar asymmetric framework subjected to self-equilibrated end loading. 4.6

Figure 4.5 The tension pair of the single-face cell of the 3-D satellite truss; the deformation is decomposed into (b) extension and (c) shear deformation. 4.7

Figure 4.6 The bending moment pair of the single-face cell of the 3-D satellite truss; the deformation represents a bending curvature only. 4.7

Figure 4.7 The mixed shear pair of the single-face cell of the 3-D satellite truss; (a) shows the force components which indicates that the cell is subjected to shearing force, compressive force and bending moment; displacement components indicate a shear deformation and cross-sectional expansion (b), and a bending curvature (c). 4.8

Figure 4.8 The pure shear pair of the single-face cell of the 3-D satellite truss; (a) shows conventional pure shear; (b) shows an equivalent combination of shear and bending moment; (c) shows the shear deformation and cross-sectional expansion; (d) shows the extension. 4.10

Figure 4.9 The extension pair of the single-face cell of the 3-D satellite truss; (a) shows the force components which indicates tension, shearing force and bending moment; the deformation is decomposed into (b) extension and Poisson's ratio contraction, and (c) a bending curvature. 4.11

Figure 4.10 Single cell subject to both tension and twisting moment having unit extension; vectors $\mathbf{T}(:,1)$ and $\mathbf{T}(:,2)$ describe the displacement and force components on the left and right hand side of the cell, respectively. Note the apparent Poisson's ratio contraction of the cross-section. 4.16

Figure 4.11 Single cell subjected to both twisting moment and compressive force, causing pure rotation about the x -axis; vectors $\mathbf{T}(:,3)$ and $\mathbf{T}(:,4)$ describe the displacement and

force components on the left and right hand side of the cell respectively. Note the apparent Poisson's ratio expansion of the cross-section. 4.17

Figure 4.12 (a) Rigid body rotation about the z -axis; (b) Rigid body rotation about the y -axis. 4.20

Figure 4.13 Ten cell 3-D pin-jointed satellite truss subject to bending moment in accordance with the force components of the bending vector $\mathbf{T}(:,8)$. 4.22

Figure 4.14 The nodal displacement solution of the numerical experiment shown in Figure 4.13. 4.22

Figure 4.15 Single cell subject to pure bending moment in the xy -plane; vectors $\mathbf{T}(:,7)$ and $\mathbf{T}(:,8)$ describe the displacement and force components on the left and right hand sides of the cell, respectively. 4.24

Figure 4.16 Single cell subject to pure bending moment in the xz -plane; vectors $\mathbf{T}(:,13)$ and $\mathbf{T}(:,14)$ describe the displacement and force components on the left and right hand sides of the cell, respectively. 4.24

Figure 4.17 Single cell subject to shearing force and bending moment in the xy -plane; vectors $\mathbf{T}(:,9)$ and $\mathbf{T}(:,10)$ describe the displacement and force components on the left and right hand side of the cell, respectively. 4.25

Figure 4.18 Single cell subject to shearing force and bending moment in the xz -plane; vectors $\mathbf{T}(:,15)$ and $\mathbf{T}(:,16)$ describe the displacement and force components on the left and right hand side of the cell, respectively. 4.26

Figure 4.19 Decomposition of the displacements of Figure 4.17 in the xy -plane; (a) shows shear angle and (b) shows bending curvature. 4.26

Figure 4.20 Decomposition of displacements of Figure 4.17 in the xz -plane; (a) shows bending curvature coupled with shear angle in the xy -plane due to shearing force, and (b) shows shear angle coupled with bending curvature in the xy -plane due to bending moment. 4.27

Figure 4.21	Decomposition of displacements of Figure 4.18 in the xz -plane; (a) shows the shear angle and (b) shows the bending curvature.	4.27
Figure 4.22	Decomposition of displacements of Figure 4.18 in the xy -plane; (a) shows bending curvature coupled with shear angle in the xz -plane due to the shearing force, and (b) shows shear angle coupled with bending curvature in the xz -plane due to the bending moment.	4.28
Figure 6.1	Local and global coordinate systems on the left and right hand side of the first cell, respectively.	6.1
Figure 6.2	A six-cell pin-jointed pre-twisted framework; the first cell is shown in bold.	6.2
Figure 6.3	Coordinates of the right hand side of the second cell	6.6
Figure 6.4	Coupling of eigenvector \mathbf{v}_7 for rigid body displacement in the x -direction, with principal vector \mathbf{w}_8 for extension; displacements are exaggerated. Dotted lines show initial configuration.	6.15
Figure 6.5	Coupling of eigenvector \mathbf{v}_9 for rigid body rotation about the x -axis, with principal vector \mathbf{w}_{10} for torsion.	6.15
Figure 6.6	(a) Principal vector \mathbf{w}_{13} for rigid body rotation about the z -axis; (b) principal vector \mathbf{w}_{14} for rigid body rotation about the y -axis.	6.17
Figure 6.7	Principal vector \mathbf{w}_{15} for bending moment in the xy -plane; (a) and (b) show the displacement and force components in the xy - and xz -planes, respectively.	6.19
Figure 6.8	Principal vector \mathbf{w}_{16} for bending moment in the xz -plane; (a) and (b) show the displacement and force components in the xz - and xy -planes, respectively.	6.19
Figure 6.9	Principal vector \mathbf{w}_{17}^* for shearing force and bending moment in the xy -plane; (a) and (b) show the displacement and force components in the xy - and xz -planes, respectively.	6.21
Figure 6.10	Principal vector \mathbf{w}_{18}^* for shearing force and bending moment in the xz -plane; (a) and (b) show the displacement	

and force components in the xz - and xy -planes, respectively.	6.22	
Figure 6.11	Decomposition of the displacements in the xy -plane of Figure 6.9; (a) shows the shear angle due to shearing force, and (b) shows the bending curvature due to bending moment.	6.22
Figure 6.12	Decomposition of the displacements in the xz -plane of Figure 6.9; (a) shows the bending curvature coupled with the shear angle in the xz -plane due to shearing force, and (b) shows the shear angle coupled with the bending curvature in the xz -plane due to bending moment.	6.23
Figure 6.13	Decomposition of the displacements in the xz -plane of Figure 6.10; (a) shows the shear angle due to shearing force, and (b) shows the bending curvature due to bending moment.	6.23
Figure 6.14	Decomposition of the displacements in the xy -plane of Figure 6.10; (a) shows the bending curvature coupled with the shear angle in the xy -plane due to shearing force, and (b) gives the shear angle coupled with the bending curvature in the xy -plane due to bending moment.	6.24
Figure 6.15	Displacements in the y -direction for the principal vector \mathbf{w}^*_{17} on the left (a) and right hand (b) sides of the cell, respectively.	6.25
Figure 6.16	Displacements in the z -direction for the principal vector \mathbf{w}^*_{18} on the left (a) and right hand (b) sides of the cell, respectively.	6.25
Figure 7.1	Variation of the lengths of different members with pre- twist angle.	7.5
Figure 7.2	Variation of mass per unit length with pre-twist angle.	7.5
Figure 7.3	Variation of rotary moment of inertia per unit length with pre-twist angle.	7.6
Figure 7.4	Variation of the distances of different members from the centroidal x -axis with pre-twist angle.	7.7
Figure 7.5	Variation of cross-sectional area with pre-twist angle.	7.8

Figure 7.6	Variation of Poisson's ratio with pre-twist angle.	7.9
Figure 7.7	Variation of shear modulus with pre-twist angle.	7.10
Figure 7.8	Variation of torsion constant with pre-twist angle.	7.11
Figure 7.9	Variation of axial stiffness with pre-twist angle.	7.12
Figure 7.10	Variation of torsional stiffness with pre-twist angle.	7.12
Figure 7.11	Variation of tension-torsion coupling coefficient with pre-twist angle.	7.13
Figure 7.12	Variation of fundamental torsional natural frequency with pre-twist angle.	7.15
Figure 7.13	Variation of fundamental longitudinal natural frequency with pre-twist angle.	7.15
Figure 7.14	Errors of the fundamental torsional and longitudinal natural frequency with pre-twist angle.	7.16

ACKNOWLEDGEMENT

I gratefully acknowledge the financial support of the School of Engineering Sciences at the University of Southampton to complete this research work.

I would like to express the greatest gratitude to Dr Neil Stephen for his invaluable guidance, advice and consistent encouragement throughout this research work.

I am deeply indebted to Professor Andy Keane and staff of the Computational Engineering and Design Centre for providing friendly environment in which to study.

I also wish to thank Dr Neil Bressloff, Mr Tony Scurr and Mrs Sarah Guest for their great assistance during my period of study within the CEDC.

NOTATIONS

A	cross-sectional area
$A_{1,2,3,4}$	constants
$A_{H,D,L}$	cross-sectional areas of horizontal, diagonal and longitudinal members, respectively
A, B	matrices of the generalised eigenvalue problem
b	constant
$B_{1,2,3,4}$	constants
$c_{1,2,3}$	constants
$C_{1,2,3,4}$	constants
C	constant matrix
d	member diameter
d	nodal displacement vector
D	length of diagonal members
$D_{1,2,3,4}$	constants
E	Young's modulus
EA	axial stiffness
EI	bending stiffness
f_{ij}	coefficients of matrix $\mathbf{F}(\omega)$
F	force vector
$\mathbf{F}(\omega)$	coefficient matrix
G	shear modulus
GJ	torsional stiffness
G	transfer matrix in global coordinate system
G'	transfer matrix in local coordinate system
G_p	<i>monodromy</i> matrix
H	height of <i>cell</i> cross-section or length of vertical members ($H = \sqrt{3}/2 \ L$)
i	$(-1)^{1/2}$
I	second moment of area
I	identity matrix
j, N	index of <i>cell</i> or section

J	torsion constant
J_x, J_y, J_z	mass moments of inertia per unit length about the x -, y - and z -axes, respectively
J	Jordan block matrix
J_m	metric matrix
J_p	Jordan canonical form
k	constant
K_{tt}	tension-torsion coupling coefficient
K_{ts}	tension-shear coupling coefficient
$K_{xy,xy'}$	bending-shear coupling coefficients in the xy -plane
$K_{xz,xz'}$	bending-shear coupling coefficients in the xz -plane
K	stiffness matrix
K_p	super-element matrix
L	left
L	length of longitudinal members
L	constant non-singular matrix
m	mass per unit length
M	bending moment
$M_{z,y}$	bending moments in the xy - and xz -planes, respectively
M_x	twisting moment
M^*	<i>unit</i> state of moment
n	integer number
N	nodal moment
N_c	compliance matrix
N	nilpotent matrix
p	constant
p	nodal force vector
P(n)	periodic matrix
q	constant
Q	shearing force
$Q_{y,z}$	shearing forces in the xy - and xz -planes, respectively
Q_p^*	<i>unit</i> state of pure shear

r	<i>cell</i> member radius
R	right
R, R'	radius of bending curvature
\mathbf{s}	state vector in global coordinate system
\mathbf{s}'	state vector in local coordinate system
\mathbf{S}_p	similarity/transformation matrix
$\mathbf{S}(n)$	square matrix
t	time
\mathbf{T}	transpose of matrix or vector
T	kinetic energy
T_x	tensile force
\mathbf{T}	<i>transmission</i> matrix
T^*	<i>unit</i> state of tension
\mathbf{T}_3	3×3 orthogonal transformation matrix
\mathbf{T}_{18}	18×18 orthogonal transformation matrix
u, v, w	displacements in the x -, y - and z -directions, respectively
$U(x)$	displacement function
U	strain energy
\mathbf{v}	eigenvector
\mathbf{V}	similarity/transformation matrix
$V(x)$	displacement function
\mathbf{w}	principal vector
$W(x)$	displacement function
x, y, z	global coordinate system
x', y', z'	local coordinate system
xy, xz	bending planes in Cartesian coordinate system
\mathbf{X}_i	eigenvector of transfer matrix
\mathbf{Y}_j	eigenvector of the transpose of transfer matrix
$\mathbf{z}(n)$	vector solution of autonomous system
α	pre-twist angle per cell
$\mathbf{\beta}$	connectivity matrix
γ	shear angle

$\varepsilon_x, \varepsilon_y, \varepsilon_z$	strains in the x -, y - and z -directions, respectively
κ	shear coefficient
$\kappa A G$	shear stiffness
ρ	material density
λ	decay factors, eigenvalues
μ, λ_p	Floquet multipliers; eigenvalues of matrix \mathbf{G}_p
ν	Poisson's ratio
ω	natural frequency (rad/sec)
θ	rotational angle about the x -axis
$\Theta(x)$	rotational function
ψ	rotation of the cross section
ψ_y, ψ_z	rotational angles about the y - and z -axes, respectively
$\Psi(x)$	rotational function
$\Psi(n)$	another fundamental matrix
<i>eig</i>	MATLAB command – eigenvalues and eigenvectors
<i>rref</i>	MATLAB command – reduced row echelon form
FEM	finite element method
JCF	Jordan canonical form
<i>NASA</i>	National Aeronautics and Space Administration (USA)

CHAPTER ONE

INTRODUCTION

Periodic, or repetitive structures consist of a basic cell, which repeats in one, two or three directions. A rail track supported on equally spaced sleepers, and a honeycomb sandwich panel, are examples of one-dimensional (beam-like) and two-dimensional (plate-like) periodic structures, respectively. This thesis is concerned primarily with the static analysis of one-dimensional (beam-like) repetitive structures. Since the manufacture and construction, or assembly, of repetitive structures is also a repetitive process, they often represent a cost effective design solution in many mechanical, civil and aerospace engineering applications. Due to their low cost, lightweight, and high stiffness, together with ease of packaging, transportation and assembly, repetitive lattice structures have become the dominant form for future space applications such as large space stations, space mirrors and deployable antenna systems.

In the majority of what follows, the repeating cell is regarded as consisting of several pin-jointed members. This choice has been made primarily because the finite element analysis (FEA) of such structures involves a rod in tension or compression only, whose finite element is “exact”; thus the computational process alone limits the accuracy of FEA of pin-jointed structures. In turn, this means that results obtained from the primary analytical tool employed in the thesis – eigenanalysis – can be verified by comparison with what may be regarded as exact results. This does not imply that pin-jointed structures are not of interest in their own right; indeed the removal of members from such a structure can reduce it to a mechanism, which in turn allows its transportation in a very compact form, an attribute which finds favour in space application. On the other hand, repetitive structures are not limited to frameworks either rigid- or pin-jointed. For example a continuum structure such as a metre rule could be regarded as repetitive were it not for the different, progressive, numbering along its edge – each centimetre of rule is identical to that preceding it.

The analysis of one-dimensional beam-like structures, be they a continuum or a framework, is historically linked to the French elastician Barre de Saint-Venant. For a continuum elastic beam of arbitrary (but constant) cross-section, solution of a practical problem such as determination of its torsional stiffness, requires the determination of stress and displacement fields, which must satisfy exactly the equilibrium equations, the strain compatibility equations¹, the Hooke's law and the boundary conditions. If the beam is loaded at its ends only, then this is one of a set of problems known as Saint-Venant's problem, the others being tension, pure bending, and bending caused by a shearing force applied to one end. In each case, the condition on part of the boundary is that the surface generator of the beam (which is, in fact, the majority of the boundary) should be free of external tractions. However, such exact solutions can generally be found only when the conditions at the ends of the beam (which are a minority of the total boundary), are relaxed in some sense, and this process is an application of what is known as Saint-Venant's principle (SVP).

In applying SVP, an actual load system on part of the elastic body or structural element is replaced by a statically equivalent load, distributed in a particular way demanded by the elastostatic solution - this represents the relaxed boundary condition at the beam ends. Statically equivalent implies that the resultant force and moment remain unchanged. The difference between the two load distributions is termed *self-equilibrating*, and since it has no resultant force or couple that requires reaction at some other locations on the structure, there is no reason why the associated stress and strain field should penetrate any great distance into the structure. That is, the self-equilibrating load should produce only a local effect, which decays exponentially as one moves away from the beam end.

The discussion above implies that the exact distribution of the end load, such as a twisting moment, is actually known; invoking SVP is then equivalent to replacing the actual means of load application by that demanded by the solution, and arguing that this has only a local effect. More often than not, however, the structural analyst knows only

¹ These may be avoided if the equilibrium equations are expressed in terms of displacement (Navier equations) rather than stress.

the magnitude of an end load, and does not know its exact distribution. Thus SVP is rarely invoked consciously, yet it underpins much of the discipline known as *Strength of Materials*.

The first proof of SVP for continuum beams was provided by Toupin [1] in 1965, and there has been extensive research in the field since that time, with reviews having been provided by Horgan and Knowles, [2-4]. Recently, several additions to the stock of exact elasticity solutions describing Saint-Venant decay in continuum beams have been made by Stephen and his co-workers at the University of Southampton [5-8]; typically these are for beams having mathematically amenable cross-sections, such as the hollow circular cross-section.

The first application of SVP to pin-jointed frameworks was provided by Hoff [9] in 1945. More recently Stephen and Wang, [10], developed an approach based upon the eigenanalysis of a state variable transfer matrix of a pin-jointed repetitive structure which unifies the two problems bearing the name of Saint-Venant: the decay of self-equilibrated loading (Saint-Venant's principle) and the transmission of resultant forces and moments applied at the end of the structure only (Saint-Venant's problem). The Saint-Venant decay rates are the non-unity eigenvalues of the transfer matrix, while the equivalent continuum beam properties of the framework were determined from the eigen- and principal vectors associated with the multiple unity eigenvalues. Further, these equivalent continuum properties have been employed in conventional beam theories [11], allowing the efficient analysis of the global behaviour of the repetitive structure (for example, vibration and its feedback control, global buckling, etc) most suitable for the preliminary design process. Comparison with the predictions from FEA suggested excellent agreement of natural frequencies, provided that the semi-wavelength is greater than the depth of the cell.

Stephen and Wang [12] have extended the transfer matrix approach to investigate the Saint-Venant decay rates of prismatic continuum beam with general cross-section, for which exact analytical solutions are unavailable. A representative length of the continuum beam is first modelled using the Finite Element Method (FEM), from which

the stiffness matrix is determined. A substructure technique then generates a *super-element* whose stiffness matrix relates *master* forces and displacements components at either end of the representative length (components at *slave* nodes in the interior of the model are condensed out of the stiffness matrix), from which the transfer matrix can be formulated. Generation of this super-element is readily accomplished within a FEA package, such as ANSYS.

The transfer matrix approach of Stephen and Wang [10] may be regarded as the foundation, and also the point of departure, for the work described in this thesis. In particular, the method is applied first to repetitive structures having rigid rather than pin-joints, from which it is concluded that the method of joining has negligible effect upon the equivalent continuum properties, but introduces additional modes of decay associated with self-equilibrated moments. Second, an alternative approach is developed for determination of the equivalent continuum properties without resorting to eigenanalysis. The new method requires a knowledge of the stiffness matrix \mathbf{K} of the single repeating cell of the repetitive structure, together with the ability to deduce the cell displacement vectors for tension, bending moment and shearing force; a *once and for all* application of the principle of minimum potential energy for tension yields an analytical expression for the equivalent Poisson's ratio, from which all the remaining properties such as cross-sectional area, second moment of area and shear coefficient can be obtained.

The two topics briefly described above are preliminary to the two major topics within the thesis, the first of which is the analysis of an actual truss modelled upon a demonstrator *NASA* structure [13] deployed from the space shuttle (*NASA STS61B-120-052*), whose (rigid) welded joints are treated, justifiably in the light of the preliminary work described above, as pin-jointed. This asymmetric structure exhibits coupling between various transmission modes, including tension and torsion, and also a shear deflection perpendicular to the plane of curvature in bending. The former is reminiscent of tension-torsion coupling widely known to exist in the case of structures having a pre-twisted form, as in a turbine blade. Results from the eigenanalysis of this asymmetric structure are fully validated by comparison with ANSYS predictions for static loadings.

For the vibration analysis of this structure, it has been necessary to develop equivalent continuum dynamic beam theories that include the coupling effects observed. The natural frequency predictions have been validated by comparison with ANSYS predictions.

The second major topic is the analysis of a pre-twisted repetitive structure having a constant pre-twist angle per cell. The stiffness matrix \mathbf{K} , and hence the transfer matrix \mathbf{G} , of each cell is periodic in the pre-twist angle α and, within a global coordinate system, each of these transfer matrices is dependent upon the index of the cell, n . However, the introduction of a local coordinate system that rotates with the cross-section results in an autonomous transfer matrix that is identical for each cell of the structure. This pre-twisted structure provides a physically realisable setting for an exposition of Floquet theory, which is more often applied to systems having temporal, rather than spatial, periodicity. The eigenanalysis again provides the Saint-Venant decay rates, but attention is focussed on the equivalent continuum properties, and the coupling between various modes of deformation. These include not only tension-torsion coupling, but also coupling between bending and shear modes. This analysis is thought to be the first that provides a complete solution for a pre-twisted structure, albeit highly idealised, in an exact manner, and does not introduce any ad hoc assumptions typical of the *Strength of Materials* approach to pre-twist, or the asymptotic approaches employed within *Theory of Elasticity* investigations. As with a straight beam, eigenanalysis provides the decay modes associated with Saint-Venant's principle, and also the transmission modes associated with Saint-Venant's problem; the former have eigenvalues occurring as reciprocals, while the latter are associated with both real and complex unity eigenvalues. The equivalent continuum properties of the pre-twisted structure are readily obtained for coupled tension-torsion, where interpretation of the principal vectors is in accordance with approximate continuum theories for such coupling. However, interpretation of the principal vectors describing bending and shear has been hampered by the absence of an adequate elasticity model for the continuum behaviour of pre-twisted elastic beams or rods. Indeed, none of the previously derived bending theories provides agreement with the coupling exhibited by the bending and shear vectors determined through eigenanalysis. The equivalent continuum properties

for coupled tension-torsion are evaluated over the range of pre-twist angle, $0^\circ \leq \alpha \leq 180^\circ$.

1.1 REVIEW OF PREVIOUS STUDY OF REPETITIVE STRUCTURES

Noor [14] classified the approaches to the analysis of large repetitive structure into four main streams

- a) *Direct Method* - this is conventional Finite Element Analysis (FEA), in which the complete structure is modelled as an assemblage of discrete finite elements. For a structure with a very large number of elements, such analysis can become computationally very expensive and time consuming, and in dynamic analysis, may produce far more modes of vibration than are actually needed. It is inefficient because it does not take advantage of the periodicity or regularity of the repetitive structure. Of all the approaches, while it may provide an *answer*, it provides limited *understanding* of the behaviour of a structure.
- b) *Direct field method* - this approach involves relating the displacements on either side of the typical cell by finite difference equations, then either solving the resulting finite difference equations directly, or converting them into approximate differential equations through the use of a Taylor series. This approach has been extensively developed by Renton [15].
- c) *Periodic structure method* - this approach typically relates a state vector of displacement and force components on either side of the generic cell by a transfer matrix; application of *Bloch's theorem* for dynamic problems leads to an eigenvalue problem for propagation constants or, equivalently, natural frequencies. The theory has been highly developed, and applied to both one-dimensional (beam-like) and two-dimensional (plate-like) structures, [16-24]. Lin and co-workers [16, 17] pioneered the application of transfer matrix methods to the vibration analysis of periodic stiffened plate structures. Mead [18, 19] adopted a wave propagation approach, which can be most simply applied to infinite or semi-infinite periodic structures. An overview of the contribution to this field made by researchers at the University of Southampton was given by Mead [20]. Zhong and Williams [21, 22], while employing a dynamic stiffness matrix approach to the eigensolution of wave propagation, indicated the analogy

between structural mechanics and control theory; indeed state vector representations are at the heart of so-called *Modern Control Theory*, and this cross-fertilisation introduced the symplectic orthogonality relationship (as a consequence of the symmetry of the stiffness matrix \mathbf{K} , [25]) as a means of eigenvector expansion.

d) *Substitute continuum method* - this approach employs a continuum model to replace the original structure based on the assumption that they are equivalent in some sense. It is appealing particularly if one is only interested in the global behaviour of the structure, for example vibration and its feedback control, global buckling and thermal conductivity. The key to continuum modelling involves the determination of equivalent relationships between the geometric and material properties of the lattice and the continuum model. Noor and co-workers [26, 27] developed continuum modelling theory for lattice structures based on the concept of energy equivalence, which means the lattice structure and its continuum model contain equal kinetic and strain energies when both are subjected to the same displacement and velocity fields along the centreline. Their method was based on the assumption that displacement components vary linearly in the axial direction, but have a bilinear variation over the cross-section to ensure compatibility at the interface of two adjacent repeating cells. Member strains of the repeating cell are then expressed in terms of the strain components in the coordinate directions, and expanded using a Taylor series, allowing the members strains of the discrete structure to be replaced by those of the continuum model.

Based on the same concept of energy equivalence, Lee's approach [28] employs a continuum transformation matrix which relates the initial nodal displacement vector of the repeating cell, to equivalent nodal displacements expressed in terms of continuum rod displacements; since there are, in general, fewer of the latter displacements, this process implies a condensation of the original mass and stiffness matrices, and is not unique. Well-defined conventional finite element matrices are used to calculate the strain and kinetic energies stored in the original representative lattice and, through the transformation matrix, these are expressed in terms of the continuum degrees of freedom. Equating the (reduced) stiffness and mass matrices for the representative cell to those for the finite element of the continuum model, the equivalent continuum properties of the lattice structure were obtained. A conventional Timoshenko continuum model was employed for symmetric structures, and an extended Timoshenko

model for structures displaying asymmetry. Compared with conventional finite element analysis, Lee noted that natural frequency predictions from the equivalent continuum models tended to overestimate, particularly for asymmetric structures in the higher modes.

Sun [29] simulated static experiments, numerically, in order to effectively *measure* the equivalent continuum properties of a typical cell of the lattice. However, this method requires a prior knowledge of the magnitude and distribution of the nodal forces, and also boundary constraints must carefully specified to allow, for example, Poisson's ratio effects in a simulation of tension. Similar *a priori* knowledge is required for the method described in Chapter 3, but since this is limited to deduction of the displacement vector, not the force vector, this requirement is not so onerous. Nevertheless, the displacement vectors are not always obvious particularly if there exists coupling between the various modes of deformation.

The transfer matrix eigenanalysis approach, which forms the majority of this thesis, falls directly within Noor's *Periodic structure method* classification. On the other hand, the equivalent continuum properties obtainable from eigenanalysis leads directly to Noor's *substitute continuum method* classification; thus eigenanalysis provides a link between the two.

1.2 REVIEW ON THE PREVIOUS STUDY OF PRE-TWISTED STRUCTURES

A variety of engineering components may be modelled as (continuum) beams having initial pre-twist; these include turbine and helicopter blades, propellers and wind turbines. For a straight, prismatic, homogenous beam, the responses to end loadings are in the main uncoupled; a tensile force produces only an extension (together with a Poisson's ratio contraction), a twisting moment produces a rotation (together with axial warping if the cross-section is not circular), and a bending moment in the two principal planes produces independent curvatures also in the two principal planes. The exception to this lack of coupling is that of a shearing force, which must be coupled to a bending moment, if complementary shearing forces are not applied on the surface generators of

the beam – this possibility is, of course, excluded within *Saint-Venant's problem*.

Coupling between shear and rotation is possible if the cross-section is not doubly symmetric, but the concept of the *shear centre* allows de-coupling of these displacements.

However for a straight, pre-twisted beam, tension is coupled with torsion, and bending is generally regarded as being coupled in the two planes. This coupling has been extensively studied [30-64] because of the importance of the engineering applications; for example the considerable *centrifugal force* body loading on a high speed turbine or compressor blade will not only increase the length of the blade, but also reduce its angle of attack which has an effect on its aerodynamic performance, and this must be considered in the design process, see Ohtsuka [31].

For tension-torsion coupling, it is easy to visualise that a pre-twisted beam will increase in length if a twisting moment is applied in a direction tending to decrease the pre-twist angle – the responses are coupled in the sense that a twisting moment produces both a rotation and an extension. They are also coupled in the sense that both a twisting moment and a compressive force would need to be applied in order that the response would be a rotation only.

Bending-bending coupling is equally important, but is not so easy to visualise: consider a straight beam, such as a plastic ruler, for which the bending stiffness in the two principal planes are quite unequal; if subject to excessive compressive load, buckling would clearly favour deflection in the flexible plane. However, suppose the beam now has a total uniform pre-twist through 90° , and that a bending moment is applied at one end (left hand, say) in the flexible plane *at that end*; at the right hand end, the moment is now in the stiff plane and, assuming that no torsional buckling should take place, the resulting bending curvature at the right hand end will be clearly less than at the left hand. Thus at the two ends, there would be curvature in just one plane; bending deflection would still favour the flexible plane, and would obviously be much greater at the left hand end. The above is relatively easily to visualise: what is not, is the behaviour at locations between these two extremes – if there is bending curvature

perpendicular to that of the applied bending moment, then clearly its magnitude must vary from zero to zero over the 90° twist of the beam; in turn, there are two obvious possibilities: either that it depends on double the pre-twist angle in a sinusoidal form, or that it remains zero throughout.

In 1991, Rosen [30] provided an extensive literature survey on the static and dynamic analysis of pre-twisted rod and beams, citing over 200 references, analysis of which shows the development over the past fifty years. Initially, investigations were primarily analytical and experimental, the former relying on development of the governing equations and their solution; most of the significant contributions were made prior to the development of the FEM. The latter allowed analysis of a pre-twisted beam by idealisation as a series of uniform straight beam elements, each rotated with respect to a global coordinate system, with the number of element adjusted according to the accuracy required. As a consequence, one might argue that FEA slowed analytical developments in this area, and an exact elasticity solution for pre-twisted structure is still unavailable. The major developments in this area are summarised below, first in terms of tension-torsion coupling, and then bending-bending coupling.

One of the first investigations into the effect of pre-twist on the torsional stiffness of a thin prismatic bar was made by Chen² [32], who proposed the *helical fibre assumption*, in which it is assumed that the longitudinal stress in the bar cross-section is not parallel to the axis, but acts in the direction of the longitudinal spiral fibres of the pre-twisted bar. Chen concluded that the torsional stiffness was increased by the pre-twist, and this was validated by his experimental results. This basic assumption was employed in most subsequent investigations that employ assumptions typical of *Strength of Materials*. Rosen and Friedmann [33] noted that Chen's theory employed a non-orthogonal curvilinear coordinate system, and that simplifications would arise when the theory for such a coordinate system was correctly applied. Later, Rosen [34] noted the paradox that a rod of circular cross-section could be regarded as pre-twisted simply by painting a spiral onto its surface, yet the helical fibre assumption theory would predict an increase in the torsional stiffness; for this reason Rosen suggested that Chen had restricted the

² In the literature, Chen Chu is most often referred to according to his given name, Chu.

applicability of his theory to thin-walled cross-sections. Rosen developed a more general theory taking into account axial warping of the cross-section which, of course, is absent in the torsion of a circular cross-section, and also employed both non-orthogonal and simpler orthogonal coordinate systems; the resulting theory accommodates Chen's, and also overcame the paradox of the circular cross-section.

The coupling effect between tension and torsion of the pre-twisted rod has also been investigated employing the more exact methods of the three-dimensional *Theory of Elasticity*, although approximations are introduced at a later stage of the analysis. The typical approach is to introduce a local coordinate system, which rotates with the principal axes of the cross-section, into the governing differential equations for stress describing force equilibrium, or the equivalent (Navier) equations for displacements; in either case, the equilibrium equations become more complicated, but the advantage is that the traction free boundary condition becomes independent of the axial coordinate. Stress and strain are then typically expressed as a power series in some pre-twist parameter (assumed small), with the zeroth order term being the known Saint-Venant solution for the straight beam. This approach was taken by the majority of investigators [35-46] including, notably, Okubo [35-37] and Krenk [38, 39].

Shield [46] adopted a quite different approach to tension-torsion coupling; the starting point was again the governing equations expressed within the local (rotating) coordinate system, but terms involving the pre-twist parameter were regarded as applied surface tractions within the boundary conditions, and as body force loading within the equilibrium equations, *for a straight rod*. He then employed the reciprocal theorem, with the second load system being simple tension of a straight rod. His results show excellent agreement with those of Okubo.

De Prima [47] investigated the coupled extensional and torsional vibration of a pre-twisted rod, and found that the frequencies of the predominantly extensional modes are practically unaltered by pre-twist, while frequencies of the predominantly torsional modes increase significantly. Overall, the nature of tension-torsion coupling is well understood qualitatively: pre-twist has the effect of increasing the torsional stiffness appreciably, and at the same time decreasing the axial stiffness, although not by much.

This is exactly as one would expect: axial stiffness is generally greater than torsional stiffness (although one is not comparing like with like) and a coupling of the two displacement modes has the effect of bringing their stiffness' closer together.

The same cannot be said for the coupling of bending deformations, where there remains considerable controversy. For beams with small angles of pre-twist, it is common to treat the coupling as a problem of asymmetric bending *of a straight beam*, where a bending moment in one plane produces curvature in two orthogonal planes. However, when applied to a beam having a cross-section in which the two principal second moments of area, and hence stiffness, are equal, this approach predicts that pre-twist will have no effect. In contrast, Den Hartog [48] observed from experiment that such a pre-twisted beam with thin-walled cross-section shows considerably larger deflection than a straight beam of the same cross-section and length under the same bending load, and presented this as a challenge for further research. Zickel [49, 50] considered a pre-twisted beam with thin-walled doubly symmetric cruciform cross-section, for which the second moments of area are also equal, and developed a general theory based upon the *helical fibre assumption*, which predicts that the bending stiffness about a principal axis is a decreasing function of pre-twist rate, in accordance with Den Hartog's observation. However, experiments conducted by Maunder [51] suggested that the deflection due to bending does increase with pre-twist, but is much larger than that predicted by Zickel. Maunder [51] developed a theory by considering the interaction of pre-twist with distortion of the cross-section, based on the assumption that a form of transverse distortion is governed by a single free parameter which can be directly determined by a minimum principle; his results showed nice agreement with the experimental results. In the above, the authors considered only the decreased stiffness produced by pre-twist, but did not consider explicitly any coupling of the bending curvature with any other displacements.

Tabarrok [52] derived general buckling equations for pre-twisted rods using the principle of total potential energy, including four first order coupled force-displacement equations, which suggest that bending curvature occurs in the plane of the bending moment, coupled with a cross-sectional rotation in the perpendicular plane; identical

coupled moment-curvature relationships were developed by Vielsack [53]. On the other hand, the shearing force-displacement relationships suggested by Tabarrok [52] are similar to those of a Timoshenko beam, with the addition of the product of the pre-twist rate and a transverse displacement describing the coupling effect in the plane perpendicular to the shearing force. Vielsack's shear equations ignore shear deflection, so they cannot be regarded within the spirit of a Timoshenko beam. Rather, shearing force is equal to rate of change of bending moment, as in elementary beam theory, together with an additional term, which is the product of the pre-twist rate and bending moment in the perpendicular plane; these relationships are, in fact, a statement of moment equilibrium. Tabarrok's equations do not include the product moment of area, so the coupling effect is still present for pre-twisted structures having equal second moments of area; this is consistent with Den Hartog's experimental observation. However, neither of the above generalised moment-curvature relationships is in agreement with those found in the present work.

As with tension-torsion, the bending-bending coupling of a pre-twisted beam has been investigated employing the three-dimensional *Theory of Elasticity*, again with the governing equations expressed in a local coordinate system that rotates with the structure. Thus Goodier and Griffin [40] considered pure bending of a pre-twisted rod of elliptic cross-section, and generated a series solution as a power series to the second order in the pre-twist rate parameter, while bending by a terminal shearing force has been considered by Pucci and Risitano [41], and Guglielmino and Saccomandi [42]. There has also been several investigations by researchers from the former Soviet Union, including Druz' et al [43], who treated the general problem of pre-twist as a spectral problem of a differential operator in the cross-section; as with the transfer matrix method [10], their approach unifies the decay and transmission problems.

1.3 LAYOUT OF THE DISSERTATION

The present thesis is set out as follows:

Chapter 2 presents the state variable transfer matrix method, employed to analyse a symmetric rigid-jointed planar framework, with the results compared with the pin-jointed framework examined in [10], thereby providing justification for the treatment of

rigid-jointed structures as pin-jointed, at least as far as the equivalent continuum properties are concerned, in the analysis of long, beam-like structures. Of course, a pin-jointed structure cannot withstand local, nodal, moments.

Chapter 3 presents an alternative, analytical, approach to the continuum modelling of a symmetric repetitive structure.

Chapter 4 presents a generalised eigenvalue problem for the analysis of an asymmetric repetitive structure, for which the conventional transfer matrix of the single cell does not exist, and is applied to a 3-D *NASA* truss. The structure displays tension-torsion, and bending-shear couplings. In order to fully understand these couplings, a simple 2-D planar asymmetric framework, representing a single face of the 3-D *NASA* truss, is also analysed.

Chapter 5 deals with the dynamic analysis of the truss, employing the equivalent continuum properties determined in Chapter 4; governing equations and boundary conditions are derived from the generalised stiffness matrix, and application of Hamilton's principle. Natural frequency predictions are compared with those from FEA.

Chapter 6 extends the transfer matrix technique to the eigenanalysis of repetitive structures having uniform pre-twist. Introduction of a local coordinate system rotating with nodal cross-sections results in an autonomous transfer matrix for this Floquet system. A variety of near diagonal Jordan decompositions are possible for the multiple unity eigenvalues, and these are discussed. Equivalent continuum properties, including coupling coefficients are determined. Unusually, an asymmetric stiffness matrix is obtained for bending moment and shear coupling, which may imply that the coupled bending-shear model is inadequate for the pre-twisted bending examined here. Other possible interpretations for the bending and shear vectors are also discussed.

Chapter 7 deals with the static and dynamic analysis of the pre-twisted structure with pre-twist angles per cell over the range of 0° to 180° , focussing on the tension-torsion

coupling. The relevant equivalent continuum properties are evaluated over this range, and explained in terms of the variation in lengths of the members that make up the cell. These properties, together with mass and rotary moment of inertia per unit length, are employed in the coupled extensional-torsional dynamic equations developed in Chapter 4, for structures with a specific pre-twist angle of $\alpha = 22.5^\circ$, and compared with FEA predictions. A comparison of fundamental natural frequencies is also made for structures having pre-twist angles over the range 0° to 180° per cell.

Chapter 8 presents conclusions and recommendations for future work.

CHAPTER TWO

EIGENANALYSIS OF RIGID-JOINTED REPETITIVE STRUCTURE

2.1 INTRODUCTION

In this Chapter, the state variable transfer matrix method of Stephen and Wang [10] is applied to a repetitive structure having rigid-joints. This provides not only an exposition of the approach, but also justification for the treatment of rigid-jointed structures as pin-jointed, at least as far as determination of the equivalent continuum properties is concerned. For a pin-jointed structure, the nodal displacement is completely characterised by two components for a planar structure, or three components for a space framework. When the structure is rigid jointed, a planar structure has one additional degree of freedom – a rotation in the plane, while a space framework has three additional such rotations. Associated with these rotations are possible nodal moments. Thus treating a planar structure as rigid-jointed leads to a 50% increase in the size of the state vector, and a 100% increase for the space framework, with equivalent increases in the size of the transfer matrix.

2.2 TRANSFER MATRIX FORMULATION

The rigid-jointed planar framework under consideration is shown in Figure 2.1. The geometric and material properties are identical to those in [10]: the Young's modulus of each member is $E = 200 \times 10^9 \text{ N/m}^2$, and density $\rho = 8000 \text{ kg/m}^3$. Horizontal and vertical members are of length 1 m, and have cross-sectional area $A = 1 \text{ cm}^2$; the diagonal members have length $\sqrt{2} \text{ m}$, and cross-sectional area 0.5 cm^2 . However, since vertical members are regarded as being shared between adjacent cells, the single repetitive cell must have vertical members with half stiffness; for a pin-jointed structure this just requires that the cross-sectional areas should be $A/2$. However for a rigid-jointed structure, when the members can also carry bending moment, one also requires that the bending stiffness, and hence the second moment of area should be one half. For ANSYS validation, these requirements are achieved by treating these members as tubes, when the inner and outer radii can be adjusted to give the required stiffness.

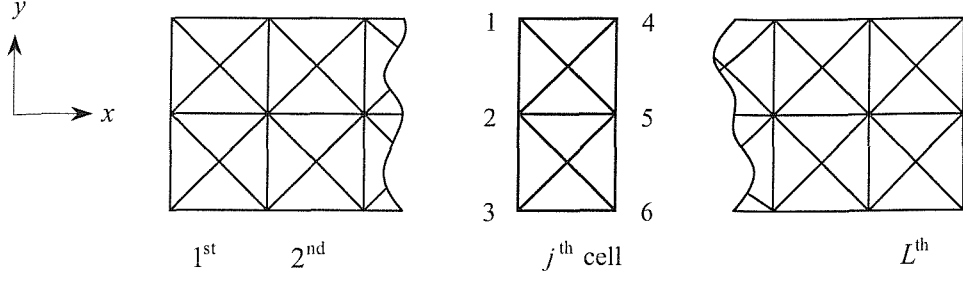


Figure 2.1. Rigid-jointed planar framework; the length of the truss is equal to the number of the cells, L .

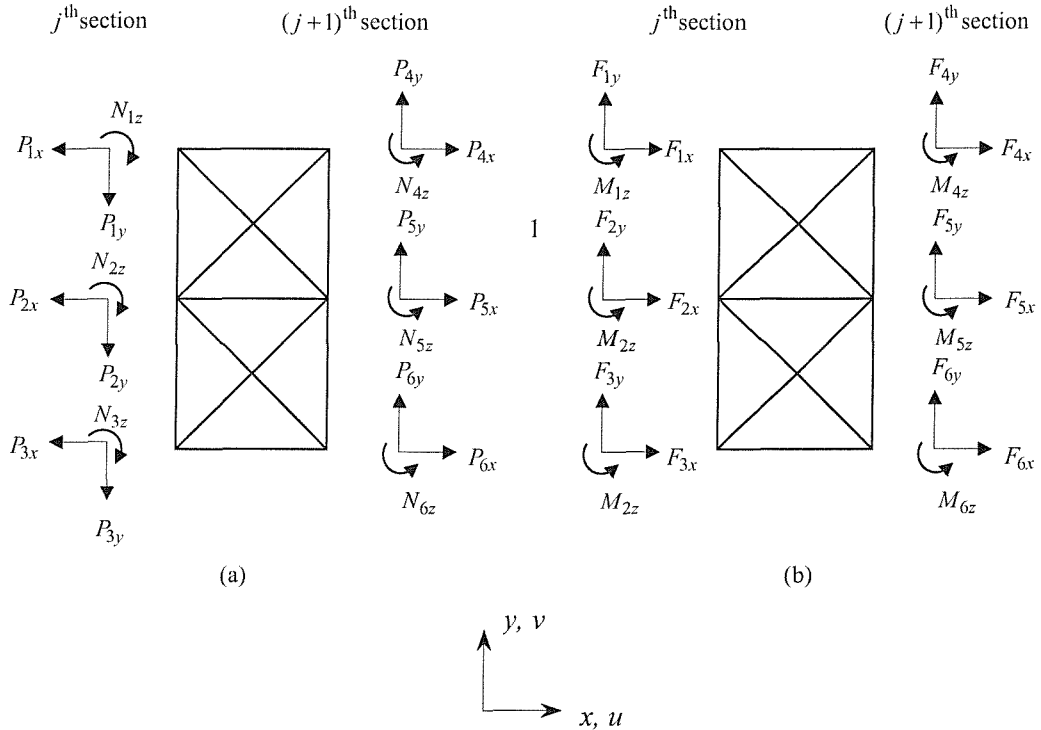


Figure 2.2. Single (j^{th}) cell of framework in Figure 2.1; (a) and (b) show positive joint force and moment according to transfer matrix and FEA conventions, respectively.

A typical cell located between the j^{th} and $(j+1)^{\text{th}}$ sections of the structure in Figure 2.1 is shown in Figure 2.2. Let \mathbf{p}_j and \mathbf{d}_j denote the nodal force and displacement vectors respectively, associated with the j^{th} section; the state vectors at the section j^{th} and

$(j+1)^{\text{th}}$ sections are then $\mathbf{s}_j = [\mathbf{d}_j^T \ \mathbf{p}_j^T]^T$ and $\mathbf{s}_{j+1} = [\mathbf{d}_{j+1}^T \ \mathbf{p}_{j+1}^T]^T$, and they are related by the transfer matrix \mathbf{G} through the equation

$$\mathbf{s}_{j+1} = \mathbf{G} \mathbf{s}_j, \quad (2.1)$$

or in partitioned form

$$\begin{bmatrix} \mathbf{d}_{j+1} \\ \mathbf{p}_{j+1} \end{bmatrix} = \begin{bmatrix} \mathbf{G}_{dd} & \mathbf{G}_{dp} \\ \mathbf{G}_{pd} & \mathbf{G}_{pp} \end{bmatrix} \begin{bmatrix} \mathbf{d}_j \\ \mathbf{p}_j \end{bmatrix}. \quad (2.2)$$

Two consecutive state vectors are also related by a constant multiple λ , as

$$\mathbf{s}_{j+1} = \lambda \mathbf{s}_j; \quad (2.3)$$

this is the static equivalent of an application of Bloch's theorem [65], for systems possessing translational symmetry. Substitution of the above into equation (2.1) leads directly to the standard eigenvalue problem

$$[\mathbf{G} - \lambda \mathbf{I}] \mathbf{s}_j = 0, \quad (2.4)$$

where \mathbf{I} is the identity matrix of the appropriate size.

Thus the eigenvalues of the transfer matrix describe how associated eigenvectors scale as one moves from one nodal section to the next. A unity eigenvalue implies that it is transmitted unchanged, while a non-unity eigenvalue $|\lambda| < 1$ implies that the nodal displacements and forces decay as one moves from cell to cell.

The transfer matrix \mathbf{G} can be obtained from the stiffness matrix \mathbf{K} of the single repeating cell. Referring to Figure 2.2(b), the generalised force and displacement vectors \mathbf{F} and \mathbf{d} , are related by the stiffness matrix equation $\mathbf{F} = \mathbf{Kd}$, or in partitioned form

$$\begin{bmatrix} \mathbf{F}_j \\ \mathbf{F}_{j+1} \end{bmatrix} = \begin{bmatrix} \mathbf{K}_{LL} & \mathbf{K}_{LR} \\ \mathbf{K}_{RL} & \mathbf{K}_{RR} \end{bmatrix} \begin{bmatrix} \mathbf{d}_j \\ \mathbf{d}_{j+1} \end{bmatrix}. \quad (2.5)$$

Transfer matrix analysis employs the sign conventions of the *Theory of Elasticity*, so set $\mathbf{F}_j = -\mathbf{p}_j$, $\mathbf{F}_{j+1} = \mathbf{p}_{j+1}$, and substitute into equation (2.5), expand and rearrange to give

$$\begin{bmatrix} \mathbf{d}_{j+1} \\ \mathbf{p}_{j+1} \end{bmatrix} = \mathbf{G} \begin{bmatrix} \mathbf{d}_j \\ \mathbf{p}_j \end{bmatrix}, \quad (2.6)$$

when the transfer matrix \mathbf{G} becomes

$$\mathbf{G} = \begin{bmatrix} -\mathbf{K}_{LR}^{-1}\mathbf{K}_{LL} & -\mathbf{K}_{LR}^{-1} \\ \mathbf{K}_{RL} - \mathbf{K}_{RR}\mathbf{K}_{LR}^{-1}\mathbf{K}_{LL} & -\mathbf{K}_{RR}\mathbf{K}_{LR}^{-1} \end{bmatrix}. \quad (2.7)$$

The $(2n \times 2n)$ transfer matrix \mathbf{G} has the property of being symplectic, see [25], and satisfies the relationship

$$\mathbf{G}^T \mathbf{J}_m \mathbf{G} = \mathbf{J}_m, \quad (2.8)$$

where \mathbf{J}_m is the metric matrix $\mathbf{J}_m = \begin{bmatrix} \mathbf{0} & \mathbf{I} \\ -\mathbf{I} & \mathbf{0} \end{bmatrix}$, with $\mathbf{J}_m^T = \mathbf{J}_m^{-1} = -\mathbf{J}_m$, and \mathbf{I} is the

$(n \times n)$ identity matrix. This relationship depends solely on the stiffness matrix \mathbf{K} being symmetric. The symplectic relationship, equation (2.8), can be rearranged to give

$\mathbf{J}_m^{-1} \mathbf{G}^T \mathbf{J}_m = \mathbf{G}^{-1}$; thus the inverse of \mathbf{G} is similar to the transpose of \mathbf{G} , which in turn has the same eigenvalues as \mathbf{G} ; the eigenvalues therefore occur as reciprocals.

The eigenvalues of any real symplectic matrix are known [66] to fall into one of five classes

- a) if it occurs, $\lambda = 1$, must occur an even number of times
- b) if it occurs, $\lambda = -1$, must occur an even number of times
- c) the real eigenvalues occur as reciprocals, that is if $\lambda = \mu$ is an eigenvalue, then so is $\lambda = \mu^{-1}$
- d) the complex unity eigenvalues occur as $\lambda = e^{i\alpha}$ and $\lambda = e^{-i\alpha}$; note that the inverse is simultaneously the complex conjugate
- e) the general complex eigenvalues occur as reciprocals and as complex conjugates, that is $\lambda = a + ib$, $\lambda = a - ib$, $\lambda = (a + ib)^{-1}$, $\lambda = (a - ib)^{-1}$ are all eigenvalues

Suppose that λ is an eigenvalue having multiplicity k , then λ^{-1} is an eigenvalue also having multiplicity k ; thus the Jordan blocks corresponding to λ and λ^{-1} have the same structure. A direct consequence of the above is that the determinant of a transfer matrix is equal to unity.

Since the transfer matrix \mathbf{G} is not symmetric, one would normally employ *bi-orthogonality* as the means of modal decomposition of an arbitrary state vector. Let \mathbf{X}_i be an eigenvector of \mathbf{G} associated with the eigenvalue λ_i , such that

$$\mathbf{G} \mathbf{X}_i = \lambda_i \mathbf{X}_i; \quad (2.9)$$

let \mathbf{Y}_j be an eigenvector of \mathbf{G}^T associated with the eigenvalue λ_j , such that

$$\mathbf{G}^T \mathbf{Y}_j = \lambda_j \mathbf{Y}_j. \quad (2.10)$$

Pre-multiply the first of these by \mathbf{Y}_j^T to give

$$\mathbf{Y}_j^T \mathbf{G} \mathbf{X}_i = \lambda_i \mathbf{Y}_j^T \mathbf{X}_i; \quad (2.11)$$

Transpose the second, and post-multiply by \mathbf{X}_i to give

$$\mathbf{Y}_j^T \mathbf{G} \mathbf{X}_i = \lambda_j \mathbf{Y}_j^T \mathbf{X}_i \quad (2.12)$$

Subtraction gives

$$(\lambda_i - \lambda_j) \mathbf{Y}_j^T \mathbf{X}_i = 0, \quad (2.13)$$

hence the bi-orthogonality relationship

$$\mathbf{Y}_j^T \mathbf{X}_i = 0, \text{ for } \lambda_i \neq \lambda_j. \quad (2.14)$$

The disadvantage of this approach is the need to perform a second eigenanalysis of the transpose of \mathbf{G} . Instead, symplectic orthogonality is determined as follows; transpose equation (2.9) to give

$$\mathbf{X}_i^T \mathbf{G}^T = \lambda_i \mathbf{X}_i^T. \quad (2.15)$$

Post-multiply by $\mathbf{J}_m \mathbf{G} \mathbf{X}_j$ to give

$$\mathbf{X}_i^T \mathbf{G}^T \mathbf{J}_m \mathbf{G} \mathbf{X}_j = \lambda_i \mathbf{X}_i^T \mathbf{J}_m \mathbf{G} \mathbf{X}_j. \quad (2.16)$$

Now $\mathbf{G}^T \mathbf{J}_m \mathbf{G} = \mathbf{J}_m$, and $\mathbf{G} \mathbf{X}_j = \lambda_j \mathbf{X}_j$, and substituting these expressions into the above yields

$$(1 - \lambda_j \lambda_i) \mathbf{X}_i^T \mathbf{J}_m \mathbf{X}_j = 0. \quad (2.17)$$

Thus an eigenvector is *symplectic orthogonal* to all vectors, including itself, but excluding the eigenvector(s) associated with its reciprocal eigenvalue. Zhong and Williams [25] have shown that the symplectic orthogonality relationship is a consequence of the reciprocal theorem of Betti-Maxwell [67]; of course this in turn is a consequence of the symmetry of the stiffness matrix \mathbf{K} . According to the reciprocal theorem, for two different load systems applied to the cell, denoted superscripts (1) and (2), the work done by the forces $\mathbf{F}^{(1)}$ acting through the displacements $\mathbf{d}^{(2)}$ is equal to the work done by the forces $\mathbf{F}^{(2)}$ acting through the displacements $\mathbf{d}^{(1)}$. For the single

cell, Figure 2.2(b), this may be written as

$$\mathbf{d}_L^{(1)T} \mathbf{F}_L^{(2)} + \mathbf{d}_R^{(1)T} \mathbf{F}_R^{(2)} = \mathbf{d}_L^{(2)T} \mathbf{F}_L^{(1)} + \mathbf{d}_R^{(2)T} \mathbf{F}_R^{(1)}. \quad (2.18)$$

Express the right hand side vectors, in terms of the left hand side vectors according to

$$\begin{aligned} \mathbf{d}_R^{(1)} &= \lambda_1 \mathbf{d}_L^{(1)}, & \mathbf{d}_R^{(2)} &= \lambda_2 \mathbf{d}_L^{(2)}, \\ \mathbf{F}_R^{(1)} &= \mathbf{p}_R^{(1)} = \lambda_1 \mathbf{p}_L^{(1)} = -\lambda_1 \mathbf{F}_L^{(1)}, & \mathbf{F}_R^{(2)} &= \mathbf{p}_R^{(2)} = \lambda_2 \mathbf{p}_L^{(2)} = -\lambda_2 \mathbf{F}_L^{(2)}, \end{aligned} \quad (2.19a, b)$$

to give

$$-\mathbf{d}_L^{(1)T} \mathbf{p}_L^{(2)} + \lambda_1 \lambda_2 \mathbf{d}_L^{(1)T} \mathbf{p}_L^{(2)} = -\mathbf{d}_L^{(2)T} \mathbf{p}_L^{(1)} + \lambda_1 \lambda_2 \mathbf{d}_L^{(2)T} \mathbf{p}_L^{(1)} \quad (2.20)$$

or

$$(1 - \lambda_1 \lambda_2) \left[\mathbf{d}_L^{(1)T} \mathbf{p}_L^{(2)} - \mathbf{d}_L^{(2)T} \mathbf{p}_L^{(1)} \right] = 0 \quad (2.21)$$

Now consider the term

$$\mathbf{X}_1^T \mathbf{J}_m \mathbf{X}_2 = \left[\mathbf{d}_L^{(1)T} \mathbf{p}_L^{(2)} - \mathbf{d}_L^{(2)T} \mathbf{p}_L^{(1)} \right] \quad (2.22)$$

which indicates that equation (2.21) is an expression of the symplectic orthogonality relationship.

2.3 EIGENANALYSIS

From Figure 2.2, the generalised force and displacement vectors are

$$\begin{aligned} \mathbf{p}_j &= \begin{bmatrix} P_{1x} & P_{1y} & M_{1z} & P_{2x} & P_{2y} & M_{2z} & P_{3x} & P_{3y} & M_{3z} \end{bmatrix}^T \\ \mathbf{p}_{j+1} &= \begin{bmatrix} P_{4x} & P_{4y} & M_{4z} & P_{5x} & P_{5y} & M_{5z} & P_{6x} & P_{6y} & M_{6z} \end{bmatrix}^T \\ \mathbf{d}_j &= \begin{bmatrix} u_1 & v_1 & \psi_1 & u_2 & v_2 & \psi_2 & u_3 & v_3 & \psi_3 \end{bmatrix}^T \\ \mathbf{d}_{j+1} &= \begin{bmatrix} u_4 & v_4 & \psi_4 & u_5 & v_5 & \psi_5 & u_6 & v_6 & \psi_6 \end{bmatrix}^T. \end{aligned} \quad (2.23)$$

The global stiffness matrix \mathbf{K} can generally be assembled using

$$\mathbf{K} = \boldsymbol{\beta}^T \mathbf{K}_L \boldsymbol{\beta}, \quad (2.24)$$

in which \mathbf{K}_L is a block diagonal matrix describing the stiffness of each individual member within the cell in local coordinate system, and $\boldsymbol{\beta}$ is the connectivity matrix.

\mathbf{K}_L can be readily determined by either FEM [68] or by matrix structural analysis [69].

The transformation matrix $\boldsymbol{\beta}$ is calculated by defining the direction cosine matrix in terms of the projections of the elements onto the global axes and then applying a series of rotations about three principal axes [67]. The transfer matrix \mathbf{G} is then determined

by simple manipulation of the stiffness matrix \mathbf{K} according to equation (2.7). Using the function *eig* within MATLAB, the eigenvalues of the transfer matrix \mathbf{G} are readily determined and these are listed in Table 2.1, together with those of the pin-jointed framework obtained in [10]. First note that the nature of the jointing has no effect on the number of unity eigenvalues; for the planar pin-jointed cell these are known to be the three rigid body modes, plus tension, bending moment and shearing force, and the method of jointing clearly has no bearing on these.

Table 2.1 Effect of jointing on eigenvalues

Rigid-jointed	Pin-jointed
1.6779×10^1	1.6870×10^1
3.5353	3.5436
5.9597×10^{-2}	5.9596×10^{-2}
<u>2.8286×10^{-1}</u>	<u>2.8292×10^{-1}</u>
-1.4331×10^1	-1.4244×10^1
-6.9779×10^{-2}	-7.0207×10^{-2}
-1.5689×10^1	1
-7.2812	1
-6.4316	1
-0.15548	1
-0.13734	1
-0.063740	1
1	
1	
1	
1	
1	
1	

Since the number of unity eigenvalues remains constant, the increase in size of the transfer matrix leads to new eigenvalues which must pertain to new decay modes. As seen in Table 2.1, rather than three reciprocal pairs for the pin-jointed case, one now has six pairs for the rigid-jointed framework. Physically, such pairs correspond to self-equilibrated loading on the left face of the cell decaying from left to right ($|\lambda| < 1$), while the inverse ($|\lambda^{-1}| > 1$) corresponds to self-equilibrated load applied on the right face of the cell decaying from right to left, which is equivalent to an increase from left to right. The two eigenvalues shown underlined in Table 2.1 are the *slowest* decay factors for the

two types of framework, and will dominate decay in the sense that they will penetrate the furthest distance into the structure. In practical terms, the effect of rigid jointing is negligible, resulting in a decrease in the *slowest* decay factor to 0.28286 from 0.28292,

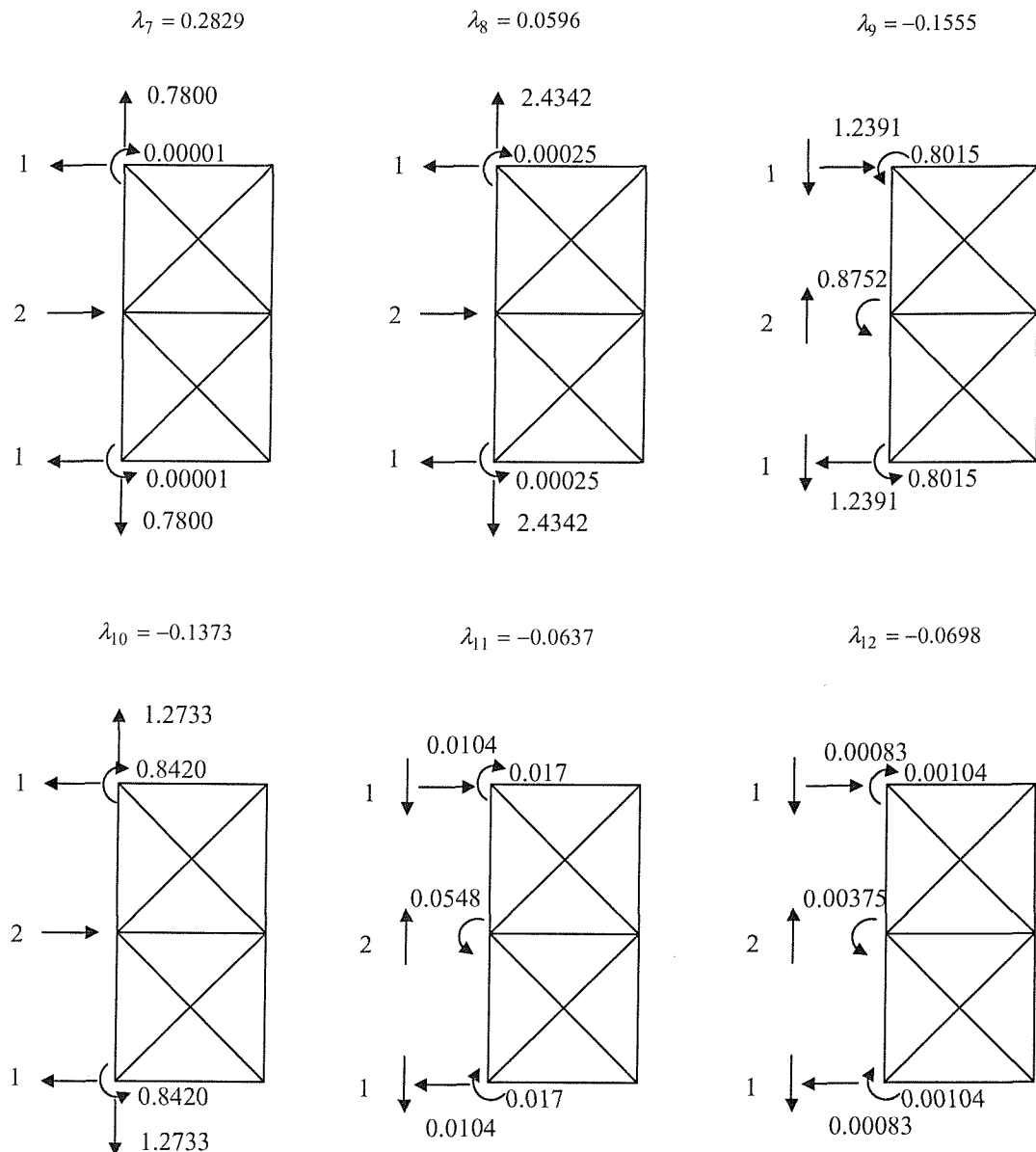


Figure 2.3. Nodal forces and moments for left-hand decay modes; displacements not shown.

indicating that the self-equilibrated loading associated with this eigenvalue would penetrate slightly further into the structure; this is as one might expect, since rigid-jointing should make the structure slightly stiffer.

The main effect of rigid-jointing is the introduction of three new decay modes, two of which ($\lambda_9 = -0.15548$, and $\lambda_{10} = -0.13734$) decay at approximately twice the rate of the dominant mode ($\lambda_7 = 0.28292$), the minus sign indicating that the decay is oscillatory from cell to cell. For the pin-jointed structure, the decay eigenvectors have self-equilibrated loading in the x - and y -directions only, it being impossible to apply a moment at a pin-joint; with rigid joints, these modes now have a very small additional self-equilibrated moment – indeed just sufficient that the displacement components of the eigenvector should decay with the specified eigenvalue. The new decay modes still have self-equilibrated loading in the x - and y -directions, but with the addition of comparatively large self-equilibrating moments. The force and moment components of the left-to-right decay eigenvectors are shown in Figure 2.3, and these were also determined using the *eig* function within MATLAB.

Determination of the vectors associated with the multiple unity eigenvalues, however, is not so simple. The QR algorithm employed within MATLAB essentially derives eigenvectors which, when combined to form a transformation matrix, *will* diagonalise the original matrix. However, there exist some matrices for which a sufficient number of independent eigenvectors do not exist for some or all of its *repeated* eigenvalues. These matrices are said to be *defective* and are not diagonalisable, but can be reduced to a near diagonal form known as the Jordan canonical form (JCF); this contains blocks in which a unity element exists on the super diagonal, indicating that a *principal vector* is coupled to an eigenvector. If the same repeated eigenvalue occurs in different Jordan blocks, then the matrix is also said to be *derogatory*. Reliable determination of the JCF of such a matrix can only be achieved when the matrix is known exactly, so its elements must be integers or ratios of small integers. Any small errors in the input matrix will completely change its JCF. Thus the six unity eigenvalues shown in Table 2.1, are computed by MATLAB as being very close, but not exactly equal, to unity as physical

argument demands they must. In turn the majority of the eigenvectors calculated by MATLAB must be discarded.

The procedures for dealing with defective matrices is best explained through a simple example [70]: suppose \mathbf{G} is a real, non-symmetric¹, 2×2 matrix. The eigenproblem is the solution of

$$(\mathbf{G} - \lambda \mathbf{I})\mathbf{s} = \mathbf{0}, \quad (2.25)$$

together with subsequent decomposition of the matrix \mathbf{G} : there exists a non-singular matrix \mathbf{V} such that

$$\mathbf{G} = \mathbf{V} \mathbf{J} \mathbf{V}^{-1}, \quad (2.26)$$

where \mathbf{J} is the Jordan canonical form.

There are three cases of interest:

- a) Suppose \mathbf{G} has eigenvalues λ_1 and λ_2 , not necessarily distinct, but having two independent eigenvectors \mathbf{v}_1 and \mathbf{v}_2 . That is, there are two solutions

$$\mathbf{G}\mathbf{v}_1 = \lambda_1 \mathbf{v}_1 \quad \text{and} \quad \mathbf{G}\mathbf{v}_2 = \lambda_2 \mathbf{v}_2. \quad (2.27)$$

Define the transformation matrix $\mathbf{V} = [\mathbf{v}_1 \ \mathbf{v}_2]$, which is non-singular, since the two vectors are linearly independent. Then

$$\mathbf{G} \mathbf{V} = [\mathbf{G}\mathbf{v}_1 \ \mathbf{G}\mathbf{v}_2] = [\lambda_1 \mathbf{v}_1 \ \lambda_2 \mathbf{v}_2] = [\mathbf{v}_1 \ \mathbf{v}_2] \begin{bmatrix} \lambda_1 & 0 \\ 0 & \lambda_2 \end{bmatrix}, \quad (2.28)$$

so, $\mathbf{G} \mathbf{V} = \mathbf{V} \mathbf{J}$, or $\mathbf{G} = \mathbf{V} \mathbf{J} \mathbf{V}^{-1}$. For this case, the Jordan form is diagonal, consisting of trivial (one-dimensional) blocks; that is, the matrix is diagonalisable.

- b) Suppose that \mathbf{G} has just one repeated eigenvalue λ_1 , and a single independent eigenvector, \mathbf{v}_1 . That is, there is just one solution

$$\mathbf{G}\mathbf{v}_1 = \lambda_1 \mathbf{v}_1 \quad (2.29)$$

Let \mathbf{w}_2 be a (principal) vector of the same dimension as, but independent of, \mathbf{v}_1 . Now, on account of the twofold eigenvalue, the characteristic equation takes the form

$(\lambda - \lambda_1)^2 = 0$, and according to the Cayley-Hamilton theorem [70], a square matrix will satisfy its own characteristic equation, that is

¹ Symmetric matrices are always diagonalisable.

$$(\mathbf{G} - \lambda_1 \mathbf{I})^2 = \mathbf{0}, \quad (2.30)$$

and post-multiply by \mathbf{w}_2 to give

$$(\mathbf{G} - \lambda_1 \mathbf{I})^2 \mathbf{w}_2 = \mathbf{0}. \quad (2.31)$$

Now define the relationship

$$(\mathbf{G} - \lambda_1 \mathbf{I}) \mathbf{w}_2 = \mathbf{v}_1, \quad (2.32)$$

this satisfies equation (2.31) as, pre-multiplying by $(\mathbf{G} - \lambda_1 \mathbf{I})$, one has

$$(\mathbf{G} - \lambda_1 \mathbf{I})^2 \mathbf{w}_2 = (\mathbf{G} - \lambda_1 \mathbf{I}) \mathbf{v}_1 = \mathbf{0}. \quad (2.33)$$

Equations (2.29) and (2.32) define a chain of eigen- and principal vectors

$$\begin{aligned} \mathbf{G} \mathbf{v}_1 &= \lambda_1 \mathbf{v}_1 \\ \mathbf{G} \mathbf{w}_2 &= \lambda_1 \mathbf{w}_2 + \mathbf{v}_1. \end{aligned} \quad (2.34)$$

Note that any multiple (c) of the eigenvector \mathbf{v}_1 may be added to the principal vector \mathbf{w}_2 , and the new vector is also a principal vector, that is, they are not unique:

$$\mathbf{G}(\mathbf{w}_2 + c\mathbf{v}_1) = \lambda_1(\mathbf{w}_2 + c\mathbf{v}_1) + \mathbf{v}_1, \quad \text{since} \quad \mathbf{G}c\mathbf{v}_1 = \lambda_1 c\mathbf{v}_1. \quad (2.35)$$

Now define the transformation matrix $\mathbf{V} = [\mathbf{v}_1 \ \mathbf{w}_2]$, which is non-singular, since the two vectors are independent. Then

$$\mathbf{G} \mathbf{V} = [\mathbf{G} \mathbf{v}_1 \ \mathbf{G} \mathbf{w}_2] = [\lambda_1 \mathbf{v}_1 \ \lambda_1 \mathbf{w}_2 + \mathbf{v}_1] = [\mathbf{v}_1 \ \mathbf{w}_2] \begin{bmatrix} \lambda_1 & 1 \\ 0 & \lambda_1 \end{bmatrix}, \quad (2.36)$$

so, $\mathbf{G} \mathbf{V} = \mathbf{V} \mathbf{J}$, or $\mathbf{G} = \mathbf{V} \mathbf{J} \mathbf{V}^{-1}$. For this case, the Jordan form is not diagonal, and consists of the repeated eigenvalue on the leading diagonal, and a unity on the super-diagonal.

c) Suppose \mathbf{G} has complex eigenvalues $\lambda_1 = \alpha - i\beta$, $\lambda_2 = \alpha + i\beta$ with associated eigenvectors $\mathbf{v}_1 = \mathbf{u} + i\mathbf{v}$ and $\mathbf{v}_2 = \mathbf{u} - i\mathbf{v}$, where \mathbf{u} and \mathbf{v} are real and independent. If one employs the transformation matrix $\mathbf{V} = [\mathbf{v}_1 \ \mathbf{v}_2]$, then

$$\mathbf{G} \mathbf{V} = [\mathbf{G} \mathbf{v}_1 \ \mathbf{G} \mathbf{v}_2] = [(\alpha - i\beta) \mathbf{v}_1 \ (\alpha + i\beta) \mathbf{v}_2] = [\mathbf{v}_1 \ \mathbf{v}_2] \begin{bmatrix} (\alpha - i\beta) & 0 \\ 0 & (\alpha + i\beta) \end{bmatrix}. \quad (2.37)$$

This formulation is just a particular case of a), with complex conjugate eigenvalues and eigenvectors. Instead, employ the real and imaginary parts of the eigenvectors as transformation matrix, that is $\mathbf{V} = [\mathbf{u} \ \mathbf{v}]$. First, however, note that

$$\mathbf{G}(\mathbf{u} + i\mathbf{v}) = (\alpha - i\beta)(\mathbf{u} + i\mathbf{v}) = \alpha\mathbf{u} + \beta\mathbf{v} + i(-\beta\mathbf{u} + \alpha\mathbf{v}), \quad (2.38)$$

and taking the real and imaginary parts, gives

$$\mathbf{G}\mathbf{u} = \alpha\mathbf{u} + \beta\mathbf{v}, \quad \mathbf{G}\mathbf{v} = -\beta\mathbf{u} + \alpha\mathbf{v}. \quad (2.39)$$

One then has

$$\mathbf{G}\mathbf{V} = [\mathbf{G}\mathbf{u} \ \mathbf{G}\mathbf{v}] = [(\alpha\mathbf{u} + \beta\mathbf{v}) \ (-\beta\mathbf{u} + \alpha\mathbf{v})] = [\mathbf{u} \ \mathbf{v}] \begin{bmatrix} \alpha & -\beta \\ \beta & \alpha \end{bmatrix}, \quad (2.40)$$

so the Jordan form now takes a real block form.

In order to determine the eigen- and principal vectors, it is generally acknowledged that one should start with the principal vector of the highest grade, when any other principal vectors in the chain, together with the *generating* eigenvector are calculated simply by matrix multiplication; for example, in equation (2.32), the eigenvector \mathbf{v}_1 can be immediately calculated once the principal vector \mathbf{w}_2 is known. On the other hand, if one starts with the eigenvector, because of the non-uniqueness of the principal vector, it is necessary to make an arbitrary choice for inclusion of multiples of the eigenvector, as in equation (2.34); for principal vectors of higher grade, one has to make an arbitrary choice for inclusion of multiples of eigenvector and principal vectors of a lower grade.

From null spaces of the extended matrices, Wong and Leung [71] developed a general approach to determine the simplest JCF of an arbitrary matrix, which is both *defective* and *derogatory*. Forward and backward processes are employed to determine first the eigen- and principal vectors of the extended matrices, and then the indeterminate constants are eliminated by requiring orthogonality of principal vectors of lower grade with those of higher grade. Mathematically, the process to determining the eigen- and principal vectors is accomplished so long as the simplest JCF is achieved. However, within the spirit of eigenanalysis by transfer matrix method, it is known that the eigen- and principal vectors pertaining to multiple unity eigenvalues represent the transmission modes of the resultants of tension, torsion, bending moments and shearing forces.

Physical interpretation of these vectors allows determination of the equivalent continuum properties of the repetitive structure. Thus, the determination of the principal vectors should not stop until both JCF and all the vectors are given in their simplest forms. Indeed, the procedure described in [71] provides a rather straightforward means to determine all the eigen- and principal vectors of the transfer matrix, which can then be transformed into the simplest JCF. Nevertheless, those principal vectors are not given in their simplest forms since principal vectors of higher grade are coupled with those of lower grade within each Jordan block. In practice, the difficulty to uncouple those lower grade vectors from the higher order ones is equivalent to making the arbitrary choices in the first step when following the chain in equation (2.31).

Therefore, despite being the least favoured method, the approach described in equation (2.34) is adopted here. This is because the eigenvectors associated with the multiple unity eigenvalues are obviously the rigid body displacements, so can be assigned their simplest value at the outset. This helps considerably in the physical interpretation of the principal vectors². The difference in the two approaches by equations (2.31, 2.32) and (2.34) is essentially whether to make a difficult choice once (the favoured method), or whether to make a simple choice, several times (the method employed here).

Mindful of the above, rather than employing the *eig* function within MATLAB, instead the set of equations (with eigenvalue set equal to unity)

$$(\mathbf{G} - \mathbf{I}) \mathbf{v}_i = 0, \quad (2.41)$$

are reduced to their simplest row echelon forms using the *rref* function, and the MATLAB command *rref*([\mathbf{G} –*eye*(18)]). This indicates that there are two independent eigenvectors: the rigid body displacements in the *x*- and *y*-directions and these are given their simplest values by setting

$$\mathbf{v}_1 = [1 \ 0 \ 0 \ 1 \ 0 \ 0 \ 0 \ 1 \ 0 \ 0 \ 0 \ 0 \ 0 \ 0 \ 0 \ 0 \ 0 \ 0]^T \quad (2.42)$$

for the former, and

$$\mathbf{v}_2 = [0 \ 1 \ 0 \ 0 \ 1 \ 0 \ 0 \ 0 \ 1 \ 0 \ 0 \ 0 \ 0 \ 0 \ 0 \ 0 \ 0 \ 0]^T \quad (2.43)$$

² This issue is considered in greater depth in Chapter 6 where one has multiple complex unity eigenvalues.

for the latter. Principal vectors associated with these independent eigenvectors are then calculated using the chain of equations

$$\begin{aligned} (\mathbf{G} - \mathbf{I}) \mathbf{v}_i &= 0 \\ (\mathbf{G} - \mathbf{I}) \mathbf{w}_{i+1} &= \mathbf{v}_i \\ &\vdots \\ (\mathbf{G} - \mathbf{I}) \mathbf{w}_k &= \mathbf{w}_{k-1} \end{aligned} \quad (2.44)$$

Now, the *rref* function is employed on the augmented matrix $[\mathbf{G} - \mathbf{I}, \mathbf{v}_i]$ to find \mathbf{w}_{i+1} , and this process is repeated to find the principal vector of the highest grade \mathbf{w}_k , after which no new vectors are generated. In this way, it is found that the principal vector describing tension is coupled to the rigid body displacement in the x -direction in a 2×2 Jordan block, while the principal vectors (in ascending grade) describing rotation about the z -axis, bending moment and shearing force are coupled with rigid body translation in the y -direction, in a 4×4 Jordan block.

A similarity matrix \mathbf{V} comprised of all eigen- and principal vectors, including both decay and transmission modes, is then constructed, and this transforms the transfer matrix \mathbf{G} to Jordan canonical form. Since the repeated unity eigenvalue appears in two distinct Jordan blocks, the transfer matrix \mathbf{G} is both *defective* and *derogatory*. Both \mathbf{V} and \mathbf{J} are given in Appendix 2.

Not only does the Jordan canonical form reveal the coupling between the various modes, it also allows one to calculate powers of the transfer matrix \mathbf{G} in the most efficient manner; suppose one knows the applied state vector $\mathbf{s}(0)$ on the zeroth left-hand end of the structure in Figure 2.1; the state vector on the right-hand side of this first cell is given by

$$\mathbf{s}(1) = \mathbf{G} \mathbf{s}(0), \quad (2.45)$$

and the state vector on the right-hand side of the n^{th} is then

$$\mathbf{s}(n) = \mathbf{G}^n \mathbf{s}(0). \quad (2.46)$$

Powers of the transfer matrix are evaluated according to

$$\mathbf{G}^n = (\mathbf{V} \mathbf{J} \mathbf{V}^{-1})^n = (\mathbf{V} \mathbf{J} \mathbf{V}^{-1})(\mathbf{V} \mathbf{J} \mathbf{V}^{-1}) \dots (\mathbf{V} \mathbf{J} \mathbf{V}^{-1}) = \mathbf{V} \mathbf{J}^n \mathbf{V}^{-1}. \quad (2.47)$$

Moreover, the n^{th} power of the JCF simply requires evaluation of the n^{th} power of the diagonal elements, although for the non-trivial Jordan blocks, a more involved treatment is required. Suppose a Jordan block pertaining to eigenvalue λ , having dimension $k \times k$, is written as

$$\mathbf{J}_i = \begin{bmatrix} \lambda & 1 & & \\ & \ddots & \ddots & \\ & & \lambda & 1 \\ & & & \lambda \end{bmatrix} = \lambda \mathbf{I} + \mathbf{N}, \quad (2.48)$$

where \mathbf{N} is the *nilpotent* matrix

$$\mathbf{N}_i = \begin{bmatrix} 0 & 1 & & \\ & \ddots & \ddots & \\ & & 0 & 1 \\ & & & 0 \end{bmatrix}. \quad (2.49)$$

The k^{th} power of the nilpotent matrix is zero, so the binomial expansion of

$\mathbf{J}_i^n = (\lambda \mathbf{I} + \mathbf{N})^n$ has a finite number of terms, as

$$(\lambda \mathbf{I} + \mathbf{N})^n = \lambda^n \mathbf{I} + \binom{n}{1} \lambda^{n-1} \mathbf{N} + \binom{n}{2} \lambda^{n-2} \mathbf{N}^2 + \cdots + \binom{n}{k-1} \lambda^{n-k+1} \mathbf{N}^{k-1}, \quad (2.50)$$

since higher powers of \mathbf{N}_i are zero; in the above the binomial coefficients are given by

$$\binom{n}{b} = \frac{n(n-1)(n-2)\cdots(n-b+1)}{b!}. \quad (2.51)$$

The n^{th} power of the Jordan block becomes

$$\mathbf{J}_i^n = \begin{bmatrix} \lambda^n & n\lambda^{n-1} & \frac{n(n-1)}{2} \lambda^{n-2} & \cdots \\ 0 & \lambda^n & n\lambda^{n-1} & \cdots \\ 0 & 0 & \lambda^n & \cdots \\ \cdots & \cdots & \cdots & \cdots \end{bmatrix}. \quad (2.52)$$

2.4 EQUIVALENT CONTINUUM PROPERTIES

Physical interpretation of the transmission eigen- and principal vectors in \mathbf{V} allows determination of the equivalent continuum beam properties of the framework, as follows:

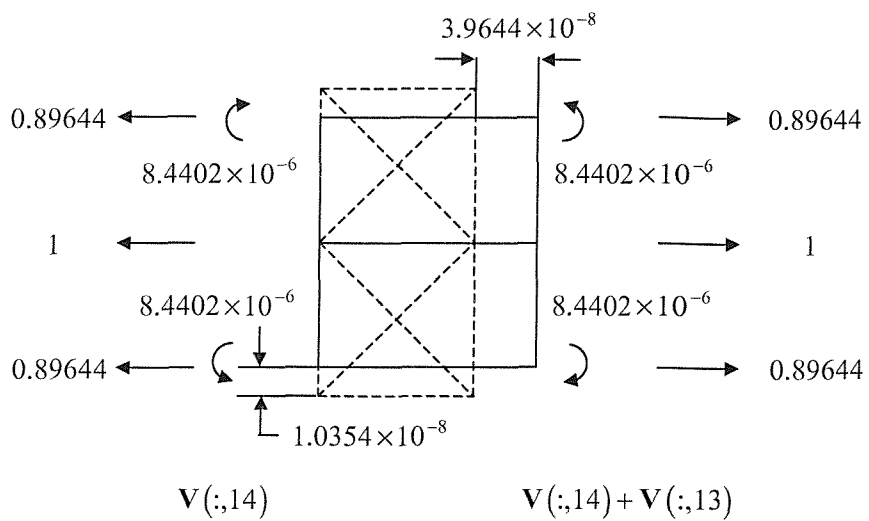


Figure 2.4. Coupling of eigenvector $\mathbf{V}(:,13)$ for rigid body displacement in the x -direction, with principal vector $\mathbf{V}(:,14)$ for tension; here and later, dotted lines show initial cell configuration.

a) Consider the vectors for tension and rigid body displacement in the x -direction, which are coupled within a 2×2 block in the JCF, and are the fourteenth and thirteenth columns of the transformation matrix \mathbf{V} . The rigid body displacement can exist in its own right if the cell is not restrained in the x -direction. According to the chain equations (2.44), these two vectors have the relationship³

$$\mathbf{G}\mathbf{V}(:,14) = \mathbf{V}(:,14) + \mathbf{V}(:,13), \quad (2.53)$$

which is interpreted as stating that when a tension vector $\mathbf{V}(:,14)$ is applied to the left hand side of the cell, on the right hand side, equivalent to pre-multiplication by \mathbf{G} , one has both the tension vector and a rigid body displacement in the x -direction, $\mathbf{V}(:,13)$. Physical representation of the above is shown in Figure 2.4, from which it can be seen that a total resultant tensile load of $T_x = 1 + 2 \times 0.89644 = 2.7929$ N is coupled with a cell elongation of 3.9644×10^{-8} m; note that vectors are shown scaled such that the largest force component has unit magnitude. The continuum beam constitutive relationship for tension is

$$T_x = \frac{EA}{L} u, \quad (2.54)$$

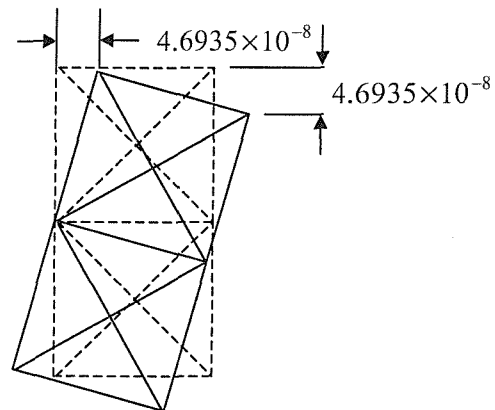
³ Vectors are now described using the MATLAB notation for a column within a matrix.

and since T_x , E , u , L are known, the equivalent cross sectional area of the framework is calculated as $A = 3.52246 \text{ cm}^2$. Additionally, there is a Poisson's ratio effect on the cross section: axial strain in the x -direction is $\varepsilon_x = u/L = 3.9644 \times 10^{-8}$, while transverse strain in the y -direction is $\varepsilon_y = (-2 \times 1.0354 \times 10^{-8})/2 = -1.0354 \times 10^{-8}$; inserting into $\varepsilon_y = -\nu\varepsilon_x$ gives the equivalent Poisson's ratio $\nu = 0.261188$, and the equivalent shear modulus is determined as $G = E/2(1+\nu) = 79.29 \times 10^9 \text{ Nm}^{-2}$, with the Young's modulus E being regarded as fixed.

b) Next consider the vectors for shear, bending moment, rigid body rotation about the z -axis and rigid body displacement in the y -direction; these are the eighteenth to fifteenth columns of the transformation matrix \mathbf{V} , and are coupled within a 4×4 block of the JCF. Again, the eigenvector $\mathbf{V}(:,15)$ for rigid body displacement in the y -direction can exist in its own right when the cell is free of constraint. The sixteenth column $\mathbf{V}(:,16)$ defines rigid body rotation of the cell about the z -axis is coupled with the rigid body transverse displacement of the cell according to the relationship

$$\mathbf{G}\mathbf{V}(:,16) = \mathbf{V}(:,16) + \mathbf{V}(:,15) \quad (2.55)$$

and is represented in Figure 2.5.



$$\mathbf{V}(:,16) \quad \mathbf{V}(:,16) + \mathbf{V}(:,15)$$

Figure 2.5. Coupling of eigenvector $\mathbf{V}(:,15)$ for rigid body displacement in the y -direction, with principal vector $\mathbf{V}(:,16)$ for rigid body rotation; y -components of displacements on the left-hand side are negligible.

The seventeenth column $\mathbf{V}(:,17)$ defines a bending moment, and is coupled with the rotation vector $\mathbf{V}(:,16)$ according to

$$\mathbf{G}\mathbf{V}(:,17) = \mathbf{V}(:,17) + \mathbf{V}(:,16). \quad (2.56)$$

Physical representation of this is given in Figure 2.6, where it is seen that a bending moment $M = (2 + 3.2974 \times 10^{-5}) \text{ Nm}$ results in a bending curvature of $1/R = 4.6935 \times 10^{-8} \text{ m}^{-1}$, where the latter is calculated from the similar triangles shown in Figure 2.6; in particular one such triangle is the deformed upper half of the left hand face of the cell, while the second is the lower half projected to the centre of curvature. According to the constitutive relationship for beam bending

$$M = EI/R, \quad (2.57)$$

the equivalent second moment of area is found to be $I = 2.13065 \times 10^{-4} \text{ m}^4$. It is noted that rigid jointing has the effect of introducing very small (indeed negligible) nodal moments into the bending moment vector, as shown in Figure 2.6.

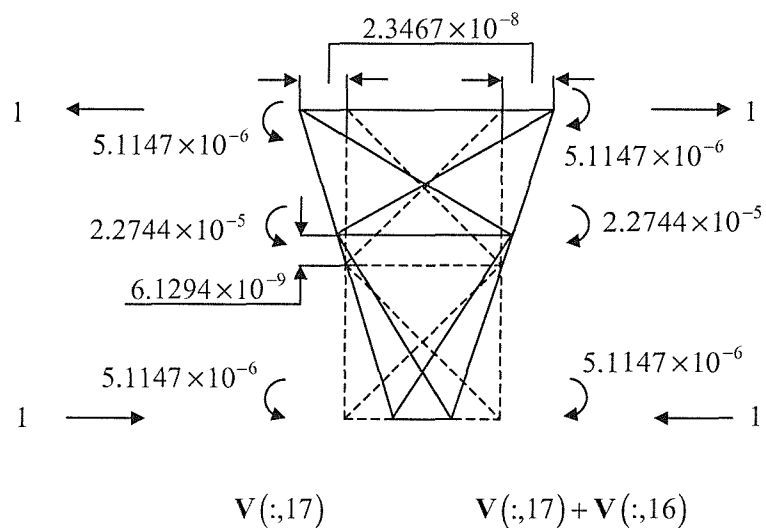


Figure 2.6. Coupling of principal vector $\mathbf{V}(:,16)$ for rigid body rotation, with principal vector $\mathbf{V}(:,17)$ for pure bending.

Finally, the eighteenth column $\mathbf{V}(:,18)$, which defines a shear vector, is coupled with the bending moment vector $\mathbf{V}(:,17)$ according to the relationship

$$\mathbf{G}\mathbf{V}(:,18) = \mathbf{V}(:,18) + \mathbf{V}(:,17), \quad (2.58)$$

and this is shown in Figure 2.7. Since a state of *pure shear* cannot exist if the upper and lower surfaces are free of traction, as in Saint-Venant's problem, so a bending moment is always required to balance the moment produced by the shearing force, as seen on the left hand face of the cell in Figure 2.7. Consequently, the shearing vector will produce both a shear angle and a bending curvature, and the displacement components in the x -direction are decomposed into these two components, as shown in Figures 2.8(a, b).

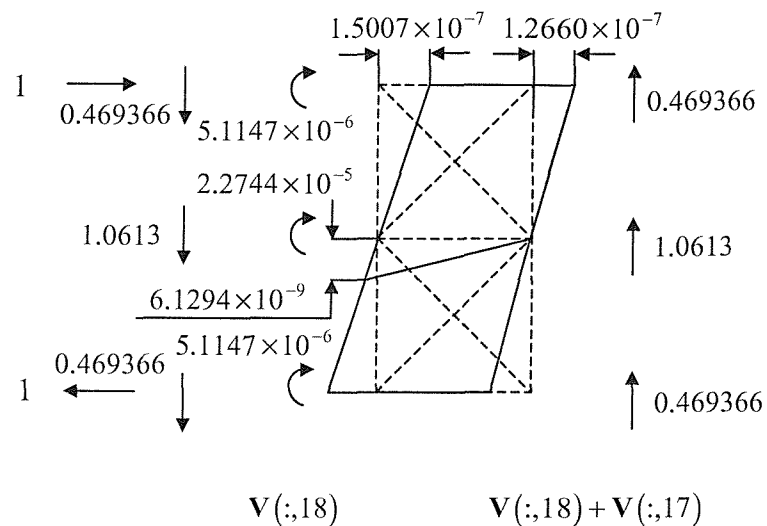


Figure 2.7. Coupling of principal vector $\mathbf{V}(:,18)$ for shearing force and left-hand bending moment, with principal vector $\mathbf{V}(:,17)$ for pure bending.

Within Timoshenko beam theory [72], the shear angle is defined according to the relationship $\gamma = \psi - dv/dx$, in which dv/dx is the centreline slope and ψ is rotation of the cross-section. The simplest method of evaluating the shear angle is to impose a rotation on the cell in Figure 2.7 to bring the centreline slope to the horizontal, when dv/dx is zero and $\gamma = \psi$; this, together with consideration of Figure 2.8(a), gives the shear angle $\gamma = 1.44465 \times 10^{-7}$, and the shearing force has magnitude $Q = 1.0613 + 2 \times 0.469366 = 2.000032$. The equation for shear is

$$Q = \kappa A G \gamma, \quad (2.59)$$

which yields the equivalent shear coefficient of the cell as $\kappa = 0.4957$. The deformation shown in Figure 2.8(b) is equivalent to a bending curvature of $1/R' = 2.3468 \times 10^{-8}$, which is exactly half of the bending curvature seen when the cell

is subject to pure bending. This is as one might expect: the bending moment varies linearly from zero on the right hand side of the cell, to the full value as expressed by the vector $\mathbf{V}(:,17)$ on the left; the average of the bending moment *resident* within the shear vector is therefore one-half of the full value and, in turn, so is the curvature.

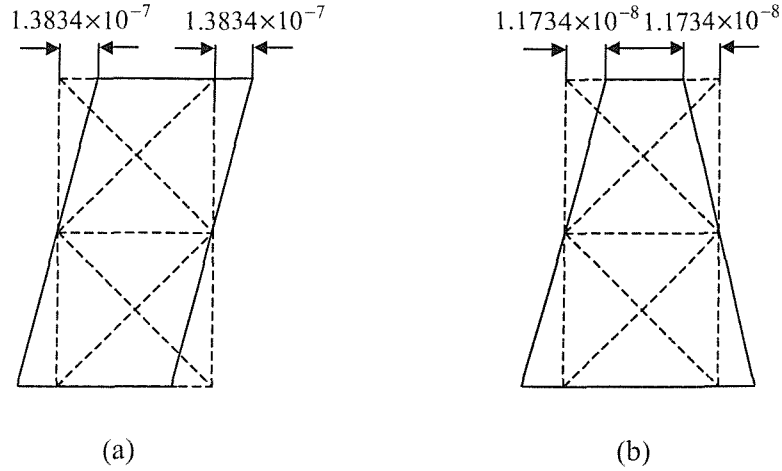


Figure 2.8. Decomposition of the displacements in the x -direction from Figure 2.7: (a) shear angle due to the shearing force; (b) bending curvature due to the left-hand bending moment.

Note that the small moment terms within both the bending moment and shear force vectors have been included in evaluation of the continuum properties; indeed they are necessary to ensure exact moment equilibrium of the cell.

Table 2.2 Effect of jointing on equivalent continuum properties

Continuum properties	Rigid-jointed	Pin-jointed
Cross-sectional area, A cm ²	3.52246	3.52241
Second moment of area, I m ⁴	2.13065×10^{-4}	2.13061×10^{-4}
Poisson's ratio, ν	0.26119	0.26120
Shear modulus, G N/m ²	79.29030×10^9	79.2893×10^9
Shear coefficient, κ	0.49569	0.49562

The equivalent continuum properties of the rigid-jointed framework determined above are listed in Table 2.2, together with those of the pin-jointed framework obtained in

[10]. Clearly the axial stiffness EA , the bending stiffness EI and the shear stiffness $\kappa A G$ are slightly increased when the cell is rigid-jointed, but the differences are negligible.

Note that an increase in the equivalent shear modulus G requires a commensurate decrease in Poisson's ratio, bearing in mind that Young's modulus E is regarded as invariant. Thus one concludes that, certainly as far as calculation of the equivalent continuum properties is concerned, treating a rigid-jointed structure as pin-jointed, is quite justified. This is in accord with Noor's view [14], *for lattice structures with rigid joints, provided that the response is not dominated by local member deformation, ordinary continuum models are good enough for the accurate prediction of the global response of lattices with rigid joints.* That is, one need not employ a micro-polar continuum model for such structures.

APPENDIX 2

TRANSFORMATION MATRIX AND JORDAN CANONICAL FORM OF 2D RIGID-JOINTED FRAMEWORK, FIGURE 2.1

$$V = \begin{bmatrix} 1.6409 \times 10^{-8} & -6.1083 \times 10^{-9} & -5.8236 \times 10^{-9} & 4.1570 \times 10^{-10} & 1.9148 \times 10^{-9} & 4.2902 \times 10^{-8} \\ 1.7431 \times 10^{-7} & 4.6051 \times 10^{-8} & 4.5165 \times 10^{-8} & 1.4971 \times 10^{-7} & 1.5542 \times 10^{-7} & 3.9539 \times 10^{-8} \\ 3.1848 \times 10^{-10} & -1.1607 \times 10^{-9} & -1.9274 \times 10^{-8} & 7.4118 \times 10^{-7} & 6.5758 \times 10^{-7} & -2.2798 \times 10^{-11} \\ -7.9833 \times 10^{-8} & 0 & 0 & -3.9625 \times 10^{-8} & 0 & -9.3071 \times 10^{-8} \\ 0 & -4.0696 \times 10^{-8} & -3.9724 \times 10^{-8} & 0 & 5.0824 \times 10^{-8} & 0 \\ 0 & 2.3823 \times 10^{-9} & 3.5558 \times 10^{-8} & 0 & 4.1160 \times 10^{-7} & 0 \\ 1.6409 \times 10^{-8} & 6.1083 \times 10^{-9} & 5.8236 \times 10^{-9} & 4.1570 \times 10^{-10} & -1.9148 \times 10^{-9} & 4.2902 \times 10^{-8} \\ -1.7431 \times 10^{-7} & 4.6051 \times 10^{-8} & 4.5165 \times 10^{-8} & -1.4971 \times 10^{-7} & 1.5542 \times 10^{-7} & -3.9539 \times 10^{-8} \\ -3.1848 \times 10^{-10} & -1.1607 \times 10^{-9} & -1.9274 \times 10^{-8} & -7.4118 \times 10^{-7} & 6.5758 \times 10^{-7} & 2.2798 \times 10^{-11} \\ 1 & 8.333 \times 10^{-4} & 1.0369 \times 10^{-2} & 1 & 1.2391 & 1 \\ 2.4342 & 1 & 1 & 1.2733 & 1 & 0.7800 \\ 2.4542 \times 10^{-4} & -1.0417 \times 10^{-3} & -1.7005 \times 10^{-2} & 8.4203 \times 10^{-1} & 8.0152 \times 10^{-1} & 1.3901 \times 10^{-5} \\ -2 & 0 & 0 & -2 & 0 & -2 \\ 0 & -2 & -2 & 0 & -2 & 0 \\ 0 & 3.7501 \times 10^{-3} & 5.4748 \times 10^{-2} & 0 & 8.7521 \times 10^{-1} & 0 \\ 1 & -8.333 \times 10^{-4} & -1.0369 \times 10^{-2} & 1 & -1.2391 & 1 \\ -2.4342 & 1 & 1 & -1.2733 & 1 & -0.7800 \\ -2.4542 \times 10^{-3} & -1.0417 \times 10^{-3} & -1.7005 \times 10^{-2} & -8.4203 \times 10^{-1} & 8.0152 \times 10^{-1} & -1.3901 \times 10^{-5} \end{bmatrix}$$

-1.6409×10^{-8}	-6.1083×10^{-9}	-5.8236×10^{-9}	-4.1570×10^{-10}	1.9148×10^{-9}	-4.2902×10^{-8}
1.7431×10^{-7}	-4.6051×10^{-8}	-4.5165×10^{-8}	1.4971×10^{-7}	-1.5542×10^{-7}	3.9539×10^{-8}
-3.1848×10^{-10}	-1.1607×10^{-9}	-1.9274×10^{-8}	-7.4118×10^{-7}	6.5758×10^{-7}	2.2798×10^{-11}
7.9833×10^{-8}	0	0	3.9625×10^{-8}	0	9.3071×10^{-8}
0	4.0696×10^{-8}	3.9724×10^{-8}	0	-5.0824×10^{-8}	0
0	2.3823×10^{-9}	3.5558×10^{-8}	0	4.1160×10^{-7}	0
-1.6409×10^{-8}	6.1083×10^{-9}	5.8236×10^{-9}	-4.1570×10^{-10}	-1.9148×10^{-9}	-4.2902×10^{-8}
-1.7431×10^{-7}	-4.6051×10^{-8}	-4.5165×10^{-8}	-1.4971×10^{-7}	-1.5542×10^{-7}	-3.9539×10^{-8}
3.1848×10^{-10}	-1.1607×10^{-9}	-1.9274×10^{-8}	7.4118×10^{-7}	6.5758×10^{-7}	-2.2798×10^{-11}
1	-8.333×10^{-4}	-1.0369×10^{-2}	1	-1.2391	1
-2.4342	1	1	-1.2733	1	-0.7800
2.4542×10^{-4}	1.0417×10^{-3}	1.7005×10^{-2}	8.4203×10^{-1}	-8.0152×10^{-1}	1.3901×10^{-5}
-2	0	0	-2	0	-2
0	-2	-2	0	-2	0
0	-3.7501×10^{-3}	-5.4748×10^{-2}	0	-8.7521×10^{-1}	0
1	8.333×10^{-4}	1.0369×10^{-2}	1	1.2391	1
2.4342	1	1	1.2733	1	0.7800
-2.4542×10^{-3}	1.0417×10^{-3}	1.7005×10^{-2}	-8.4203×10^{-1}	-8.0152×10^{-1}	-1.3901×10^{-5}

$$\begin{bmatrix}
3.9644 \times 10^{-8} & 0 & 0 & 4.6935 \times 10^{-8} & -2.3467 \times 10^{-8} & 1.5007 \times 10^{-7} \\
0 & -1.0354 \times 10^{-8} & -4.6935 \times 10^{-8} & 0 & 0 & 0 \\
0 & 0 & 0 & 0 & 2.3467 \times 10^{-11} & -5.8754 \times 10^{-11} \\
3.9644 \times 10^{-8} & 0 & 0 & -4.6935 \times 10^{-8} & 0 & 0 \\
0 & 0 & -4.6935 \times 10^{-8} & 0 & 6.1294 \times 10^{-9} & -6.1294 \times 10^{-9} \\
0 & 0 & 0 & 0 & 2.3467 \times 10^{-11} & -8.8992 \times 10^{-11} \\
3.9644 \times 10^{-8} & 0 & 0 & 0 & 2.3467 \times 10^{-8} & -1.5007 \times 10^{-7} \\
0 & 1.0354 \times 10^{-8} & -4.6935 \times 10^{-8} & 0 & 0 & 0 \\
0 & 0 & 0 & 0 & 2.3467 \times 10^{-11} & -5.8754 \times 10^{-11} \\
0 & 8.9644 \times 10^{-1} & 0 & 0 & 1 & -1 \\
0 & 0 & 0 & 0 & 0 & 4.6937 \times 10^{-1} \\
0 & 8.4402 \times 10^{-6} & 0 & 0 & -5.1147 \times 10^{-6} & 5.1147 \times 10^{-6} \\
0 & 1 & 0 & 0 & 0 & 0 \\
0 & 0 & 0 & 0 & 0 & 1.0613 \\
0 & 0 & 0 & 0 & -2.2744 \times 10^{-5} & 2.2744 \times 10^{-5} \\
0 & 8.9644 \times 10^{-1} & 0 & 0 & -1 & 1 \\
0 & 0 & 0 & 0 & 0 & 4.6937 \times 10^{-1} \\
0 & -8.4402 \times 10^{-6} & 0 & 0 & -5.1147 \times 10^{-6} & 5.1147 \times 10^{-6}
\end{bmatrix}$$

$\mathbf{V}^{-1} \mathbf{G} \mathbf{V} = \mathbf{J}$, where \mathbf{J} is the Jordan block matrix

$$\mathbf{J} = \begin{bmatrix} 1.6779 \times 10 & 0 & 0 & 0 & 0 & 0 \\ 0 & -1.4331 \times 10 & 0 & 0 & 0 & 0 \\ 0 & 0 & -1.5689 \times 10 & 0 & 0 & 0 \\ 0 & 0 & 0 & -7.2812 & 0 & 0 \\ 0 & 0 & 0 & 0 & -6.4316 & 0 \\ 0 & 0 & 0 & 0 & 0 & 3.5353 \\ 0 & 0 & 0 & 0 & 0 & 0 \\ 0 & 0 & 0 & 0 & 0 & 0 \\ 0 & 0 & 0 & 0 & 0 & 0 \\ 0 & 0 & 0 & 0 & 0 & 0 \\ 0 & 0 & 0 & 0 & 0 & 0 \\ 0 & 0 & 0 & 0 & 0 & 0 \\ 0 & 0 & 0 & 0 & 0 & 0 \\ 0 & 0 & 0 & 0 & 0 & 0 \\ 0 & 0 & 0 & 0 & 0 & 0 \\ 0 & 0 & 0 & 0 & 0 & 0 \end{bmatrix}$$

0	0	0	0	0	0
0	0	0	0	0	0
0	0	0	0	0	0
0	0	0	0	0	0
0	0	0	0	0	0
2.8286×10^{-1}	0	0	0	0	0
0	5.9597×10^{-2}	0	0	0	0
0	0	-1.5548×10^{-1}	0	0	0
0	0	0	-1.3743×10^{-1}	0	0
0	0	0	0	-6.3740×10^{-2}	0
0	0	0	0	0	-6.9779×10^{-2}
0	0	0	0	0	0
0	0	0	0	0	0
0	0	0	0	0	0
0	0	0	0	0	0
0	0	0	0	0	0
0	0	0	0	0	0
0	0	0	0	0	0

[0 1 1]

0 1 1 0

0 1 1 0 0

0 1 0 0 0

0 1 1 0 0 0

0 1 0 0 0 0 0

2.27

CHAPTER THREE

AN ALTERNATIVE APPROACH FOR DETERMINATION OF EQUIVALENT CONTINUUM PROPERTIES

3.1 INTRODUCTION

In this Chapter, the continuum properties of repetitive structure are found without resorting to eigenanalysis. The cell is first defined by its stiffness matrix, \mathbf{K} . The approach then relies upon the ability to deduce the displacement vectors for tension, bending moment and shear; this is straightforward for tension and bending. The shear displacement vector is not immediately obvious, but can be deduced employing elementary requirements of force and moment equilibrium of the cell. A once and for all application of the principle of minimum potential energy for tension yields the equivalent continuum Poisson's ratio, from which all the remaining properties follow. For simplicity, we consider again the planar structure treated in [10] and then without derivation, present more general expressions for the continuum properties in terms of length and cross-sectional area for this particular cell configuration, allowing more general conclusions to be drawn. When compared with eigenanalysis, which is essentially a numerical technique, the new approach has the advantage of yielding analytical expressions for the continuum properties.

3.2 EXAMPLE STRUCTURE

We consider the beam-like repetitive pin-jointed framework previously shown in Figure 2.1; the typical repeating cell is shown in bold, together with nodal numbering. Horizontal and vertical members have a cross-sectional area of 1 cm^2 , while the diagonal members have area of 0.5 cm^2 . However, since vertical members are regarded as being shared between adjacent cells, *for the single cell* their cross-sectional area is also 0.5 cm^2 . Young's modulus for each member is taken to be $200 \times 10^9 \text{ N/m}^2$ and this, together with the length and depth of the cell of 1 m and 2 m, respectively, is regarded as applying equally to the equivalent continuum beam.

3.3 EXACT EQUIVALENT CONTINUUM PROPERTIES OF THE EXAMPLE STRUCTURE

The stiffness matrix \mathbf{K} for the single cell can be found by a variety of means, see for example [69], and relates the nodal force and displacement components according to

$$\mathbf{F} = \mathbf{K} \mathbf{d}, \quad (3.1)$$

which is presented explicitly in the Appendix 3.

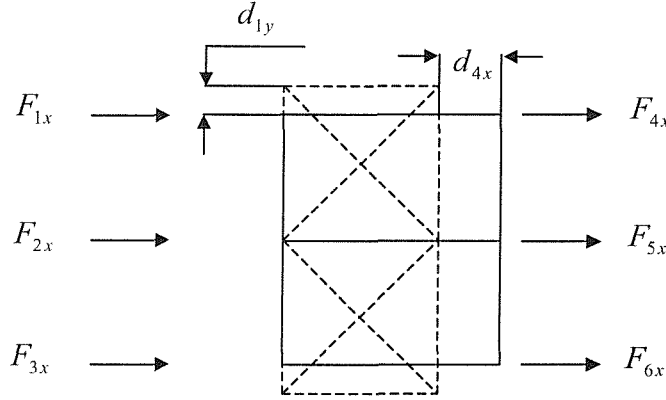


Figure 3.1. Single cell loaded in tension; dotted lines show initial cell configuration.

We presume the cell to be loaded in tension, as shown in Figure 3.1, and restrained in such a way as to prevent rigid body displacements, but to allow Poisson's ratio contraction. This immediately implies that displacement components

$d_{1x} = d_{2x} = d_{3x} = d_{2y} = d_{5y} = 0$. Set $d_{4x} = d_{5x} = d_{6x} = u$, when the strain in the x -

direction is $\varepsilon_x = \frac{u}{L} = u$, since $L = 1$. The strain in the y -direction is

$\varepsilon_y = \frac{d_{4y} - d_{6y}}{2L} = \frac{d_{1y} - d_{3y}}{2L}$, and by virtue of the symmetry of the cell,

$d_{1y} = -d_{3y}$, $d_{4y} = -d_{6y}$, so $\varepsilon_y = \frac{d_{4y}}{L} = \frac{d_{1y}}{L} = d_{4y} = d_{1y}$. But $\varepsilon_y = -\nu \varepsilon_x$, so

$d_{1y} = d_{4y} = -\nu u$, $d_{3y} = d_{6y} = \nu u$, and the cell displacement vector for tension is

$$\mathbf{d} = [0 \ -\nu u \ 0 \ 0 \ 0 \ \nu u \ u \ -\nu u \ u \ 0 \ u \ \nu u]^T. \quad (3.2)$$

The strain energy of the cell U is calculated as

$$U = \frac{1}{2} \mathbf{d}^T \mathbf{K} \mathbf{d} = \frac{E u^2}{10^4} \times \left(\nu^2 \left(1 + \frac{1}{2\sqrt{2}} \right) - \frac{\nu}{\sqrt{2}} + \frac{3}{2} + \frac{1}{2\sqrt{2}} \right). \quad (3.3)$$

The cell will deform in such a way as to minimise the above, that is

$$\frac{\partial U}{\partial \nu} = 0, \quad (3.4)$$

which gives $\nu = \frac{1}{1+2\sqrt{2}} = 0.261204$. An equivalent shear modulus G can then be

defined using $G = \frac{E}{2(1+\nu)}$, with Young's modulus being regarded as invariant.

The tensile force T_x applied to the cell is

$$T_x = F_{4x} + F_{5x} + F_{6x} \quad (3.5)$$

and these force components are calculated from (3.1), employing displacement vector (3.2) as

$$F_{4x} = F_{6x} = \frac{E}{10^4} \left(1 + \frac{1-\nu}{4\sqrt{2}} \right) \times u, \quad F_{5x} = \frac{E}{10^4} \left(1 + \frac{1-\nu}{2\sqrt{2}} \right) \times u \quad (3.6)$$

and

$$T_x = \frac{E}{10^4} \left(3 + \frac{1-\nu}{\sqrt{2}} \right) \times u. \quad (3.7)$$

For a continuum beam, we have $T_x = \frac{EA}{L} u$, and with $L = 1$, the equivalent cross-

sectional area is $A = \left(3 + \frac{1-\nu}{\sqrt{2}} \right) \times 10^{-4} = 3.5224 \times 10^{-4} \text{ m}^2$.

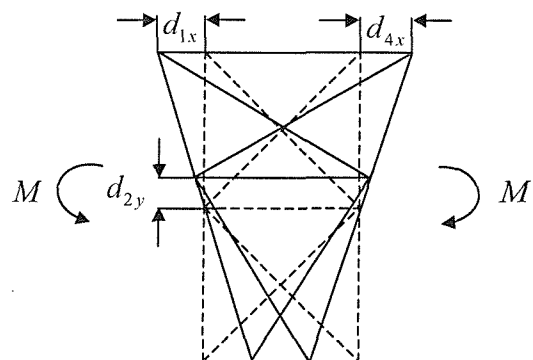


Figure 3.2. Single cell loaded in pure bending.

Next consider the displacements during bending, as shown in Figure 3.2; assume displacements $d_{1x} = d_{6x} = -u$, $d_{3x} = d_{4x} = u$, which is consistent with rotations of the side faces of the cell, and $d_{2x} = d_{5x} = 0$, which is consistent with zero axial strain on the neutral axis. For a continuum beam, a fibre coinciding with the member joining nodes 1 and 4 would have strain $\varepsilon_x = \frac{y}{R}$, where y is distance from the neutral axis and R is the radius of curvature; but the strain $\varepsilon_x = \frac{2u}{L}$ and $y = 1$, hence

$$\frac{M}{EI} = \frac{1}{R} = \frac{2u}{L} = 2u. \quad (3.8)$$

Also shown in Figure 3.2 is an apparent shift of the neutral axis (the member joining nodes 2 and 5) toward the tension (upper) side of the cell. In fact, the upper side moves toward the neutral axis while the lower, compression side moves away by an equal amount, both displacements being Poisson's ratio effects. For a continuum beam, [73]

gives the transverse displacement during pure bending as $v = -\frac{M}{2EI} (x^2 + v y^2) + c$; here the x^2 term represents the curvature due to bending, while the constant c , representing a rigid body displacement in the y -direction. The latter is adjusted such that $v = 0$ on

$y = \pm 1$ to give $v = \frac{Mv}{2EI} (1 - y^2)$. Nodes 2 and 5 have $y = 0$, and employing expression

(3.8) gives $d_{2y} = d_{5y} = vu$. The cell displacement vector for bending is then

$$\mathbf{d} = [-u \ 0 \ 0 \ vu \ u \ 0 \ u \ 0 \ 0 \ vu \ -u \ 0]^T. \quad (3.9)$$

The bending moment is

$$M = (F_{4x} - F_{6x}) \times L; \quad (3.10)$$

the force components in the above are calculated from (3.1) employing displacement vector (3.9) as

$$F_{4x} = -F_{6x} = \frac{Eu}{10^4} \left(2 + \frac{1-v}{4\sqrt{2}} \right), \quad (3.11)$$

hence

$$M = \frac{2Eu}{10^4} \left(2 + \frac{1-v}{4\sqrt{2}} \right), \quad (3.12)$$

from which the second moment of area is $I = \left(2 + \frac{1-\nu}{4\sqrt{2}}\right) \times 10^{-4} = 2.130602 \times 10^{-4} \text{ m}^4$.

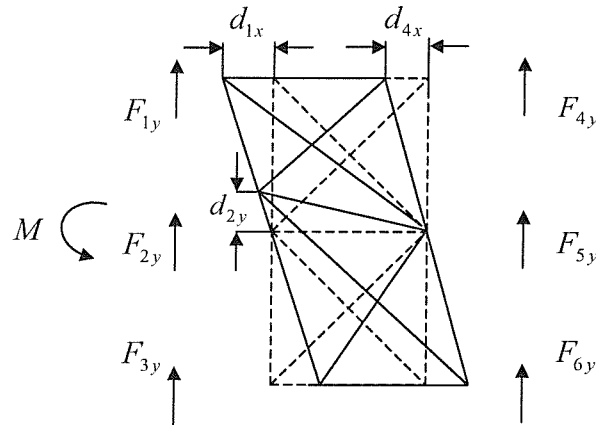


Figure 3.3. Single cell subject to shear and bending moment

Figure 3.3 shows the cell subjected to a shearing force, together with a bending moment; again the nodal displacements are guided by the solution for a cantilevered continuum beam subjected to a shearing force [73]. Rotations on both sides of the cell are different, so we set $d_{1x} = -u_1$, $d_{3x} = u_1$ and $d_{4x} = -u_2$, $d_{6x} = u_2$. As with pure bending, there is a Poisson's ratio effect of an apparent shift of the neutral axis in the y -direction (d_{2y}), but this effect is absent on the right face of the cell where the bending moment is zero, that is $d_{5y} = 0$. The shear displacement vector is written initially as

$$\mathbf{d} = \begin{bmatrix} -u_1 & 0 & 0 & d_{2y} & u_1 & 0 & -u_2 & 0 & 0 & 0 & u_2 & 0 \end{bmatrix}^T; \quad (3.13)$$

the associated force components are then calculated from equation (3.1), as

$$\begin{aligned} F_{1x} = -F_{3x} &= \frac{E}{10^4} \left(u_2 - \left(1 + \frac{1}{4\sqrt{2}}\right) u_1 \right), \quad F_{4x} = -F_{6x} = \frac{E}{10^4} \left(u_1 - \frac{1}{4\sqrt{2}} d_{2y} - \left(1 + \frac{1}{4\sqrt{2}}\right) u_2 \right), \quad F_{2x} = F_{5x} = 0 \\ F_{1y} = F_{3y} &= \frac{E}{10^4} \left(\frac{u_1}{4\sqrt{2}} - \frac{d_{2y}}{2} \right), \quad F_{2y} = \frac{E}{10^4} \left(\left(1 + \frac{1}{2\sqrt{2}}\right) d_{2y} + \frac{u_1 + u_2}{4\sqrt{2}} \right), \\ F_{4y} = F_{6y} &= -\frac{E}{10^4} \left(\frac{u_2 + d_{2y}}{4\sqrt{2}} \right), \quad F_{5y} = -\frac{E}{10^4} \left(\frac{u_1}{2\sqrt{2}} \right). \end{aligned} \quad (3.14)$$

These components satisfy vertical force equilibrium for the complete cell, and there is zero horizontal resultant on both sides. Moment equilibrium requires the relationship

$$u_1 = \frac{d_{2y}}{4\sqrt{2}} + \left(1 + \frac{1}{4\sqrt{2}}\right)u_2 \quad (3.15)$$

while asymmetry of the shear force vector requires

$$F_{1y} = -F_{4y}, \quad F_{2y} = -F_{5y}, \quad F_{3y} = -F_{6y}, \quad (3.16)$$

which yield the single relationship

$$u_1 = u_2 + (1 + 2\sqrt{2})d_{2y} \quad (3.17)$$

hence

$$u_1 = (16 + 6\sqrt{2})d_{2y}, \quad u_2 = (15 + 4\sqrt{2})d_{2y} \quad (3.18)$$

The shearing force is then

$$Q = F_{1y} + F_{2y} + F_{3y} = \frac{E}{10^4} (5 + 8\sqrt{2})d_{2y}. \quad (3.19)$$

As in Chapter 2, the shear angle γ is defined as $\gamma = \psi - dv/dx$, in which ψ is the cross-sectional rotation and dv/dx is the centre line slope; again, we take the rotation as the average of the rotations on either side of the cell when the shear angle is, Figure 3.3, equal to

$$\gamma = \frac{u_1 + u_2}{2} + d_{2y}, \quad (3.20)$$

bearing in mind that cell has unity length. Finally, introduce the above expressions into the shear equation $Q = GA\kappa\gamma$ to give the shear coefficient as

$$\kappa = \frac{4(5 + 8\sqrt{2})(1 + \nu)}{(33 + 10\sqrt{2})\left(3 + \frac{1 - \nu}{\sqrt{2}}\right)} = 0.49562. \quad (3.21)$$

The equivalent properties as derived above are in agreement with those determined in Table 2.2.

3.4 ANALYTICAL EXPRESSIONS FOR THE EQUIVALENT CONTINUUM PROPERTIES OF A MORE GENERALLY DEFINED FRAMEWORK

Consider a cell, as in Figure 2.1, but having more general lengths and cross-sectional areas. In particular, the longitudinal members have length L , and cross-sectional area A_L , while the vertical and diagonal members have lengths H and $D = \sqrt{L^2 + H^2}$, and

areas A_H and A_D , respectively. The equivalent properties are expressed first in terms of the absolute parameters of the cell and then more simply in terms of derived equivalent properties, in particular the Poisson's ratio, which is

$$\nu = \frac{A_D H L^2}{A_H D^3 + A_D H^3}. \quad (3.22)$$

For isotropic homogenous materials, Poisson's ratio can take values within the range $-1 \leq \nu \leq 0.5$. For this particular cell configuration, ν cannot be negative; it has a minimum value of zero when A_D is zero, when the cell can withstand tension and bending – for shear it is a mechanism.

The equivalent cross-sectional area is

$$A = 3A_L + \frac{4A_D A_H L^3}{A_H D^3 + A_D H^3} = 3A_L + 4\nu \frac{L}{H} A_H \quad (3.23)$$

which is equal to that of the three longitudinal members together with a necessarily positive contribution from the vertical and diagonal members.

The equivalent second moment of area is

$$I = 2A_L H^2 + \frac{A_D A_H H^2 L^3}{A_H D^3 + A_D H^3} = 2A_L H^2 + \nu A_H L H \quad (3.24)$$

and consists of a “parallel-axes theorem” contribution from the top and bottom longitudinal members ($2A_L H^2$) together with a positive contribution from the vertical and diagonal members. Moreover, this additional contribution is consistent with a “parallel-axes theorem” treatment of the additional area term, $4\nu \frac{L}{H} A_H$, in expression (3.23). In particular, it is reasonable that one-half of this additional area should be placed symmetrically about the neutral axis, at distance $H/2$, when the parallel-axes theorem gives

$$2 \times \left(2\nu \frac{L}{H} A_H \right) \times \left(\frac{H}{2} \right)^2 = \nu A_H L H. \quad (3.25)$$

It is interesting to note that I reduces to $2A_L H^2$, and not zero, when the diagonal members are absent, as one might argue that these members are required to transmit shear from the upper (tensile) to the lower (compressive) members of the cell; in practice these diagonals are clearly necessary. On the other hand, the displacement vector for bending prescribes that the cell deforms in the required manner.

The shear coefficient becomes

$$\begin{aligned}\kappa &= \frac{8(A_H D^3 + A_D H^3 + A_D H L^2)(2A_L A_H D^3 + 2A_L A_D H^3 + A_D A_H L^3)A_D H^2 L}{(3A_L A_H D^3 + 3A_L A_D H^3 + 4A_D A_H L^3)(2A_L D^3 + A_D L^3)(A_H D^3 + A_D H^3)} \quad (3.26) \\ &= \frac{8(1+\nu)(2A_L H + \nu A_H L)A_D H^3 L}{(3A_L H + 4\nu A_H L)(2A_L H D^3 + \nu A_H D^3 L + \nu A_D L H^3)};\end{aligned}$$

the above reduces to zero when $A_D = 0$, as the cell cannot withstand shear.

APPENDIX 3

STIFFNESS MATRIX OF 2D PIN-JOINTED FRAMEWORK

$$\begin{bmatrix}
 F_{1x} \\
 F_{1y} \\
 F_{2x} \\
 F_{2y} \\
 F_{3x} \\
 F_{3y} \\
 F_{4x} \\
 F_{4y} \\
 F_{5x} \\
 F_{5y} \\
 F_{6x} \\
 F_{6y}
 \end{bmatrix} = \frac{E}{10^4} \times
 \begin{bmatrix}
 1 + \frac{1}{4\sqrt{2}} & \frac{-1}{4\sqrt{2}} & 0 & 0 & 0 & -1 & 0 & \frac{-1}{4\sqrt{2}} & \frac{1}{4\sqrt{2}} & 0 & 0 \\
 \frac{-1}{4\sqrt{2}} & \frac{1}{2} + \frac{1}{4\sqrt{2}} & 0 & \frac{-1}{2} & 0 & 0 & 0 & \frac{1}{4\sqrt{2}} & \frac{-1}{4\sqrt{2}} & 0 & 0 \\
 0 & 0 & 1 + \frac{1}{2\sqrt{2}} & 0 & 0 & 0 & \frac{-1}{4\sqrt{2}} & \frac{-1}{4\sqrt{2}} & -1 & 0 & \frac{-1}{4\sqrt{2}} & \frac{1}{4\sqrt{2}} \\
 0 & \frac{-1}{2} & 0 & 1 + \frac{1}{2\sqrt{2}} & 0 & \frac{-1}{2} & \frac{-1}{4\sqrt{2}} & \frac{-1}{4\sqrt{2}} & 0 & 0 & \frac{1}{4\sqrt{2}} & \frac{-1}{4\sqrt{2}} \\
 0 & 0 & 0 & 0 & 1 + \frac{1}{4\sqrt{2}} & \frac{1}{4\sqrt{2}} & 0 & 0 & \frac{-1}{4\sqrt{2}} & \frac{-1}{4\sqrt{2}} & -1 & 0 \\
 0 & 0 & 0 & \frac{-1}{2} & \frac{1}{4\sqrt{2}} & \frac{1}{2} + \frac{1}{4\sqrt{2}} & 0 & 0 & \frac{-1}{4\sqrt{2}} & \frac{-1}{4\sqrt{2}} & 0 & 0 \\
 -1 & 0 & \frac{-1}{4\sqrt{2}} & \frac{-1}{4\sqrt{2}} & 0 & 0 & 1 + \frac{1}{4\sqrt{2}} & \frac{1}{4\sqrt{2}} & 0 & 0 & 0 & 0 \\
 0 & 0 & \frac{-1}{4\sqrt{2}} & \frac{-1}{4\sqrt{2}} & 0 & 0 & \frac{1}{4\sqrt{2}} & \frac{1}{2} + \frac{1}{4\sqrt{2}} & 0 & \frac{-1}{2} & 0 & 0 \\
 \frac{-1}{4\sqrt{2}} & \frac{1}{4\sqrt{2}} & -1 & 0 & \frac{-1}{4\sqrt{2}} & \frac{-1}{4\sqrt{2}} & 0 & 0 & 1 + \frac{1}{2\sqrt{2}} & 0 & 0 & 0 \\
 \frac{1}{4\sqrt{2}} & \frac{-1}{4\sqrt{2}} & 0 & 0 & \frac{-1}{4\sqrt{2}} & \frac{-1}{4\sqrt{2}} & 0 & \frac{-1}{2} & 0 & 1 + \frac{1}{2\sqrt{2}} & 0 & \frac{-1}{2} \\
 0 & 0 & \frac{-1}{4\sqrt{2}} & \frac{1}{4\sqrt{2}} & -1 & 0 & 0 & 0 & 0 & 0 & 1 + \frac{1}{4\sqrt{2}} & \frac{-1}{4\sqrt{2}} \\
 0 & 0 & \frac{1}{4\sqrt{2}} & \frac{-1}{4\sqrt{2}} & 0 & 0 & 0 & 0 & 0 & \frac{-1}{2} & \frac{-1}{4\sqrt{2}} & \frac{1}{2} + \frac{1}{4\sqrt{2}}
 \end{bmatrix}
 \begin{bmatrix}
 d_{1x} \\
 d_{1y} \\
 d_{2x} \\
 d_{2y} \\
 d_{3x} \\
 d_{3y} \\
 d_{4x} \\
 d_{4y} \\
 d_{5x} \\
 d_{5y} \\
 d_{6x} \\
 d_{6y}
 \end{bmatrix}$$

CHAPTER FOUR

EIGENANALYSIS OF AN ASYMMETRIC REPETITIVE STRUCTURE

4.1 INTRODUCTION

In this Chapter, eigenanalysis of the transfer matrix is applied to an actual structure modelled on a deployable satellite boom structure [13] whose repeating cell is asymmetric about the mid-plane; a ten-cell model is illustrated in Figure 4.1. Based on the conclusion drawn from Chapter 2 – that the continuum properties are unaffected by the method of jointing – the actual rigid-jointed structure is modelled as being pin-jointed. This has the advantage of simplicity and also allows the results obtained from eigenanalysis to be verified by *exact* predictions from FEA. The pin-jointed idealisation of the structure requires the transfer matrix approach to be posed as a *generalised* eigenvalue problem; this modification is necessary because inversion of one particular partition of the stiffness matrix \mathbf{K} is impossible, as it is singular. This means that construction of the transfer matrix \mathbf{G} , as defined in equation (2.7), is impossible; on the other hand, the generalised eigenvalue problem avoids the ill conditioning associated with inversion of the stiffness matrix partition, and the numerical inaccuracies that ensue. The generalised eigenvalue problem employs state vectors comprised of the displacement components on both sides of a cell, rather than displacement and force on one side, as for the standard eigenvalue problem.

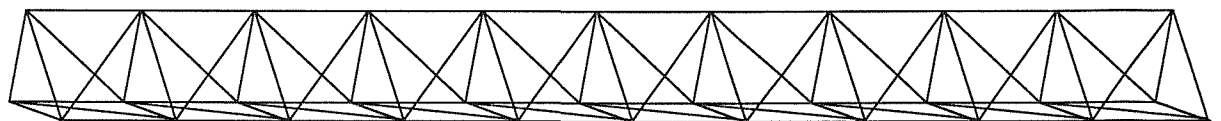


Figure 4.1. A ten-cell 3-D pin-jointed satellite truss with equilateral triangular cross-section.

Beside the twelve unity eigenvalues for the transmission modes, eigenanalysis of the structure shows three eigenvalues equal to zero (and three equal to infinity, since they must occur as reciprocals), and nothing else. This implies that any self-equilibrated load

is confined to the cross-section on which it is applied, and does not penetrate the structure, not even to the next nodal cross-section. Of course, this is exactly why the matrix partition is singular – displacement components of some nodes on the right hand side of the cell are quite unaffected by force components applied at nodes on the left hand side of the cell.

Since the eigen- and principal vectors of the generalised problem contain only displacement components, a new *transmission* matrix \mathbf{T} is defined as being comprised of transmission vectors consisting of both displacement and force components, and is calculated employing the stiffness matrix \mathbf{K} . Physical interpretation of the vectors in \mathbf{T} shows coupling between various modes of displacement. First, tension is coupled with torsion, which is reminiscent of the established behaviour of pre-twisted beams.

However, coupling indicated in the displacement components of the bending moment vectors were not readily identified, but simple (ANSYS) FEA of a 10-cell pin-jointed model subjected to a bending moment showed coupling between bending curvature, and shear perpendicular to the plane of curvature.

Calculation of the equivalent continuum beam properties of the structure, including the coupling coefficients between the modes, revealed several *numerical coincidences* between actual properties of the structure, and the equivalent continuum properties, often involving an apparent Poisson's ratio of $\nu = 0.2612$. In order to more fully understand the physical causes behind these coincidences, and the nature of coupling in general, a simpler 2-D planar asymmetric framework, Figure 4.2, is first considered. This simple planar structure is representative of a single face of the *NASA* structure, and displays tension-shear coupling; this behaviour is sufficient to explain the tension-torsion, and the bending-shear couplings evident in the 3-D structure.

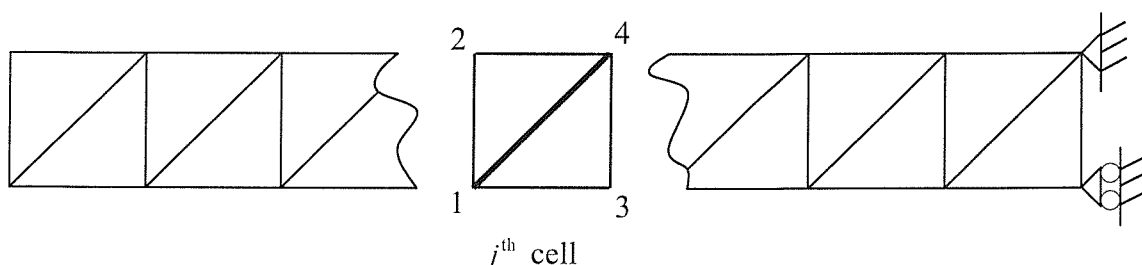


Figure 4.2. A 2-D planar asymmetric framework with typical cell.

4.2 GENERALISED EIGENVALUE PROBLEM

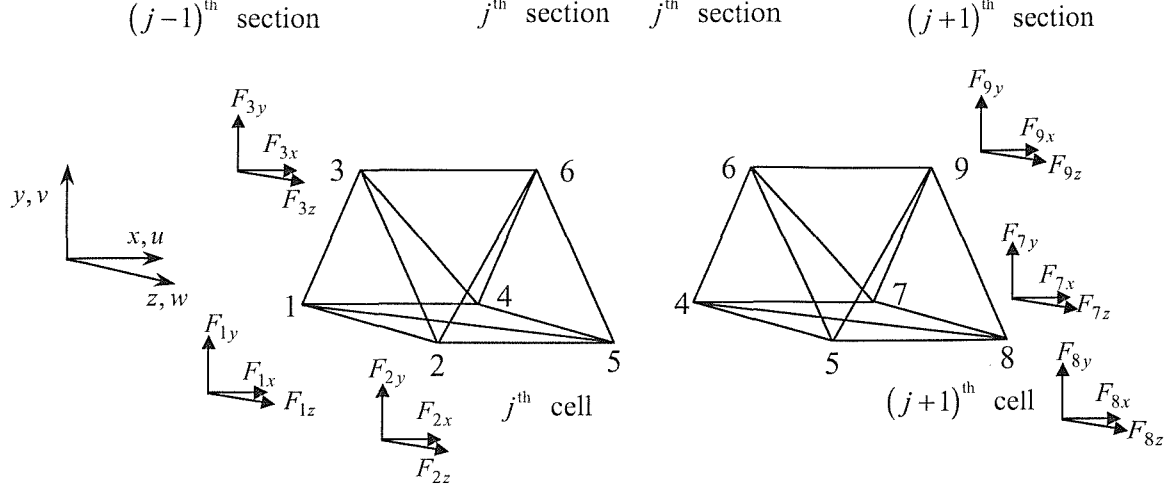


Figure 4.3. Two consecutive cells, j^{th} and $(j+1)^{\text{th}}$, of the framework shown in Figure 4.1.

Consider two consecutive cells of the *NASA* truss shown in Figure 4.3; let \mathbf{d}_{j-1} , \mathbf{d}_j and \mathbf{d}_{j+1} denote the nodal displacement vectors associated with the $(j-1)^{\text{th}}$, j^{th} , and $(j+1)^{\text{th}}$ sections respectively. Their corresponding nodal force vectors \mathbf{F}_{j-1} , \mathbf{F}_j and \mathbf{F}_{j+1} are related to the displacements through the equations

$$\begin{bmatrix} \mathbf{F}_{j-1} \\ \mathbf{F}_j \end{bmatrix} = \mathbf{K} \begin{bmatrix} \mathbf{d}_{j-1} \\ \mathbf{d}_j \end{bmatrix}, \quad \begin{bmatrix} \mathbf{F}_j \\ \mathbf{F}_{j+1} \end{bmatrix} = \mathbf{K} \begin{bmatrix} \mathbf{d}_j \\ \mathbf{d}_{j+1} \end{bmatrix}. \quad (4.1a, b)$$

where $\mathbf{K} = \begin{bmatrix} \mathbf{K}_{LL} & \mathbf{K}_{LR} \\ \mathbf{K}_{RL} & \mathbf{K}_{RR} \end{bmatrix}$ is the stiffness matrix of the single cell. The force

component \mathbf{F}_j appears in both of the relationships for the two adjacent cells, and can be eliminated to give

$$\mathbf{K}_{LL}\mathbf{d}_j + \mathbf{K}_{LR}\mathbf{d}_{j+1} + \mathbf{K}_{RL}\mathbf{d}_{j-1} + \mathbf{K}_{RR}\mathbf{d}_j = 0. \quad (4.2)$$

Define state vectors for adjacent cells as $\mathbf{s}_j = [\mathbf{d}_{j-1}^T \ \mathbf{d}_j^T]^T$ and $\mathbf{s}_{j+1} = [\mathbf{d}_j^T \ \mathbf{d}_{j+1}^T]^T$, when equation (4.2) can be expressed as

$$\mathbf{A}\mathbf{s}_j = \mathbf{B}\mathbf{s}_{j+1}. \quad (4.3)$$

where

$$\mathbf{A} = \begin{bmatrix} \mathbf{0} & \mathbf{I} \\ -\mathbf{K}_{RL} & -\mathbf{K}_{RR} \end{bmatrix}, \quad \mathbf{B} = \begin{bmatrix} \mathbf{I} & \mathbf{0} \\ \mathbf{K}_{LL} & \mathbf{K}_{LR} \end{bmatrix}, \quad (4.4)$$

and \mathbf{I} is the identity matrix. Now set

$$\mathbf{s}_{j+1} = \lambda \mathbf{s}_j, \quad (4.5)$$

to give the generalised eigenvalue problem

$$\mathbf{A}\mathbf{s}_j = \lambda \mathbf{B}\mathbf{s}_j \quad \text{or} \quad (\mathbf{A} - \lambda \mathbf{B})\mathbf{s}_j = \mathbf{0}. \quad (4.6)$$

Eigenvectors for the non-repeating eigenvalues were determined from the MATLAB *eig* command. The principal vectors are determined from the near diagonalised form

$$\mathbf{AV} = \mathbf{BVJ}. \quad (4.7)$$

where \mathbf{V} is the similarity matrix of eigen- and principal vectors, and \mathbf{J} is the JCF. For the multiple unity eigenvalues this implies the chain of equations

$$\begin{aligned} (\mathbf{A} - \mathbf{B}) \mathbf{v}_1 &= \mathbf{0} \\ (\mathbf{A} - \mathbf{B}) \mathbf{w}_2 &= \mathbf{B} \mathbf{v}_1 \\ \dots & \\ (\mathbf{A} - \mathbf{B}) \mathbf{w}_k &= \mathbf{B} \mathbf{w}_{k-1} \end{aligned} \quad (4.8)$$

for a Jordan block of size $k \times k$, and a principal vector \mathbf{w}_{i+1} is found using the *rref* command on the augmented matrix $[\mathbf{A} - \mathbf{B}, \mathbf{B} \mathbf{w}_i]$. In fact the JCF cannot be determined numerically through a similarity transformation, since matrix \mathbf{B} cannot be inverted; however, the structures of the Jordan blocks for the vectors pertaining to the unity eigenvalues are obvious through physical reasoning: thus one has a 2×2 block coupling extension and the combination of loads necessary to produce that extension (a tensile force for the symmetric structure considered in Chapter 2, but here other loads are required), and likewise a 2×2 block coupling rotation and the necessary loads to produce that rotation. On the other hand, one has 4×4 block(s) coupling transverse displacement, rotation, bending, and shear – in one plane for the planar structure, and two planes for the space framework.

From the above, it is clear that the eigen- and principal vectors consist only of displacement components; a *transmission* matrix \mathbf{T} is thus defined as being comprised of vector pairs $\mathbf{s}_{j-i} = [\mathbf{d}_{j-i}^T \ \mathbf{p}_{j-i}^T]^T$ and $\mathbf{s}_j = [\mathbf{d}_j^T \ \mathbf{p}_j^T]^T$, each of which is derived from

two of the vectors coupled in the above chain, for example \mathbf{w}_{k-1} and \mathbf{w}_{k-2} . The force components within the new vectors can be readily determined through equations (4.1), and the complete *transmission* matrix \mathbf{T} is given in Appendices 4.A and 4.B for the planar and *NASA* structures, respectively. Pairs of columns of \mathbf{T} describe the displacement and force components on either side of a single repeating cell for the transmission of the stress resultants of tension, torsion, bending moments and shearing forces, together with the principal vector rigid body rotations; the eigenvector rigid body displacements and rotation are resident within one vector of the pair.

4.3 SIMPLE 2-D PLANAR ASYMMETRIC FRAMEWORK

A planar pin-jointed asymmetric framework is shown in Figure 4.2, together with the nodal numbering of the typical cell; the material and geometric properties are as follows: the Young's modulus and density, $E = 70 \times 10^9 \text{ Nm}^{-2}$ and $\rho = 2700 \text{ kg/m}^3$ is the same for all members; the lengths of the two vertical bars are $L = 342.8 \text{ mm}$, and their cross-sectional areas are taken as $A/2$ since these vertical bars are regarded as being shared by two adjacent cells. The diagonal bar has length $\sqrt{2} \times 342.8 = 484.8 \text{ mm}$ as demanded by geometry, together with cross-sectional area A . The lengths of the two horizontal bars are L , and their cross-sectional area is $A/2$; this planar structure is now equivalent to one face of the *NASA* structure whose horizontal member cross-sectional areas are regarded as being shared between adjacent faces. The full cross-sectional area A is calculated from member diameter $d = 6.35 \text{ mm}$. Since there is only one diagonal bar in the typical cell, the structure is clearly asymmetric about its mid-plane.

The stiffness matrix \mathbf{K} for the single cell is given in Appendix 4.C. Referring to equation (2.7) of Chapter 2, in order to construct the transfer matrix \mathbf{G} one must invert the partition \mathbf{K}_{LR} ; however from Appendix 4.C, it is clear that both \mathbf{K}_{LR} and \mathbf{K}_{RL} are singular. More specifically, the zero columns within \mathbf{K}_{LR} and \mathbf{K}_{RL} indicate that displacement d_{3y} is quite independent of the force components on nodes 1 and 2, and likewise for displacement d_{2y} and the force components on nodes 3 and 4.

Figure 4.4 shows the 2-D asymmetric structure subjected to the only possible self-equilibrated load ($F_{1y} + F_{2y} = 0$) at its free end; nodal force equilibrium then requires the following relationships

$$\begin{aligned} F_a + F_e \cos \frac{\pi}{4} + F_{1y} &= 0 \\ F_d + F_e \sin \frac{\pi}{4} &= 0 \\ F_a - F_{2y} &= 0 \\ F_c &= 0 \end{aligned} \quad (4.9)$$

Bearing in mind that $F_{1y} = -F_{2y}$, solution of the above requires $F_a = F_{2y}$, $F_c = F_d = F_e = 0$ and thence $F_b = 0$, which clearly indicates a zero decay rate, and hence the reciprocal eigenvalue pair $[\inf, 0]^T$; the remaining six eigenvalues must be equal to unity.

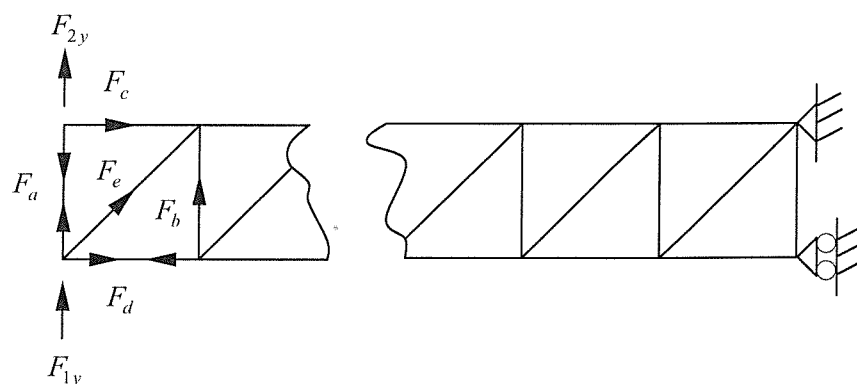


Figure 4.4. A 2-D planar asymmetric framework subjected to self-equilibrated end loading.

4.3.1 Equivalent Continuum Properties and Coupling Coefficients

The nodal force components, together with decomposition of the displacements, of the transmission matrix, Appendix 4.A, are shown in Figures 4.5 – 4.8.

a) The first two columns of the transmission matrix, $T(:,1)$ and $T(:,2)$, are termed the *tension pair* and are derived from the principal vector for tension, which is coupled to x -direction rigid body displacement, in the principal vector chain, and is shown in Figure 4.5; it is seen that a tensile force $T_x = 6.4668 \times 10^{-2}$ N, when applied to both left and right hand sides of the cell, produces an extension $u = 1 \times 10^{-8}$ m in the x -direction,

together with a shear in the xy -plane $\gamma_{xy} = \frac{10^{-8}}{L}$; note the absence of a Poisson's ratio contraction.

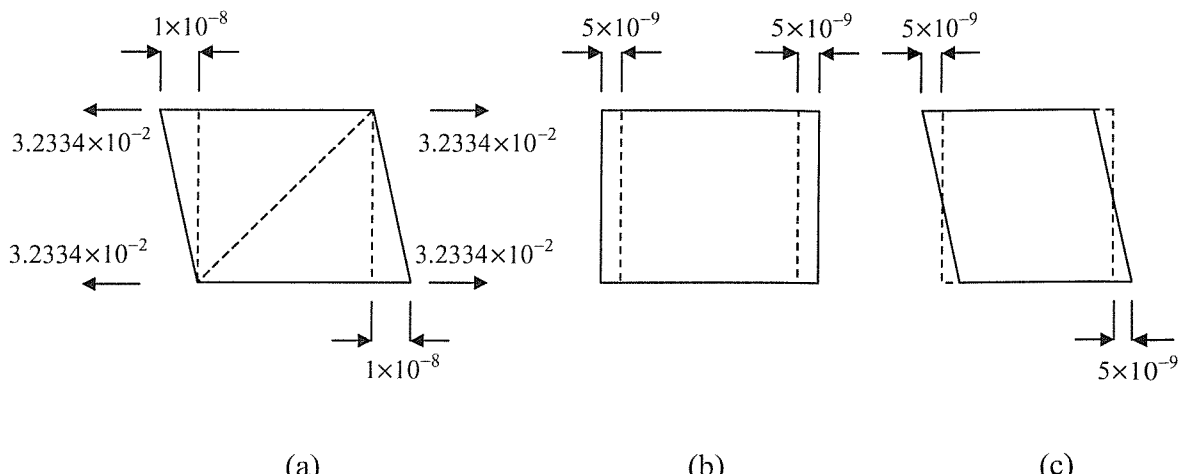


Figure 4.5. The tension pair of the single-face cell of the 3-D satellite truss; the deformation is decomposed into (b) extension and (c) shear deformation.

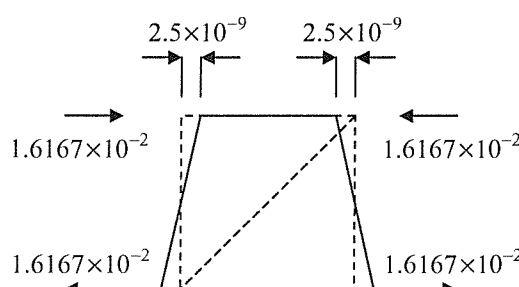


Figure 4.6. The bending moment pair of the single-face cell of the 3-D satellite truss; the deformation represents a bending curvature only.

b) The third and fourth columns of the transmission matrix, $\mathbf{T}(:,3)$ and $\mathbf{T}(:,4)$, are termed the *bending moment pair*, and are derived from the principal vector for bending moment, which is coupled to rigid body rotation about the z -axis in the principal vector chain; from Figure 4.6, it is seen that the moment $M = 1.6167 \times L \times 10^{-2}$ Nm when applied to both left and right hand sides of the cell, produces a bending curvature of

$$\frac{1}{R} = \frac{10^{-8}}{L^2} \text{ m}^{-1}.$$

Again, note the absence of any Poisson's ratio effects.

c) The fifth and sixth columns $\mathbf{T}(:,5)$ and $\mathbf{T}(:,6)$ are termed the *mixed shear pair*, and are derived from the principal vector, which is coupled to the bending moment in the principal vector chain. From Figure 4.7, the force components of these two vectors show shearing and compressive forces on both sides of the cell, together with a bending moment on the left hand side. The displacements show a combination of shear, curvature, and an apparent Poisson's ratio *expansion* of the cross-section, at first sight connected with the compressive force, despite there being no axial contraction.

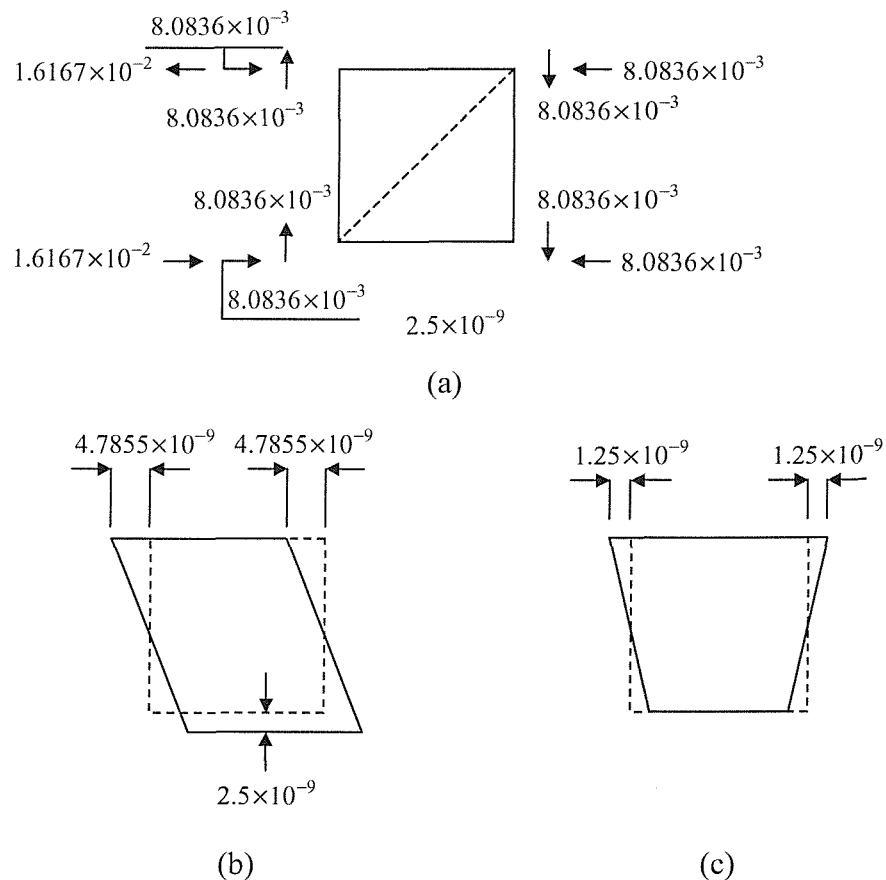


Figure 4.7. The mixed shear pair of the single-face cell of the 3-D satellite truss; (a) shows the force components which indicates that the cell is subjected to shearing force, compressive force and bending moment; displacement components indicate a shear deformation and cross-sectional expansion (b), and a bending curvature (c).

The above vector pairs are those produced by the numerical procedures described above for this generalised eigenproblem and contain all potential information; however, linear

combinations of these pairs are more useful for determination of the equivalent properties, and in particular for a numerical understanding of the various couplings.

Before developing new vector pairs, however, we first note the physical arguments that lie behind the observed couplings. As regards the tension pair, Figure 4.5, it is not difficult to see that the tensile force is carried by the horizontal members only, and that the diagonal member is free of load; in turn, this diagonal does not change its length and, because the cell is pin-jointed, this is accommodated by the transverse shear of the cell by just sufficient amount that the length of the diagonal remain constant. A consequence of the diagonal being free of load is that the vertical members are also free of load, and since their lengths remain constant, the equivalent Poisson's ratio for the cell is zero. Inserting the relevant magnitudes of tensile force T_x and extension u from Figure 4.5 into the expression $T_x = EA \frac{u}{L}$, with E regarded as constant, leads to an equivalent cross-sectional area *exactly* equal to the actual area of the two horizontal members, which is

$$A_{actual} = \frac{\pi d^2}{4} = 31.6688 \times 10^{-6} \text{ m}^2.$$

For the bending moment pair, Figure 4.6, again the horizontal members carry the tensile and compressive loads, while the diagonal is free of load. But now, the contraction of the upper member, and extension of the lower, is exactly as required to maintain the length of the diagonal member, which now has no influence on the behaviour; again there is no Poisson's ratio effect. Inserting the relevant magnitudes of moment M and curvature $\frac{1}{R}$ from Figure 4.6 into the expression $M = \frac{EI}{R}$ leads to an equivalent second moment of area $I = 9.30377 \times 10^{-7} \text{ m}^4$, which is exactly what one would expect from application of the parallel axes theorem, assuming *actual* values for the areas of the horizontal members.

We now propose that one can conceptually trade the *anisotropic* coupling exhibited above, with more appealing isotropic characteristics; in particular, since tension produces a shear deformation, one might reasonably assume that a shearing force will produce a

Poisson's ratio effect, and that these effects are reciprocal. To develop this idea further one needs the first of the combined vector pairs, describing pure shear which is shown in Figure 4.8(a); we note that such a state of pure shear, as depicted, would not be allowed within the context of Saint-Venant's problem since shearing loads are applied to the upper and lower faces of the cell (the surface generators) rather than just the cross-section. However a nodal force in the x -direction can belong equally to the cross-section, so the shearing forces on the upper and lower faces of Figure 4.8(a) are indistinguishable from the combination of bending moments shown in Figure 4.8(b), which is here defined as the state of *pure shear*. Now superpose sufficient pure shear ($-5/6.0355$) to suppress the shear deformation due to tension, to give the combination of extension and apparent

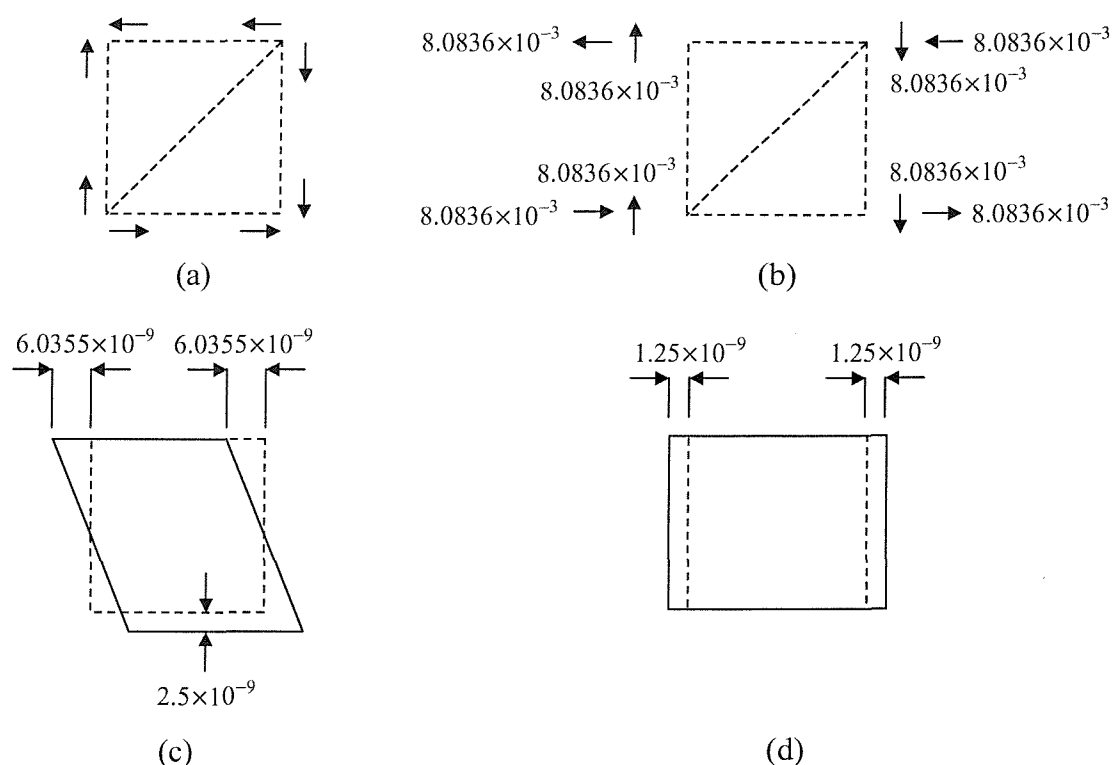


Figure 4.8. The pure shear pair of the single-face cell of the 3-D satellite truss; (a) shows conventional pure shear; (b) shows an equivalent combination of shear and bending moment; (c) shows the shear deformation and cross-sectional expansion; (d) shows the extension.

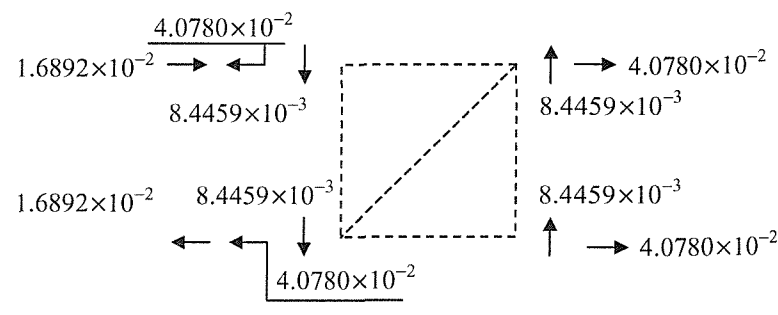
Poisson's ratio contraction shown in Figure 4.9; the strains are

$$\varepsilon_x = \frac{2 \times 3.96446 \times 10^{-9}}{L}, \quad \varepsilon_y = \frac{2.07108 \times 10^{-9}}{L}, \quad \text{and hence the apparent Poisson's ratio}$$

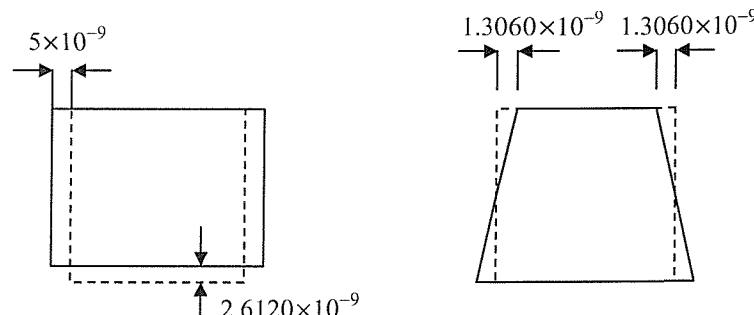
$\nu = 0.2612$. Now calculate an equivalent cross-sectional area A based upon the extension caused by this tension-shear combination, and one finds

$$A = 39.94093 \times 10^{-6} \text{ m}^2 = A_{\text{actual}} (1 + \nu); \text{ moreover, one now has as the equivalent shear}$$

$$\text{modulus } G = \frac{E}{2(1+\nu)} = 27.7514 \times 10^9 \text{ N/m}^2.$$



(a)



(b)

(c)

Figure 4.9. The extension pair of the single-face cell of the 3-D satellite truss; (a) shows the force components which indicates tension, shearing force and bending moment; the deformation is decomposed into (b) extension and Poisson's ratio contraction, and (c) a bending curvature.

Returning to the *mixed shear pair*, Figure 4.7, one sees that a shearing force of magnitude $Q = 2 \times 8.0836 \times 10^{-3} = 1.61672 \times 10^{-2} \text{ N}$ produces a shear angle of

$$\gamma = \frac{4.7855 \times 10^{-9}}{L/2}; \text{ to define a shear coefficient } \kappa \text{ within the expression } Q = \kappa A G \gamma$$

requires a choice of the appropriate cross-sectional area A and shear modulus G . For

example one might choose the actual cross-sectional area, zero Poisson's ratio, when the shear modulus $G = E/2$; on the other hand one might choose the calculated equivalent cross-sectional area, the apparent Poisson's ratio, and the shear modulus $G = \frac{E}{2(1+\nu)}$.

In fact, both these choices lead to the same value for the shear coefficient, since

$$A_{actual} \frac{E}{2} = A_{actual} (1+\nu) \frac{E}{2(1+\nu)}, \quad (4.10)$$

and hence the value $\kappa = 0.5224$, which is noted to be numerically twice that of the apparent Poisson's ratio.

Now the mixed shear pair contains a compressive force, suppressing elongation of the cell which, in turn, is coupled to a shear angle. If this compressive load is removed to give the shear pair, Figure 4.8, one now has a shear angle of $\gamma = \frac{6.0355 \times 10^{-9}}{L/2}$, which

leads to a shear coefficient $\kappa = 0.4142 = \frac{2\nu}{1+\nu}$, numerically.

We now formalise three states of *pure* load, and employ these to determine the governing coupled equations; *unit* states of tension T^* , moment M^* and pure shear Q_p^* are defined according to Figures 4.5, 4.6 and 4.8, with magnitudes

$$T^* = 2 \times 3.2334 \times 10^{-3} = 6.4668 \times 10^{-3} \text{ N}, \quad M^* = 1.61672 \times 10^{-2} \times L \text{ Nm}, \\ Q_p^* = 2 \times 8.0836 \times 10^{-3} = 1.61672 \times 10^{-2} \text{ N}. \quad (4.11)$$

In addition a shear load Q^* is defined according to Figure 4.7, which represents the mixed shear pair, but with the compressive load removed.

Now construct the *cause and effect* Table 4.1, for arbitrary T , Q_p , Q , and M , where each row shows the deformations caused by the pure loads; note that, numerically, the coefficient $4.8284 = \frac{1+\nu}{\nu}$. It is now easy to see that by adding an appropriate, negative, multiple of the second row (pure shear) to the first (tension) one may suppress the shear angle while introducing an apparent Poisson's ratio cross-sectional contraction, the strain ε_y .

Table 4.1 Deformation produced by arbitrary loads T , Q_p , M and Q .

	ε_x	γ	$1/R$	ε_y
T	$\frac{10^{-8}T}{LT^*}$	$\frac{10^{-8}T}{LT^*}$	0	0
Q_p	$\frac{10^{-8}Q_p}{4LQ_p^*}$	$\frac{4.8284 \times 10^{-8}Q_p}{4LQ_p^*}$	0	$\frac{10^{-8}Q_p}{4LQ_p^*}$
M	0	0	$\frac{10^{-8}M}{L^2M^*}$	0
Q	$\frac{10^{-8}Q}{4LQ^*}$	$\frac{4.8284 \times 10^{-8}Q}{4LQ^*}$	$-\frac{10^{-8}Q}{2L^2Q^*}$	$\frac{10^{-8}Q}{4LQ^*}$

The governing equations are determined by adding the effects of each of these causes, as

$$\begin{bmatrix} \varepsilon_x \\ \gamma \\ \frac{1}{R} \\ \varepsilon_y \end{bmatrix} = \frac{15.464 \times 10^{-8}}{L} \begin{bmatrix} 1 & 0 & 1 & 1 \\ 1 & 0 & 4.8284 & 4.8284 \\ 0 & \frac{4}{L^2} & 0 & -\frac{2}{L} \\ 0 & 0 & 1 & 1 \end{bmatrix} \begin{bmatrix} T \\ M \\ Q_p \\ Q \end{bmatrix} \quad (4.12)$$

where numerical values for the unit loads have been inserted. Moreover, numerically

the coefficient $\frac{15.464 \times 10^{-8}}{L} = \frac{1}{EA_{actual}}$, enabling one to write

$$\begin{bmatrix} \varepsilon_x \\ \gamma \\ \frac{1}{R} \\ \varepsilon_y \end{bmatrix} = \frac{1}{EA_{actual}} \begin{bmatrix} 1 & 0 & 1 & 1 \\ 1 & 0 & 4.8284 & 4.8284 \\ 0 & \frac{4}{L^2} & 0 & -\frac{2}{L} \\ 0 & 0 & 1 & 1 \end{bmatrix} \begin{bmatrix} T \\ M \\ Q_p \\ Q \end{bmatrix}. \quad (4.13)$$

The above compliance matrix is not invertible, as it is singular having rank 3; the information contained within the fourth column, pertaining to the shear force Q , is clearly a linear combination of columns two and three, as one would expect since Q is constructed from M and Q_p . A variety of non-singular matrices may be extracted from the above, and these allow the equivalent properties to be determined in different ways. First, delete the second row and the fourth column, and invert to give

$$\begin{bmatrix} T_x \\ M \\ Q_p \end{bmatrix} = EA_{actual} \begin{bmatrix} 1 & 0 & -1 \\ 0 & \frac{L^2}{4} & 0 \\ 0 & 0 & 1 \end{bmatrix} \begin{bmatrix} \varepsilon_x \\ \frac{1}{R} \\ \varepsilon_y \end{bmatrix}. \quad (4.14)$$

From the above, one has equivalent second moment of area $I = A_{actual} \frac{L^2}{4}$, as previously calculated. The tensile force $T_x = EA_{actual} (\varepsilon_x - \varepsilon_y)$, but if the pure shear Q_p is sufficient to suppress the shear angle such that $\varepsilon_y = -\nu \varepsilon_x$, then one has $T_x = EA_{actual} (1+\nu) \varepsilon_x$, and the equivalent cross-sectional area as calculated previously.

Instead, if one deletes the fourth row and the third column and invert, one finds

$$\begin{bmatrix} T_x \\ M \\ Q \end{bmatrix} = EA_{actual} \begin{bmatrix} 1.2612 & -0.2612 & 0 \\ -0.2612L & 0.2612L & \frac{L^2}{4} \\ \frac{2}{2} & \frac{2}{2} & 0 \end{bmatrix} \begin{bmatrix} \varepsilon_x \\ \gamma \\ \frac{1}{R} \end{bmatrix}; \quad (4.15)$$

from the above, one may pick out the tension-shear coupling which is numerically equivalent to

$$\begin{bmatrix} T_x \\ Q \end{bmatrix} = EA_{actual} \begin{bmatrix} 1+\nu & -\nu \\ -\nu & \nu \end{bmatrix} \begin{bmatrix} \varepsilon_x \\ \gamma \end{bmatrix}. \quad (4.16)$$

If one compares this with

$$\begin{bmatrix} T_x \\ Q \end{bmatrix} = \begin{bmatrix} EA & K_{ts} \\ K_{ts} & \kappa AG \end{bmatrix} \begin{bmatrix} \varepsilon_x \\ \gamma \end{bmatrix} \quad (4.17)$$

it is clear that the shear coefficient takes the value $\kappa = 2\nu = 0.5224$ because of the relationship between E and G described above. The coupling coefficient relating tension and shear, $K_{ts} = -5.7905 \times 10^5$ N is also clearly dependent upon the apparent Poisson's ratio. As will be seen, the tension-shear coupling observed for this single face planar structure, manifests itself as both tension-torsion coupling, and bending-shear coupling in the *NASA* structure.

4.4 THE 3-D ASYMMETRIC NASA TRUSS

The structure illustrated in Figure 4.1 is an actual truss, modelled on one employed by *NASA*. According to Figure 4.3, the displacement vectors are defined as

$$\begin{aligned}\mathbf{d}_{j-1} &= [u_1 \ v_1 \ w_1 \ u_2 \ v_2 \ w_2 \ u_3 \ v_3 \ w_3]^T \\ \mathbf{d}_j &= [u_4 \ v_4 \ w_4 \ u_5 \ v_5 \ w_5 \ u_6 \ v_6 \ w_6]^T \\ \mathbf{d}_{j+1} &= [u_7 \ v_7 \ w_7 \ u_8 \ v_8 \ w_8 \ u_9 \ v_9 \ w_9]^T.\end{aligned}\quad (4.18a, b, c)$$

Eigenanalysis gives the reciprocal pair eigenvalues $[\text{inf}, \ 0]^T$ having multiplicity of three, together with twelve eigenvalues very close to unity; of course, the latter must be exactly equal to unity. The zero eigenvalues imply that *any* self-equilibrated load applied to the left hand end of the structure does not penetrate into the structure beyond the first cell. Its reciprocal (inf) implies that the same is true for any self-equilibrated load at the right hand end of the structure.

For a space frame beam-like structure, physical argument requires twelve exactly unity eigenvalues, whose eigen- and principal vectors pertain to the three rigid body translations in the x -, y - and z -directions, and three rigid body rotations about these axes, and six transmitting modes of tension, torsion, and bending moments and shearing forces in both the xy - and xz -planes. For $\lambda = 1$, the set of equations

$$(\mathbf{A} - \mathbf{B})\mathbf{v}_i = \mathbf{0}, \quad (4.19)$$

and use of the *rref* command within MATLAB, shows that there are only four independent eigenvectors – rigid body displacements in the x -, y -, and z -directions and a rigid body rotation about the x -axis. They are

$$\begin{aligned}\mathbf{v}_{rigidx} &= [1 \ 0 \ 0 \ 1 \ 0 \ 0 \ 1 \ 0 \ 0 \ 1 \ 0 \ 0 \ 1 \ 0 \ 0 \ 0]^T, \\ \mathbf{v}_{rigidy} &= [0 \ 1 \ 0 \ 0 \ 1 \ 0 \ 0 \ 1 \ 0 \ 0 \ 1 \ 0 \ 0 \ 1 \ 0 \ 0]^T, \\ \mathbf{v}_{rigidz} &= [0 \ 0 \ 1 \ 0 \ 0 \ 1 \ 0 \ 0 \ 1 \ 0 \ 0 \ 1 \ 0 \ 0 \ 1 \ 0 \ 0 \ 1]^T, \\ \mathbf{v}_{rotx} &= \left[0 \ \frac{L\theta}{2} \ -\frac{H\theta}{3} \ 0 \ -\frac{L\theta}{2} \ -\frac{H\theta}{3} \ 0 \ 0 \ \frac{2H\theta}{3} \ 0 \ \frac{L\theta}{2} \ -\frac{H\theta}{3} \ 0 \ -\frac{L\theta}{2} \ -\frac{H\theta}{3} \ 0 \ 0 \ \frac{2H\theta}{3} \right]^T,\end{aligned}\quad (4.20a, b, c, d)$$

where L is both the length of the cell, and the length of the members which make up the cross-section, and H is the height of the cell; the small angle θ is arbitrarily chosen to

be 5×10^{-8} radian. The coupled principal vectors were determined according to the procedures described in Section 4.2.

4.4.1 Equivalent Continuum Properties and Coupling Coefficients

Physical interpretation of the transmission vectors allows one to calculate the equivalent beam properties and coupling coefficients, as follows:

a) The first two columns of the transmission matrix, $\mathbf{T}(:,1)$ and $\mathbf{T}(:,2)$, are derived from the principal vector for tension, which is coupled to rigid body displacement in the x -direction in the principal vector chain, and represent displacement and force on the left and right hand sides of the cell, as shown in Figure 4.10; it is seen that a combination of tensile force $T_x = 2.4468 \times 10^{-1}$ N and twisting moment $M_x = -5.0147 \times 10^{-3}$ Nm, when applied to both the left and right hand sides of the cell, produces an extension $u = 1 \times 10^{-8}$ m in the x -direction. These two vectors are termed the *extension pair*.

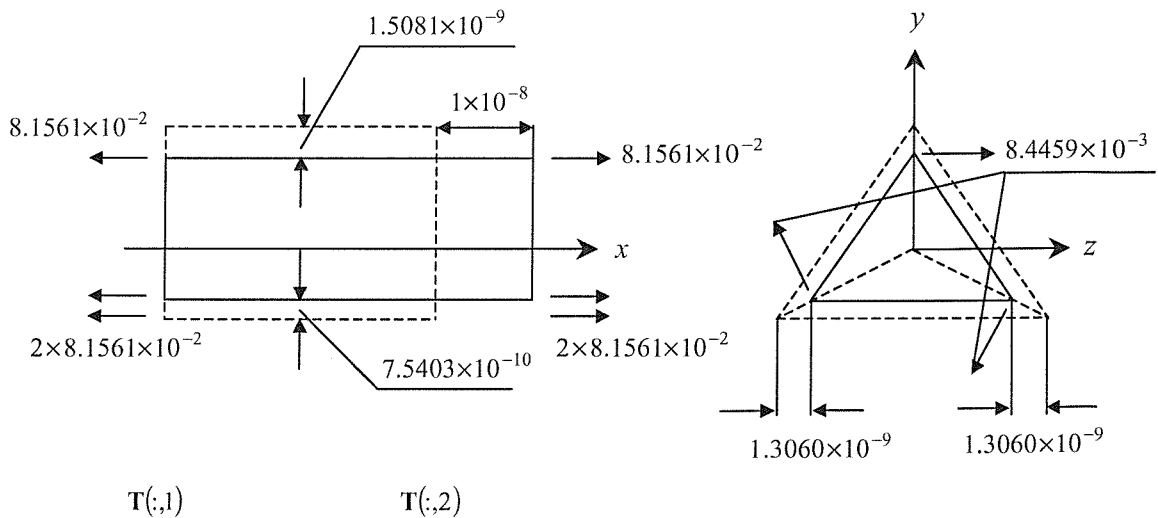


Figure 4.10. Single cell subject to both tension and twisting moment having unit extension; vectors $\mathbf{T}(:,1)$ and $\mathbf{T}(:,2)$ describe the displacement and force components on the left and right hand side of the cell, respectively. Note the apparent Poisson's ratio contraction of the cross-section.

b) The third and fourth columns of the transmission matrix, $\mathbf{T}(:,3)$ and $\mathbf{T}(:,4)$, are derived from the principal vector for torsion, which is coupled to rigid body rotation about the x -axis in the principal vector chain; from Figure 4.11, it is seen that a

combination of twisting moment $M_x = 2.4812 \times 10^{-3}$ Nm and compressive force $T_x = 2.5073 \times 10^{-2}$ N, when applied to the left and right hand sides of the cell, produces a pure rotation $\theta = 5.0 \times 10^{-8}$ radian about the x -axis. These two vectors are termed the *torsional rotation pair*.

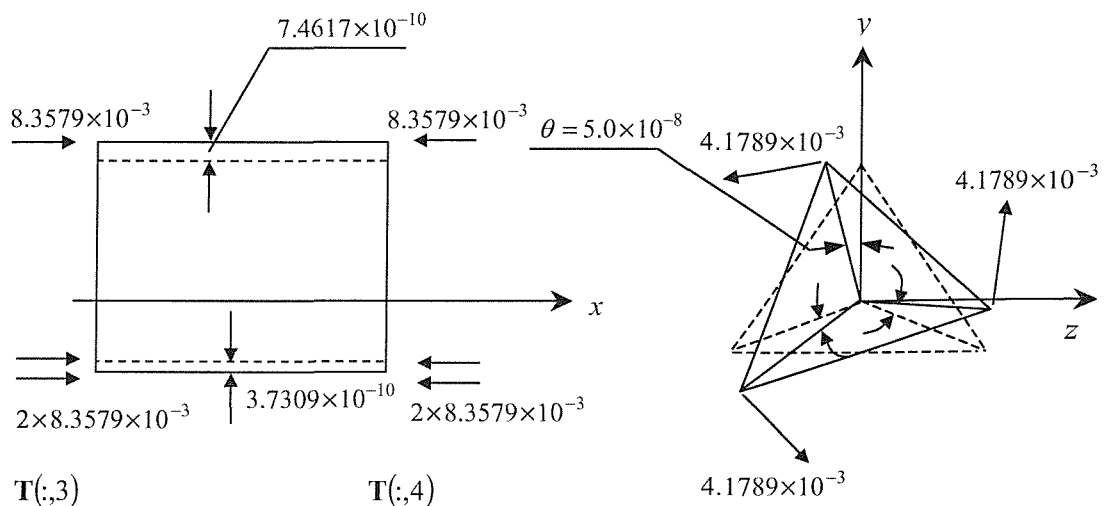


Figure 4.11. Single cell subjected to both twisting moment and compressive force, causing pure rotation about the x -axis; vectors $\mathbf{T}(:,3)$ and $\mathbf{T}(:,4)$ describe the displacement and force components on the left and right hand side of the cell respectively. Note the apparent Poisson's ratio expansion of the cross-section.

The above tension-torsion coupling may be written in matrix form

$$\begin{bmatrix} T_x \\ M_x \end{bmatrix} = \begin{bmatrix} EA & K_u \\ K_u & GJ \end{bmatrix} \begin{bmatrix} \frac{\partial u}{\partial x} \\ \frac{\partial \theta}{\partial x} \end{bmatrix}. \quad (4.21)$$

where K_u is the tension-torsion coupling coefficient. For the *extension pair*, one knows parameters T_x , M_x , L and E , and $\partial u / \partial x = u / L = 2.9172 \times 10^{-8}$; in particular one has $\partial \theta / \partial x = 0$ and substitution into equation (4.21) gives

$$T_x = EA(\partial u / \partial x), \text{ or } A = T_x / (E \partial u / \partial x) = 119.8240 \times 10^{-6} \text{ m}^2,$$

$$M_x = K_u(\partial u / \partial x), \text{ or } K_u = M_x / (\partial u / \partial x) = -1.7190 \times 10^5 \text{ Nm}. \quad (4.22a, b)$$

Additionally from Figure 4.10, one can see displacements in the y -and z -directions; these are an *apparent* Poisson's ratio contraction of the cross-section, from which the equivalent Poisson's ratio would be determined as follows: strain in the x -direction is

$\varepsilon_x = u/L = 2.9172 \times 10^{-8}$, while strain in the y -direction is

$\varepsilon_y = -v/H = -(d_{1y} - d_{3y})/H = -7.6197 \times 10^{-8}$ and strain in the z -direction is

$\varepsilon_z = -w/L = -(d_{1z} - d_{2z})/L = -7.6197 \times 10^{-8}$. Writing $\varepsilon_y = -v\varepsilon_x$, $\varepsilon_z = -v\varepsilon_x$, gives the *apparent* equivalent Poisson's ratio $v = 0.2612$. The equivalent shear modulus would then be found as $G = E/[2(1+v)] = 2.7752 \times 10^{10} \text{ Nm}^{-2}$.

From the *torsional rotation pair*, vectors $\mathbf{T}(:,3)$ and $\mathbf{T}(:,4)$, one knows parameters, T_x , M_x , L and E , and $\partial\theta/\partial x = \theta/L = 1.4586 \times 10^{-7}$; in particular one has $\partial u/\partial x = 0$ which gives

$$M_x = GJ(\partial\theta/\partial x), \text{ or } J = M_x/[G(\partial\theta/\partial x)] = 6.1297 \times 10^{-7} \text{ m}^4,$$

$$T_x = K_u(\partial\theta/\partial x), \text{ or } K_u = T_x/(\partial\theta/\partial x) = -1.7190 \times 10^5 \text{ Nm}, \quad (4.23a, b)$$

where the above equivalent shear modulus G is employed in the determination of J .

Note that identical coupling coefficients are obtained from the two separate vector pairs, which is exactly as one would expect from the reciprocal theorem. Just as the *extension* pair indicates an apparent Poisson's ratio contraction, the *torsional rotation* pair also suggests such an effect: the combination of twisting moment and compressive force necessary to produce rotation, but no extension, also results in a cross-sectional expansion, Figure 4.11, which are the nodal displacements in vector $\mathbf{T}(:,3)$, suggesting

equivalent strains $\varepsilon_y = \varepsilon_z = \frac{1.2924}{L} \times 10^{-9}$. Calculation of an equivalent Poisson's ratio

from this vector pair, would suggest that it should be infinite, since the strain in the x -direction is zero.

Now, the *extension* pair of vectors, and the *torsional rotation* pair, are ideal for determination of the equivalent continuum properties according to equation (4.21), since they describe the necessary combination of tensile force and twisting moment such that the deformation should consist of only *extension* and *torsional rotation*, respectively. This implies that $\partial\theta/\partial x$ and $\partial u/\partial x$ is zero, in turn. These vector pairs may be combined in appropriate proportion to generate *tension* and *torsion* pairs; the former describes the coupled extension and rotation produced by just a tensile force, the latter

the coupled extension and rotation produced by just a torsional moment. These revised vectors are given in Appendix 4.D, where it can be seen why the equivalent Poisson's ratio contraction was referred to above, as *apparent*. The left hand column of the *tension pair*, $\mathbf{T}(:,17)$, shows that all nodal displacements on the left hand side of the cell are zero, while the nodal displacements on the right hand side, $\mathbf{T}(:,18)$, consists of an extension $u = 1 \times 10^{-8}$ m, together with nodal displacements equivalent to a cross-

$$\text{sectional rotation of } \theta = \frac{2\sqrt{3}}{L} \times 10^{-8} = \frac{3}{H} \times 10^{-8} \text{ indicating the relationship } u = \frac{H\theta}{3};$$

however, there are no displacements (on either side of the cell) consistent with a cross-sectional contraction, suggesting that the equivalent Poisson's ratio is zero. The reason behind this simple relationship between u and θ is discussed in Section 4.4.2.

The *torsion pair* has a cross-sectional rotation on the right hand side of

$$\theta = \frac{9.8958 \times 10^{-9}}{2H/3} = 5 \times 10^{-8} \text{ radian; also indicated is a cross-sectional expansion, again}$$

suggesting an anomalous value of Poisson's ratio. The equivalent strain in the x -direction may be expressed as $\varepsilon_x = 1.0247 \times 10^{-9} / L$, where L is the length of the cell; the equivalent strains in the y - and z -directions turn out to have identical value, which would suggest an equivalent Poisson's ratio of $\nu = -1$. These issues are discussed further in Section 4.4.2; however it is sufficient at this stage to note that calculation of the equivalent continuum properties for employment within simple dynamic theories are unaffected by this dilemma. In particular, an incorrect designation of equivalent Poisson's ratio would lead to an incorrect value for the shear modulus G and, in turn, the torsion constant J ; however, the product GJ employed in the dynamic theories remains constant, irrespective of the choice of Poisson's ratio.

- c) The fifth and sixth columns of the *transmission matrix* $\mathbf{T}(:,5)$ and $\mathbf{T}(:,6)$ are determined from the principal vector describing rigid body rotation about the z -axis, which is coupled to rigid body displacement in the y -direction, in the principal vector chain. Similarly, the eleventh and twelfth columns $\mathbf{T}(:,11)$ and $\mathbf{T}(:,12)$ are determined from the principal vector describing rigid body rotation about the y -axis, which is

coupled to rigid body displacement in the z -direction, in the principal vector chain. These two vector pairs are shown in Figure 4.12(a, b) and are termed the *rigid rotation pairs*.

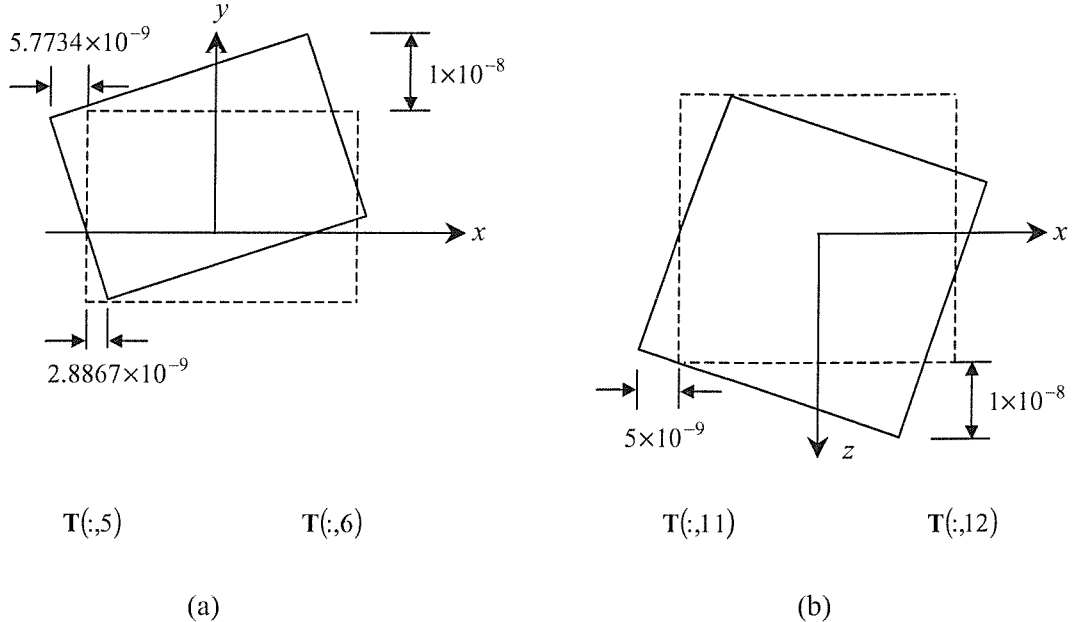


Figure 4.12. (a) Rigid body rotation about the z -axis; (b) Rigid body rotation about the y -axis.

d) The seventh and eighth columns $\mathbf{T}(:,7)$ and $\mathbf{T}(:,8)$ are determined from the principal vector describing a bending moment the xy -plane, which is coupled to rigid body rotation about the z -axis, in the principal vector chain. The force components of these two vectors show a pure bending moment in the xy -plane on both sides of the cell. However, the displacement components in the x -direction indicate not solely a bending curvature in the xy -plane, but rather rotations in the two principal planes and can be expressed in the form

$$\begin{bmatrix} d_{1x} \\ d_{2x} \\ d_{3x} \end{bmatrix}^{\mathbf{T}(:,7)} = a \times \begin{bmatrix} d_{1x} \\ d_{2x} \\ d_{3x} \end{bmatrix}^{\mathbf{T}(:,5)} + b \times \begin{bmatrix} d_{1x} \\ d_{2x} \\ d_{3x} \end{bmatrix}^{\mathbf{T}(:,11)}, \quad \begin{bmatrix} d_{1x} \\ d_{2x} \\ d_{3x} \end{bmatrix}^{\mathbf{T}(:,8)} = c \times \begin{bmatrix} d_{1x} \\ d_{2x} \\ d_{3x} \end{bmatrix}^{\mathbf{T}(:,6)} + d \times \begin{bmatrix} d_{1x} \\ d_{2x} \\ d_{3x} \end{bmatrix}^{\mathbf{T}(:,12)}. \quad (4.24)$$

Similarly, the thirteenth and fourteenth columns $\mathbf{T}(:,13)$ and $\mathbf{T}(:,14)$ are determined from a bending moment vector in the xz -plane which is coupled to rigid body rotation about the y -axis, in the principal vector chain. Again the force components show a pure

bending moment in the xz -plane, while the displacement components in the x -direction can be decomposed as

$$\begin{bmatrix} d_{1x} \\ d_{2x} \\ d_{3x} \end{bmatrix}^{T(,13)} = e \times \begin{bmatrix} d_{1x} \\ d_{2x} \\ d_{3x} \end{bmatrix}^{T(,11)} + f \times \begin{bmatrix} d_{1x} \\ d_{2x} \\ d_{3x} \end{bmatrix}^{T(,5)}, \quad \begin{bmatrix} d_{1x} \\ d_{2x} \\ d_{3x} \end{bmatrix}^{T(,14)} = g \times \begin{bmatrix} d_{1x} \\ d_{2x} \\ d_{3x} \end{bmatrix}^{T(,12)} + h \times \begin{bmatrix} d_{1x} \\ d_{2x} \\ d_{3x} \end{bmatrix}^{T(,6)}. \quad (4.25)$$

Simple calculations from equations (4.24) and (4.25) give the values of $a = -0.5$, $b = -0.28849$, $c = 0.5$, $d = -0.28849$; $e = -0.5$, $f = 0.28849$, $g = 0.5$ and $h = 0.28849$.

The sign of the coefficients in the above decomposition allows one to characterise the nature of the coupling through interpretation of the cross-sectional rotations; for

example, the two columns $\begin{bmatrix} d_{1x} \\ d_{2x} \\ d_{3x} \end{bmatrix}^{T(,5)}$ and $\begin{bmatrix} d_{1x} \\ d_{2x} \\ d_{3x} \end{bmatrix}^{T(,11)}$ represent rotations of the left hand face of the cell about the y - and z -axes, respectively, while $\begin{bmatrix} d_{4x} \\ d_{5x} \\ d_{6x} \end{bmatrix}^{T(,6)}$ and $\begin{bmatrix} d_{4x} \\ d_{5x} \\ d_{6x} \end{bmatrix}^{T(,12)}$ are

rotations of the right hand face cell about the y - and z -axes, respectively. Thus the fact that coefficients a and c are of equal magnitude but opposite sign indicates that this is a curvature in the xy -plane; on the other hand, the fact that coefficients b and d are equal indicates equal rotation of both faces of the cell, which is equivalent to a shear of the cell in the xz -plane.

The nature of the above coupling has been confirmed through an ANSYS model of the ten cell pin-jointed structure loaded by a bending moment in the xy -plane according to the force components of the bending vector $\mathbf{T}(,8)$, as in Figure 4.13. The nodal displacement solutions in the y - and z -directions from this numerical experiment are shown in Figure 4.14, from which bending curvature in the xy -plane and a shear deformation in the xz -plane are obvious. The analytical expressions shown were obtained by curve fitting and, as will be seen, are in complete agreement with the above decomposition. Similar agreement is found when the bending moment is in the xz -

plane. Vector pairs $\mathbf{T}(:,7)$ and $\mathbf{T}(:,8)$, and $\mathbf{T}(:,13)$ and $\mathbf{T}(:,14)$, are each one of two *bending moment pairs*.

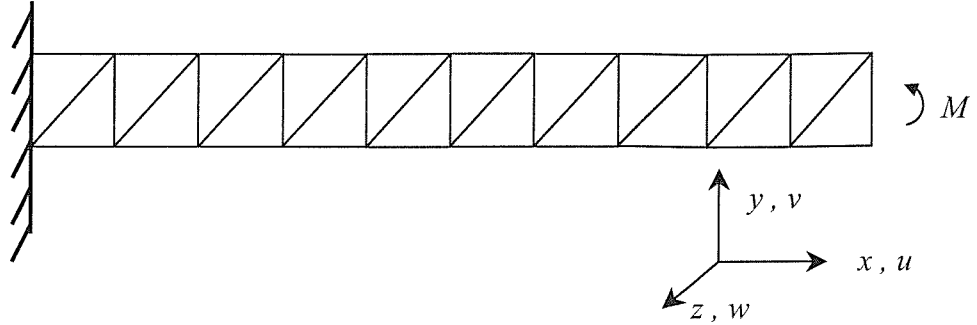
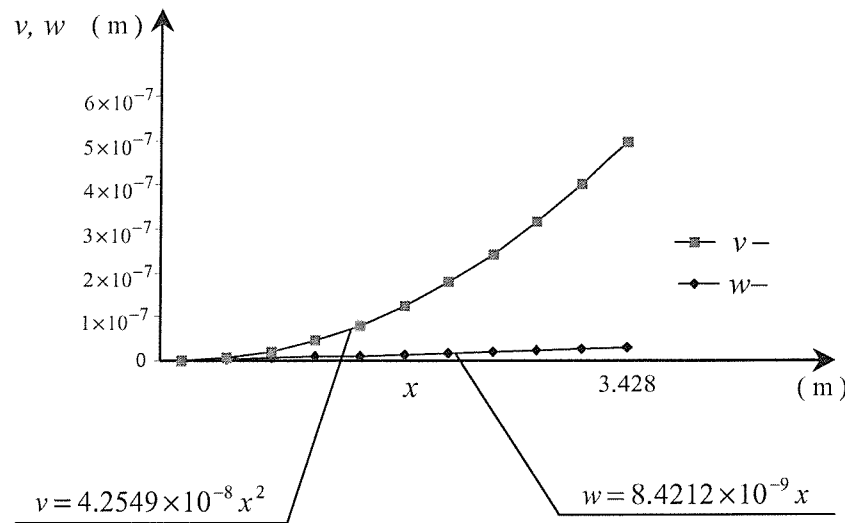


Figure 4.13. Ten cell 3-D pin-jointed satellite truss subject to bending moment in accordance with the force components of the bending vector $\mathbf{T}(:,8)$.



$$\begin{cases} M_z = EI_z \frac{\partial \psi_z}{\partial x} + K_{xz} \left(\psi_y - \frac{\partial w}{\partial x} \right) \\ M_y = EI_y \frac{\partial \psi_y}{\partial x} + K_{xy} \left(\psi_z - \frac{\partial v}{\partial x} \right) \end{cases}, \quad (4.26)$$

$$\begin{cases} Q_z = \kappa_{xz} AG \left(\psi_y - \frac{\partial w}{\partial x} \right) + K_{xz} \frac{\partial \psi_z}{\partial x} \\ Q_y = \kappa_{xy} AG \left(\psi_z - \frac{\partial v}{\partial x} \right) + K_{xy} \frac{\partial \psi_y}{\partial x} \end{cases}. \quad (4.27)$$

where K_{xz} and K_{xy} are defined as the coupling coefficients for bending and shear in the two orthogonal principal planes, xz and xy , respectively

The bending moment vector pairs $\mathbf{T}(:,7)$ and $\mathbf{T}(:,8)$, and $\mathbf{T}(:,13)$ and $\mathbf{T}(:,14)$ are shown in Figures 4.15 and 4.16, respectively, from which geometric consideration yields the two bending curvatures in the xy - and xz -planes

$$1/R_y = 1.4434 \times 10^{-9} / (H/3 \times L/2) = 8.5098 \times 10^{-8} \text{ m}^{-1},$$

$$1/R_z = 2.5 \times 10^{-9} / (L/2 \times L/2) = 8.5098 \times 10^{-8} \text{ m}^{-1},$$

and their coupled shear angles

$$\gamma_{xz} = 1.4434 \times 10^{-9} / (L/2) = 8.4211 \times 10^{-9}$$

in the xz -plane, and

$$\gamma_{xy} = 8.3333 \times 10^{-10} / (H/3) = 8.4211 \times 10^{-9}$$

in the xy -plane, respectively.

According to the definitions of bending curvature and shear angle, one has

$$\frac{1}{R_y} = \frac{d^2 v}{dx^2}, \quad (4.28)$$

$$\gamma_{xz} = \frac{dw}{dx}. \quad (4.29)$$

Integrating equation (4.28) twice and imposing $dv/dx = 0$ and $v = 0$ at the fixed end $x = 0$, and insert the calculated curvature gives

$$v = \frac{1}{2R_y} x^2 = 4.2549 \times 10^{-8} x^2 \text{ m}, \quad (4.30)$$

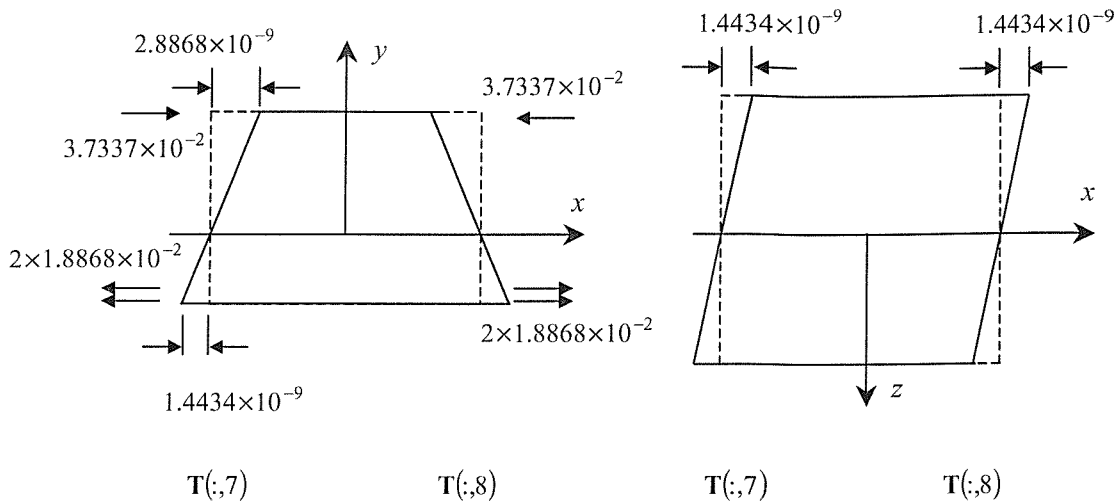


Figure 4.15. Single cell subject to pure bending moment in the xy -plane; vectors $\mathbf{T}(:,7)$ and $\mathbf{T}(:,8)$ describe the displacement and force components on the left and right hand sides of the cell respectively.

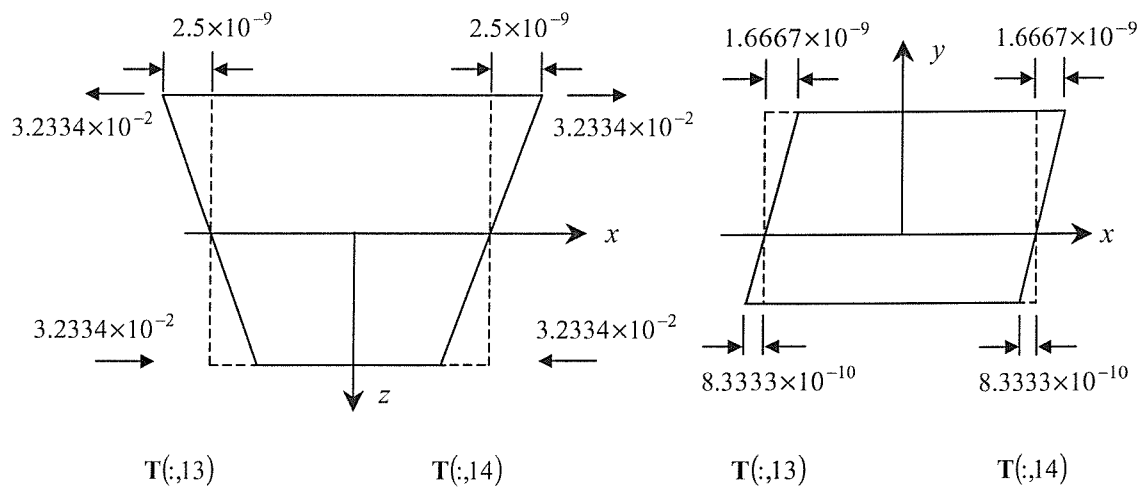


Figure 4.16. Single cell subject to pure bending moment in the xz -plane; vectors $\mathbf{T}(:,13)$ and $\mathbf{T}(:,14)$ describe the displacement and force components on the left and right hand sides of the cell respectively.

while integrating equation (4.29) and imposing $w=0$ at the fixed end $x=0$, and inserting the calculated coupled shear angle gives

$$w = \gamma_{xz} x = 8.4211 \times 10^{-9} x \text{ m.} \quad (4.31)$$

Equations (4.30) and (4.31) are in near exact agreement (error $\cong 0.001\%$) with the two corresponding curves fits shown in Figure 4.14, obtained from the ANSYS model. Last, note that there are no Poisson's ratio effects evident within these bending moment vectors, again indicating $\nu=0$.

e) Finally, the ninth and tenth columns $\mathbf{T}(:,9)$ and $\mathbf{T}(:,10)$, and the fifteenth and sixteenth columns $\mathbf{T}(:,15)$ and $\mathbf{T}(:,16)$ of the transmission matrix describe the displacement and force components when the cell is subjected to both a shearing force and a bending moment in the xy -and xz -planes, respectively, and each is termed a *shearing force pair*. These shear pairs are determined from two principal vectors: the shear vectors in the xy - and xz -planes which are coupled with bending moments in the principal vector chains, and also coupled with the two bending vectors in the two orthogonal planes. The two shear pairs are shown in Figures 4.17 and 4.18, and are decomposed as shown in Figures 4.19 - 4.22.

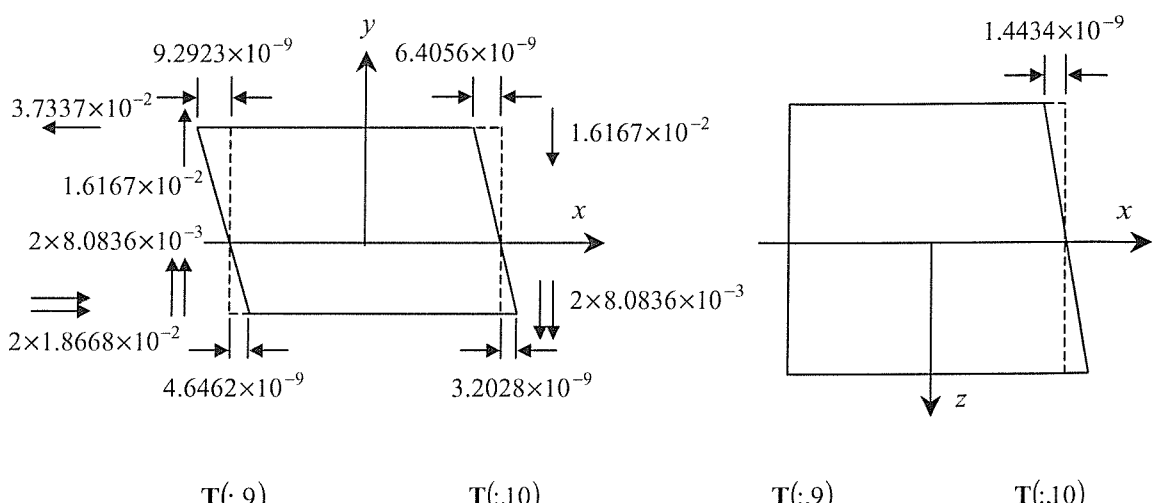


Figure 4.17. Single cell subject to shearing force and bending moment in the xy -plane; vectors $\mathbf{T}(:,9)$ and $\mathbf{T}(:,10)$ describe the displacement and force components on the left and right hand side of the cell respectively.

As in Chapter 2, the shear angle is defined according to the relationship $\gamma = \psi - dv/dx$, in which dv/dx is the centreline slope and ψ is rotation of the cross-section. Now since the centreline slope rotations shown in both Figures 4.17 and 4.18 are already zero, one has $dv/dx = dw/dx = 0$. Thus, from Figures 4.19(a) and 4.21(a), cross-sectional rotations on either side of the cell give the shear angles

$$\gamma_{xy} = 3.9245 \times 10^{-9} / (H/3) = 3.9658 \times 10^{-8},$$

$$\gamma_{xz} = 6.7974 \times 10^{-8} / (L/2) = 3.9658 \times 10^{-8}. \quad (4.32a, b)$$

The coupled bending curvatures can be determined from Figures 4.20(a) and 4.22(a), and are

$$1/R_z = 1.4434 \times 10^{-9} \left/ \left(\frac{L}{2} \times L \right) \right. = 2.4566 \times 10^{-8} \text{ m}^{-1},$$

$$1/R_y = 8.3333 \times 10^{-10} \left/ \left(\frac{H}{3} \times L \right) \right. = 2.4566 \times 10^{-8} \text{ m}^{-1}. \quad (4.33a, b)$$

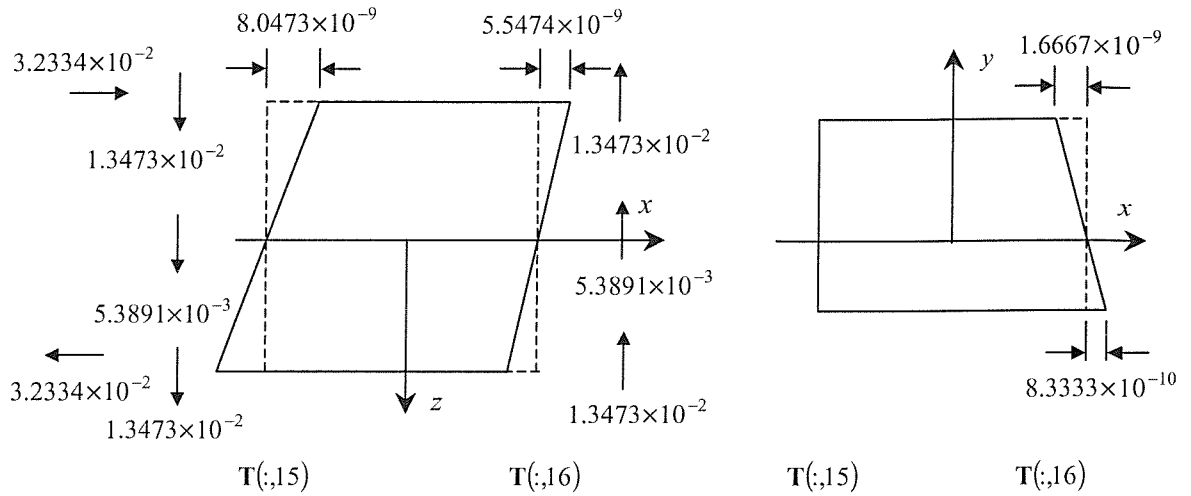


Figure 4.18. Single cell subject to shearing force and bending moment in the xz -plane; vectors $\mathbf{T}(:,15)$ and $\mathbf{T}(:,16)$ describe the displacement and force components on the left and right hand side of the cell respectively.

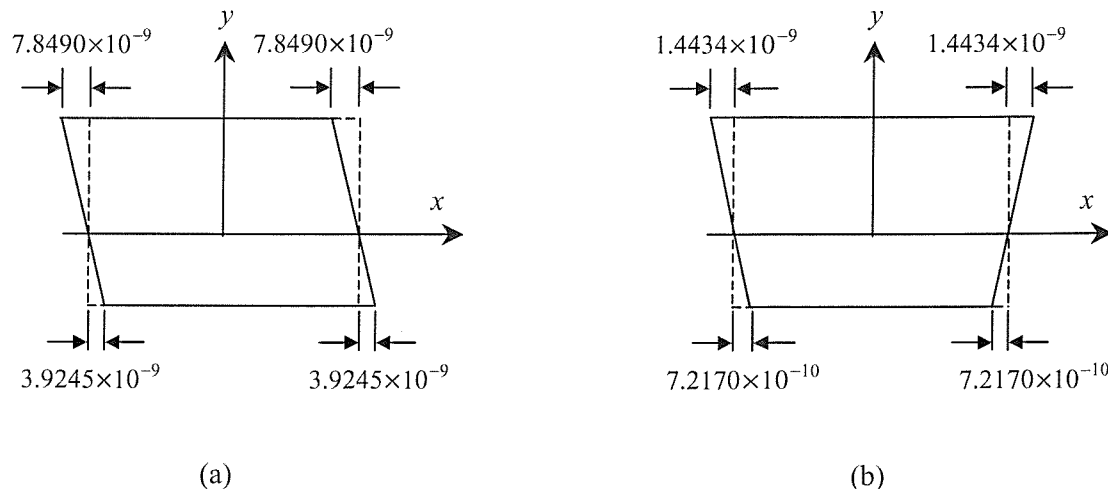


Figure 4.19. Decomposition of the displacements of Figure 4.17 in the xy -plane; (a) shows shear angle and (b) shows bending curvature.

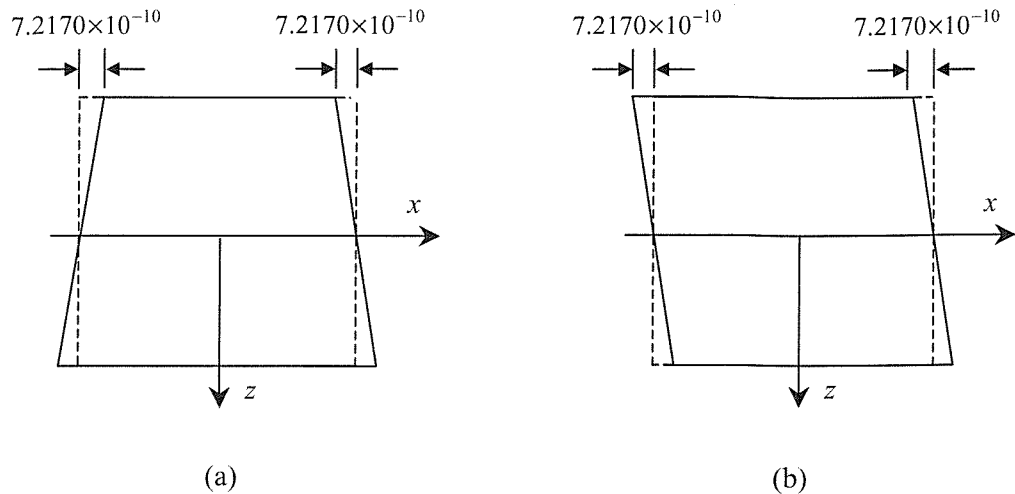


Figure 4.20. Decomposition of displacements of Figure 4.17 in the xz -plane; (a) shows bending curvature coupled with shear angle in the xy -plane due to shearing force, and (b) shows shear angle coupled with bending curvature in the xy -plane due to bending moment.

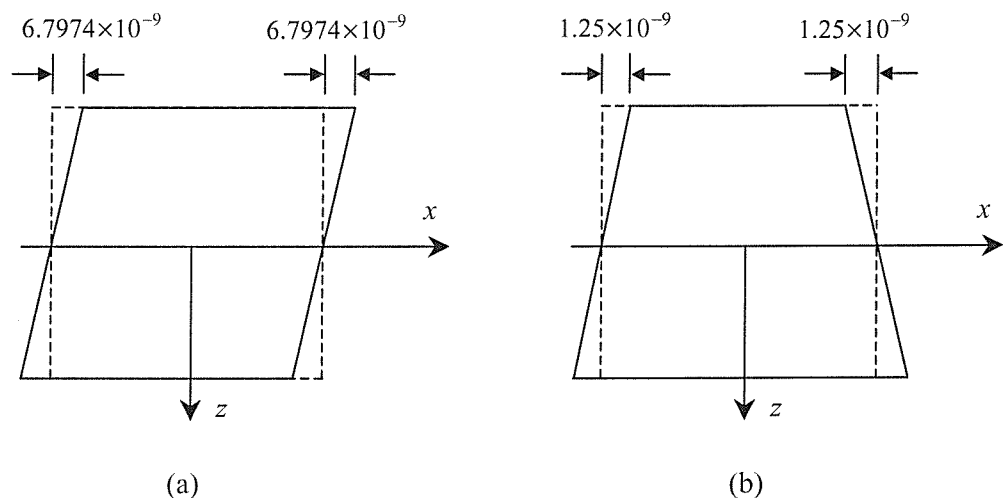


Figure 4.21. Decomposition of displacements of Figure 4.18 in the xz -plane; (a) shows the shear angle and (b) shows the bending curvature.

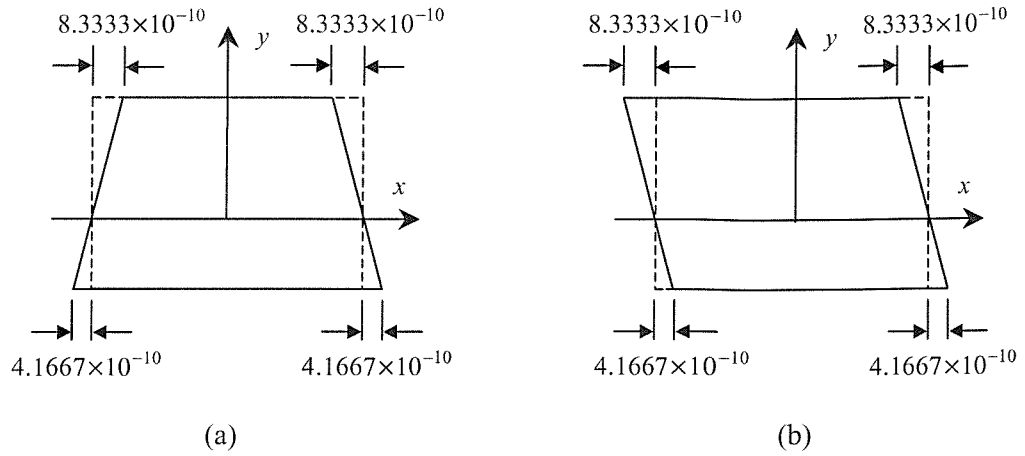


Figure 4.22. Decomposition of displacements of Figure 4.18 in the xy -plane; (a) shows bending curvature coupled with shear angle in the xz -plane due to the shearing force, and (b) shows shear angle coupled with bending curvature in the xz -plane due to the bending moment.

As with the previous analysis of the rigid jointed planar structure, a shearing force gives rise to a bending moment which is effectively one-half, in magnitude, of the full bending vector, but averaged over the cell length, which in turn produces half curvature, which is coupled with half shear angle, as shown in Figures 4.19(b) and 4.21(b). This gives the curvatures due to the bending moments within the two shear vectors as

$$1/R'_y = 7.2170 \times 10^{-10} / (H/3 \times L/2) = 4.2549 \times 10^{-8} \text{ m}^{-1},$$

$$1/R'_z = 1.25 \times 10^{-9} / (L/2 \times L/2) = 4.2549 \times 10^{-8} \text{ m}^{-1}, \quad (4.34a, b)$$

while Figures 4.20(b) and 4.22(b) gives the coupled shear angles in the perpendicular planes

$$\gamma'_{xz} = 7.2170 \times 10^{-10} / (L/2) = 4.2106 \times 10^{-9},$$

$$\gamma'_{xy} = 4.1667 \times 10^{-10} / (H/3) = 4.2106 \times 10^{-9}. \quad (4.35a, b)$$

Compared with the bending curvatures and coupled shear angles obtained in the bending vectors, it is gratifying to see these *half* deformations are consistent with the above argument.

From equations (4.26) and (4.27), the stiffness relationship for the bending and shear coupling of M_z and Q_z can be expressed in the matrix form

$$\begin{bmatrix} Q_z \\ M_z \end{bmatrix} = \begin{bmatrix} \kappa_{xz} AG & K_{xz} \\ K_{xz} & EI_z \end{bmatrix} \begin{bmatrix} \psi_y - \frac{\partial w}{\partial x} \\ \frac{\partial \psi_z}{\partial x} \end{bmatrix}. \quad (4.36)$$

However, in order to determine the equivalent second moment of area, and the shear coefficient, it is more convenient to write the above in the inverted form

$$\begin{bmatrix} \gamma_{xz} \\ \frac{1}{R_y} \end{bmatrix} = \mathbf{N}_c \begin{bmatrix} Q_z \\ M_z \end{bmatrix}. \quad (4.37)$$

where \mathbf{N}_c is now a *compliance* matrix, and

$$\gamma_{xz} = \psi_y - \frac{\partial w}{\partial x}, \quad \frac{1}{R_y} = \frac{\partial \psi_z}{\partial x} \quad (4.38)$$

$$\mathbf{N}_c = \begin{bmatrix} n_{11} & n_{12} \\ n_{21} & n_{22} \end{bmatrix} = \begin{bmatrix} \kappa_{xz} AG & K_{xz} \\ K_{xz} & EI_z \end{bmatrix}^{-1} = \begin{bmatrix} \frac{EI_z}{\kappa_{xz} AG EI_z - K_{xz}^2} & \frac{-K_{xz}}{\kappa_{xz} AG EI_z - K_{xz}^2} \\ \frac{K_{xz}}{\kappa_{xz} AG EI_z - K_{xz}^2} & \frac{-\kappa_{xz} AG}{\kappa_{xz} AG EI_z - K_{xz}^2} \end{bmatrix}. \quad (4.39)$$

For the bending vector pair in the xy -plane, $\mathbf{T}(:,7)$ and $\mathbf{T}(:,8)$, one has, $Q_z = 0$,

$$M_z = 1.10842 \times 10^{-2} \text{ Nm}, \quad 1/R_y = 8.5098 \times 10^{-8} \text{ m}^{-1}, \quad \gamma_{xz} = 8.4211 \times 10^{-8}, \text{ and}$$

substituting into equation (4.37) gives

$$n_{12} = \frac{\gamma_{xz}}{M_z} = 7.5974 \times 10^{-7}, \quad (4.40)$$

$$n_{22} = \frac{1/R_y}{M_z} = 7.6774 \times 10^{-6}. \quad (4.41)$$

From the shear vector pair in the xz -plane, $\mathbf{T}(:,15)$ and $\mathbf{T}(:,16)$, one has $M_z = 0 \text{ Nm}$,

$$Q_z = 3.2334 \times 10^{-2} \text{ N}, \quad 1/R_y = 2.4566 \times 10^{-8} \text{ m}^{-1}, \quad \gamma_{xz} = 3.9658 \times 10^{-8}, \text{ and substituting}$$

into equation (4.37) gives

$$n_{11} = \frac{\gamma_{xz}}{Q_z} = 1.2265 \times 10^{-6}, \quad (4.42)$$

$$n_{21} = \frac{1/R_y}{Q_z} = 7.5974 \times 10^{-7}. \quad (4.43)$$

Note that n_{12} and n_{21} are found to be identical from the two vector pairs, which is as one would expect from the reciprocal theorem. Inversion of the matrix \mathbf{N}_c gives

$$\begin{bmatrix} \kappa_{xz}AG & K_{xz} \\ K_{xz} & EI_z \end{bmatrix} = \begin{bmatrix} n_{11} & n_{12} \\ n_{21} & n_{22} \end{bmatrix}^{-1} = \begin{bmatrix} 8.6857 \times 10^5 & -8.5952 \times 10^4 \\ -8.5952 \times 10^4 & 1.3876 \times 10^5 \end{bmatrix}. \quad (4.44)$$

The equivalent second moment of area I_z , shear coefficient κ_{xz} , and the coupling coefficient for bending and shear K_{xz} , are then determined as: $\kappa_{xz} = 0.2612$, $I_z = 1.9823 \times 10^{-6} \text{ m}^4$, $K_{xz} = -8.5952 \times 10^4 \text{ Nm}$. As with the single face, note that the shear coefficient is again a (now single) multiple of the apparent Poisson's ratio.

Consideration of the bending vector pair in the xz -plane, $\mathbf{T}(:,11)$ and $\mathbf{T}(:,12)$, and the shear vector pair in the xy -plane, $\mathbf{T}(:,9)$ and $\mathbf{T}(:,10)$, and following similar procedures, it is found that $\kappa_{xy} = \kappa_{xz}$, $I_y = I_z$ and $K_{xy} = K_{xz}$.

4.4.2 Coupling Behaviour

All of the observed couplings for the 3-D structure can be explained in terms of the tension-shear coupling seen in the *single face* 2-D planar structure; recall that an extension u ($= 1 \times 10^{-8} \text{ m}$) was coupled with a shear angle of u/L . During tension, each of the three faces would both extend, and undergo a shear deformation, *if the three faces were disconnected*; however, compatibility of nodal displacement of the three faces, requires an out-of-plane rotation of the face, for which it is a mechanism and so does not affect the stiffness. Thus shear deformation in the three planes at 120° , together with this out-of-plane rotation, is nothing other than a rotation of the cross-section as a whole; hence a tensile force produces both an extension and a rotation, as in the *tension* pair, $\mathbf{T}(:,18)$; as with the single face, there is no Poisson's ratio contraction associated with this extension. Moreover, the relationship $u = \frac{H\theta}{3}$ noted in Section 4.4.1, is entirely consistent with the shear of the single face.

Bending-shear coupling is easily understood by considering a cell having a square cross-section, comprised of four 2-D planar face cells, as depicted in Figure 4.23a.

Decompose this into two side faces, and an upper and lower face, Figure 4.23b, with the nodal forces that constitute the pure bending moment being shared accordingly. Now, the side faces contribute nothing towards coupling, and there is zero Poisson's ratio contraction in the y -direction. The lower face is in tension and will both extend and shear; the upper face is in compression, and will both contract and shear in the same sense as the lower face, since the diagonal is in the opposite direction to that of the lower face. Thus the pure bending moment would produce a bending curvature in the xy -plane, coupled with shear in the xz -plane. These arguments may be transferred to the triangular structure by imagining that the upper face is removed, and the two side faces are folded in, to meet at the apex, nodes 3 and 6 of the cell. Now the shear deformation arises from just the lower face being in tension.

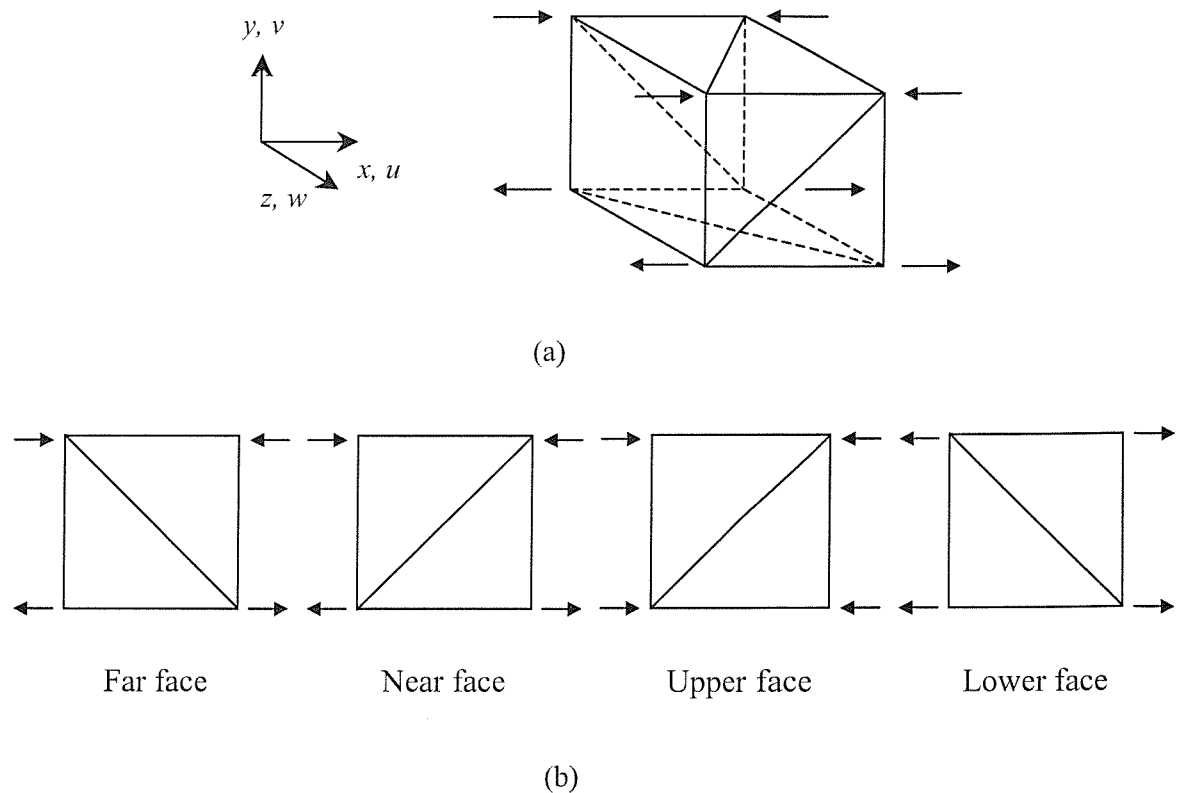


Figure 4.23. (a) Single repeating cell of an asymmetric framework with square cross section subjected to bending moment; (b) four decomposed faces subject to tension or compression

At first sight, the tension-torsion coupling, and the bending curvature-shear coupling, of this asymmetric structure, may seem unusual; however this is solely because one is trying to characterise the equivalent continuum behaviour according to the precepts of



isotropic, rather than anisotropic, elasticity. This is particularly evident in attempts to determine an equivalent value for Poisson's ratio: suppose that the single diagonal bar in each face of the structure were to be replaced two such diagonals, each having a one-half cross-sectional area; the equivalent cross-sectional area would remain unchanged. However the now symmetry of the structure leads to a quite unambiguous value for Poisson's ratio as $\nu = 0.2612$; indeed this value of ν and the equivalent cross-sectional area, are given in Chapter 7, where a pre-twisted structure having two such diagonals is considered over a wide range of pre-twist angles, α , including the straight case, $\alpha = 0$. For this latter case, one has a cross-sectional contraction (the Poisson's ratio effect), rather than a rotation, coupled to an extension – however the term *coupling* is rarely, if ever, employed, since this Poisson's ratio effect is regarded as *normal* within the field of isotropic elasticity. Returning to the 3-D asymmetric structure, and the *extension pair*, one requires a twisting moment to suppress cross-sectional rotation, when one has an *apparent* Poisson's ratio of the same expected value $\nu = 0.2612$. Thus one sees an entirely consistent *trade-off* between Poisson's ratio coupling (normally *contraction*) and rotational coupling, according to the symmetry or asymmetry of the structure.

APPENDIX 4.A

TRANSMISSION MATRIX OF A SINGLE-FACE CELL OF THE 3-D SATELLITE TRUSS, FIGURE 4.2

$$\mathbf{T} = \begin{bmatrix} 0 & 1 \times 10^{-8} & -2.5 \times 10^{-9} & 2.5 \times 10^{-9} & 6.0355 \times 10^{-9} & 3.5355 \times 10^{-9} \\ 0 & 0 & 0 & 0 & -2.5 \times 10^{-9} & -2.5 \times 10^{-9} \\ -1 \times 10^{-8} & 0 & 2.5 \times 10^{-9} & -2.5 \times 10^{-9} & -6.0355 \times 10^{-9} & -3.5355 \times 10^{-9} \\ 0 & 0 & 0 & 0 & 0 & 0 \\ 3.2334 \times 10^{-2} & 3.2334 \times 10^{-2} & 1.6167 \times 10^{-2} & 1.6167 \times 10^{-2} & -2.4251 \times 10^{-2} & -8.0836 \times 10^{-3} \\ 0 & 0 & 0 & 0 & -8.0836 \times 10^{-3} & -8.0836 \times 10^{-3} \\ 3.2334 \times 10^{-2} & 3.2334 \times 10^{-2} & -1.6167 \times 10^{-2} & -1.6167 \times 10^{-2} & 8.0836 \times 10^{-3} & -8.0836 \times 10^{-3} \\ 0 & 0 & 0 & 0 & -8.0836 \times 10^{-3} & -8.0836 \times 10^{-3} \end{bmatrix}$$

$$\mathbf{T}_{\text{derived}} = \begin{bmatrix} -6.3060 \times 10^{-9} & 6.3060 \times 10^{-9} & 4.7855 \times 10^{-9} & 7.2855 \times 10^{-9} & 6.0355 \times 10^{-9} & 6.0355 \times 10^{-9} \\ 2.6120 \times 10^{-9} & 2.6120 \times 10^{-9} & -2.5 \times 10^{-9} & -2.5 \times 10^{-9} & -2.5 \times 10^{-9} & -2.5 \times 10^{-9} \\ -3.6940 \times 10^{-9} & 3.6940 \times 10^{-9} & -7.2855 \times 10^{-9} & -4.7855 \times 10^{-9} & -8.5355 \times 10^{-9} & -3.5355 \times 10^{-9} \\ 0 & 0 & 0 & 0 & 0 & 0 \\ 5.7672 \times 10^{-2} & 4.0780 \times 10^{-2} & -8.0836 \times 10^{-3} & 8.0836 \times 10^{-3} & -1.6167 \times 10^{-2} & 0 \\ 8.4459 \times 10^{-3} & 8.4459 \times 10^{-3} & -8.0836 \times 10^{-3} & -8.0836 \times 10^{-3} & -8.0836 \times 10^{-3} & -8.0836 \times 10^{-3} \\ 2.3889 \times 10^{-2} & 4.0780 \times 10^{-2} & 8.0836 \times 10^{-3} & -8.0836 \times 10^{-3} & 1.6167 \times 10^{-2} & 0 \\ 8.4459 \times 10^{-3} & 8.4459 \times 10^{-3} & -8.0836 \times 10^{-3} & -8.0836 \times 10^{-3} & -8.0836 \times 10^{-3} & -8.0836 \times 10^{-3} \end{bmatrix}$$

APPENDIX 4.B

TRANSMISSION MATRIX FOR THE 3-D PIN-JOINTED ASYMMETRIC FRAMEWORK, FIGURE 4.3

$$\mathbf{T} = \begin{bmatrix}
 0 & 1 \times 10^{-8} & 0 & 0 & 2.8868 \times 10^{-9} & 2.8868 \times 10^{-9} & 0 & 2.8868 \times 10^{-9} \\
 7.5403 \times 10^{-10} & 7.5403 \times 10^{-10} & 0 & 8.57 \times 10^{-9} & 0 & 1 \times 10^{-8} & 0 & 0 \\
 1.3060 \times 10^{-9} & 1.3060 \times 10^{-9} & 0 & -4.9479 \times 10^{-9} & 0 & 0 & 0 & 0 \\
 0 & 1 \times 10^{-8} & 0 & 0 & 2.8868 \times 10^{-9} & 2.8868 \times 10^{-9} & -2.8868 \times 10^{-9} & 0 \\
 7.5403 \times 10^{-10} & 7.5403 \times 10^{-10} & 0 & -8.57 \times 10^{-9} & 0 & 1 \times 10^{-8} & 0 & 0 \\
 -1.3060 \times 10^{-9} & -1.3060 \times 10^{-9} & 0 & -4.9749 \times 10^{-9} & 0 & 0 & 0 & 0 \\
 0 & 1 \times 10^{-8} & 0 & 0 & -5.7735 \times 10^{-9} & -5.7735 \times 10^{-9} & 2.8868 \times 10^{-9} & -2.8868 \times 10^{-9} \\
 -1.5081 \times 10^{-9} & -1.5081 \times 10^{-9} & 0 & 0 & 0 & 1 \times 10^{-8} & 0 & 0 \\
 0 & 0 & 0 & 9.8958 \times 10^{-8} & 0 & 0 & 0 & 0 \\
 8.1560 \times 10^{-2} & 8.1560 \times 10^{-2} & -8.3578 \times 10^{-3} & -8.3578 \times 10^{-3} & 0 & 0 & 1.8868 \times 10^{-2} & 1.8868 \times 10^{-2} \\
 -7.3143 \times 10^{-3} & -7.3143 \times 10^{-3} & 3.6191 \times 10^{-3} & 3.6191 \times 10^{-3} & 0 & 0 & 0 & 0 \\
 4.2229 \times 10^{-3} & 4.2229 \times 10^{-3} & -2.0895 \times 10^{-3} & -2.0895 \times 10^{-3} & 0 & 0 & 0 & 0 \\
 8.1560 \times 10^{-2} & 8.1560 \times 10^{-2} & -8.3578 \times 10^{-3} & -8.3578 \times 10^{-3} & 0 & 0 & 1.8868 \times 10^{-2} & 1.8868 \times 10^{-2} \\
 7.3143 \times 10^{-3} & 7.3143 \times 10^{-3} & -3.6191 \times 10^{-3} & -3.6191 \times 10^{-3} & 0 & 0 & 0 & 0 \\
 4.2229 \times 10^{-3} & 4.2229 \times 10^{-3} & -2.0859 \times 10^{-3} & -2.0859 \times 10^{-3} & 0 & 0 & 0 & 0 \\
 8.1560 \times 10^{-2} & 8.1560 \times 10^{-2} & -8.3578 \times 10^{-3} & -8.3578 \times 10^{-3} & 0 & 0 & -3.7337 \times 10^{-2} & -3.7337 \times 10^{-2} \\
 0 & 0 & 0 & 0 & 0 & 0 & 0 & 0 \\
 -8.4459 \times 10^{-3} & -8.4459 \times 10^{-3} & 4.1789 \times 10^{-3} & 4.1789 \times 10^{-3} & 0 & 0 & 0 & 0
 \end{bmatrix}$$

$$\begin{bmatrix}
4.6462 \times 10^{-9} & 1.7594 \times 10^{-9} & 5 \times 10^{-9} & 5 \times 10^{-9} & -3.3333 \times 10^{-9} & 1.6667 \times 10^{-9} & 8.0474 \times 10^{-9} & 6.3807 \times 10^{-9} \\
3.3333 \times 10^{-9} & 3.3333 \times 10^{-9} & 0 & 0 & 0 & 0 & 9.6225 \times 10^{-10} & 9.6225 \times 10^{-10} \\
0 & 0 & 0 & 1 \times 10^{-8} & 0 & 0 & -1.6667 \times 10^{-9} & -1.6667 \times 10^{-1} \\
4.6462 \times 10^{-9} & 4.6462 \times 10^{-9} & -5 \times 10^{-9} & -5 \times 10^{-9} & 1.6667 \times 10^{-9} & -3.3333 \times 10^{-9} & -8.0474 \times 10^{-9} & -4.7140 \times 10^{-9} \\
-3.3333 \times 10^{-9} & -3.3333 \times 10^{-9} & 0 & 0 & 0 & 0 & 9.6225 \times 10^{-10} & 9.6225 \times 10^{-10} \\
0 & 0 & 0 & 1 \times 10^{-8} & 0 & 0 & 1.6667 \times 10^{-9} & 1.6667 \times 10^{-9} \\
-9.2923 \times 10^{-9} & -6.4056 \times 10^{-9} & 0 & 0 & 1.6667 \times 10^{-9} & 1.6667 \times 10^{-9} & 0 & -1.6667 \times 10^{-9} \\
0 & 0 & 0 & 0 & 0 & 0 & -1.9245 \times 10^{-9} & -1.9245 \times 10^{-9} \\
0 & 0 & 0 & 1 \times 10^{-8} & 0 & 0 & 0 & 0 \\
-1.8668 \times 10^{-2} & 0 & 0 & 0 & 3.2334 \times 10^{-2} & 3.2334 \times 10^{-2} & -3.2334 \times 10^{-2} & 0 \\
-8.0836 \times 10^{-3} & -8.0836 \times 10^{-3} & 0 & 0 & 0 & 0 & -4.6671 \times 10^{-3} & -4.6671 \times 10^{-3} \\
-4.6671 \times 10^{-3} & -4.6671 \times 10^{-3} & 0 & 0 & 0 & 0 & -1.3473 \times 10^{-2} & -1.3473 \times 10^{-2} \\
-1.8668 \times 10^{-2} & 0 & 0 & 0 & -3.2334 \times 10^{-2} & -3.2334 \times 10^{-2} & 3.2334 \times 10^{-2} & 0 \\
-8.0836 \times 10^{-3} & -8.0836 \times 10^{-3} & 0 & 0 & 0 & 0 & 4.6671 \times 10^{-3} & 4.6671 \times 10^{-3} \\
4.6671 \times 10^{-3} & 4.6671 \times 10^{-3} & 0 & 0 & 0 & 0 & -1.3473 \times 10^{-2} & -1.3473 \times 10^{-2} \\
3.7337 \times 10^{-2} & 0 & 0 & 0 & 0 & 0 & 0 & 0 \\
-1.6167 \times 10^{-2} & -1.6167 \times 10^{-2} & 0 & 0 & 0 & 0 & 0 & 0 \\
0 & 0 & 0 & 0 & 0 & 0 & -5.3891 \times 10^{-3} & -5.3891 \times 10^{-3}
\end{bmatrix}$$

APPENDIX 4.C

STIFFNESS MATRIX OF THE SINGLE FACE OF THE 3-D SATELLITE TRUSS, FIGURE 4.2

$$\begin{bmatrix}
 F_{1x} \\
 F_{1y} \\
 F_{2x} \\
 F_{2y} \\
 F_{3x} \\
 F_{3y} \\
 F_{4x} \\
 F_{4y}
 \end{bmatrix} = \frac{EA}{L} \begin{bmatrix}
 \frac{1}{2} + \frac{\sqrt{2}}{4} & \frac{\sqrt{2}}{4} & 0 & 0 & | & -\frac{1}{2} & 0 & -\frac{\sqrt{2}}{4} & -\frac{\sqrt{2}}{4} \\
 \frac{\sqrt{2}}{4} & \frac{1}{2} + \frac{\sqrt{2}}{4} & 0 & -\frac{1}{2} & | & 0 & 0 & -\frac{\sqrt{2}}{4} & -\frac{\sqrt{2}}{4} \\
 0 & 0 & \frac{1}{2} & 0 & | & 0 & 0 & -\frac{1}{2} & 0 \\
 0 & -\frac{1}{2} & 0 & \frac{1}{2} & | & 0 & 0 & 0 & 0 \\
 -\frac{1}{2} & 0 & 0 & 0 & | & \frac{1}{2} & 0 & 0 & 0 \\
 0 & 0 & 0 & 0 & | & 0 & \frac{1}{2} & 0 & -\frac{1}{2} \\
 -\frac{\sqrt{2}}{4} & -\frac{\sqrt{2}}{4} & -\frac{1}{2} & 0 & | & 0 & 0 & \frac{1}{2} + \frac{\sqrt{2}}{4} & \frac{\sqrt{2}}{4} \\
 -\frac{\sqrt{2}}{4} & -\frac{\sqrt{2}}{4} & 0 & 0 & | & 0 & -\frac{1}{2} & \frac{\sqrt{2}}{4} & \frac{1}{2} + \frac{\sqrt{2}}{4}
 \end{bmatrix} \begin{bmatrix}
 d_{1x} \\
 d_{1y} \\
 d_{2x} \\
 d_{2y} \\
 d_{3x} \\
 d_{3y} \\
 d_{4x} \\
 d_{4y}
 \end{bmatrix}$$

APPENDIX 4.D

TENSION AND TORSION PAIRS FOR THE 3-D ASYMMETRIC PIN-JOINTED FRAMEWORK, FIGURE 4.3

$$\begin{aligned}
 [\text{Tension}] &= [T(:,17) T(:,18)] = \begin{bmatrix} 0 & 1 \times 10^{-8} \\ 0 & 1.7321 \times 10^{-8} \\ 0 & -1 \times 10^{-8} \\ 0 & 1 \times 10^{-8} \\ 0 & -1.7321 \times 10^{-8} \\ 0 & -1 \times 10^{-8} \\ 0 & 1 \times 10^{-8} \\ 0 & 0 \\ 0 & 2 \times 10^{-8} \\ 6.4669 \times 10^{-2} & 6.4669 \times 10^{-2} \\ 0 & 0 \\ 0 & 0 \\ 6.4669 \times 10^{-2} & 6.4669 \times 10^{-2} \\ 0 & 0 \\ 0 & 0 \\ 6.4669 \times 10^{-2} & 6.4669 \times 10^{-2} \\ 0 & 0 \\ 0 & 0 \end{bmatrix} \\
 [\text{Torsion}] &= [T(:,19) T(:,20)] = \begin{bmatrix} 0 & 1.0247 \times 10^{-9} \\ -2.9582 \times 10^{-10} & 8.2742 \times 10^{-9} \\ -5.1237 \times 10^{-10} & -5.4603 \times 10^{-9} \\ 0 & 1.0247 \times 10^{-9} \\ -2.9582 \times 10^{-10} & -8.8658 \times 10^{-9} \\ 5.1237 \times 10^{-10} & -4.4355 \times 10^{-9} \\ 0 & 1.0247 \times 10^{-9} \\ 5.9164 \times 10^{-10} & 5.9164 \times 10^{-10} \\ 0 & 9.8958 \times 10^{-9} \\ 0 & 0 \\ 2.8695 \times 10^{-3} & 2.8695 \times 10^{-3} \\ -1.6567 \times 10^{-3} & -1.6567 \times 10^{-3} \\ 0 & 0 \\ -2.8695 \times 10^{-3} & -2.8695 \times 10^{-3} \\ -1.6567 \times 10^{-3} & -1.6567 \times 10^{-3} \\ 0 & 0 \\ 0 & 0 \\ 3.3134 \times 10^{-3} & 3.3134 \times 10^{-3} \end{bmatrix}
 \end{aligned}$$

CHAPTER FIVE

DYNAMIC ANALYSIS OF A REPETITIVE STRUCTURE

5.1 INTRODUCTION

In this Chapter, continuum dynamic beam theories are constructed for the asymmetric structure considered in Chapter 4, which allow for the tension-torsion and bending-shear couplings revealed between these displacement modes. The analysis employs a generalised stiffness matrix for the cell, whose elements are the equivalent continuum properties as determined in Chapter 4, and the use of Hamilton's principle. Inertia properties are determined from first principles, and may be regarded as *exact*.

The frequency predictions are compared with those obtained from ANSYS, the latter being regarded as the benchmark for accuracy. However, unlike static FEA of pin-jointed structures, dynamic analysis may no longer be regarded as exact; one has a choice of *lumped* or *consistent* mass matrices, neither of which will lead to the exact frequency. The lumped mass matrix is diagonal, which is computationally advantageous, and usually leads to an underestimate of natural frequencies. Its use is considered essential in problems involving wave propagation, and is generally regarded as better for *skinny* structures [74]. The consistent mass matrix is symmetric and banded, and according to Desai and Abel [75], the principal advantage is more accurate modes shapes and frequencies that are proven upper bounds. On the other hand, use of the consistent matrix can lead to spurious modes of oscillation, and this was found with an ANSYS model of a rigid-jointed truss.

The ANSYS predictions employed here, are those which provide best agreement with the continuum models derived below; for the flexural frequency predictions of the coupled Timoshenko beam theory, this is achieved using the lumped mass option; on the other hand, for the coupled tension-torsion frequency predictions, better agreement is found using the consistent mass matrix.

5.2 MASS AND MOMENT OF INERTIA PER UNIT LENGTH

a) The mass per unit length is calculated simply as the sum of the individual masses of the members that constitute the generic cell, divided by the length of the cell (0.3428 m), and is found to be 0.8758 kg/m. Note that cross-sectional members are regarded as being shared between adjacent cells, so their contribution is halved.

b) The moments of inertia of the cell are calculated as follows: first, the moments of inertia of each member is calculated about its own centre of gravity, taken as the origin of a local coordinate system, with the local x -axis along the length of the member, and using the simple formulae $J_y = J_z = mL^2/12$, and $J_x = mr^2/2$; however, for the structure under consideration, the moment of inertia J_x of a typical member is approximately $1/2000^{\text{th}}$ of J_y , so the former is ignored. These are then converted to moments of inertia about the three global principal axes, using coordinate transformations and the parallel axis theorem, as appropriate [76]. Last, they are added to give the moments of inertia for the complete cell, which is then divided by the length. The moments of inertia about the x -, y - and z -axes per unit length are found to be

$$J_x = 2.2177 \times 10^{-2} \text{ kgm} \text{ and } J_y = J_z = 2.4689 \times 10^{-2} \text{ kgm}.$$

Again note that contributions from the members that constitute the cross-section are halved. It should be noted that these properties may be regarded as exact, notwithstanding the above approximation, while the equivalent continuum properties determined through eigenanalysis are regarded as approximate.

5.3 CONTINUUM DYNAMIC THEORY

5.3.1 Dynamic Equations

The generalised stiffness for the truss examined in Chapter 4 may be written as

$$\mathbf{F} = \mathbf{Kd}, \quad (5.1)$$

or in full

$$\begin{bmatrix} T_x \\ M_x \\ Q_y \\ M_y \\ Q_z \\ M_z \end{bmatrix} = \begin{bmatrix} EA & K_u & 0 & 0 & 0 & 0 \\ K_u & GJ & 0 & 0 & 0 & 0 \\ 0 & 0 & \kappa_{xy}AG & K_{xy} & 0 & 0 \\ 0 & 0 & K_{xy} & EI_y & 0 & 0 \\ 0 & 0 & 0 & 0 & \kappa_{xz}AG & K_{xz} \\ 0 & 0 & 0 & 0 & K_{xz} & EI_z \end{bmatrix} \begin{bmatrix} \frac{\partial u}{\partial x} \\ \frac{\partial \theta}{\partial x} \\ \psi_z - \frac{\partial v}{\partial x} \\ \frac{\partial \psi_y}{\partial x} \\ \psi_y - \frac{\partial w}{\partial x} \\ \frac{\partial \psi_z}{\partial x} \end{bmatrix}; \quad (5.2)$$

Note that this matrix is block diagonal, so the tension-torsion coupling can be treated separately; at first sight the same is true for bending in the two planes, but closer inspection shows that cross-sectional rotations, and their derivatives provide coupling in the displacement vector.

According to Hamilton's principle [77], the governing equations and boundary conditions may be generated according to

$$\delta \int_{t_1}^{t_2} (T - U) dt = 0, \quad (5.3)$$

where the kinetic and strain energies are

$$T = \int_0^L \frac{1}{2} \left\{ m \left(\frac{\partial u}{\partial t} \right)^2 + J_x \left(\frac{\partial \theta}{\partial t} \right)^2 + m \left(\frac{\partial v}{\partial t} \right)^2 + J_y \left(\frac{\partial \psi_y}{\partial t} \right)^2 + m \left(\frac{\partial w}{\partial t} \right)^2 + J_z \left(\frac{\partial \psi_z}{\partial t} \right)^2 \right\} dx, \quad (5.4)$$

$$U = \int_0^L \left\{ \frac{1}{2} \mathbf{d}^T \mathbf{K} \mathbf{d} \right\} dx. \quad (5.5)$$

Carry out the first variation of equation (5.3), and integrate by parts in the usual way, gives the dynamic equations:

$$EA \frac{\partial^2 u}{\partial x^2} + K_u \frac{\partial^2 \theta}{\partial x^2} = m \frac{\partial^2 u}{\partial t^2}, \quad (5.6a)$$

$$GJ \frac{\partial^2 \theta}{\partial x^2} + K_u \frac{\partial^2 u}{\partial x^2} = J_x \frac{\partial^2 \theta}{\partial t^2}, \quad (5.6b)$$

$$m \frac{\partial^2 v}{\partial t^2} + \kappa_{xy}AG \left(\frac{\partial \psi_z}{\partial x} - \frac{\partial^2 v}{\partial x^2} \right) + K_{xy} \frac{\partial^2 \psi_y}{\partial x^2} = 0, \quad (5.6c)$$

$$m \frac{\partial^2 w}{\partial t^2} + \kappa_{xz} AG \left(\frac{\partial \psi_y}{\partial x} - \frac{\partial^2 w}{\partial x^2} \right) + K_{xz} \frac{\partial^2 \psi_z}{\partial x^2} = 0, \quad (5.6d)$$

$$J_y \frac{\partial^2 \psi_y}{\partial t^2} + \kappa_{xz} AG \left(\psi_y - \frac{\partial w}{\partial x} \right) + (K_{xz} - K_{xy}) \frac{\partial \psi_z}{\partial x} + K_{xy} \frac{\partial^2 \nu}{\partial x^2} - EI_y \frac{\partial^2 \psi_y}{\partial x^2} = 0, \quad (5.6e)$$

$$J_z \frac{\partial^2 \psi_z}{\partial t^2} + \kappa_{xy} AG \left(\psi_z - \frac{\partial \nu}{\partial x} \right) + (K_{xy} - K_{xz}) \frac{\partial \psi_y}{\partial x} + K_{xz} \frac{\partial^2 w}{\partial x^2} - EI_z \frac{\partial^2 \psi_z}{\partial x^2} = 0, \quad (5.6f)$$

together with the boundary conditions:

$$\text{either } EA \frac{\partial u}{\partial x} + K_u \frac{\partial \theta}{\partial x} = 0; \text{ or } \delta u = 0, u \text{ is specified,} \quad (5.7a)$$

$$\text{either } GJ \frac{\partial \theta}{\partial x} + K_u \frac{\partial u}{\partial x} = 0; \text{ or } \delta \theta = 0, \theta \text{ is specified,} \quad (5.7b)$$

$$\text{either } \kappa_{xy} AG \left(\psi_z - \frac{\partial \nu}{\partial x} \right) + K_{xy} \frac{\partial \psi_y}{\partial x} = 0; \text{ or } \delta \nu = 0, \nu \text{ is specified,} \quad (5.7c)$$

$$\text{either } K_{xy} \left(\psi_z - \frac{\partial \nu}{\partial x} \right) + EI_y \frac{\partial \psi_y}{\partial x} = 0; \text{ or } \delta \psi_y = 0, \psi_y \text{ is specified,} \quad (5.7d)$$

$$\text{either } \kappa_{xz} AG \left(\psi_y - \frac{\partial w}{\partial x} \right) + K_{xz} \frac{\partial \psi_z}{\partial x} = 0; \text{ or } \delta w = 0, w \text{ is specified,} \quad (5.7e)$$

$$\text{either } K_{xz} \left(\psi_y - \frac{\partial w}{\partial x} \right) + EI_z \frac{\partial \psi_z}{\partial x} = 0; \text{ or } \delta \psi_z = 0, \psi_z \text{ is specified.} \quad (5.7f)$$

5.3.2 Solution of the Dynamic Equations

a) Coupled Tension-Torsion

First separate variables by writing

$$u(x, t) = U(x) \sin \omega t \text{ and } \theta(x, t) = \Theta(x) \sin \omega t \quad (5.8)$$

in equations (5.6a, b), which leads to the coupled ordinary differential equations

$$\begin{aligned} EA \frac{d^2 U}{dx^2} + K_u \frac{d^2 \Theta}{dx^2} + m\omega^2 U &= 0 \\ GJ \frac{d^2 \Theta}{dx^2} + K_u \frac{d^2 U}{dx^2} + J_x \omega^2 \Theta &= 0. \end{aligned} \quad (5.9a, b)$$

These may be uncoupled, which leads to the two fourth order equations

$$(EAGJ - K_u^2) \begin{bmatrix} U''' \\ \Theta''' \end{bmatrix} + \omega^2 (GJm + EAJ_x) \begin{bmatrix} U'' \\ \Theta'' \end{bmatrix} + \omega^4 J_x m \begin{bmatrix} U \\ \Theta \end{bmatrix} = \mathbf{0}, \quad (5.10)$$

where prime denotes differentiation with respect to x . Setting

$$\begin{bmatrix} U(x) \\ \Theta(x) \end{bmatrix} = \begin{bmatrix} U \\ \Theta \end{bmatrix} e^{\lambda x} \quad (5.11)$$

leads to a characteristic equation whose roots are

$$\frac{\lambda_{1,2}^2}{\omega^2} = \frac{-(EAJ_x + GJm) \mp \sqrt{(EAJ_x - GJm)^2 + 4mJ_x K_u^2}}{2(EAGJ - K_u^2)} \quad (5.12)$$

and hence general solutions

$$\begin{bmatrix} U(x) \\ \Theta(x) \end{bmatrix} = \begin{bmatrix} U_1 \\ \Theta_1 \end{bmatrix} \sin \lambda_1 x + \begin{bmatrix} U_2 \\ \Theta_2 \end{bmatrix} \cos \lambda_1 x + \begin{bmatrix} U_3 \\ \Theta_3 \end{bmatrix} \sin \lambda_2 x + \begin{bmatrix} U_4 \\ \Theta_4 \end{bmatrix} \cos \lambda_2 x. \quad (5.13)$$

The eight constants in the above are not independent, but are related by

$$\begin{aligned} \Theta_1 &= \frac{(m\omega^2 - EA\lambda_1^2)}{K_u \lambda_1^2} U_1, & \Theta_2 &= \frac{(m\omega^2 - EA\lambda_1^2)}{K_u \lambda_1^2} U_2, \\ \Theta_3 &= \frac{(m\omega^2 - EA\lambda_2^2)}{K_u \lambda_2^2} U_3, & \Theta_4 &= \frac{(m\omega^2 - EA\lambda_2^2)}{K_u \lambda_2^2} U_4. \end{aligned} \quad (5.14)$$

End conditions are free, fixed, or *mixed*: at a free end, U and Θ are unspecified, so conditions (5.7a, b) become

$$\begin{bmatrix} EA & K_u \\ K_u & GJ \end{bmatrix} \begin{bmatrix} \frac{dU}{dx} \\ \frac{d\Theta}{dx} \end{bmatrix} = \mathbf{0}. \quad (5.15)$$

The determinant of the above continuum property matrix will, in general, not be equal to zero, in which case one has $\frac{dU}{dx} = \frac{d\Theta}{dx} = 0$. At a fixed end, one has simply $U = \Theta = 0$.

Two types of *mixed* end conditions are possible: it is possible to allow extension but not rotation, in which case one has $\Theta = 0$ and $\frac{dU}{dx} = -\frac{K_u}{EA} \frac{d\Theta}{dx}$; alternatively, if rotation is allowed, but not extension, then $U = 0$ and $\frac{d\Theta}{dx} = -\frac{K_u}{GJ} \frac{dU}{dx}$.

For a free-free beam, application of the boundary condition at the end $x = 0$ leads to the equations

$$U_1\lambda_1 + U_3\lambda_2 = 0, \quad \Theta_1\lambda_1 + \Theta_3\lambda_2 = 0 \quad (5.16)$$

which, combined with equations (5.14), provides the condition

$$\begin{bmatrix} \lambda_1 & \lambda_2 \\ \frac{m\omega^2 - EA\lambda_1^2}{K_u\lambda_1} & \frac{m\omega^2 - EA\lambda_2^2}{K_u\lambda_2} \end{bmatrix} \begin{bmatrix} U_1 \\ U_3 \end{bmatrix} = \mathbf{0} \quad (5.17)$$

The determinant in the above is only zero for the degenerate case $\lambda_1 = \lambda_2$; the more general requirement is $U_1 = U_3 = 0$, and hence $\Theta_1 = \Theta_3 = 0$. Application of the boundary conditions at the end $x = L$, leads to the frequency equations

$$\sin \lambda_1 L = 0, \quad \sin \lambda_2 L = 0 \quad (5.18)$$

and hence the natural frequency predictions are

i) torsional

$$\omega = \frac{n\pi}{l} \sqrt{\frac{mGJ + EJ_x A - \sqrt{(mGJ - EJ_x A)^2 + 4mJ_x K_u^2}}{2mJ_x}}. \quad (5.19)$$

ii) extensional

$$\omega = \frac{n\pi}{l} \sqrt{\frac{mGJ + EJ_x A + \sqrt{(mGJ - EJ_x A)^2 + 4mJ_x K_u^2}}{2mJ_x}} \quad (5.20)$$

with mode shapes

$$U(x) = U_2 \cos \frac{n\pi x}{L}, \quad \Theta(x) = \Theta_2 \cos \frac{n\pi x}{L}, \quad (n = 1, 2, 3, \dots \text{ etc}). \quad (5.21)$$

For a fixed-free (cantilevered) beam, one finds from the conditions at $x = 0$,

$$U_2 = U_4 = \Theta_2 = \Theta_4 = 0 \quad (5.22)$$

while the conditions at $x = L$ lead to the frequency equations

$$\cos \lambda_1 L = 0, \quad \cos \lambda_2 L = 0 \quad (5.23)$$

and hence the frequency predictions are

i) torsional

$$\omega = \frac{n\pi}{2L} \sqrt{\frac{mGJ + EJ_x A - \sqrt{(mGJ - EJ_x A)^2 + 4mJ_x K_u^2}}{2mJ_x}}. \quad (5.24)$$

ii) extensional

$$\omega = \frac{n\pi}{2L} \sqrt{\frac{mGJ + EJ_x A + \sqrt{(mGJ - EJ_x A)^2 + 4mJ_x K_{tt}^2}}{2mJ_x}}, \quad (5.25)$$

with modes shapes

$$U(x) = U_1 \sin \frac{n\pi x}{2L}, \quad \Theta(x) = \Theta_1 \sin \frac{n\pi x}{2L} \quad (n = 1, 3, 5, \dots \text{ etc}). \quad (5.26)$$

It is noted that equations (5.24) and (5.25) are also equally applicable to fixed-fixed end conditions.

b) Coupled Bending-Shear

Separate variables by writing

$$\begin{aligned} v(x, t) &= V(x) \sin \omega t, \quad w(x, t) = W(x) \sin \omega t, \\ \psi_y(x, t) &= \Psi_y(x) \sin \omega t, \quad \psi_z(x, t) = \Psi_z(x) \sin \omega t, \end{aligned} \quad (5.27)$$

in equations (5.6c, d, e, f), which leads to the coupled ordinary differential equations

$$\begin{aligned} -m\omega^2 V + \kappa_{xy} AG(\Psi'_z - V'') + K_{xy} \Psi'_y &= 0, \\ -m\omega^2 W + \kappa_{xz} AG(\Psi'_y - W'') + K_{xz} \Psi''_z &= 0, \\ -J_y \omega^2 \Psi_y + \kappa_{xz} AG(\Psi_y - W') + K_{xy} V'' - EI_y \Psi''_y &= 0, \\ -J_z \omega^2 \Psi_z + \kappa_{xy} AG(\Psi_z - V') + K_{xz} W'' - EI_z \Psi''_z &= 0. \end{aligned} \quad (5.28a, b, c, d)$$

For the structure under consideration, one has (Chapter 4) $I_y = I_z$ and $\kappa_{xy} = \kappa_{xz}$, and also we know that $J_y = J_z$, so set

$$k^4 = \frac{m\omega^2}{EI_{y(z)}}, \quad q = \frac{EI_{y(z)}}{\kappa_{xy(xz)} AG}, \quad p = \frac{J_{y(z)}}{m}, \quad b = \frac{K_{xy(xz)}}{\kappa_{xy(xz)} AG}, \quad (5.29)$$

when equations (5.28) reduce to

$$\begin{aligned} -k^4 q V + (\Psi'_z - V'') + b \Psi''_y &= 0, \\ -k^4 q W + (\Psi'_y - W'') + b \Psi''_z &= 0, \\ -k^4 p q \Psi_y + (\Psi_y - W') + b V'' - q \Psi''_y &= 0, \\ -k^4 p q \Psi_z + (\Psi_z - V') + b W'' - q \Psi''_z &= 0. \end{aligned} \quad (5.30a, b, c, d)$$

Uncoupling the variables in equation (5.30) leads to four fourth order ordinary differential equations

$$\begin{aligned} c_1 V''' + c_2 V'' + c_3 V &= 0, \\ c_1 W''' + c_2 W'' + c_3 W &= 0, \\ c_1 \Psi_y''' + c_2 \Psi_y'' + c_3 \Psi_y &= 0, \\ c_1 \Psi_z''' + c_2 \Psi_z'' + c_3 \Psi_z &= 0. \end{aligned} \quad (5.31a, b, c, d)$$

where

$$\begin{aligned} c_1 &= q - b^2 \\ c_2 &= k^4 pq + k^4 q^2 \\ c_3 &= k^8 pq^2 - k^4 q \end{aligned}$$

Setting

$$\begin{bmatrix} V(x) \\ W(x) \\ \Psi_y(x) \\ \Psi_z(x) \end{bmatrix} = \begin{bmatrix} A \\ B \\ C \\ D \end{bmatrix} e^{\lambda x}, \quad (5.32)$$

leads to the characteristic equation

$$c_1 \lambda^4 + c_2 \lambda^2 + c_3 = 0 \quad (5.33)$$

with roots

$$\begin{aligned} \lambda_{1,2} &= \pm \sqrt{\frac{-c_2 + \sqrt{c_2^2 - 4c_1c_3}}{2c_1}} \\ \lambda_{3,4} &= \pm i \sqrt{\frac{c_2 + \sqrt{c_2^2 - 4c_1c_3}}{2c_1}} \end{aligned} \quad (5.34)$$

The general solutions are then

$$\begin{bmatrix} V(x) \\ W(x) \\ \Psi_y(x) \\ \Psi_z(x) \end{bmatrix} = \begin{bmatrix} A_1 \\ B_1 \\ C_1 \\ D_1 \end{bmatrix} \sinh rx + \begin{bmatrix} A_2 \\ B_2 \\ C_2 \\ D_2 \end{bmatrix} \cosh rx + \begin{bmatrix} A_3 \\ B_3 \\ C_3 \\ D_3 \end{bmatrix} \sin sx + \begin{bmatrix} A_4 \\ B_4 \\ C_4 \\ D_4 \end{bmatrix} \cos sx, \quad (5.35a, b, c, d)$$

where

$$\begin{aligned} r &= \sqrt{\frac{-c_2 + \sqrt{c_2^2 - 4c_1c_3}}{2c_1}} \\ s &= \sqrt{\frac{c_2 + \sqrt{c_2^2 - 4c_1c_3}}{2c_1}} \end{aligned}$$

Only half of the constants in equations (5.35) are independent, being related as

$$\begin{aligned}
 B_1 &= K_{55}C_2 + K_{22}A_2 \\
 B_2 &= K_{55}C_1 + K_{22}A_1 \\
 B_3 &= K_{66}C_4 - K_{44}A_4 \\
 B_4 &= -K_{66}C_3 + K_{44}A_3 \\
 D_1 &= K_{11}A_2 - K_{22}C_2 \\
 D_2 &= K_{11}A_1 - K_{22}C_1 \\
 D_3 &= K_{33}A_4 + K_{44}C_4 \\
 D_4 &= -K_{33}A_3 - K_{44}C_3
 \end{aligned} \tag{5.36a, b}$$

where

$$\begin{aligned}
 K_{11} &= \frac{k^4 q + r^2}{r} \\
 K_{22} &= br \\
 K_{33} &= \frac{k^4 q - s^2}{s} \\
 K_{44} &= bs \\
 K_{55} &= \frac{-k^4 pq + 1 - qr^2}{r} \\
 K_{66} &= \frac{-k^4 pq + 1 + qs^2}{s}
 \end{aligned}$$

Substitution of equation (5.36) into equations (5.35b) and (5.35d) gives

$$\begin{aligned}
 W(x) &= (K_{55}C_2 + K_{22}A_2) \sinh rx + (K_{55}C_1 + K_{22}A_1) \cosh rx \\
 &\quad + (K_{66}C_4 - K_{44}A_4) \sin sx + (-K_{66}C_3 + K_{44}A_3) \cos sx, \\
 \Psi_z(x) &= (K_{11}A_2 - K_{22}C_2) \sinh rx + (K_{11}A_1 - K_{22}C_1) \cosh rx \\
 &\quad + (K_{33}A_4 + K_{44}C_4) \sin sx + (-K_{33}A_3 - K_{44}C_3) \cos sx.
 \end{aligned} \tag{5.37a, b}$$

Application of boundary conditions leads to a matrix equation of the form

$$[\mathbf{F}(\omega)] [A_1 \ A_2 \ A_3 \ A_4 \ C_1 \ C_2 \ C_3 \ C_4]^T = 0. \tag{5.38}$$

where

$$[\mathbf{F}(\omega)] = [f_{ij}], \quad i = 1, 2, \dots, 8, \quad j = 1, 2, \dots, 8.$$

Non-trivial solution of equation (5.38) requires that the determinant of $[F(\omega)]$ be equal to zero, from which the natural frequencies are determined. The coefficients f_{ij} are derived in Appendix 5 for free-free and fixed-fixed end conditions.

5.4 COMPARISON OF NATURAL FREQUENCY PREDICTIONS

Table 5.1 shows bending frequency predictions for a slender truss having thirty cells, length $L = 10.284$ m, for free-free and fixed-fixed boundary conditions, compared with the ANSYS predictions, employing the *lumped mass* matrix option. Because the continuum properties are identical in the xz - and xy -planes, the continuum dynamic theory predicts double natural frequencies for each flexural mode, and this is confirmed by the ANSYS prediction; for brevity only one is shown.

Table 5.1 Comparison of natural frequencies (Hz) in bending according to ANSYS and present method; free-free and fixed-fixed beam, $L = 10.284$ m (30 cells)

Free-free beam			Fixed-fixed beam		
n	ANSYS	Flexural	n	ANSYS	Flexural
1	12.769	12.7841 (+0.12%)	1	12.561	12.5263 (-0.28%)
2	34.194	34.1673 (-0.08%)	2	33.333	33.0858 (-0.74%)
3	64.428	64.1955 (-0.36%)	3	62.398	61.6122 (-1.26%)
4	101.05	100.8062 (-0.24%)	4	97.884	96.1320 (-1.79%)
5	143.65	142.2425 (-0.98%)	5	138.21	135.0844 (-2.26%)
6	189.29	187.0587 (-1.18%)	6	182	177.2388 (-2.62%)
7	237.12	234.1562 (-1.25%)	7	228.15	221.6850 (-2.83%)
8	286.07	282.7337 (-1.17%)	8	275.71	267.7650 (-2.88%)
9	335.3	332.2210 (-0.92%)	9	323.92	315.0056 (-2.75%)
10	384.13	382.2177 (-0.50%)	10	372.13	363.0634 (-2.44%)

The frequency predictions of the modified Timoshenko beam model shows excellent agreement with the ANSYS predictions, with an accuracy of +0.12% to -1.18% for the free-free beam, and -0.28% to -2.88% for the fixed-fixed beam, for the first 10 modes.

For the short (10 cell) beam, Table 5.2, agreement is very good for the first four modes of the free-free beam (+0.59% to +3.72%), and the first six modes of the fixed-fixed beam (+4.79% to -4%). For the higher bending modes of a short beam, with the wavelength being closer to the depth of the truss, the in-depth vibration or local effect become important and even dominates, however, the continuum model does not represent local effects accurately.

Table 5.2 Comparison of natural frequencies (Hz) in bending according to ANSYS and present method; free-free and fixed-fixed beam, $L = 3.428$ m (10 cells)

Free-free beam			Fixed-fixed beam		
n	ANSYS	Flexural	n	ANSYS	Flexural
1	102.47	103.6206 (+1.12%)	1	92.421	90.5258 (-2.05%)
2	236.49	237.8928 (+0.59%)	2	211.3	202.9266 (-3.96%)
3	382.21	388.3985 (+1.62%)	3	347.6	333.6894 (-4.00%)
4	519.2	538.5257 (+3.72%)	4	484.84	472.2709 (-2.59%)
5	639.24	684.7989 (+7.13%)	5	612.78	615.5551 (+0.45%)
6	741.43	817.040 (+10.20%)	6	725.49	760.220 (+4.79%)
7	825.71	937.250 (+13.51%)	7	819.13	905.544 (+10.55%)

Next, consider the coupled torsion-extension predictions, Table 5.3, for the long (30 cell) beam, length $L = 10.284$ m, again for free-free and fixed-fixed end conditions.

Better agreement with ANSYS predictions arises when the latter employs the *consistent mass* matrix, and only these are shown. Again, the results show excellent agreement; for the predominantly torsional modes, the accuracy is within +0.02% to +1.30% for the free-free beam, and +0.02% to +1.25% for the fixed-fixed beam for the first 9 modes.

For the first two extensional modes, the maximum error is -0.05% and -0.33% for free-free and fixed-fixed beams, respectively.

Table 5.3 Comparison of natural frequencies (Hz) in torsion and extension according to ANSYS and present method; free-free and fixed-fixed beam, $L = 10.284$ m (30 cells)

Free-free beam				Fixed-fixed beam			
n	ANSYS	Torsional	Extensional	n	ANSYS	Torsional	Extensional
1	37.578	37.5858 (+0.02%)		1	37.83	37.5858 (-0.65%)	
2	75.111	75.1715 (+0.08%)		2	75.618	75.1715 (-0.59%)	
3	112.55	112.7572 (+0.18%)		3	113.31	112.7572 (-0.49%)	
4	149.86	150.343 (+0.32%)		4	150.89	150.343 (-0.36%)	
5	151.81		151.7855 (-0.02%)	5	152.12		151.7855 (-0.22%)
6	186.98	187.9287 (+0.51%)		6	188.3	187.9287 (-0.20%)	
7	223.88	225.5146 (+0.73%)		7	225.46	225.5146 (+0.02%)	
8	260.51	263.1003 (+0.99%)		8	262.39	263.1003 (+0.27%)	
9	296.82	300.686 (+1.30%)		9	298.8	300.686 (+0.63%)	
10	303.73		303.5711 (-0.05%)	10	304.59		303.571 (-0.33%)
11	332.77	332.2210 (-0.92%)		11	335.29	332.2210 (+1.25%)	

For the short (10 cell) beam, Table 5.4, good agreement is obtained up to the fourth torsional mode for free-free (0.21% to +3.49%) and up to the sixth torsional mode for fixed-fixed beam end conditions (-1.81% to +2.76%); again the agreement for the extensional modes is excellent. Similar accuracy and trends for the natural frequency agreement can be seen in Table 5.5, for both long and short cantilevered beams.

Generally, as noted by many other authors, for any type of mode, it is found that the long beam always gives better accuracy for the natural frequency prediction. According to Lee [14]: *Physically, the number of repeating cells per wave-length increases as the*

Table 5.4 Comparison of natural frequencies (Hz) in torsion and extension according to ANSYS and present method; free-free and fixed-fixed beam, $L = 3.428\text{m}$ (10 cells)

Free-free beam				Fixed-fixed beam			
n	ANSYS	Torsional	Extensional	n	ANSYS	Torsional	Extensional
1	112.52	112.7573 (+0.21%)		1	114.84	112.7573 (-1.81%)	
2	223.64	225.5146 (+0.84%)		2	228.46	225.5146 (-1.29%)	
3	331.92	338.2718 (+1.91%)		3	339.42	338.2718 (-0.34%)	
4	435.82	451.0291 (+3.49%)		4	446.74	451.0291 (+0.96%)	
5	455.84		455.3566 (-0.11%)	5	458.85		455.3566 (-0.76%)
6	533.53	563.7864 (+5.67%)		6	548.67	563.7864 (+2.76%)	
7	622.63	676.5437 (+7.97%)		7	641.72	676.5437 (+5.43%)	

Table 5.5 Comparison of natural frequencies (Hz) in torsion and extension according to ANSYS and present method; cantilever beam

10 cell structure				30 cell structure			
n	ANSYS	Torsional	Extensional	n	ANSYS	Torsional	Extensional
1	56.92	56.3786 (-0.95%)		1	18.855	18.7929 (-0.33%)	
2	170.08	169.1359 (-0.56%)		2	56.541	56.3786 (-0.29%)	
3	228.46		227.6783 (-0.34%)	3	75.973		75.8927 (-0.11%)
4	281.30	281.8932 (+0.21%)		4	94.164	93.964 (-0.21%)	
5	389.06	394.6505 (+1.44%)		5	131.67	131.5502 (-0.09%)	
6	491.81	507.4078 (+3.17)		6	169.02	169.1359 (+0.07%)	
7	587.52	620.165 (+5.56)		7	206.17	206.7217 (+0.27%)	
8	672.36	732.9223 (+9.01%)		8	227.98		227.6783 (-0.13%)
9	688.20		688.0349 (-0.75%)	9	243.11	244.3071 (+0.49%)	
10	745.46	845.6796 (+13.44%)		10	279.72	281.8932 (+0.78%)	

total length of lattice structure increases. Thus the wavelength of a mode spans more repeating cells so that the effect of the nonbeam-like characteristic of lattice structure become less important.

APPENDIX 5

DERIVATION OF MATRIX $\mathbf{F}(\omega)$

Free-free beam. Insert equation (5.27) into (5.7c, d, e, f) gives the boundary conditions in matrix form

$$\begin{bmatrix} \kappa_{xy}AG & K_{xy} & 0 & 0 \\ K_{xy} & EI_y & 0 & 0 \\ 0 & 0 & \kappa_{xz}AG & K_{xz} \\ 0 & 0 & K_{xz} & EI_z \end{bmatrix} \begin{bmatrix} \Psi_z - V' \\ \Psi'_y \\ \Psi_y - W' \\ \Psi'_z \end{bmatrix} = \mathbf{0}, \quad (\text{A1})$$

because $\det \begin{bmatrix} \kappa_{xy}AG & K_{xy} & 0 & 0 \\ K_{xy} & EI_y & 0 & 0 \\ 0 & 0 & \kappa_{xz}AG & K_{xz} \\ 0 & 0 & K_{xz} & EI_z \end{bmatrix} \neq 0$, the boundary conditions become

$$\begin{aligned} \Psi_z - V' &= 0, \\ \Psi'_y &= 0, \\ \Psi_y - W' &= 0, \\ \Psi'_z &= 0. \end{aligned} \quad (\text{A2a, b, c, d})$$

Substitution of equation (5.35a) into (A2a) gives

$$\begin{aligned} (K_{11}A_2 - K_{22}C_2) \sinh rx + (K_{11}A_1 - K_{22}C_1) \cosh rx + \\ (K_{33}A_4 + K_{44}C_4) \sin sx + (-K_{33}A_3 - K_{44}C_3) \cos sx - \\ A_1 r \cosh rx - A_2 r \sinh rx - A_3 s \cos sx + A_4 s \sin sx = 0; \end{aligned} \quad (\text{A3})$$

at $x = 0$, equation (A3) becomes

$$(K_{11} - r)A_1 + (-K_{33} - s)A_3 - K_{22}C_1 - K_{44}C_3 = 0, \quad (\text{A4a})$$

at $x = L$, equation (A3) becomes

$$\begin{aligned} (K_{11} - r)A_1 \cosh rL + (K_{11} - r)A_2 \sinh rL + (-K_{33} - s)A_3 \cos sL + (K_{33} + s)A_4 \sin sL - \\ K_{22}C_1 \cosh rL - K_{22}C_2 \sinh rL - K_{44}C_3 \cos sL + K_{44}C_4 \sin sL = 0. \end{aligned} \quad (\text{A4b})$$

Substitution of equation (5.35c) into (A2b) gives

$$C_1 r \cosh rx + C_2 r \sinh rx + C_3 s \cos sx - C_4 s \sin sx = 0; \quad (\text{A5})$$

at $x = 0$, equation (A5) becomes

$$rC_1 + sC_3 = 0, \quad (\text{A6a})$$

at $x = L$, equation (A5) becomes

$$rC_1 \cosh rL + rC_2 \sinh rL + sC_3 \cos sL - sC_4 \sin sL = 0. \quad (\text{A6b})$$

Substitution of equation (5.37a) into (A2c) gives

$$\begin{aligned} C_1 \sinh rx + C_2 \cosh rx + C_3 \sin sx + C_4 \cos sx - (K_{55}C_2 + K_{22}A_2)r \cosh rx \\ - (K_{55}C_1 + K_{22}A_1)r \sinh rx - (K_{66}C_4 - K_{44}A_4)s \cos sx + \\ (-K_{66}C_3 + K_{44}A_3)s \sin sx = 0; \end{aligned} \quad (\text{A7})$$

at $x = 0$, equation (A7) becomes

$$C_2 + C_4 - (K_{55}C_2 + K_{22}A_2)r - (K_{66}C_4 - K_{44}A_4)s = 0, \quad (\text{A8a})$$

at $x = L$, equation (A7) becomes

$$\begin{aligned} -K_{22}A_1r \sinh rL - K_{22}A_2r \cosh rL + K_{44}A_3s \sin sL + K_{44}A_4s \cos sL + \\ (1 - rK_{55})C_1 \sinh rL + (1 - rK_{55})C_2 \cosh rL + (1 - sK_{66})C_3 \sin sL + \\ (1 - sK_{66})C_4 \cos sL = 0. \end{aligned} \quad (\text{A8b})$$

Substitution of equation (5.37b) into (A2d) gives

$$\begin{aligned} (K_{11}A_1 - K_{22}C_1)r \sinh rx + (K_{11}A_2 - K_{22}C_2)r \cosh rx + \\ (K_{33}A_4 + K_{44}C_4)s \cos sx + (K_{33}A_3 + K_{44}C_3)s \sin sx = 0; \end{aligned} \quad (\text{A9})$$

at $x = 0$, equation (A9) becomes

$$(K_{11}A_2 - K_{22}C_2)r + (K_{33}A_4 + K_{44}C_4)s = 0, \quad (\text{A10a})$$

at $x = L$, equation (A9) becomes

$$\begin{aligned} K_{11}A_1r \sinh rL + K_{11}A_2r \cosh rL + K_{33}A_3s \sin sL + K_{33}A_4s \cos sL \\ - K_{22}C_1r \sinh rL - K_{22}C_2r \cosh rL + K_{44}C_3s \sin sL + K_{44}C_4s \cos sL = 0. \end{aligned} \quad (\text{A10b})$$

equations (A4), (A6), (A8) and (A10) give the coefficient (f_{ij}) matrix $[\mathbf{F}(\omega)]$ under free-free boundary conditions.

$$\left\{ \begin{array}{l} f_{11} = K_{11} - r \\ f_{12} = 0 \\ f_{13} = -K_{33} - s \\ f_{14} = 0 \\ f_{15} = -K_{22} \\ f_{16} = 0 \\ f_{17} = -K_{44} \\ f_{18} = 0 \end{array} \right. , \left\{ \begin{array}{l} f_{21} = (K_{11} - r) \cosh rL \\ f_{22} = (K_{11} - r) \sinh rL \\ f_{23} = (-K_{33} - s) \cos sL \\ f_{24} = (K_{33} + s) \sin sL \\ f_{25} = -K_{22} \cosh rL \\ f_{26} = -K_{22} \sinh rL \\ f_{27} = -K_{44} \cos sL \\ f_{28} = K_{44} \sin sL \end{array} \right. , \left\{ \begin{array}{l} f_{31} = 0 \\ f_{32} = 0 \\ f_{33} = 0 \\ f_{34} = 0 \\ f_{35} = r \\ f_{36} = 0 \\ f_{37} = s \\ f_{38} = 0 \end{array} \right. , \left\{ \begin{array}{l} f_{41} = 0 \\ f_{42} = 0 \\ f_{43} = 0 \\ f_{44} = 0 \\ f_{45} = r \cosh rL \\ f_{46} = r \sinh rL \\ f_{47} = s \cos sL \\ f_{48} = -s \sin sL \end{array} \right. , \end{array} \right.$$

$$\left\{ \begin{array}{l} f_{51} = 0 \\ f_{52} = -rK_{22} \\ f_{53} = 0 \\ f_{54} = sK_{44} \\ f_{55} = 0 \\ f_{56} = 1 - rK_{55} \\ f_{57} = 0 \\ f_{58} = 1 - sK_{66} \end{array} \right. , \left\{ \begin{array}{l} f_{61} = -rK_{22} \sinh rL \\ f_{62} = -rK_{22} \cosh rL \\ f_{63} = sK_{44} \sin sL \\ f_{64} = sK_{44} \cos sL \\ f_{65} = (1 - rK_{55}) \sinh rL \\ f_{66} = (1 - rK_{55}) \cosh rL \\ f_{67} = (1 - sK_{66}) \sin sL \\ f_{68} = (1 - sK_{66}) \cos sL \end{array} \right. , \left\{ \begin{array}{l} f_{71} = 0 \\ f_{72} = rK_{11} \\ f_{73} = 0 \\ f_{74} = sK_{33} \\ f_{75} = 0 \\ f_{76} = -rK_{22} \\ f_{77} = 0 \\ f_{78} = sK_{44} \end{array} \right. , \left\{ \begin{array}{l} f_{81} = rK_{11} \sinh rL \\ f_{82} = rK_{11} \cosh rL \\ f_{83} = sK_{33} \sin sL \\ f_{84} = sK_{33} \\ f_{85} = -rK_{22} \sinh rL \\ f_{86} = -rK_{22} \cosh rL \\ f_{87} = sK_{44} \sin sL \\ f_{88} = sK_{44} \cos sL \end{array} \right. \quad (A11)$$

Fixed-fixed beam. Insert equation (5.27) into (5.7c, d, e f) gives the boundary conditions

$$V = W = \Psi_y = \Psi_z = 0. \quad (A12)$$

At the fixed end, $x = 0$, substitution of equation (5.35a), (5.35c), (5.37a) and (5.37b) into above equation gives

$$A_2 + A_4 = 0,$$

$$K_{11}A_1 - K_{22}C_1 - K_{33}A_3 - K_{44}C_3 = 0,$$

$$C_2 + C_4 = 0,$$

$$K_{55}C_1 + K_{22}A_1 - K_{66}C_3 + K_{44}A_3 = 0. \quad (A13a, b, c, d)$$

At the fixed end, $x = L$, substitution of equation (5.35a), (5.35c), (5.37a) and (5.38b) into (A12) gives

$$A_1 \sinh rL + A_2 \cosh rL + A_3 \sin sL + A_4 \cos sL = 0, \quad (A14a)$$

$$C_1 \sinh rL + C_2 \cosh rL + C_3 \sin sL + C_4 \cos sL = 0, \quad (A14b)$$

$$\begin{aligned} & A_1 K_{22} \cosh rL + A_2 K_{22} \sinh rL + A_3 K_{44} \cos sL - A_4 K_{44} \sin sL \\ & + C_1 K_{55} \cosh rL + C_2 K_{55} \sinh rL - C_3 K_{66} \cos sL + C_4 K_{66} \sin sL = 0, \end{aligned} \quad (A14c)$$

$$\begin{aligned} & A_1 K_{11} \cosh rL + A_2 K_{11} \sinh rL - A_3 K_{33} \cos sL + A_4 K_{33} \sin sL \\ & - C_1 K_{22} \cosh rL - C_2 K_{22} \sinh rL - C_3 K_{44} \cos sL + C_4 K_{44} \sin sL = 0. \end{aligned} \quad (A14d)$$

Combining equation (A13) together with (A14) gives the coefficients (f_{ij}) of the matrix $[\mathbf{F}(\omega)]$ under fixed-fixed boundary conditions

$$\begin{aligned}
& \left\{ \begin{array}{l} f_{11} = 0 \\ f_{12} = 1 \\ f_{13} = 0 \\ f_{14} = 1 \\ f_{15} = 0 \\ f_{16} = 0 \\ f_{17} = 0 \\ f_{18} = 0 \end{array} \right. , \left\{ \begin{array}{l} f_{21} = 0 \\ f_{22} = 0 \\ f_{23} = 0 \\ f_{24} = 0 \\ f_{25} = 0 \\ f_{26} = 1 \\ f_{27} = 0 \\ f_{28} = 1 \end{array} \right. , \left\{ \begin{array}{l} f_{31} = K_{22} \\ f_{32} = 0 \\ f_{33} = K_{44} \\ f_{34} = 0 \\ f_{35} = K_{55} \\ f_{36} = 0 \\ f_{37} = -K_{66} \\ f_8 = 0 \end{array} \right. , \left\{ \begin{array}{l} f_{41} = K_{11} \\ f_{42} = 0 \\ f_{43} = -K_{33} \\ f_{44} = 0 \\ f_{45} = -K_{22} \\ f_{46} = 0 \\ f_{47} = -K_{44} \\ f_{48} = 0 \end{array} \right. \\
& \left\{ \begin{array}{l} f_{51} = \sinh rL \\ f_{52} = \cosh rL \\ f_{53} = \sin sL \\ f_{54} = \cos sL \\ f_{55} = 0 \\ f_{56} = 0 \\ f_{57} = 0 \\ f_{58} = 0 \end{array} \right. , \left\{ \begin{array}{l} f_{61} = 0 \\ f_{62} = 0 \\ f_{63} = 0 \\ f_{64} = 0 \\ f_{65} = \sinh rL \\ f_{66} = \cosh rL \\ f_{67} = \sin sL \\ f_{68} = \cos sL \end{array} \right. , \left\{ \begin{array}{l} f_{71} = K_{22} \cosh rL \\ f_{72} = K_{22} \sinh rL \\ f_{73} = K_{44} \cos sL \\ f_{74} = -K_{44} \sin sL \\ f_{75} = K_{55} \cosh rL \\ f_{76} = K_{55} \sinh rL \\ f_{77} = -K_{66} \cos sL \\ f_{78} = K_{66} \sin sL \end{array} \right. , \left\{ \begin{array}{l} f_{81} = K_{11} \cosh rL \\ f_{82} = K_{11} \sinh rL \\ f_{83} = -K_{33} \cos sL \\ f_{84} = K_{33} \sin sL \\ f_{85} = -K_{22} \cosh rL \\ f_{86} = -K_{22} \sinh rL \\ f_{87} = -K_{44} \cos sL \\ f_{88} = K_{44} \sin sL \end{array} \right. . \quad (A15)
\end{aligned}$$

CHAPTER SIX

EIGENANALYSIS OF PRE-TWISTED REPETITIVE STRUCTURES

6.1 INTRODUCTION

In this Chapter, the transfer matrix approach described in Chapter 2 is extended to structures having a pre-twisted form; again the structure is regarded as pin-jointed, allowing comparison of the results to be checked against exact FEA predictions.

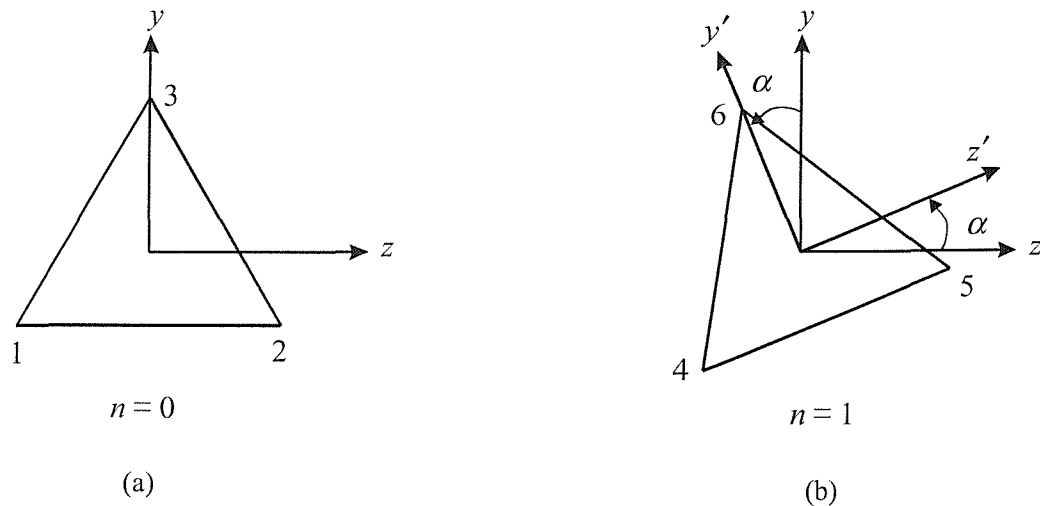


Figure 6.1. Local and global coordinate systems on the left and right hand side of the first cell, respectively

6.2 EXAMPLE AND THEORY

To focus ideas, consider a pin-jointed beam-like framework whose cross-section is in the form of an equilateral triangle of side length $L = 0.3428$ m. The zeroth nodal cross-section is assumed to align with a global $x y z$ coordinate system (x is the axial direction), Figure 6.1(a), while the adjacent $n = 1$ nodal cross-section, Figure 6.1(b), is pre-twisted through angle α radians, here taken as $\alpha = \pi/8$; also shown is a local coordinate system $x' y' z'$ which rotates with the cross-section. The axial length of the cell is also taken to be $L = 0.3428$ m. Individual members of the cell are of aluminium, having Young's modulus $E = 70 \times 10^3$ N/mm² and diameter $d = 6.35$ mm. The longitudinal (helical) members, together with the two diagonals in each external face of

the cell, have length as demanded by the relevant nodal locations, that is, the pre-twisted structure is free of any residual stress or deformation prior to loading. The complete first cell of the framework, Figure 6.2, is shown in bold.

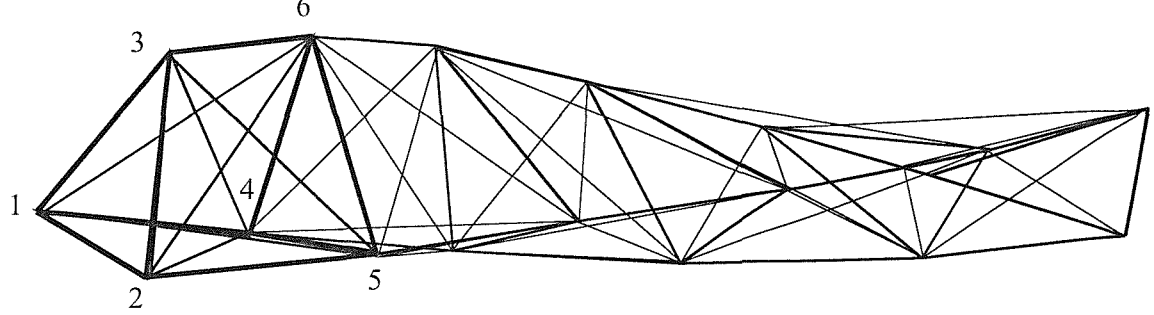


Figure 6.2. A six cell pin-jointed pre-twisted framework; the first cell is shown in bold.

6.2.1 Transfer Matrix

For a *straight* repetitive structure, a stiffness matrix \mathbf{K} for a typical cell is first constructed employing the global coordinate system, which, of course, is applicable to all cells. Symbolically, the stiffness matrix relates nodal force and displacement components as

$$\mathbf{F} = \mathbf{K} \mathbf{d}, \quad (6.1)$$

and the transfer matrix \mathbf{G} in global coordinates is calculated from \mathbf{K} , as in equation (2.7), and relates state vectors on either side of the cell as

$$\mathbf{s}_R = \mathbf{G} \mathbf{s}_L. \quad (6.2)$$

In the above, the subscripts L and R are employed to denote left and right hand sides of the cell, while \mathbf{G} shows no dependence on the cell index; this is an adequate description for the straight structure, which possesses translational symmetry, but is quite inadequate for the pre-twisted structure, when, in global coordinates, the transfer matrix for each cell within a cycle is different. Instead we write for the first cell, Figure 6.2,

$$\mathbf{s}(1) = \mathbf{G}(1) \mathbf{s}(0), \quad (6.3)$$

and for the typical n^{th} cell

$$\mathbf{s}(n) = \mathbf{G}(n) \mathbf{s}(n-1), \quad (6.4)$$

where the state vector subscript has been replaced by an argument, to denote the nodal location, and the transfer matrix \mathbf{G} also requires an index to identify the cell.

Assuming that the pre-twist angle α for each cell is constant, then the transfer matrix $\mathbf{G}(n)$ is periodic, with period $p = 2\pi/\alpha$, that is

$$\mathbf{G}(n+p) = \mathbf{G}(n), \quad (6.5)$$

and for the present example $p = 16$.

For simplicity, suppose that the N^{th} nodal cross-section aligns with the global coordinate system; so too will the $(N+p)^{\text{th}}$. Suppose that one constructs a stiffness matrix for all p cells, and then condense this to form a superelement matrix \mathbf{K}_p relating force and displacement components on the N^{th} and the $(N+p)^{\text{th}}$ nodal locations. Note that the subscript p has been employed to denote a complete cycle of p cells. From this one could construct a transfer matrix \mathbf{G}_p , using equation (2.7), which is known as the *monodromy* matrix, and perform eigenanalysis in the usual way; that is, denoting the state vectors as $\mathbf{s}_p(N)$ and $\mathbf{s}_p(N+p)$, respectively, then

$$\mathbf{s}_p(N+p) = \mathbf{G}_p \mathbf{s}_p(N) \text{ and } \mathbf{s}_p(N+p) = \lambda_p \mathbf{s}_p(N), \quad (6.6)$$

to give the eigenproblem

$$(\mathbf{G}_p - \lambda_p \mathbf{I}) \mathbf{s}_p(N) = 0. \quad (6.7)$$

Denote the square matrix comprised of the eigen- and principal vectors of the above as $\mathbf{S}_p(N)$; this transforms the transfer matrix to the Jordan canonical form \mathbf{J}_p , according to

$$\mathbf{S}_p(N)^{-1} \mathbf{G}_p \mathbf{S}_p(N) = \mathbf{J}_p. \quad (6.8)$$

Pre-multiply by $\mathbf{S}_p(N)$ to give

$$\mathbf{G}_p \mathbf{S}_p(N) = \mathbf{S}_p(N) \mathbf{J}_p. \quad (6.9)$$

But $\mathbf{S}_p(N+p) = \mathbf{G}_p \mathbf{S}_p(N)$, so we have

$$\mathbf{S}_p(N+p) = \mathbf{S}_p(N) \mathbf{J}_p. \quad (6.10)$$

The process described above allows one to treat the pre-twisted beam as if it were straight; however, state vectors are only defined at those cross-sections that align with the global coordinate system, and the information contained within the eigen- and principal vectors describes the behaviour of a complete cycle of p cells. However, no information is available at other cross-sections. Such a procedure is exactly how

periodic systems are usually treated using Floquet theory. The eigenvalues λ_p are known as Floquet multipliers, and they define the stability of a (usually dynamic) periodic system, and this information is all that is normally required.

It is not difficult to define an autonomous transfer matrix \mathbf{G}' , which does not depend upon the index of the cell, n , by employing a local coordinate system. Refer to Figure 6.1(a) for the first cell, and note that the left hand side aligns with the global $x y z$ coordinate system. The local right hand side nodal coordinates transform as

$$\begin{bmatrix} x' \\ y' \\ z' \end{bmatrix} = \begin{bmatrix} 1 & 0 & 0 \\ 0 & \cos \alpha & \sin \alpha \\ 0 & -\sin \alpha & \cos \alpha \end{bmatrix} \begin{bmatrix} x \\ y \\ z \end{bmatrix} \quad (6.11)$$

or, symbolically

$$\mathbf{x}'_i = \mathbf{T}_3 \mathbf{x}_i \quad (6.12)$$

where the 3×3 orthogonal transformation matrix \mathbf{T}_3 is defined accordingly. On the other hand, nodal displacement and force components transform, Figure 6.1(b), referring to node 4, as

$$\begin{bmatrix} P'_{4x} \\ P'_{4y} \\ P'_{4z} \end{bmatrix} = \begin{bmatrix} 1 & 0 & 0 \\ 0 & \cos \alpha & -\sin \alpha \\ 0 & \sin \alpha & \cos \alpha \end{bmatrix} \begin{bmatrix} P_{4x} \\ P_{4y} \\ P_{4z} \end{bmatrix} \quad (6.13)$$

and

$$\begin{bmatrix} d'_{4x} \\ d'_{4y} \\ d'_{4z} \end{bmatrix} = \begin{bmatrix} 1 & 0 & 0 \\ 0 & \cos \alpha & -\sin \alpha \\ 0 & \sin \alpha & \cos \alpha \end{bmatrix} \begin{bmatrix} d_{4x} \\ d_{4y} \\ d_{4z} \end{bmatrix} \quad (6.14)$$

or

$$\mathbf{P}'_{4i} = \mathbf{T}_3^T \mathbf{P}_{4i} \quad \text{and} \quad \mathbf{d}'_{4i} = \mathbf{T}_3^T \mathbf{d}_{4i}. \quad (6.15)$$

Extending the above to the other nodes, the state vector on the right hand side may be written in the local coordinate system as

$$\mathbf{s}'(1) = \mathbf{T}_{18}^T \mathbf{s}(1) \quad (6.16)$$

where \mathbf{T}_{18}^T is the 18×18 transformation matrix consisting of \mathbf{T}_3^T blocks on the leading diagonal. Pre-multiply equation (6.3) by \mathbf{T}_{18}^T to give

$$\mathbf{s}'(1) = \mathbf{G}' \mathbf{s}(0) \quad (6.17)$$

where

$$\mathbf{G}' = \mathbf{T}_{18}^T \mathbf{G}; \quad (6.18)$$

note that $\mathbf{s}'(0) = \mathbf{s}(0)$, since for this first cell, the local and global coordinate systems coincide on the left hand side. It will be asserted that this transfer matrix \mathbf{G}' for the first cell applies equally to all cells within the structure. In principle, each cell within the period requires a transformation matrix to relate the local coordinate system with the global; the pattern is easily discerned by considering the second cell, Figure 6.3, whose local right hand side coordinates transform as

$$\begin{bmatrix} x'' \\ y'' \\ z'' \end{bmatrix} = \begin{bmatrix} 1 & 0 & 0 \\ 0 & \cos \alpha & \sin \alpha \\ 0 & -\sin \alpha & \cos \alpha \end{bmatrix} \begin{bmatrix} x' \\ y' \\ z' \end{bmatrix} = \begin{bmatrix} 1 & 0 & 0 \\ 0 & \cos \alpha & \sin \alpha \\ 0 & -\sin \alpha & \cos \alpha \end{bmatrix}^2 \begin{bmatrix} x \\ y \\ z \end{bmatrix} \quad (6.19)$$

or

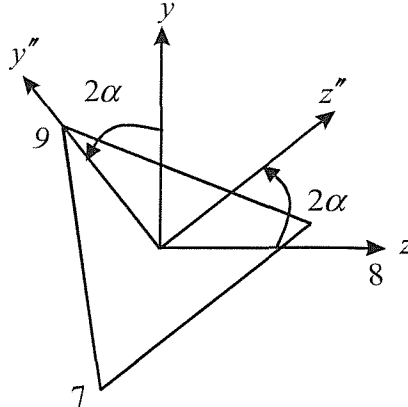
$$\begin{bmatrix} x'' \\ y'' \\ z'' \end{bmatrix} = \begin{bmatrix} 1 & 0 & 0 \\ 0 & \cos 2\alpha & \sin 2\alpha \\ 0 & -\sin 2\alpha & \cos 2\alpha \end{bmatrix} \begin{bmatrix} x \\ y \\ z \end{bmatrix} \quad (6.20)$$

or, symbolically,

$$\mathbf{x}_i'' = \mathbf{T}_3(2) \mathbf{x}_i, \quad (6.21)$$

where the index 2 denotes a rotation by angle 2α , and the transformation matrices previously introduced require index 1. Indeed, using this notation, transformations for the first cell may be re-written as follows: in global coordinates $\mathbf{s}(1) = \mathbf{G}(1)\mathbf{s}(0)$. In the local coordinate *for this cell*, one has $\mathbf{s}'(1) = \mathbf{T}_{18}^T(1)\mathbf{s}(1)$, $\mathbf{s}'(0) = \mathbf{T}_{18}(0)\mathbf{s}(0) = \mathbf{s}(0)$, since $\mathbf{T}_{18}(0)$ is the identity matrix. Pre-multiply by $\mathbf{T}_{18}^T(1)$ in the above to give $\mathbf{T}_{18}^T(1)\mathbf{s}(1) = \mathbf{T}_{18}^T(1)\mathbf{G}(1)\mathbf{s}(0)$ or $\mathbf{s}'(1) = \mathbf{G}'(1)\mathbf{s}'(0)$ where

$$\mathbf{G}'(1) = \mathbf{T}_{18}^T(1)\mathbf{G}(1). \quad (6.22)$$



$$n = 2$$

Figure 6.3. Coordinates of the right hand side of the second cell.

For the second cell, suppose that the transfer matrix had been calculated in global coordinates according to $\mathbf{s}(2) = \mathbf{G}(2)\mathbf{s}(1)$. However, in the local coordinates *for this particular cell*, one has $\mathbf{s}'(2) = \mathbf{T}_{18}^T(2)\mathbf{s}(2)$, and $\mathbf{s}'(1) = \mathbf{T}_{18}^T(1)\mathbf{s}(1)$, or $\mathbf{s}(1) = \mathbf{T}_{18}(1)\mathbf{s}'(1)$, since the transformation matrix is orthogonal. Pre-multiply by $\mathbf{T}_{18}^T(2)$ in the above to give $\mathbf{T}_{18}^T(2)\mathbf{s}(2) = \mathbf{T}_{18}^T(2)\mathbf{G}(2)\mathbf{s}(1)$ or $\mathbf{s}'(2) = \mathbf{G}'(2)\mathbf{s}'(1)$ where

$$\mathbf{G}'(2) = \mathbf{T}_{18}^T(2)\mathbf{G}(2)\mathbf{T}_{18}(1). \quad (6.23)$$

For the n^{th} cell, one has in global coordinates, $\mathbf{s}(n) = \mathbf{G}(n)\mathbf{s}(n-1)$. In the local coordinates, $\mathbf{s}'(n) = \mathbf{T}_{18}^T(n)\mathbf{s}(n)$, $\mathbf{s}(n-1) = \mathbf{T}_{18}(n-1)\mathbf{s}'(n-1)$; pre-multiply by $\mathbf{T}_{18}^T(n)$ in the above to give $\mathbf{T}_{18}^T(n)\mathbf{s}(n) = \mathbf{T}_{18}^T(n)\mathbf{G}(n)\mathbf{s}(n-1)$ or $\mathbf{s}'(n) = \mathbf{G}'(n)\mathbf{s}'(n-1)$ where

$$\mathbf{G}'(n) = \mathbf{T}_{18}^T(n)\mathbf{G}(n)\mathbf{T}_{18}(n-1). \quad (6.24)$$

We now make the assertion that the transfer matrix expressed in the local coordinates pertaining to the cell under consideration, is invariant; that is

$$\mathbf{G}' = \mathbf{G}'(1) = \mathbf{G}'(2) = \cdots \mathbf{G}'(n) \cdots = \mathbf{G}'(p). \quad (6.25)$$

6.2.2 Floquet Theory

The pre-twisted rod is a realisation of discrete Floquet theory for which the following general results are relevant:

- a) let $\mathbf{s}(n)$ be a vector solution to the periodic system $\mathbf{s}(n+1) = \mathbf{G}(n+1)\mathbf{s}(n)$.
- b) the matrix analogue of (a) is $\mathbf{S}(n+1) = \mathbf{G}(n+1)\mathbf{S}(n)$ where $\mathbf{S}(n)$ is a square matrix of column vector solutions to (a).
- c) $\mathbf{S}(n)$ is a *fundamental matrix* of (b) provided that it is a solution such that $\det \mathbf{S}(n) \neq 0$, for all integer n ; in principle there are an infinite number of fundamental matrix solutions; indeed, set $n = 0$ in b), then $\mathbf{S}(0)$ represents the infinite number of (initial) end conditions which are possible on the left hand side of the first cell of the structure. Fundamental matrix solutions are characterised as follows:
- d) if $\mathbf{S}(n)$ is a fundamental matrix, then $\Psi(n)$ is another fundamental matrix if and only if there is a constant non-singular matrix \mathbf{C} such that $\Psi(n) = \mathbf{S}(n)\mathbf{C}$ for all n .

There is a *unique* fundamental matrix solution defined according to the imposed end condition on the left hand side being equal to the identity matrix, that is $\mathbf{S}(0) = \mathbf{I}$, in which case $\Psi(0) = \mathbf{C}$, the *monodromy* matrix.

- e) if \mathbf{C} is a nonsingular matrix and p is a positive integer, there is a constant nonsingular matrix \mathbf{L} such that $\mathbf{L}^p = \mathbf{C}$.
- f) if $\Psi(n)$ is a fundamental matrix, then so is $\Psi(n+p)$ and, $\Psi(n+p) = \Psi(n)\mathbf{C}$, where

$$\mathbf{C} = \mathbf{G}(p)\mathbf{G}(p-1)\dots\mathbf{G}(2)\mathbf{G}(1).$$

Furthermore, there is a nonsingular matrix function $\mathbf{P}(n)$ such that $\mathbf{S}(n) = \mathbf{P}(n)\mathbf{L}^n$; further, $\mathbf{P}(n)$ is periodic, with period p .

- g) the eigenvalues μ of matrix \mathbf{C} are known as the Floquet multipliers of the system
- h) $\mathbf{s}(n)$ is a solution of the Floquet system if and only if $\mathbf{z}(n) = \mathbf{P}(n)^{-1}\mathbf{s}(n)$ where $\mathbf{z}(n)$ is a solution of the autonomous system $\mathbf{z}(n+1) = \mathbf{L}\mathbf{z}(n)$; this is the Floquet decomposition, that is $\mathbf{s}(n) = \mathbf{P}(n)\mathbf{z}(n)$.

The above are largely from Kelley and Peterson [70], but with the notations modified to conform with those already introduced.

In h), one may readily identify the autonomous matrix \mathbf{L} with the transfer matrix, written in local coordinates, \mathbf{G}' , and vector solution $\mathbf{z}(n)$ with $\mathbf{s}'(n)$. Moreover, the matrix function $\mathbf{P}(n)$ is identified as $\mathbf{T}_{18}(n)$. In turn, $\mathbf{L}^p = (\mathbf{G}')^p = \mathbf{G}_p$, so one may identify matrix \mathbf{C} with \mathbf{G}_p , as in e) and f). The Floquet multipliers μ are then equivalent to the λ_p , as in g).

From the knowledge of Equations (6.22-6.25), the following expression can be given,

$$\begin{aligned} (\mathbf{G}')^n &= \mathbf{G}'(n)\mathbf{G}'(n-1)\cdots\mathbf{G}'(2)\mathbf{G}'(1) \\ &= \mathbf{T}_{18}^T(n)\mathbf{G}(n)\mathbf{T}_{18}(n-1)\mathbf{T}_{18}^T(n-1)\mathbf{G}(n-1)\mathbf{T}_{18}(n-2)\cdots\mathbf{T}_{18}^T(2)\mathbf{G}(2)\mathbf{T}_{18}(1)\mathbf{T}_{18}^T(1)\mathbf{G}(1) \\ &= \mathbf{T}_{18}^T(n)\mathbf{G}(n)\mathbf{G}(n-1)\cdots\mathbf{G}(2)\mathbf{G}(1) \end{aligned} \quad (6.26)$$

According to (6.2.2.f), if $\Psi(n)$ is a fundamental matrix for the Floquet system

$$\mathbf{s}(n+1) = \mathbf{G}(n+1)\mathbf{s}(n), \quad (6.27)$$

$\Psi(n+p)$ is also a fundamental matrix and

$$\Psi(n+p) = \Psi(n)\mathbf{C}, \quad (6.28)$$

where $\mathbf{C} = \mathbf{G}(p)\mathbf{G}(p-1)\cdots\mathbf{G}(1)$.

Furthermore, there is a non-singular matrix function $\mathbf{T}_{18}(n)$ and a non-singular matrix \mathbf{G}' such that

$$\Psi(n) = \mathbf{T}_{18}(n)(\mathbf{G}')^n, \quad (6.29)$$

where $\mathbf{T}_{18}(n+p) = \mathbf{T}_{18}(n)$.

According to equation (6.29), left-hand side of equation (6.28) becomes

$$\Psi(n+p) = \mathbf{T}_{18}(n+p)(\mathbf{G}')^{n+p}, \quad (6.30)$$

or

$$\Psi(n+p) = \mathbf{T}_{18}(n)(\mathbf{G}')^n(\mathbf{G}')^p. \quad (6.31)$$

Consideration of (6.26) gives

$$\Psi(n+p) = \mathbf{T}_{18}(n)(\mathbf{G}')^n \mathbf{T}_{18}^T(p) \mathbf{C}, \quad (6.32)$$

but, $\mathbf{T}_{18}^T(p) = \mathbf{I}$, so the above equation becomes

$$\Psi(n+p) = \mathbf{T}_{18}(n)(\mathbf{G}')^n \mathbf{C}. \quad (6.33)$$

While considering equation (6.29), the right hand side of (6.28) becomes

$$\Psi(n) \mathbf{C} = \mathbf{T}_{18}(n)(\mathbf{G}')^n \mathbf{C}. \quad (6.34)$$

Therefore, equations (6.33) and (6.34) do satisfy equation (6.28).

According to (6.2.2.h), let $\Psi(n) = \mathbf{T}_{18}(n)(\mathbf{G}')^n$ as in Floquet Theorem. Then $\mathbf{s}(n)$ is a solution of the Floquet system, equation (6.27), if and only if

$$\mathbf{s}'(n) = \mathbf{T}_{18}^T(n) \mathbf{s}(n) \quad (6.35)$$

is a solution of the autonomous system

$$\mathbf{s}'(n+1) = \mathbf{G}' \mathbf{s}'(n). \quad (6.36)$$

Hence, the autonomous system is verified.

6.2.3 Eigenanalysis

Two consecutive state vectors are related by the scalar λ as

$$\mathbf{s}'(n+1) = \lambda \mathbf{s}'(n), \quad (6.37)$$

which, together with the transfer matrix relation, equation (6.36), immediately leads to the eigenvalue problem

$$\mathbf{G}' \mathbf{s}'(n) = \lambda \mathbf{s}'(n). \quad (6.38)$$

The *eig* command within MATLAB gives the eigenvalues of the transfer matrix \mathbf{G}' as the three reciprocal pairs

$$\begin{bmatrix} -22.3303 \\ -0.0488 \end{bmatrix}, \begin{bmatrix} -10.0110 - 10.0110i \\ -0.0499 + 0.0499i \end{bmatrix}, \begin{bmatrix} -10.0110 + 10.0110i \\ -0.0499 - 0.0499i \end{bmatrix}$$

which pertain to decay of self-equilibrated loading, and four real unity eigenvalues pertaining to rigid body displacement in, and rigid body rotation about, the x -direction, together with tension and torsion. Also there are eight complex unity eigenvalues of the form $4 \times e^{\pm i\alpha}$, in which α is the angle of pre-twist per cell and $i = \sqrt{-1}$, and these

pertain to rigid body displacements in, and rigid body rotations about, both the y' -and z' -directions, together with bending moments and shearing forces in both planes.

As with the eigenanalysis described in Chapter 2, the eigenvectors associated with the distinct decay eigenvalues are correctly calculated by the QR algorithm employed within MATLAB, and these are designated \mathbf{v}_1 to \mathbf{v}_6 . The four (real) unity eigenvalues pertain to eigenvectors describing rigid body displacements in the x -direction, \mathbf{v}_7 , and rotation about the x -axis, \mathbf{v}_9 , these being unaffected by the choice of global or local coordinates. The reduced row echelon form of $\mathbf{G}' - \mathbf{I}$ yields these two independent eigenvectors, which may be written as

$$\mathbf{v}_7 = [1 \ 0 \ 0 \ 1 \ 0 \ 0 \ 1 \ 0 \ 0 \ 0 \ 0 \ 0 \ 0 \ 0 \ 0 \ 0 \ 0 \ 0 \ 0 \ 0]^T, \\ \mathbf{v}_9 = \left[0 \ \frac{L\theta}{2} \ \frac{-H\theta}{3} \ 0 \ \frac{-L\theta}{2} \ \frac{-H\theta}{3} \ 0 \ 0 \ \frac{2H\theta}{3} \ 0 \ 0 \ 0 \ 0 \ 0 \ 0 \ 0 \ 0 \ 0 \ 0 \right]^T, \quad (6.39a, b)$$

where the angle of rotation θ is taken to be small, $\theta = 5 \times 10^{-8}$ radians. Two principal vectors \mathbf{w}_8 and \mathbf{w}_{10} are coupled to the eigenvectors \mathbf{v}_7 and \mathbf{v}_9 , respectively and are found using the MATLAB *rref* command on the augmented matrix, again as described in Chapter 2, followed by appropriate interpretation. Principal vector \mathbf{w}_8 , consists of the necessary combination of tensile force and twisting moment which, when applied to the left and right hand sides of the cell, produces the unit extension defined by vector \mathbf{v}_7 . Principal vector \mathbf{w}_{10} consists of the necessary combination of twisting moment and tensile force which, when applied to the left and right hand sides of the cell, produces the rotation defined by vector \mathbf{v}_9 . Therefore, there are two 2×2 Jordan blocks associated with these vectors, which are

$$\mathbf{J}^1_{2 \times 2} = \begin{bmatrix} 1 & 1 \\ 0 & 1 \end{bmatrix}, \quad \mathbf{J}^2_{2 \times 2} = \begin{bmatrix} 1 & 1 \\ 0 & 1 \end{bmatrix}. \quad (6.40)$$

This coupling between tension and torsion is similar in nature to that described in Chapter 4, for the asymmetric *NASA* structure.

For determination of the eigen- and principal vectors associated with the multiple complex unity eigenvalues, $4 \times e^{\pm i\alpha}$, a variety of strategies are possible. For example, two chains of equations relating eigen- and principal vectors may be expressed as

$$\begin{aligned} (\mathbf{G}' - e^{i\alpha} \mathbf{I}) \mathbf{v}_{11} &= 0 & (\mathbf{G}' - e^{-i\alpha} \mathbf{I}) \mathbf{v}_{15} &= 0 \\ (\mathbf{G}' - e^{i\alpha} \mathbf{I}) \mathbf{w}_{12} &= \mathbf{v}_{11} & (\mathbf{G}' - e^{-i\alpha} \mathbf{I}) \mathbf{w}_{16} &= \mathbf{v}_{15} \\ (\mathbf{G}' - e^{i\alpha} \mathbf{I}) \mathbf{w}_{13} &= \mathbf{w}_{12}, & (\mathbf{G}' - e^{-i\alpha} \mathbf{I}) \mathbf{w}_{17} &= \mathbf{w}_{16} \\ (\mathbf{G}' - e^{i\alpha} \mathbf{I}) \mathbf{w}_{14} &= \mathbf{w}_{13} & (\mathbf{G}' - e^{-i\alpha} \mathbf{I}) \mathbf{w}_{18} &= \mathbf{w}_{17} \end{aligned} \quad (6.41a, b)$$

The reduced row echelon forms of the matrices $(\mathbf{G}' - e^{i\alpha} \mathbf{I})$ and $(\mathbf{G}' - e^{-i\alpha} \mathbf{I})$, respectively, yields the two eigenvectors

$$\begin{aligned} \mathbf{v}_{11} &= [0 \ i \ 1 \ 0 \ i \ 1 \ 0 \ i \ 1 \ 0 \ 0 \ 0 \ 0 \ 0 \ 0 \ 0 \ 0 \ 0]^T, \\ \mathbf{v}_{15} &= [0 \ -i \ 1 \ 0 \ -i \ 1 \ 0 \ -i \ 1 \ 0 \ 0 \ 0 \ 0 \ 0 \ 0 \ 0 \ 0 \ 0]^T; \end{aligned} \quad (6.42a, b)$$

which is a combination of real and imaginary rigid body displacements in the y - and z -directions.

The principal vectors \mathbf{w}_{12} to \mathbf{w}_{14} and \mathbf{w}_{16} to \mathbf{w}_{18} can then be determined by following the chains, equations (6.41a) and (6.41b), respectively. If one then constructs a similarity matrix \mathbf{V} from these eigen- and principal vectors, this gives the JCF in its simplest form

$$\mathbf{J} = \mathbf{V}^{-1} \mathbf{G}' \mathbf{V} = \begin{bmatrix} \lambda_1 & 0 & 0 & 0 & 0 & 0 & 0 & 0 & 0 & 0 & 0 \\ 0 & \lambda_2 & 0 & 0 & 0 & 0 & 0 & 0 & 0 & 0 & 0 \\ 0 & 0 & \bar{\lambda}_2 & 0 & 0 & 0 & 0 & 0 & 0 & 0 & 0 \\ 0 & 0 & 0 & \lambda_1^{-1} & 0 & 0 & 0 & 0 & 0 & 0 & 0 \\ 0 & 0 & 0 & 0 & \lambda_2^{-1} & 0 & 0 & 0 & 0 & 0 & 0 \\ 0 & 0 & 0 & 0 & 0 & \bar{\lambda}_2^{-1} & 0 & 0 & 0 & 0 & 0 \\ 0 & 0 & 0 & 0 & 0 & 0 & \mathbf{J}_{2 \times 2}^1 & 0 & 0 & 0 & 0 \\ 0 & 0 & 0 & 0 & 0 & 0 & 0 & \mathbf{J}_{2 \times 2}^2 & 0 & 0 & 0 \\ 0 & 0 & 0 & 0 & 0 & 0 & 0 & 0 & \mathbf{J}_{4 \times 4}^1 & 0 & 0 \\ 0 & 0 & 0 & 0 & 0 & 0 & 0 & 0 & 0 & \mathbf{J}_{4 \times 4}^2 & 0 \end{bmatrix} \quad (6.43)$$

where the two 4×4 Jordan blocks associated with the multiple complex unity eigenvalues are

$$\mathbf{J}^1_{4 \times 4} = \begin{bmatrix} e^{i\alpha} & 1 & 0 & 0 \\ 0 & e^{i\alpha} & 1 & 0 \\ 0 & 0 & e^{i\alpha} & 1 \\ 0 & 0 & 0 & e^{i\alpha} \end{bmatrix}, \quad \mathbf{J}^2_{4 \times 4} = \begin{bmatrix} e^{-i\alpha} & 1 & 0 & 0 \\ 0 & e^{-i\alpha} & 1 & 0 \\ 0 & 0 & e^{-i\alpha} & 1 \\ 0 & 0 & 0 & e^{-i\alpha} \end{bmatrix} \quad (6.44a, b)$$

and the 2×2 Jordan blocks associated with the real unity eigenvalues are as equation (6.40)

Now, while the JCF may be in its simplest form, because of the complex eigenvalues, and complex eigen- and principal vectors, interpretation of the vectors is at its most difficult. Obviously a complex vector is not physically permissible, but when considered in conjunction with its conjugate, the (real) displacement and force components are the real and imaginary parts, in turn. Indeed, if one replaces the complex conjugate columns of the similarity matrix by their real and imaginary parts, one obtains the real JCF

$$\mathbf{J} = \begin{bmatrix} \lambda_1 & 0 & 0 & 0 & 0 & 0 & 0 & 0 & 0 \\ 0 & \text{real}(\lambda_2) & -\text{imag}(\lambda_2) & 0 & 0 & 0 & 0 & 0 & 0 \\ 0 & \text{imag}(\lambda_2) & \text{real}(\lambda_2) & 0 & 0 & 0 & 0 & 0 & 0 \\ 0 & 0 & 0 & \lambda_1^{-1} & 0 & 0 & 0 & 0 & 0 \\ 0 & 0 & 0 & 0 & \text{real}(\bar{\lambda}_2) & -\text{imag}(\bar{\lambda}_2) & 0 & 0 & 0 \\ 0 & 0 & 0 & 0 & \text{imag}(\bar{\lambda}_2) & \text{real}(\bar{\lambda}_2) & 0 & 0 & 0 \\ 0 & 0 & 0 & 0 & 0 & 0 & \mathbf{J}_{2 \times 2}^1 & 0 & 0 \\ 0 & 0 & 0 & 0 & 0 & 0 & 0 & \mathbf{J}_{2 \times 2}^2 & 0 \\ 0 & 0 & 0 & 0 & 0 & 0 & 0 & 0 & \mathbf{J}_{8 \times 8} \end{bmatrix} \quad (6.45)$$

where

$$\mathbf{J}_{8 \times 8} = \begin{bmatrix} \cos \alpha & -\sin \alpha & 1 & 0 & 0 & 0 & 0 & 0 \\ \sin \alpha & \cos \alpha & 0 & 1 & 0 & 0 & 0 & 0 \\ 0 & 0 & \cos \alpha & -\sin \alpha & 1 & 0 & 0 & 0 \\ 0 & 0 & \sin \alpha & \cos \alpha & 0 & 1 & 0 & 0 \\ 0 & 0 & 0 & 0 & \cos \alpha & -\sin \alpha & 1 & 0 \\ 0 & 0 & 0 & 0 & \sin \alpha & \cos \alpha & 0 & 1 \\ 0 & 0 & 0 & 0 & 0 & 0 & \cos \alpha & -\sin \alpha \\ 0 & 0 & 0 & 0 & 0 & 0 & \sin \alpha & \cos \alpha \end{bmatrix}; \quad (6.46)$$

note that the single complex unity eigenvalues on the leading diagonal are replaced by 2×2 real blocks. Within this formulation, the principal vectors \mathbf{w}_{13} and \mathbf{w}_{14} describe rigid body rotations of the left-hand side of the cell, but employ the local y' - and z' -axes of the right-hand cross section, respectively. In turn, their coupled principal vectors \mathbf{w}_{15} , \mathbf{w}_{16} , \mathbf{w}_{17} and \mathbf{w}_{18} describe bending moment and shear vectors applied to the left-hand side of the cell, but employ the local coordinate system of the right-hand side of the cell. For interpretation of these vectors it is easier if they are expressed within the local coordinate system of the left-hand side, for which the local and global coordinate systems coincide. This is achieved by employing a *near diagonal* Jordan decomposition in which the complex unity eigenvalue replaces the real unity on the super diagonal; the chains then become

$$\begin{aligned} (\mathbf{G}' - e^{i\alpha} \mathbf{I}) \mathbf{v}_{11} &= 0 & (\mathbf{G}' - e^{-i\alpha} \mathbf{I}) \mathbf{v}_{15} &= 0 \\ (\mathbf{G}' - e^{i\alpha} \mathbf{I}) \mathbf{w}_{12} &= e^{i\alpha} \mathbf{v}_{11} & (\mathbf{G}' - e^{-i\alpha} \mathbf{I}) \mathbf{w}_{16} &= e^{-i\alpha} \mathbf{v}_{15} \\ (\mathbf{G}' - e^{i\alpha} \mathbf{I}) \mathbf{w}_{13} &= e^{i\alpha} \mathbf{w}_{12} & (\mathbf{G}' - e^{-i\alpha} \mathbf{I}) \mathbf{w}_{17} &= e^{-i\alpha} \mathbf{w}_{16} \\ (\mathbf{G}' - e^{i\alpha} \mathbf{I}) \mathbf{w}_{14} &= e^{i\alpha} \mathbf{w}_{13} & (\mathbf{G}' - e^{-i\alpha} \mathbf{I}) \mathbf{w}_{18} &= e^{-i\alpha} \mathbf{w}_{17} \end{aligned} \quad (6.47a, b)$$

The new complex similarity matrix \mathbf{V} comprised of these eigen- and principal vectors transforms the transfer matrix \mathbf{G}' into a new JCF, which remains broadly as in equation (6.43), but with two new 4×4 blocks, which are

$$\mathbf{J}^1_{4 \times 4} = \begin{bmatrix} e^{i\alpha} & e^{i\alpha} & 0 & 0 \\ 0 & e^{i\alpha} & e^{i\alpha} & 0 \\ 0 & 0 & e^{i\alpha} & e^{i\alpha} \\ 0 & 0 & 0 & e^{i\alpha} \end{bmatrix}, \quad \mathbf{J}^2_{4 \times 4} = \begin{bmatrix} e^{-i\alpha} & e^{-i\alpha} & 0 & 0 \\ 0 & e^{-i\alpha} & e^{-i\alpha} & 0 \\ 0 & 0 & e^{-i\alpha} & e^{-i\alpha} \\ 0 & 0 & 0 & e^{-i\alpha} \end{bmatrix}. \quad (6.48a, b)$$

Again, this leads to complex conjugate eigen- and principal vectors, and replacing these by their real and imaginary parts, allows one to construct a new real similarity matrix which transforms \mathbf{G}' into a new real JCF, which differs from equation (6.46), in that the 8×8 block becomes

$$\mathbf{J}_{8 \times 8} = \begin{bmatrix} \cos \alpha & -\sin \alpha & \cos \alpha & -\sin \alpha & 0 & 0 & 0 & 0 \\ \sin \alpha & \cos \alpha & \sin \alpha & \cos \alpha & 0 & 0 & 0 & 0 \\ 0 & 0 & \cos \alpha & -\sin \alpha & \cos \alpha & -\sin \alpha & 0 & 0 \\ 0 & 0 & \sin \alpha & \cos \alpha & \sin \alpha & \cos \alpha & 0 & 0 \\ 0 & 0 & 0 & 0 & \cos \alpha & -\sin \alpha & \cos \alpha & -\sin \alpha \\ 0 & 0 & 0 & 0 & \sin \alpha & \cos \alpha & \sin \alpha & \cos \alpha \\ 0 & 0 & 0 & 0 & 0 & 0 & \cos \alpha & -\sin \alpha \\ 0 & 0 & 0 & 0 & 0 & 0 & \sin \alpha & \cos \alpha \end{bmatrix}. \quad (6.49)$$

This real similarity matrix \mathbf{V} and the associated JCF are given in Appendix 6.A. The eigen- and principal vectors pertaining to the multiple complex unity eigenvalues are now expressed within the local/global coordinate system of the left-hand cross section. This greatly simplifies the physical interpretation of these vectors and, in turn, determination of the equivalent continuum properties.

6.2.4 Equivalent Continuum Properties

a) The two vectors \mathbf{v}_7 and \mathbf{w}_8 are coupled according to

$$\mathbf{G}' \mathbf{w}_8 = \mathbf{w}_8 + \mathbf{v}_7, \quad (6.50)$$

as shown in Figure 6.4, where it is seen that a tensile force and a twisting moment are applied on both hand sides of the cell in order to produce unit extension in the x -direction, only. The two vectors \mathbf{v}_9 and \mathbf{w}_{10} are coupled according to

$$\mathbf{G}' \mathbf{w}_{10} = \mathbf{w}_{10} + \mathbf{v}_9, \quad (6.51)$$

as shown in Figure 6.5, where it is seen that a twisting moment and a compressive force are applied on both sides of the cell in order to produce rotation about the x -axis, only.

For a pre-twisted structure, the coupled force-displacement equations for tension and torsion may be written exactly as in Chapter 4, as

$$\begin{aligned} T_x &= \frac{EA}{L} u + \frac{K_u}{L} \theta, \\ M_x &= \frac{GJ}{L} \theta + \frac{K_u}{L} u. \end{aligned} \quad (6.52a, b)$$

where K_u is the coupling coefficient for tension-torsion.

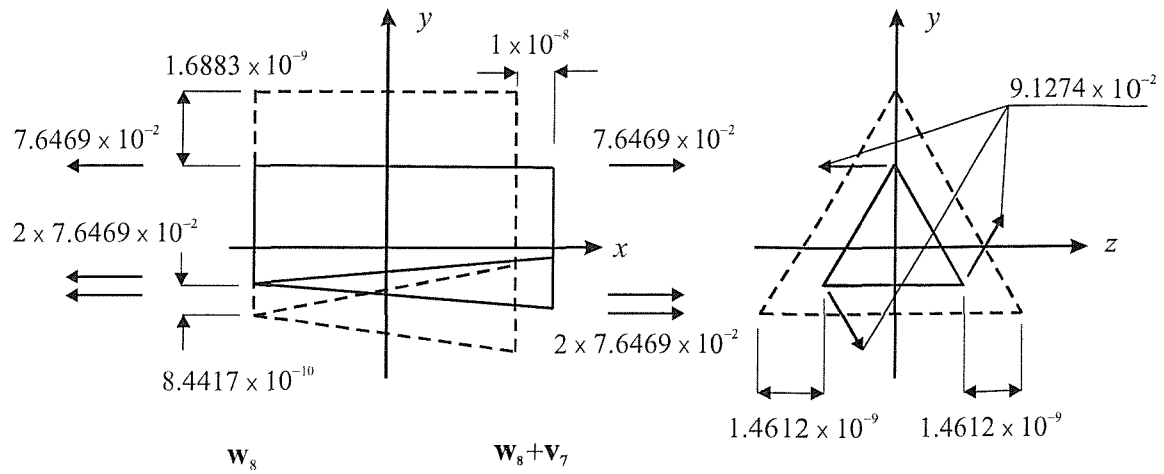


Figure 6.4. Coupling of eigenvector \mathbf{v}_7 for rigid body displacement in the x -direction, with principal vector \mathbf{w}_8 for extension; displacement are exaggerated. Dotted lines show initial configuration

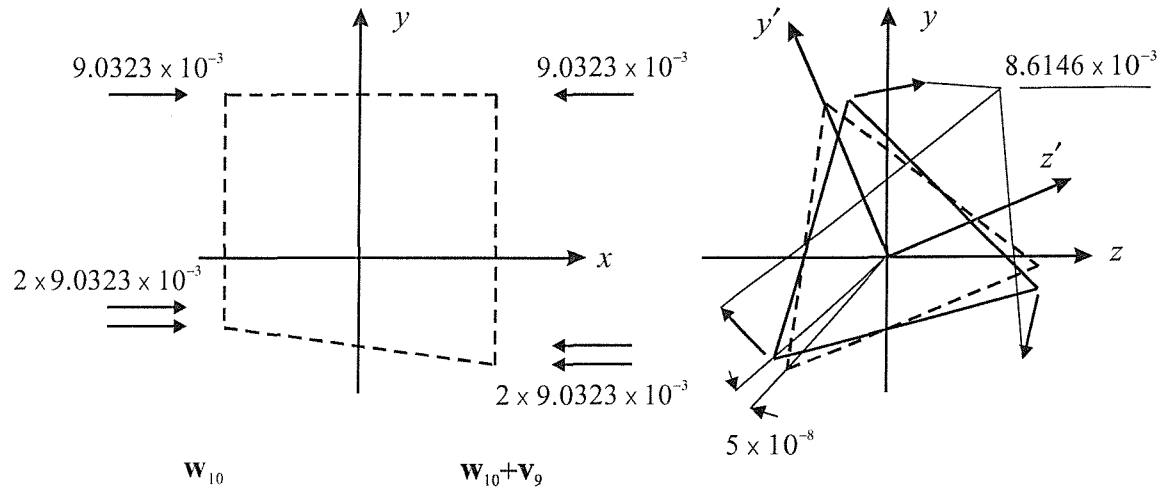


Figure 6.5. Coupling of eigenvector \mathbf{v}_9 for rigid body rotation about the x -axis, with principal vector \mathbf{w}_{10} for torsion.

From vectors \mathbf{w}_8 and \mathbf{v}_7 , the quantities T_x , M_x , and u are known (θ is zero), and the equivalent cross-sectional area and coupling coefficient are calculated as $A = (2.2941 \times 10^{-1}) / (7 \times 10^{10} \times 1 \times 10^{-8}) = 1.1234 \times 10^{-4} \text{ m}^2$, $K_u = -1.8578 \times 10^5 \text{ Nm}$.

Additionally, there is a Poisson's ratio effect on the cross section; the strain in the x -direction $\varepsilon_x = 1 \times 10^{-8} / 0.3428 = 2.9172 \times 10^{-8}$, and the strains in the y -and z -directions are $\varepsilon_y = (-1.6883 - 0.8442) \times 10^{-9} / (0.3428 \times \sqrt{3}/2) = -8.5306 \times 10^{-9}$, $\varepsilon_z = -(1.6214 \times 10^{-9}) / 0.3428 = -8.5306 \times 10^{-9}$. Employing $\nu = -\varepsilon_y / \varepsilon_x = -\varepsilon_z / \varepsilon_x$, the Poisson's ratio is calculated as $\nu = 0.2924$. In turn, the equivalent shear modulus is found to be $G = E / 2(1 + \nu) = 2.7081 \times 10^{10}$ N/m², with Young's modulus E being regarded as invariant.

From vectors \mathbf{w}_{10} and \mathbf{v}_9 , quantities T_x , M_x , and θ are known (u is zero), and equation (6.52) gives the equivalent torsion constant and coupling coefficient as

$$J = (8.6146 \times 10^{-3} \times 0.3428 / \sqrt{3}) / (2.7081 \times 10^{10} \times 5 \times 10^{-8}) = 1.2949 \times 10^{-6}$$
 m⁴,

$K_u = -1.8578 \times 10^5$ Nm; the latter is identical to that found from vectors \mathbf{w}_8 and \mathbf{v}_7 , as one would expect from the reciprocal theorem.

b) The two principal vectors \mathbf{w}_{13} and \mathbf{w}_{14} are coupled to the eigenvectors \mathbf{v}_{11} and \mathbf{v}_{12} , describing rigid body displacements in the y - and z -directions, respectively, according to

$$\mathbf{G}' \mathbf{w}_{13} = \cos \alpha \mathbf{v}_{11} + \sin \alpha \mathbf{v}_{12} + \cos \alpha \mathbf{w}_{13} + \sin \alpha \mathbf{w}_{14},$$

$$\mathbf{G}' \mathbf{w}_{14} = -\sin \alpha \mathbf{v}_{11} + \cos \alpha \mathbf{v}_{12} - \sin \alpha \mathbf{w}_{13} + \cos \alpha \mathbf{w}_{14}. \quad (6.53a, b)$$

Vectors \mathbf{w}_{13} and \mathbf{w}_{14} describe rigid body rotations of the left-hand cross section about the z - and y -axes, respectively, within the global coordinate system. Pre-multiplication of these vectors by the transfer matrix \mathbf{G}' will give rigid body rotations of the right-hand side about the local z' - and y' -axes, respectively, as indicated by equation (6.53).

However, for interpretation of these vectors, it is preferable that these right-hand rotations be expressed within the global coordinate system, which is achieved by pre-multiplication by \mathbf{G} , according to

$$\mathbf{w}_{13R} = \mathbf{G} \mathbf{w}_{13}, \quad \mathbf{w}_{14R} = \mathbf{G} \mathbf{w}_{14}. \quad (6.54)$$

where \mathbf{G} is the transfer matrix defined within the global coordinate system and the additional subscript R denotes the right-hand side vector. The physical representation of vectors \mathbf{w}_{13} , \mathbf{w}_{13R} , and \mathbf{w}_{14} and \mathbf{w}_{14R} , is shown in Figure 6.6.

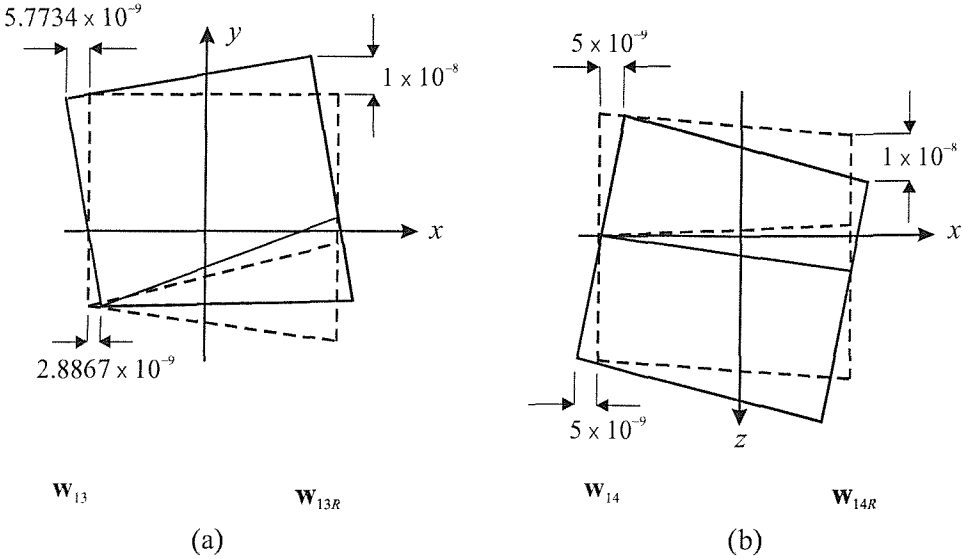


Figure 6.6(a). Principal vector \mathbf{w}_{13} for rigid body rotation about the z -axis; (b) principal vector \mathbf{w}_{14} for rigid body rotation about the y -axis.

c) Vectors \mathbf{w}_{15} and \mathbf{w}_{16} describe the bending moments on the left-hand side of the cell in the xy -and xz -planes, respectively, within the global coordinate system, and are coupled to the rotations according to

$$\mathbf{G}' \mathbf{w}_{15} = \cos \alpha \mathbf{w}_{13} + \sin \alpha \mathbf{w}_{14} + \cos \alpha \mathbf{w}_{15} + \sin \alpha \mathbf{w}_{16},$$

$$\mathbf{G}' \mathbf{w}_{16} = -\sin \alpha \mathbf{w}_{13} + \cos \alpha \mathbf{w}_{14} - \sin \alpha \mathbf{w}_{15} + \cos \alpha \mathbf{w}_{16}. \quad (6.55a, b)$$

Again, pre-multiplication by \mathbf{G}' would give the two bending moment vectors on the right-hand side of the cell in the local $x'y'$ - and $x'z'$ -planes, and for interpretation of the vectors, it is preferable that these right hand vectors be expressed within the global coordinate system, which is achieved by pre-multiplication by \mathbf{G} , to give

$$\mathbf{w}_{15R} = \mathbf{G} \mathbf{w}_{15}, \quad \mathbf{w}_{16R} = \mathbf{G} \mathbf{w}_{16}. \quad (6.56)$$

Analysis of the x -direction displacement components within vectors \mathbf{w}_{15} and \mathbf{w}_{16} , shows that they are comprised of two rotations of the left-hand cross section, about the y - and z -axes, and can therefore be decomposed into

$$\begin{bmatrix} d_{1x} \\ d_{2x} \\ d_{3x} \end{bmatrix}^{w_{15}} = a \times \begin{bmatrix} d_{1x} \\ d_{2x} \\ d_{3x} \end{bmatrix}^{w_{13}} + b \times \begin{bmatrix} d_{1x} \\ d_{2x} \\ d_{3x} \end{bmatrix}^{w_{14}}, \quad \begin{bmatrix} d_{1x} \\ d_{2x} \\ d_{3x} \end{bmatrix}^{w_{16}} = c \times \begin{bmatrix} d_{1x} \\ d_{2x} \\ d_{3x} \end{bmatrix}^{w_{14}} + d \times \begin{bmatrix} d_{1x} \\ d_{2x} \\ d_{3x} \end{bmatrix}^{w_{13}}. \quad (6.57a, b)$$

On the other hand, analysis of the x -direction displacement components within the right-hand side vectors \mathbf{w}_{15R} and \mathbf{w}_{16R} , shows that they are comprised of two rotations of the left-hand cross section, about the y - and z -axes, and can therefore be decomposed as

$$\begin{bmatrix} d_{1x} \\ d_{2x} \\ d_{3x} \end{bmatrix}^{w_{15R}} = e \times \begin{bmatrix} d_{1x} \\ d_{2x} \\ d_{3x} \end{bmatrix}^{w_{13R}} + f \times \begin{bmatrix} d_{1x} \\ d_{2x} \\ d_{3x} \end{bmatrix}^{w_{14R}}, \quad \begin{bmatrix} d_{1x} \\ d_{2x} \\ d_{3x} \end{bmatrix}^{w_{16R}} = g \times \begin{bmatrix} d_{1x} \\ d_{2x} \\ d_{3x} \end{bmatrix}^{w_{14R}} + h \times \begin{bmatrix} d_{1x} \\ d_{2x} \\ d_{3x} \end{bmatrix}^{w_{13R}}. \quad (6.58a, b)$$

Simple calculations from equations (6.57) and (6.58) give $a = -0.5$, $b = 0.2109$, $c = -0.5$, $d = -0.2109$; $e = 0.5$, $f = 0.2109$, $g = 0.5$ and $h = -0.2109$.

The physical representations of these bending moment vectors are shown in Figures 6.7 and 6.8. Geometric consideration of Figures 6.7(a) and 6.8(a) gives the two bending curvatures in the xy -and xz -planes, respectively, as

$$\begin{aligned} 1/R_y &= 1.4434 \times 10^{-9} \left/ \left(\frac{H}{3} \times \frac{L}{2} \right) \right. = 8.5098 \times 10^{-8} \text{ m}^{-1}, \\ 1/R_z &= 2.5 \times 10^{-9} \left/ \left(\frac{L}{2} \times \frac{L}{2} \right) \right. = 8.5098 \times 10^{-8} \text{ m}^{-1}, \end{aligned} \quad (6.59a, b)$$

while consideration of Figures 6.7(b) and 6.8(b) gives the two coupled shear angles in the xz - and xy -planes, respectively, as

$$\begin{aligned} \gamma_{xz} &= 1.0546 \times 10^{-9} \left/ \left(\frac{L}{2} \right) \right. = 6.1527 \times 10^{-9}, \\ \gamma_{xy} &= 6.0886 \times 10^{-10} \left/ \left(\frac{H}{2} \right) \right. = 6.1527 \times 10^{-9}. \end{aligned} \quad (6.60a, b)$$

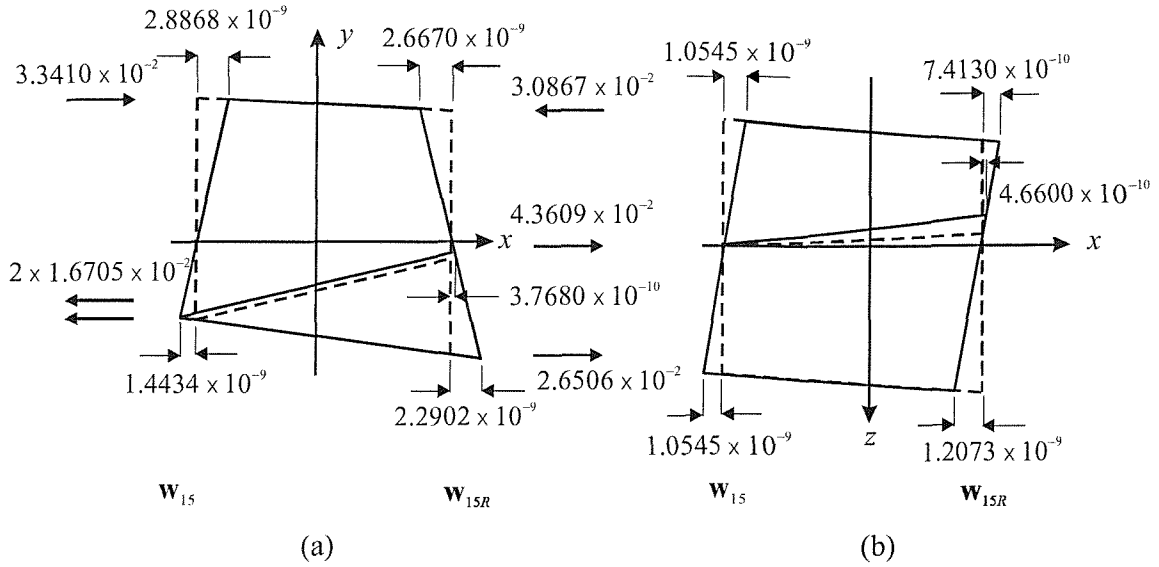


Figure 6.7. Principal vector \mathbf{w}_{15} for bending moment in the xy -plane; (a) and (b) show the displacement and force components in the xy - and xz -planes, respectively.

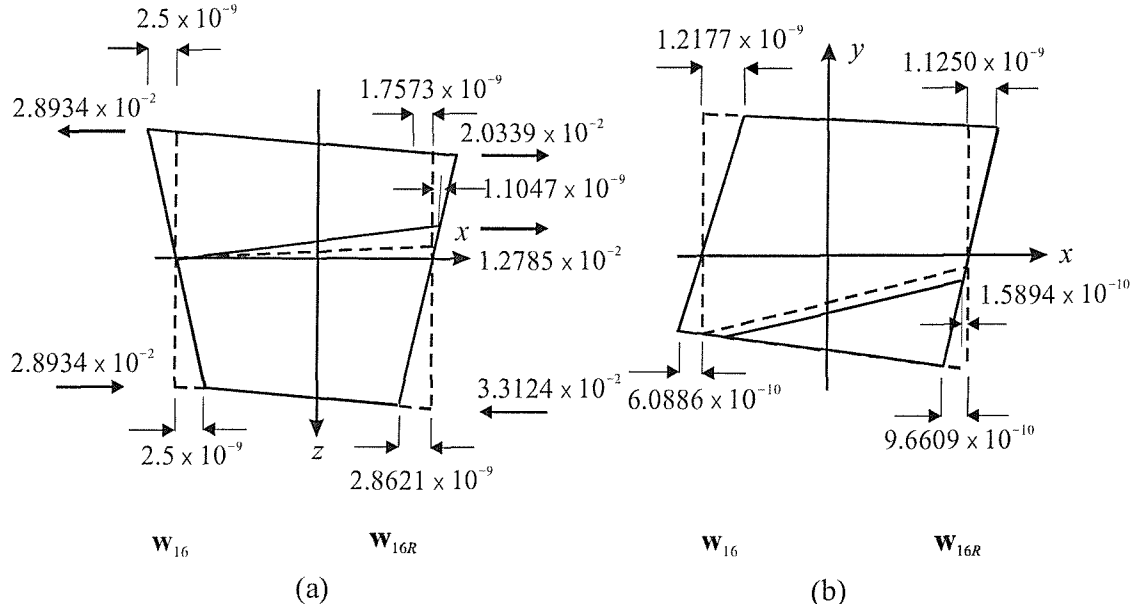


Figure 6.8. Principal vector \mathbf{w}_{16} for bending moment in the xz -plane; (a) and (b) show the displacement and force components in the xz - and xy -planes, respectively.

The above indicates that a bending moment produces a bending curvature, and shear deformations in both the plane of bending and the perpendicular plane. This contradicts widely accepted theory, but partially agrees with Tabarrok's bending theory of pre-

twisted beams [52], since his coupled equations also suggest that a coupled shear deformation takes place in the plane perpendicular to the bending curvature.

c) Vectors \mathbf{w}_{17} and \mathbf{w}_{18} are coupled to the bending moments on the left-hand side of the cell, according to

$$\mathbf{G}' \mathbf{w}_{17} = \cos \alpha \mathbf{w}_{15} + \sin \alpha \mathbf{w}_{16} + \cos \alpha \mathbf{w}_{17} + \sin \alpha \mathbf{w}_{18},$$

$$\mathbf{G}' \mathbf{w}_{18} = -\sin \alpha \mathbf{w}_{15} + \cos \alpha \mathbf{w}_{16} - \sin \alpha \mathbf{w}_{17} + \cos \alpha \mathbf{w}_{18}. \quad (6.61a, b)$$

Previous experience from the eigenanalysis of a straight repetitive structure suggests that these two vectors should describe shear; however analysis of the force components within vectors \mathbf{w}_{17} and \mathbf{w}_{18} gives a resultant shear force Q_y , and moments M_z , M_y for the former, and a resultant shear force Q_z , and moments M_y , M_z for the latter. In fact, only Q_y and M_z , and Q_z and M_y are required to define the simplest left-hand shear vectors in the xy -and xz -planes, respectively, and the unnecessary bending moments are removed according to the scheme

$$\begin{aligned} \mathbf{w}_{17}^* &= \mathbf{w}_{17} - \frac{\text{resultant}(M_y) \text{ within } \mathbf{w}_{17}}{\text{resultant}(M_y) \text{ within } \mathbf{w}_{16}} \times \mathbf{w}_{16}, \\ \mathbf{w}_{18}^* &= \mathbf{w}_{17} - \frac{\text{resultant}(M_z) \text{ within } \mathbf{w}_{18}}{\text{resultant}(M_z) \text{ within } \mathbf{w}_{15}} \times \mathbf{w}_{15}. \end{aligned} \quad (6.62a, b)$$

The two new shear vectors \mathbf{w}_{17}^* and \mathbf{w}_{18}^* are given in Appendix 6.B. Again, it is preferable that the shear vectors on the right-hand side of the cell should be given within the global coordinate system, and these are determined by

$$\mathbf{w}_{17R}^* = \mathbf{G} \mathbf{w}_{17}^*, \quad \mathbf{w}_{18R}^* = \mathbf{G} \mathbf{w}_{18}^*. \quad (6.63)$$

These describe the shear vectors in the xy -and xz -planes on both sides of the single cell, in global coordinates, in their simplest forms.

Consideration of the x -direction displacement components in the vectors \mathbf{w}_{17}^* and \mathbf{w}_{18}^* shows that they can be decomposed into rotations about the z - and y -axes, as

$$\begin{bmatrix} d_{1x} \\ d_{2x} \\ d_{3x} \end{bmatrix}^{w_{17}^*} = a \times \begin{bmatrix} d_{1x} \\ d_{2x} \\ d_{3x} \end{bmatrix}^{w_{13}} + b \times \begin{bmatrix} d_{1x} \\ d_{2x} \\ d_{3x} \end{bmatrix}^{w_{14}}, \quad \begin{bmatrix} d_{1x} \\ d_{2x} \\ d_{3x} \end{bmatrix}^{w_{18}^*} = c \times \begin{bmatrix} d_{1x} \\ d_{2x} \\ d_{3x} \end{bmatrix}^{w_{14}} + d \times \begin{bmatrix} d_{1x} \\ d_{2x} \\ d_{3x} \end{bmatrix}^{w_{13}}, \quad (6.64a, b)$$

On the other hand, consideration of the x -direction displacement components in the vectors w_{17R}^* and w_{18R}^* shows that they are also comprised of rotations of the right-hand side about the y - and z -axes, as

$$\begin{bmatrix} d_{1x} \\ d_{2x} \\ d_{3x} \end{bmatrix}^{w_{17R}^*} = e \times \begin{bmatrix} d_{1x} \\ d_{2x} \\ d_{3x} \end{bmatrix}^{w_{13R}} + f \times \begin{bmatrix} d_{1x} \\ d_{2x} \\ d_{3x} \end{bmatrix}^{w_{14R}}, \quad \begin{bmatrix} d_{1x} \\ d_{2x} \\ d_{3x} \end{bmatrix}^{w_{18R}^*} = g \times \begin{bmatrix} d_{1x} \\ d_{2x} \\ d_{3x} \end{bmatrix}^{w_{14R}} + h \times \begin{bmatrix} d_{1x} \\ d_{2x} \\ d_{3x} \end{bmatrix}^{w_{13R}}. \quad (6.65a, b)$$

Simple calculations from equations (6.64) and (6.65) gives $a = 1.1678$, $b = 0.0307$, $c = 1.1678$, and $d = -0.0307$; $e = 0.6678$, $f = -0.2416$, $g = 0.6678$ and $h = 0.2416$.

Physical representations of the shear vectors w_{17}^* and w_{17R}^* , and w_{18}^* and w_{18R}^* are given in Figures 6.9 and 6.10, respectively. The x -direction displacement components in the shear vectors can be further decomposed, as illustrated in Figures 6.11-6.14.

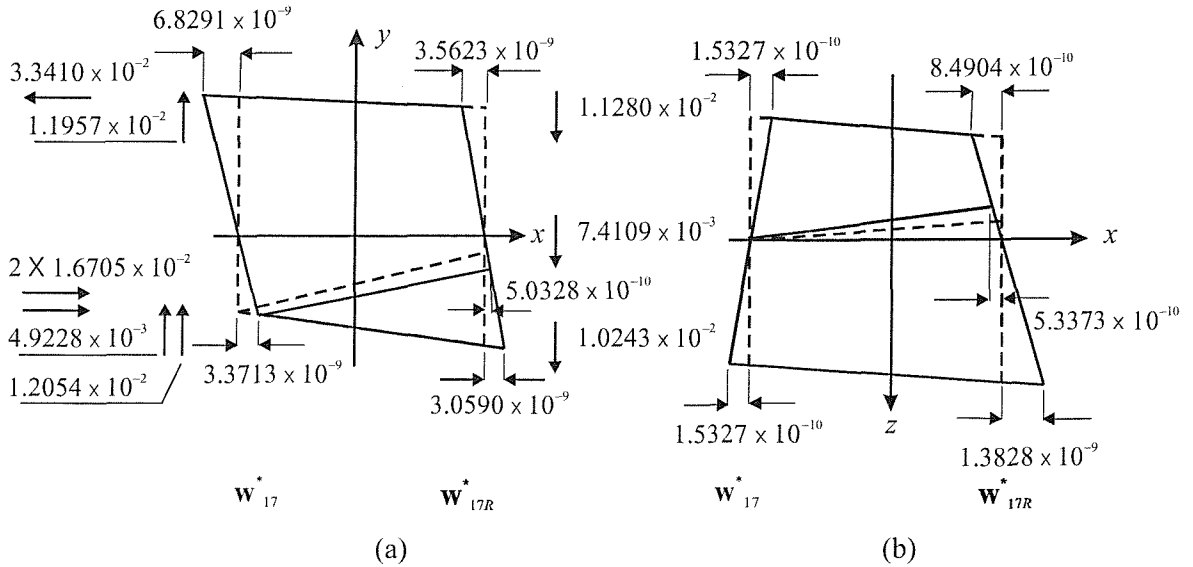


Figure 6.9. Principal vector w_{17}^* for shearing force and bending moment in the xy -plane; (a) and (b) show the displacement and force components in the xy - and xz -planes, respectively.

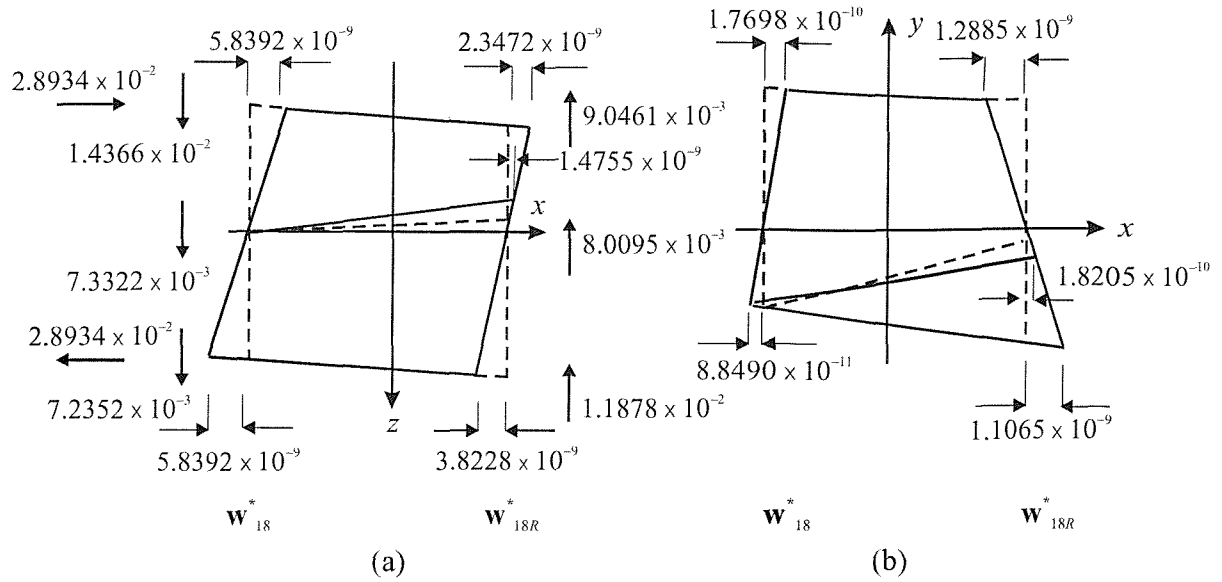


Figure 6.10. Principal vector \mathbf{w}^*_{18} for shearing force and bending moment in the xz -plane; (a) and (b) show the displacement and force components in the xz - and xy -planes, respectively.

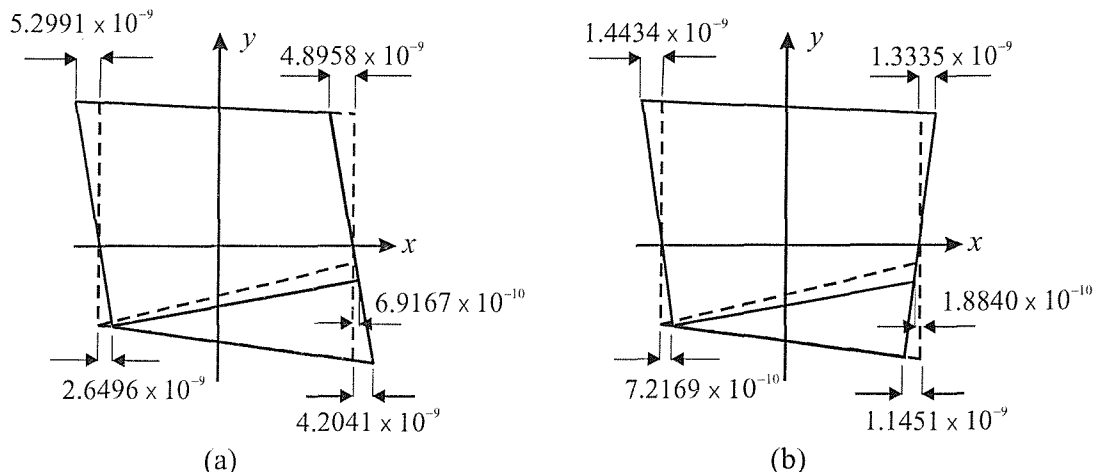


Figure 6.11. Decomposition of the displacements in the xy -plane of Figure 6.9; (a) shows the shear angle due to shearing force, and (b) shows the bending curvature due to bending moment.

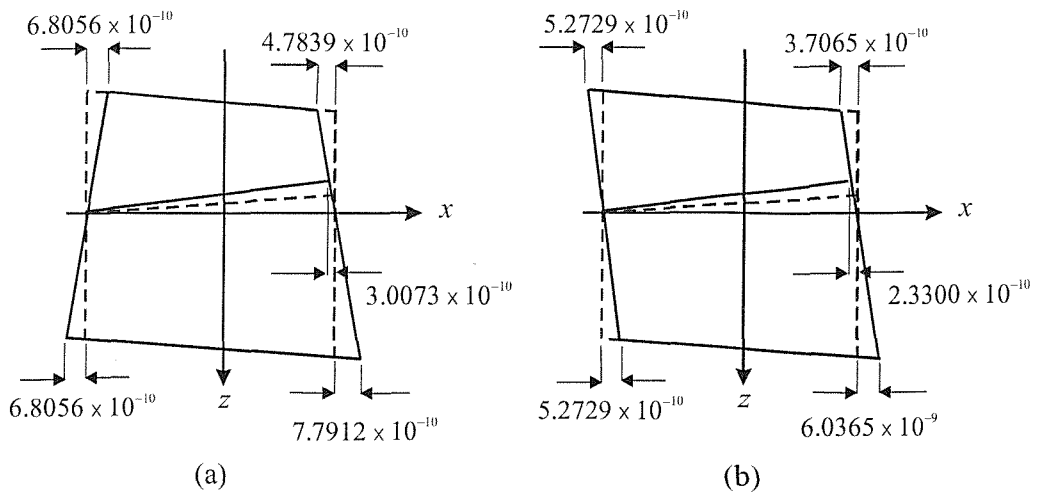


Figure 6.12. Decomposition of the displacements in the xz -plane of Figure 6.9; (a) shows the bending curvature coupled with the shear angle in the xz -plane due to shearing force, and (b) shows the shear angle coupled with the bending curvature in the xz -plane due to bending moment.

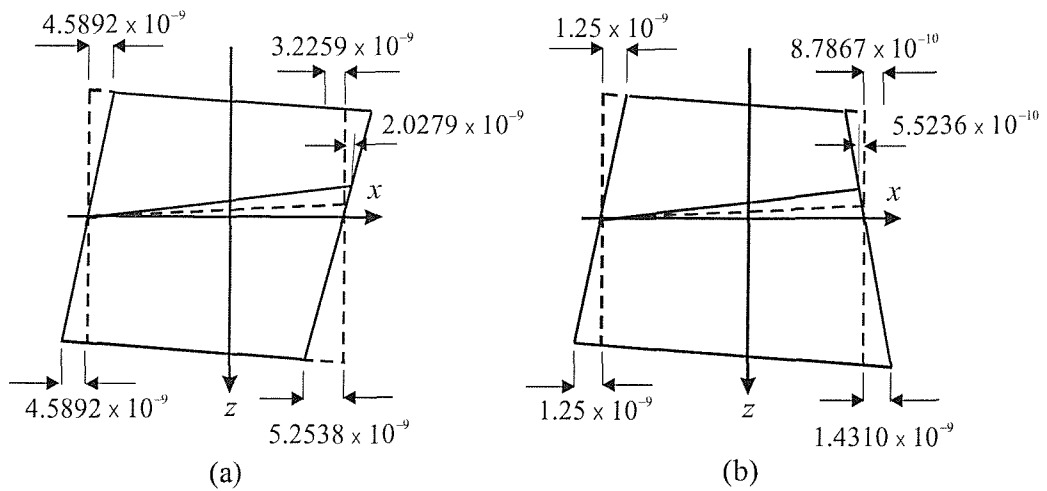


Figure 6.13. Decomposition of the displacements in the xz -plane of Figure 6.10; (a) shows the shear angle due to shearing force, and (b) shows the bending curvature due to bending moment.

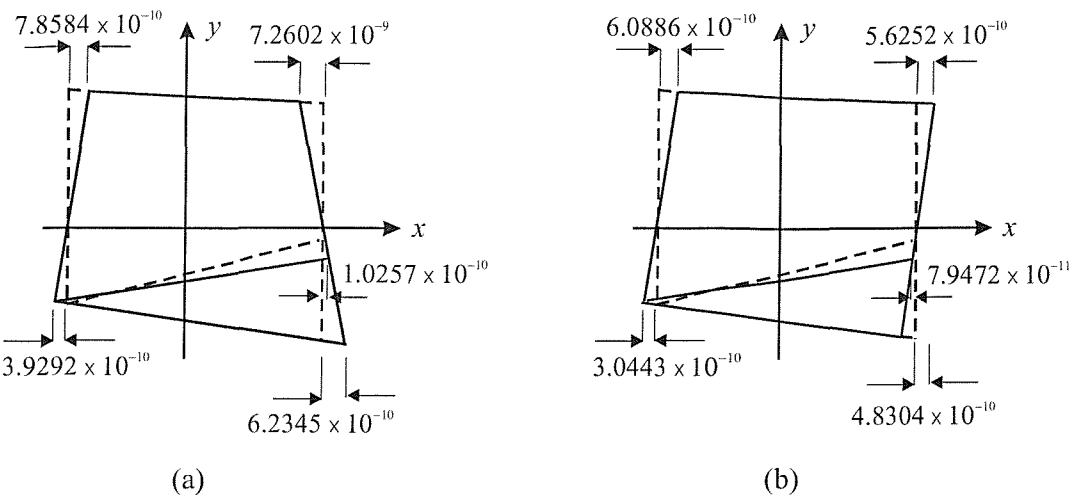


Figure 6.14. Decomposition of the displacements in the xy -plane of Figure 6.10; (a) shows the bending curvature coupled with the shear angle in the xy -plane due to shearing force, and (b) shows the shear angle coupled with the bending curvature in the xy -plane due to bending moment.

As in Chapter 2, the shear angle is defined according to the relationship $\gamma = \psi - dv/dx$, in which dv/dx is the centreline slope and ψ is rotation of the cross-section. Again, the simplest method of evaluating the shear angle is to impose a rotation on the cell to bring the centreline slope to the horizontal, and then take the average of the cross-sectional rotation on both sides of the cell. Geometric consideration of Figures 6.11(a) and 6.13(a) then gives the cross-sectional rotation on either end of the cell in the two planes, as

$$\begin{aligned}\psi_y &= \frac{2.6496 \times 10^{-9}}{H/3} = 2.6775 \times 10^{-8}, \\ \psi_z &= \frac{4.5892 \times 10^{-9}}{L/2} = 2.6775 \times 10^{-8}.\end{aligned}\quad (6.66a, b)$$

Moreover, the y -and z -direction displacements within vectors \mathbf{w}_{17}^* and \mathbf{w}_{17R}^* , and \mathbf{w}_{18}^* and \mathbf{w}_{18R}^* suggests a shift of the centre of area on the left-hand side of the cell for both, as shown in Figures 6.15 and 6.16, respectively. The centre line slope rotations within the two shear vectors can then be determined by geometric consideration as

$$\frac{dv}{dx} = \frac{7.1807 \times 10^{-10}}{0.3428} = 2.0947 \times 10^{-9},$$

$$\frac{dw}{dx} = \frac{7.1807 \times 10^{-10}}{0.3428} = 2.0947 \times 10^{-9}, \quad (6.67a, b)$$

so the shear angles in the two planes are

$$\gamma_{xy} = \psi_y - \frac{dv}{dx} = 2.4680 \times 10^{-8},$$

$$\gamma_{xz} = \psi_z - \frac{dw}{dx} = 2.4680 \times 10^{-8}. \quad (6.68a, b)$$

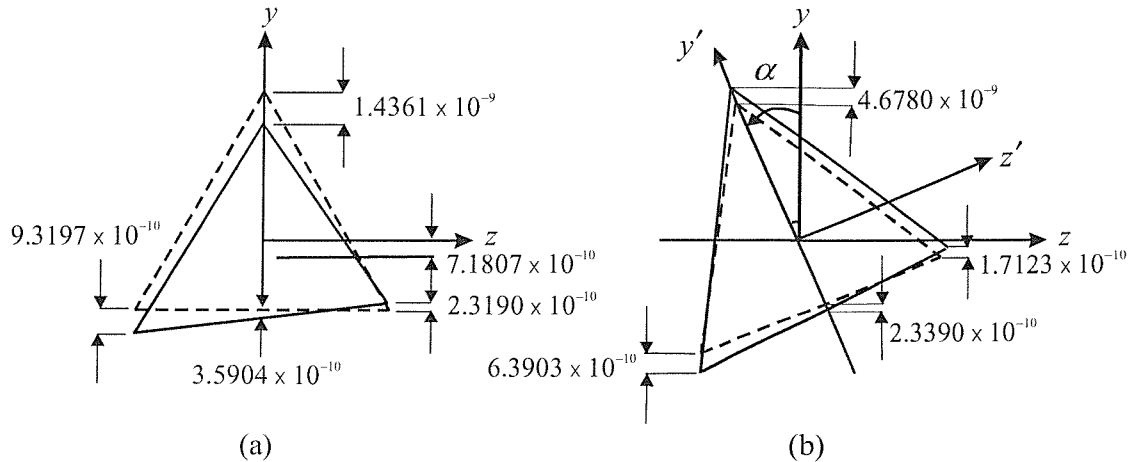


Figure 6.15. Displacements in the y -direction for the principal vector \mathbf{w}^*_{17} on the left hand (a) and right hand (b) sides of the cell, respectively.

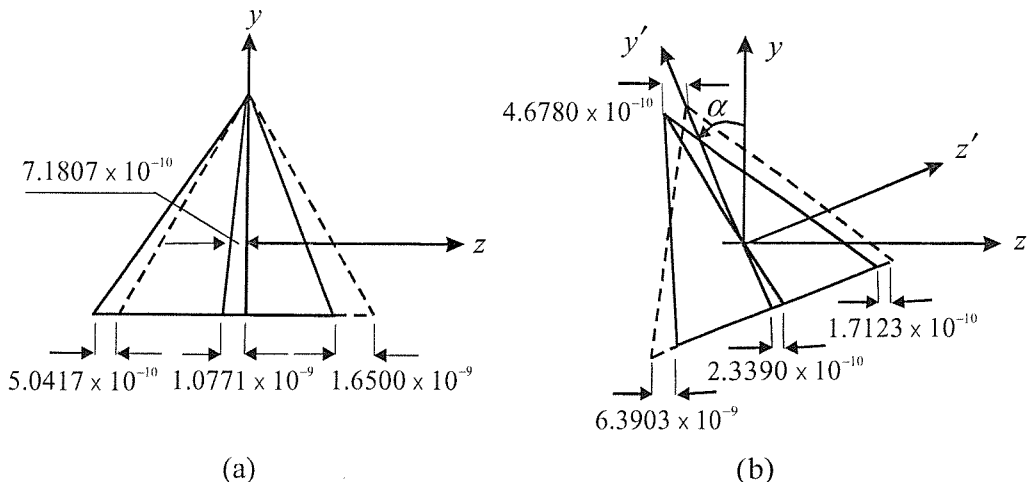


Figure 6.16. Displacements in the z -direction for the principal vector \mathbf{w}^*_{18} on the left hand (a) and right hand (b) sides of the cell, respectively.

From the above discussion of the bending moment vectors, it is known that when a pure bending moment is applied to the typical cell, a bending curvature in the principal plane is coupled with a shear deformation in the perpendicular plane. According to the reciprocal theorem, when the cell is subject to a shear, it should result in a shear deformation in the principal plane, coupled with a bending curvature in the perpendicular plane; from Figures 6.12(a) and 6.14(a), these two secondary bending curvatures are, respectively

$$\begin{aligned} 1/R_z &= \frac{6.8056 \times 10^{-10}}{L/2 \times L/2} = 2.3166 \times 10^{-8} \text{ m}^{-1}, \\ 1/R_y &= \frac{3.9292 \times 10^{-10}}{H/3 \times L/2} = 2.3166 \times 10^{-8} \text{ m}^{-1}. \end{aligned} \quad (6.69a, b)$$

Moreover, the bending moments M_z and M_y applied on the left-hand side of the cell, vectors \mathbf{w}_{17}^* and \mathbf{w}_{18}^* , can be regarded as being linearly distributed along the cell from the left side to the right which, from Figures 6.11(b) and 6.13(b) gives the bending curvatures as

$$\begin{aligned} 1/R'_y &= \frac{7.2169 \times 10^{-10}}{H/3 \times L/2} = 4.2549 \times 10^{-8} \text{ m}^{-1}, \\ 1/R'_z &= \frac{1.25 \times 10^{-9}}{L/2 \times L/2} = 4.2549 \times 10^{-8} \text{ m}^{-1}. \end{aligned} \quad (6.70a, b)$$

Also, geometric consideration of Figures 6.12(b) and 6.14(b) gives the coupled shear angles due to the applied bending moments in the perpendicular planes, respectively, as

$$\begin{aligned} \gamma'_{xy} &= \frac{5.2729 \times 10^{-9}}{L/2} = 3.0764 \times 10^{-9}, \\ \gamma'_{xz} &= \frac{3.0443 \times 10^{-10}}{H/3} = 3.0764 \times 10^{-9}. \end{aligned} \quad (6.71a, b)$$

It is noted that the bending curvatures and shear angles obtained in equation (6.70) and (6.71) are exactly one-half of those obtained in equation (6.59) and (6.60), respectively. This is consistent with the view that the bending moments resident within the two shear vectors are exactly one-half of those within the bending moment vectors \mathbf{w}_{15} and \mathbf{w}_{16} , respectively.

For the pin-jointed pre-twisted repetitive structure examined here, having equal second moments of area, analysis of the bending and shear vectors for the single cell suggests a bending and shear coupling, similar to the asymmetric *NASA* truss examined in Chapter 4. However, such coupling cannot be explained by any existing bending theory for pre-twisted beams; equation (2b,c) of [30] suggests no such coupling, while Tabarrok's pre-twisted bending theory [52] suggests that a displacement rather than a bending curvature should occur in the plane perpendicular to that of the shear. In the following section, the equivalent continuum properties of second moment of area, shear coefficient and the bending-shear coupling coefficient of the pre-twisted structure are determined using the procedures described in Chapter 4.

As with equation (4.36), the coupled force-displacement equation for bending moment in the xy -plane and shear in the xz -plane can be written in the matrix form

$$\begin{bmatrix} Q_z \\ M_z \end{bmatrix} = \begin{bmatrix} \kappa_{xz} AG & K_{xz} \\ K_{xz} & EI_z \end{bmatrix} \begin{bmatrix} \psi_y - \frac{\partial w}{\partial x} \\ \frac{\partial \psi_z}{\partial x} \end{bmatrix}. \quad (6.72)$$

However, in order to determine the equivalent second moment of area and shear coefficient, it is more convenient to write equation (6.72) in its inverted form

$$\begin{bmatrix} \gamma_{xz} \\ \frac{1}{R_y} \end{bmatrix} = \mathbf{N}_c \begin{bmatrix} Q_z \\ M_z \end{bmatrix}. \quad (6.73)$$

where

$$\gamma_{xz} = \psi_y - \frac{\partial w}{\partial x}, \quad \frac{1}{R_y} = \frac{\partial \psi_z}{\partial x} \quad (6.74)$$

and \mathbf{N}_c is the compliance matrix

$$\mathbf{N}_c = \begin{bmatrix} n_{11} & n_{12} \\ n_{21} & n_{22} \end{bmatrix} = \begin{bmatrix} \kappa_{xz} AG & K_{xz} \\ K_{xz} & EI_z \end{bmatrix}^{-1}. \quad (6.75)$$

From the bending vector in the xy -plane, \mathbf{w}_{15} , one has $M_z = 9.9185 \times 10^{-3}$ Nm, $Q_z = 0$, $1/R_y = 8.5098 \times 10^{-8}$ m $^{-1}$, $\gamma_{xz} = 6.1527 \times 10^{-9}$, and substituting into equation (6.73) gives

$$n_{12} = \frac{\gamma_{xz}}{M_z} = 6.2033 \times 10^{-7},$$

$$n_{22} = \frac{1/R_y}{M_z} = 8.5797 \times 10^{-6}. \quad (6.76a, b)$$

From the shear vector in the xz -plane \mathbf{w}_{18}^* , one has $M_z = 0 \text{ Nm}$, $Q_z = 2.8934 \times 10^{-2} \text{ N}$, $1/R_y = 2.3166 \times 10^{-8} \text{ m}^{-1}$, $\gamma_{xz} = 2.4680 \times 10^{-8}$, and substituting into equation (6.73) gives

$$n_{11} = \frac{\gamma_{xz}}{Q_z} = 8.5298 \times 10^{-7},$$

$$n_{21} = \frac{1/R_y}{Q_z} = 8.0064 \times 10^{-7}. \quad (6.77a, b)$$

Inversion of the matrix \mathbf{N}_c gives

$$\begin{bmatrix} \kappa_{xz}AG & K_{xz} \\ K_{xz} & EI_z \end{bmatrix} = \begin{bmatrix} n_{11} & n_{12} \\ n_{21} & n_{22} \end{bmatrix}^{-1} = \begin{bmatrix} 1.2577 \times 10^6 & -9.0935 \times 10^4 \\ -1.1737 \times 10^5 & 1.2504 \times 10^5 \end{bmatrix}. \quad (6.78)$$

From the above, the equivalent second moment of area is $I_z = 1.7863 \times 10^{-6} \text{ m}^4$, and shear coefficient $\kappa_{xz} = 0.4134$. However, equation (6.78) clearly suggests two unequal coupling coefficients for bending and shear, since $n_{12} \neq n_{21}$. Therefore, the coupled equations are modified, to read

$$\begin{bmatrix} Q_z \\ M_z \end{bmatrix} = \begin{bmatrix} \kappa_{xz}AG & K_{xz} \\ K'_{xz} & EI_z \end{bmatrix} \begin{bmatrix} \psi_y - \frac{\partial w}{\partial x} \\ \frac{\partial \psi_z}{\partial x} \end{bmatrix}, \quad (6.79)$$

and the two coupling coefficients are $K_{xz} = -9.0935 \times 10^4 \text{ Nm}$, $K'_{xz} = -1.1737 \times 10^5 \text{ Nm}$.

Similarly, from the bending vector in the xz -plane, \mathbf{w}_{16} , and the shear vector in the xy -plane, \mathbf{w}_{17}^* , it is found that $\kappa_{xy} = \kappa_{xz}$, $I_y = I_z$, $K_{xy} = K_{xz}$ and $K'_{xy} = K'_{xz}$, within the coupled equations

$$\begin{bmatrix} Q_y \\ M_y \end{bmatrix} = \begin{bmatrix} \kappa_{xy}AG & K_{xy} \\ K'_{xy} & EI_y \end{bmatrix} \begin{bmatrix} \psi_z - \frac{\partial v}{\partial x} \\ \frac{\partial \psi_y}{\partial x} \end{bmatrix}. \quad (6.80)$$

Thus, equation (6.79) and (6.80) suggest two asymmetric stiffness matrices coupling the moment and shearing force, which is contrary to the usual expectations of the reciprocal theorem.

This asymmetry in the stiffness matrix may imply that the coupled bending-shear model employed for the straight, but asymmetric, 3-D *NASA* truss is not adequate for the pre-twisted structure examined here. However, other interpretations are possible. First, note that the cross-sectional displacements, that is, rotation and shear, are based on the three nodal axial displacements on both sides of the cell, and that it is always possible for a plane to pass through three given points. Thus it is entirely possible, at least for this triangular cross-section, for a cross-sectional warping to be misinterpreted as a rotation. This possibility could be confirmed, or discounted by the analysis of a pre-twisted rod having, say, a square cross-section. Another possibility is a lack of work conjugacy in relation to moments and rotations, which is known to lead to asymmetric tangent matrices in large displacement, small strain analysis.

It is quite possible that the particular way of presenting the moment-shear coupling needs modification for a pre-twisted structure: thus when one calculates the nodal stiffness matrix \mathbf{K} , in global coordinates, which is the first step of the analysis procedure, one is relating nodal force and displacement components *on both sides* of the cell. However, in writing relationships such as those expressed in equation (6.80), moment and shearing force are only explicitly given for the left hand side of the cell, while those on the right hand are understood; likewise, curvature and shear are interpreted from the rotation of the cross-section on both sides of the cell. For the straight *NASA* truss, this appears to be acceptable – for example, moment equilibrium would require that there is an equal but opposite moment on the right hand side, while cross-sectional rotations are always expressed within a global coordinate system. For the pre-twisted cell, the implied right hand side moment is only equal and opposite within the global coordinate system, not the local; the greater difficulty lies with the cross-sectional rotation, as finite rotations are known not to commute. Thus, while the curvature and shear have been calculated from cross-sectional rotations of both sides of the cell in the global system, it is possible that one should in some way be treating these in the local coordinate system on the right hand side. Of course, none of these problems arise in the case of tension-torsion coupling, since the cross-sectional rotation (deformation) does commute with angle of pre-twist, as they are both about the same axis.

The inability to resolve this issue highlights the need for further research in the general area of bending of pre-twisted structures – for both the idealised structure considered here, and also for continuum rods, as in a pre-twisted turbine blade. However, one should emphasise that this issue represents a weakness in interpretation and current understanding, not an error in the principal vectors obtained by the eigenanalysis described in this Chapter – these must be correct, otherwise one would not obtain the correct Jordan canonical form.

APPENDIX 6.A
TRANSFORMATION MATRIX AND JORDAN CANONICAL FORM FOR 3D PIN-JOINTED PRE-TWISTED
FRAMEWORK, FIGURE 6.2

$$V = \begin{bmatrix} -2.6441 \times 10^{-8} & -5.9282 \times 10^{-8} & -1.6709 \times 10^{-8} & -1.5171 \times 10^{-8} & 5.9694 \times 10^{-8} & -2.6441 \times 10^{-8} \\ -7.8780 \times 10^{-8} & -2.2359 \times 10^{-7} & -1.3240 \times 10^{-7} & 8.6401 \times 10^{-8} & 1.3240 \times 10^{-7} & 1.5472 \times 10^{-8} \\ -6.3349 \times 10^{-8} & -4.6575 \times 10^{-8} & 8.6401 \times 10^{-8} & 4.6575 \times 10^{-8} & -2.2359 \times 10^{-7} & 9.9900 \times 10^{-8} \\ -2.6441 \times 10^{-8} & 1.5171 \times 10^{-8} & 5.9694 \times 10^{-8} & 5.9282 \times 10^{-8} & -1.6709 \times 10^{-8} & -2.6441 \times 10^{-8} \\ -1.5472 \times 10^{-8} & 8.6410 \times 10^{-8} & -1.3240 \times 10^{-7} & -2.2359 \times 10^{-7} & 1.3240 \times 10^{-7} & 7.8782 \times 10^{-8} \\ 9.9900 \times 10^{-8} & -4.6575 \times 10^{-8} & -2.2359 \times 10^{-7} & 4.6575 \times 10^{-8} & 8.6401 \times 10^{-8} & -6.3349 \times 10^{-8} \\ -2.6441 \times 10^{-8} & 4.4111 \times 10^{-8} & -4.2986 \times 10^{-8} & -4.4111 \times 10^{-8} & -4.2986 \times 10^{-8} & -2.6441 \times 10^{-8} \\ 9.4252 \times 10^{-8} & -6.8595 \times 10^{-8} & 1.3606 \times 10^{-7} & -6.8595 \times 10^{-8} & -1.3606 \times 10^{-7} & -9.4252 \times 10^{-8} \\ -3.6650 \times 10^{-8} & 2.2189 \times 10^{-7} & -6.8595 \times 10^{-8} & -2.2189 \times 10^{-7} & -6.8595 \times 10^{-8} & -3.6550 \times 10^{-8} \\ 0 & 0 & 0 & 0 & 0 & 0 \\ -1/2 & -\sqrt{3}/2 & -1/2 & -\sqrt{3}/2 & -1/2 & -1/2 \\ -\sqrt{3}/2 & -1/2 & \sqrt{3}/2 & -1/2 & \sqrt{3}/2 & -\sqrt{3}/2 \\ 0 & 0 & 0 & 0 & 0 & 0 \\ -1/2 & \sqrt{3}/2 & -1/2 & \sqrt{3}/2 & -1/2 & -1/2 \\ \sqrt{3}/2 & -1/2 & -\sqrt{3}/2 & -1/2 & -\sqrt{3}/2 & \sqrt{3}/2 \\ 0 & 0 & 0 & 0 & 0 & 0 \\ 1 & 0 & 1 & 0 & 1 & 1 \\ 0 & 1 & 0 & 1 & 0 & 0 \end{bmatrix}$$

1×10^{-8}	0	0	0	0	0	0
0	8.4417×10^{-10}	8.57×10^{-8}	3.8019×10^{-11}	1×10^{-8}	0	0
0	1.4621×10^{-9}	-4.9479×10^{-8}	6.5851×10^{-11}	0	1×10^{-8}	
1×10^{-8}	0	0	0	0	0	0
0	8.4417×10^{-10}	-8.57×10^{-8}	3.8019×10^{-11}	1×10^{-8}	0	0
0	-1.4621×10^{-9}	-4.9479×10^{-8}	-6.5851×10^{-11}	0	1×10^{-8}	
1×10^{-8}	0	0	0	0	0	0
0	-1.6883×10^{-9}	0	-7.6039×10^{-11}	1×10^{-8}	0	
0	0	9.8958×10^{-8}	0	0	1×10^{-8}	
0	7.6469×10^{-2}	0	-9.0323×10^{-3}	0	0	
0	-7.9046×10^{-3}	0	7.4604×10^{-3}	0	0	
0	4.5637×10^{-3}	0	-4.3073×10^{-3}	0	0	
0	7.6469×10^{-2}	0	-9.0323×10^{-3}	0	0	
0	7.9046×10^{-3}	0	-7.4604×10^{-3}	0	0	
0	4.5637×10^{-3}	0	-4.3073×10^{-3}	0	0	
0	7.6469×10^{-2}	0	-9.0323×10^{-3}	0	0	
0	0	0	0	0	0	
0	-9.1274×10^{-3}	0	8.6146×10^{-3}	0	0	

$$\begin{bmatrix}
2.8868 \times 10^{-9} & 5 \times 10^{-9} & -3.8880 \times 10^{-10} & -3.1089 \times 10^{-9} & 2.0225 \times 10^{-9} & 5.9385 \times 10^{-9} \\
0 & 0 & 3.5904 \times 10^{-10} & 6.2187 \times 10^{-10} & -6.3152 \times 10^{-10} & -4.6455 \times 10^{-10} \\
0 & 0 & 6.2187 \times 10^{-10} & 1.0771 \times 10^{-9} & -1.0938 \times 10^{-9} & -8.0462 \times 10^{-10} \\
2.8868 \times 10^{-9} & -5 \times 10^{-9} & -2.4980 \times 10^{-9} & 1.8911 \times 10^{-9} & 4.1317 \times 10^{-9} & -4.7208 \times 10^{-9} \\
0 & 0 & 3.5904 \times 10^{-10} & -6.2187 \times 10^{-10} & -8.6547 \times 10^{-11} & 7.7919 \times 10^{-10} \\
0 & 0 & -6.2187 \times 10^{-10} & 1.0771 \times 10^{-9} & 1.4990 \times 10^{-10} & -1.3496 \times 10^{-9} \\
-5.7735 \times 10^{-9} & 0 & 2.8868 \times 10^{-9} & 1.2177 \times 10^{-9} & -6.1542 \times 10^{-9} & -1.2177 \times 10^{-9} \\
0 & 0 & 1.4361 \times 10^{-9} & 0 & -1.4361 \times 10^{-9} & 6.2928 \times 10^{-10} \\
0 & 0 & 0 & 0 & 0 & 0 \\
0 & 0 & 1.6705 \times 10^{-2} & 2.8934 \times 10^{-2} & -2.7259 \times 10^{-3} & -3.7005 \times 10^{-2} \\
0 & 0 & -3.5656 \times 10^{-3} & -2.0586 \times 10^{-3} & -5.9174 \times 10^{-3} & 1.7786 \times 10^{-3} \\
0 & 0 & -2.0586 \times 10^{-3} & 3.5656 \times 10^{-3} & 1.7787 \times 10^{-3} & -1.3372 \times 10^{-2} \\
0 & 0 & 1.6705 \times 10^{-2} & -2.8934 \times 10^{-2} & -3.0684 \times 10^{-2} & 2.0863 \times 10^{-2} \\
0 & 0 & 3.5656 \times 10^{-3} & -2.0586 \times 10^{-3} & -1.3049 \times 10^{-2} & 2.3385 \times 10^{-3} \\
0 & 0 & -2.0586 \times 10^{-3} & -3.5656 \times 10^{-3} & 2.3385 \times 10^{-3} & -6.2406 \times 10^{-3} \\
0 & 0 & -3.3410 \times 10^{-2} & 0 & 3.3410 \times 10^{-2} & 1.6142 \times 10^{-2} \\
0 & 0 & 0 & 4.1142 \times 10^{-3} & -9.9678 \times 10^{-3} & -4.1172 \times 10^{-3} \\
0 & 0 & 4.1172 \times 10^{-3} & 0 & -4.1172 \times 10^{-3} & -9.3213 \times 10^{-3}
\end{bmatrix}$$

$\mathbf{V}^{-1}\mathbf{G}'\mathbf{V} = \mathbf{J}$, where \mathbf{J} is the Real Jordan block matrix

$$\mathbf{J} = \begin{bmatrix} -22.3303 & 0 & 0 & 0 & 0 & 0 \\ 0 & -10.0110 & -10.0110 & 0 & 0 & 0 \\ 0 & 10.0110 & -10.0110 & 0 & 0 & 0 \\ 0 & 0 & 0 & -0.0499 & -0.0499 & 0 \\ 0 & 0 & 0 & 0.0499 & -0.0499 & 0 \\ 0 & 0 & 0 & 0 & 0 & -0.0448 \\ 0 & 0 & 0 & 0 & 0 & 0 \\ 0 & 0 & 0 & 0 & 0 & 0 \\ 0 & 0 & 0 & 0 & 0 & 0 \\ 0 & 0 & 0 & 0 & 0 & 0 \\ 0 & 0 & 0 & 0 & 0 & 0 \\ 0 & 0 & 0 & 0 & 0 & 0 \\ 0 & 0 & 0 & 0 & 0 & 0 \\ 0 & 0 & 0 & 0 & 0 & 0 \\ 0 & 0 & 0 & 0 & 0 & 0 \\ 0 & 0 & 0 & 0 & 0 & 0 \end{bmatrix}$$

0	0	0	0	0	0	0	0	0	0	0	0
0	0	0	0	0	0	0	0	0	0	0	0
0	0	0	0	0	0	0	0	0	0	0	0
0	0	0	0	0	0	0	0	0	0	0	0
0	0	0	0	0	0	0	0	0	0	0	0
0	0	0	0	0	0	0	0	0	0	0	0
0	0	0	0	0	0	0	0	0	0	0	0
0	0	0	0	0	0	0	0	0	0	0	0
1	1	0	0	0	0	0	0	0	0	0	0
0	1	0	0	0	0	0	0	0	0	0	0
0	0	1	1	0	0	0	0	0	0	0	0
0	0	0	1	0	0	0	0	0	0	0	0
0	0	0	0	0.9236	-0.3828	0.9236	-0.3828	0	0	0	0
0	0	0	0	0.3828	0.9236	0.3828	0.9236	0	0	0	0
0	0	0	0	0	0	0.9236	-0.3828	0.9236	-0.3828	0	0
0	0	0	0	0	0	0.3828	0.9236	0.3828	0.9236	0	0
0	0	0	0	0	0	0	0	0.9236	-0.3828	0.9236	-0.3828
0	0	0	0	0	0	0	0	0.3828	0.9236	0.3828	0.9236
0	0	0	0	0	0	0	0	0	0	0.9236	-0.3828
0	0	0	0	0	0	0	0	0	0	0.3828	0.9236

APPENDIX 6.B

TWO *PURE SHEAR VECTORS FOR THE PIN-JOINTED PRE-TWISTED FRAMEWORK, FIGURE 6.2*

$$\begin{bmatrix} \mathbf{w}_{17}^* & \mathbf{w}_{18}^* \end{bmatrix} = \begin{bmatrix} 3.5245 \times 10^{-9} & 5.7507 \times 10^{-9} \\ -9.3197 \times 10^{-10} & -2.9108 \times 10^{-10} \\ -1.6142 \times 10^{-9} & -5.0417 \times 10^{-10} \\ 3.2180 \times 10^{-9} & -5.9277 \times 10^{-9} \\ 2.1390 \times 10^{-10} & 9.5265 \times 10^{-10} \\ -3.7049 \times 10^{-10} & -1.6500 \times 10^{-9} \\ -6.7425 \times 10^{-9} & 1.7698 \times 10^{-9} \\ -1.4361 \times 10^{-9} & 1.3231 \times 10^{-10} \\ 0 & 0 \\ -1.6705 \times 10^{-3} & -2.8934 \times 10^{-2} \\ -4.9228 \times 10^{-3} & 5.5975 \times 10^{-5} \\ 5.5975 \times 10^{-5} & -1.4366 \times 10^{-2} \\ -1.6705 \times 10^{-2} & 2.8934 \times 10^{-2} \\ -1.2054 \times 10^{-2} & 4.0612 \times 10^{-3} \\ 4.0612 \times 10^{-3} & -7.2352 \times 10^{-3} \\ 3.3410 \times 10^{-2} & 0 \\ -1.1957 \times 10^{-2} & -4.1172 \times 10^{-3} \\ -4.1172 \times 10^{-3} & -7.3322 \times 10^{-3} \end{bmatrix}$$

CHAPTER SEVEN

TENSION-TORSION COUPLING OF PRE-TWISTED REPETITIVE STRUCTURES

7.1 INTRODUCTION

In this Chapter, the tension-torsion coupling of the pre-twisted structure is further investigated. First, there is a detailed study of the natural frequencies of vibration of a pre-twisted structure having $\alpha = 22.5^\circ$ (as in Chapter 6). The governing equations of motion for tension-torsion developed in Chapter 5 for the asymmetric structure are equally applicable to the pre-twisted structure, and application of the approach requires calculation of the mass and rotational moment of inertia about the x -axis, per unit length. As with the asymmetric structure, these inertia properties are calculated from first principles, and their values may be regarded as exact. Natural frequency predictions, for structures of different lengths and boundary conditions, are compared with predictions provided by ANSYS, the latter again being taken as the benchmark for accuracy, in order to gauge the range of applicability of the present equivalent continuum approach.

Following the procedures developed in Chapter 6, the equivalent continuum properties relevant to tension-torsion are determined for angles of pre-twist per cell over the range 0° to 180° ; this allows one to gauge the sensitivity of the various parameters to the angle of pre-twist and, in turn, allows one to qualify the remarks of previous researchers on the effects of pre-twist. For example, Di Prima [47] concluded that both changes of pre-twist rate and the depth-to-width ratios of a bar's rectangular cross section would have considerable effect on the natural frequencies of the predominantly torsional modes, but the predominantly extensional modes would not be affected significantly. An understanding of the dependence of these equivalent continuum properties on the angle of pre-twist is gained largely from a knowledge of how the lengths of individual members in the cell depend on pre-twist, which is explored in some detail.

Finally, the natural frequencies for the fundamental modes of both torsional and extensional modes under various boundary conditions are determined for a 10-cell structure with pre-twist angle over the range 0° to 180° per cell; comparison with ANSYS predictions shows very nice agreement.

Table 7.1 Comparison of natural frequencies (Hz) in torsion and extension according to ANSYS and present method; free-free and cantilever beam, $L = 10.284$ m (30 cells)

Free-free beam				Cantilever beam			
n	ANSYS	Torsional	Extensional	n	ANSYS	Torsional	Extensional
1	56.4051	56.4216 (+0.03%)		1	28.2216	28.2108 (-0.04%)	
2	112.7111	112.8432 (+0.12%)		2	73.7293		73.6365 (-0.13%)
3	147.2962		147.2730 (-0.02%)	3	84.6157	84.6324 (+0.02%)	
4	168.8179	169.2648 (+0.26%)		4	140.8601	141.0540 (+0.14%)	
5	224.6235	225.6864 (+0.47%)		5	196.8542	197.4756 (+0.32%)	
6	280.0243	282.1080 (+0.74%)		6	221.2605		220.9095 (-0.16%)
7	294.7308		294.5460 (-0.06%)	7	252.4977	253.8972 (+0.55%)	
8	334.9093	338.5296 (+1.08%)		8	307.6788	310.3188 (+0.86%)	
9	389.1687	394.9512 (+1.49%)		9	362.2828	366.7404 (+1.23%)	
10	442.4367		441.8090 (-0.14%)	10	369.0115		368.1825 (-0.22%)
11	442.6843	451.3728 (+1.96%)		11	416.2216	423.1620 (+1.67%)	
12	495.3336	507.7944 (+2.52%)		12	469.3422	479.5836 (+2.18%)	
13	546.9881	564.2160 (+3.15%)		13	517.0671		515.4555 (-0.31%)
14	590.5353		589.1030 (-0.24%)	14	521.5608	536.0052 (+2.77%)	

7.2 VIBRATION ANALYSIS FOR PRE-TWIST ANGLE OF 22.5° PER CELL

First the mass and rotational moment of inertia, both per unit length, are calculated from first principles as $m = 0.8794 \text{ kg/m}$, and $J_x = 2.2203 \times 10^{-2} \text{ kgm}^2$. The natural frequency predictions shown in Tables 7.1 and 7.2 employ the relevant equations from Chapter 5, and are compared with those from ANSYS, again employing *consistent mass* matrices; the latter are regarded as the benchmark for accuracy.

Table 7.2 Comparison of natural frequencies (Hz) in torsion and extension according to ANSYS and present method; free-free and fixed-fixed beam, $L = 3.428\text{m}$ (10 cells)

Free-free beam				Cantilever beam			
n	ANSYS	Torsional	Extensional	n	ANSYS	Torsional	Extensional
1	168.8107	169.2468 (+0.26%)		1	84.6916	84.6324 (-0.07%)	
2	334.8527	338.5296 (+1.10%)		2	221.7947		220.9095 (-0.40%)
3	442.3925		441.8190 (-0.13%)	3	252.7148	253.8972 (+0.47%)	
4	495.1505	507.7944 (+2.55%)		4	416.984	423.1620 (+1.60%)	
5	646.3602	677.0592 (+4.75%)		5	572.9175	592.4268 (+3.41%)	
6	784.7169	846.3240 (+7.85%)		6	667.2068		662.7285 (-0.67%)
7	887.8699		883.6380 (-0.48%)	7	718.4749	761.6916 (+6.02%)	

For the slender rod, Table 7.1, there is excellent agreement up to the 10th torsional mode (+0.03% to +3.15% for the free-free beam, -0.04% to +2.77% for the cantilever beam), and up to the 4th extensional mode (-0.02% to -0.24% for the free-free beam, and -0.13% to -0.31% for the cantilever beam). For the short beam, Table 7.2, the agreement is still very good up to the 5th torsional mode (+0.26% to +7.85% for the free-free beam, -0.07% to +6.02% for the cantilever beam), and up to the 2nd extensional mode (-0.13% to -0.48% for the free-free beam, and -0.40% to -0.67% for the cantilever beam).

7.3 EQUIVALENT CONTINUUM PROPERTIES FOR ANGLES OF PRE-TWIST OVER THE RANGE 0° TO 180°

Here, interest is focused on the two principal vectors of tension and torsion, which, together with their coupled eigenvectors of rigid body displacement in the x -direction, and rigid body rotation about the x -axis, are associated with the fourfold multiple (real) unity eigenvalue. These allow calculation of the equivalent stiffness properties within the coupled equations

$$T_x = \frac{EA}{L}u + \frac{K_u}{L}\theta, \quad (7.1)$$

$$M_x = \frac{GJ}{L}\theta + \frac{K_u}{L}u. \quad (7.2)$$

Here A is the equivalent cross-sectional area, J is the equivalent torsion constant and K_u is the coupling coefficient for tension-torsion. The shear modulus G is determined from the expression $G = E/2(1+\nu)$, in which Young's modulus E is regarded as the same as the members that make up the framework; Poisson's ratio ν is calculated from the cross-sectional contraction contained within the tension vector. These quantities were calculated in Chapter 6 for an angle of pre-twist of 22.5° ; now they have been calculated and plotted over the range 0° to 180° , with steps of 1° .

However, before discussing these results, first consider Figure 7.1, which shows how the lengths of three typical members depend upon pre-twist angle, α . H_{36} denotes the length of the member joining nodes 3 and 6, and for the straight structure it is horizontal and parallel to the x -axis. D_{26} and D_{35} are the lengths of the diagonals in the face defined by nodes 2, 3, 6 and 5. Each is representative of three of its type; obviously, the angle of pre-twist has no effect on the length of the members that constitute the cross-sections. It is convenient to consider three distinct ranges (A, B and C) of pre-twist angle: for $0^\circ \leq \alpha \leq 60^\circ$ (A), H_{36} and D_{26} both increase in length, while D_{35} decreases. For $60^\circ \leq \alpha \leq 120^\circ$ (B), H_{36} increases *rapidly* while both (initially) diagonal members decrease in length, and for $120^\circ \leq \alpha \leq 180^\circ$ (C), H_{36} and D_{35} both increase in length, while D_{26} decreases.

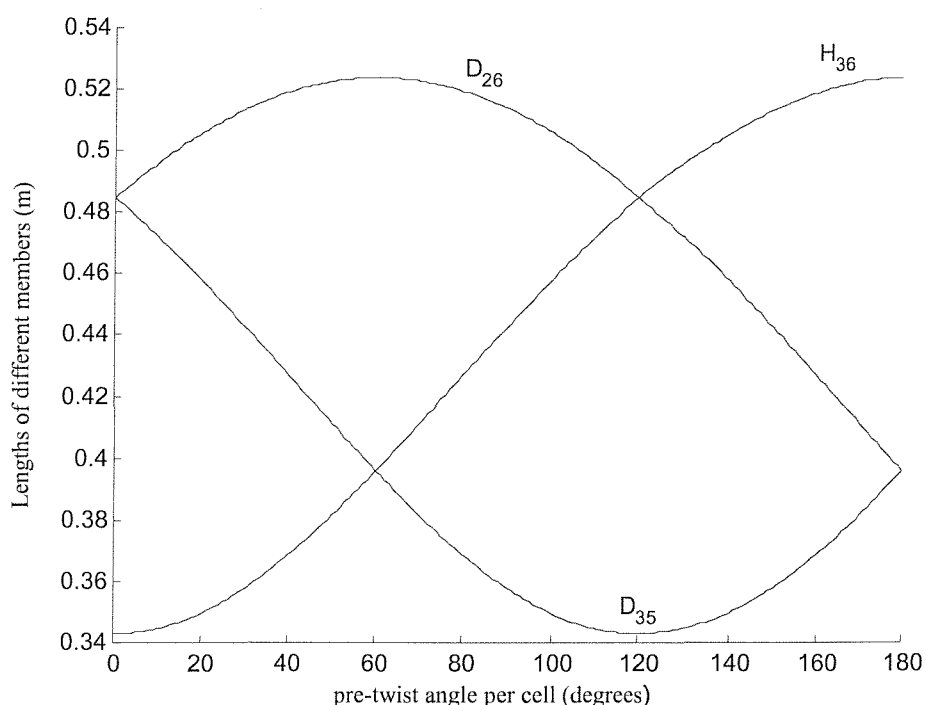


Figure 7.1. Variation of the lengths of different members with pre-twist angle.

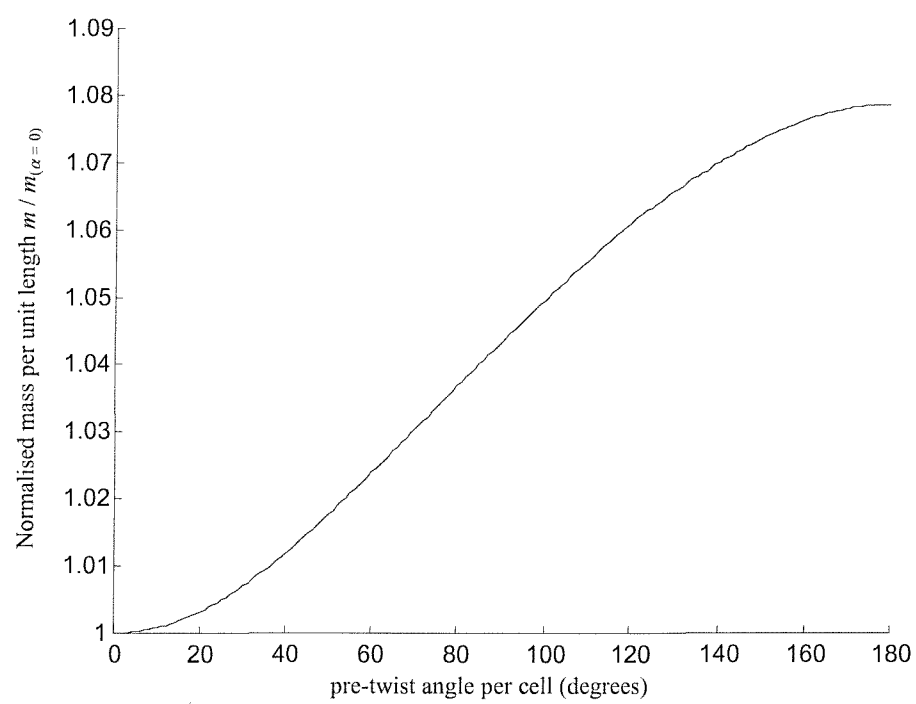


Figure 7.2. Variation of mass per unit length with pre-twist angle.

Now the mass per unit length, m , depends solely on the length of the members; but in the example structure, the initially horizontal member H_{36} has a cross-sectional area double that of a diagonal member, so its contribution is dominant. Thus over range A, the contributions from the (initially) diagonal members lead to a reduction in m , but this is more than offset by the increasing contribution from H_{36} . Over range B, the contribution from H_{36} increases at a near linear rate, while both diagonal members lead to a near linear reduction, and the net effect is again a linear increase. Finally, in range C, the contribution from H_{36} increases at a declining rate, while the contributions from the diagonals leads to a reduction in m , as in range A; however, the contribution from H_{36} is still dominant. Thus the length changes clearly explain the characteristic shown in Figure 7.2.

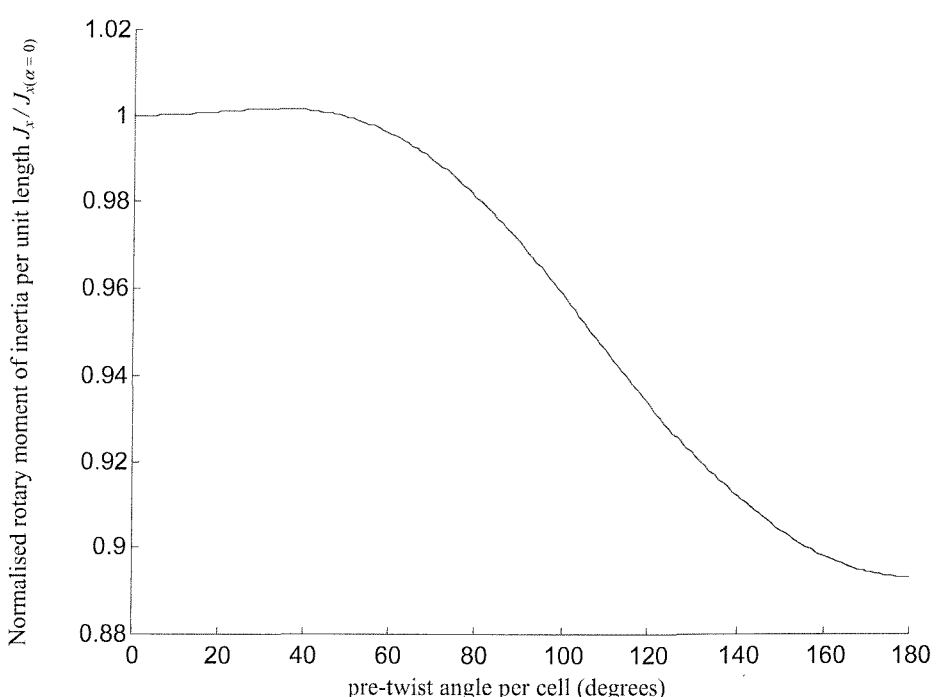


Figure 7.3. Variation of rotary moment of inertia per unit length with pre-twist angle.

The variation in moment of inertia per unit length, J_x , is shown in Figure 7.3; again this may be discussed over the three ranges. However, at first sight, one might expect the increase in mass per unit length to automatically lead to an increase in J_x , which is not the case. Rather, the moment of inertia is linearly dependent on the mass of a member, but depends also on the square of the distance from the centroidal x -axis, through the

parallel axes theorem, and this is the dominant feature. Moreover, inclination of the members changes throughout the range, so one has several factors contributing to the characteristic.

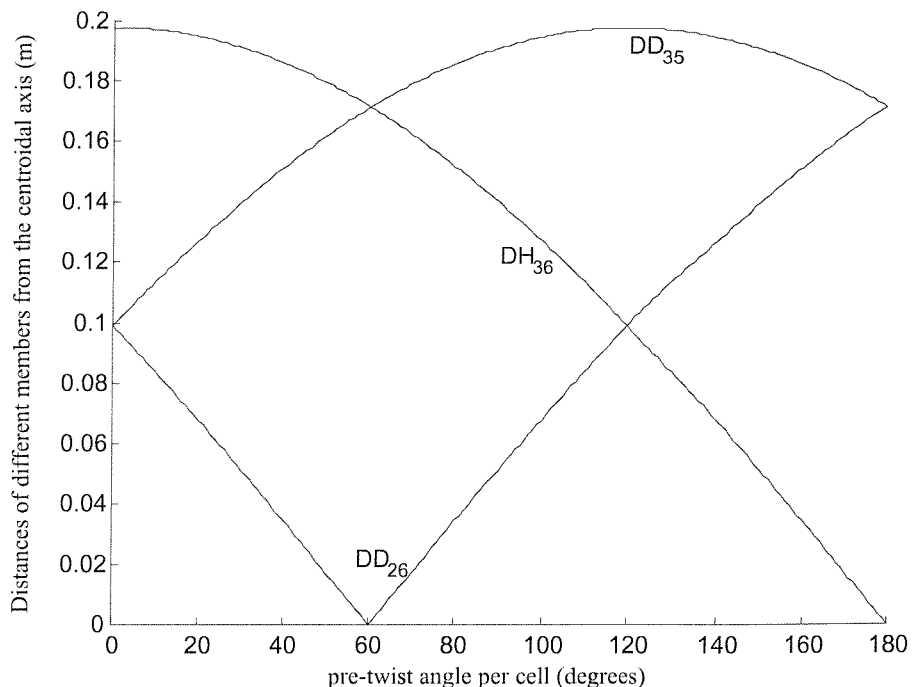


Figure 7.4. Variation of the distances of different members from the centroidal x -axis with pre-twist angle.

Figure 7.4 shows how the distances of three typical members from the centroidal x -axis depend upon pre-twist angle, α . DH_{36} denotes the distance of the horizontal member joining nodes 3 and 6 from the centroidal x -axis, and DD_{26} and DD_{35} are the distances of the diagonals in the face defined by nodes 2, 3, 6 and 5 from the centroidal x -axis. Over range A, the initially horizontal members move closer to the x -axis, but not by much; of the diagonal members, one will move close, while the other will move further away, and the net result is that J_x remains essentially constant. Over range B, as indicated in Figure 7.4, the initial horizontal members move toward the x -axis at a rather fast rate, while both diagonal members move away from the x -axis. Consider two pre-twist angles, 0° and 120° : the length of DD_{26} at $\alpha = 120^\circ$ is equal to DD_{35} at $\alpha = 0^\circ$, while DH_{36} and DD_{26} at $\alpha = 120^\circ$ are equal to DD_{26} and DH_{36} at $\alpha = 0^\circ$, respectively. Therefore, only three horizontal members and three diagonal members are considered for their contribution to the overall variations of J_x . Note that the horizontal members

are dominant. Thus, over this range, J_x decreases at a near constant rate, as does DH_{36} . Over range C, DH_{36} keeps on decreasing at a constant rate, which is slightly faster than that of range B, and DD_{26} increases at a similar rate as that of range B, while DD_{35} decreases slowly. Therefore, compared with range B, one would expect an even faster decreasing rate of J_x over range C. However, the net result is that J_x decreases at a slower rate, and this may be due to contributions from other factors such as the overall increase of mass and more inclination of members.

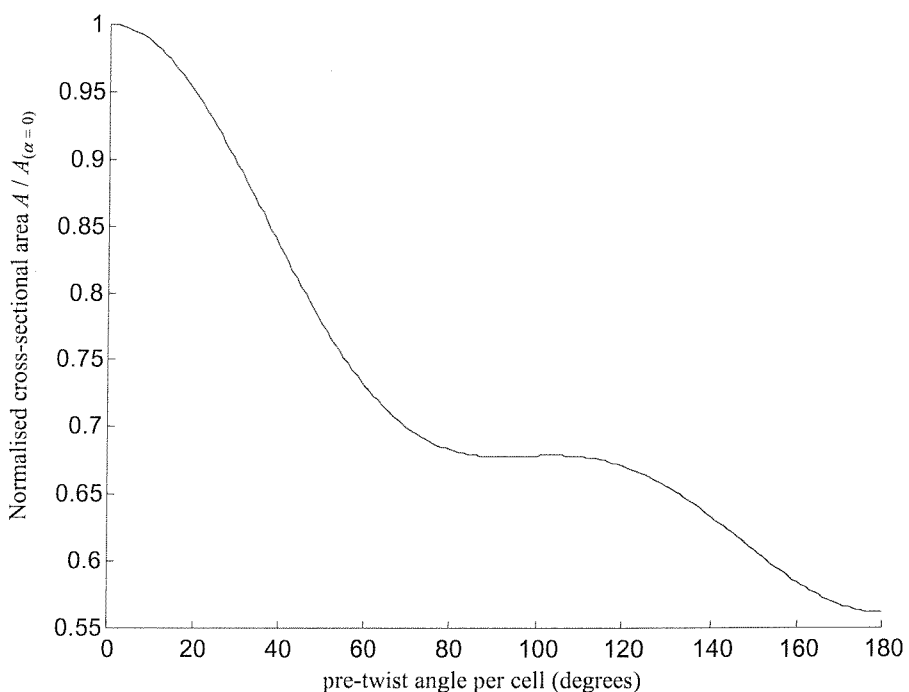


Figure 7.5. Variation of cross-sectional area with pre-twist angle.

Figure 7.5 shows variation in the equivalent cross-sectional area, and this is equivalent to axial stiffness; again it is convenient to consider the three regions. For the straight structure the equivalent axial stiffness is equal to that of the horizontal members together with necessarily positive contribution from the diagonal members and also from the members which constitute the cross-section, as discussed in Chapter 3. Over range A, the length of the (initially) horizontal bars increases as H_{36} , Figure 7.1, and since the stiffness of a member is inversely proportional to its length, this leads to a reduction in axial stiffness. In addition, the inclination of these members to the x -axis, compounds this reduction, since inclined members contribute less. The length changes

for the diagonal members leads to an overall increase in stiffness, and the angle changes will be largely neutral, but the horizontal members are dominant.

For range B, the equivalent stiffness remains essentially constant; the lengths of all diagonal members decrease, leading to increased stiffness, while the horizontal members increase in length, leading to reduction in stiffness. Clearly, the two effects more or less cancel. Over the region C, lengths of three originally diagonal members will decrease and lengths of another three will increase, again, the effect of three originally horizontal members on the changing of the equivalent axial stiffness will dominates, therefore it starts to decrease more rapidly again.

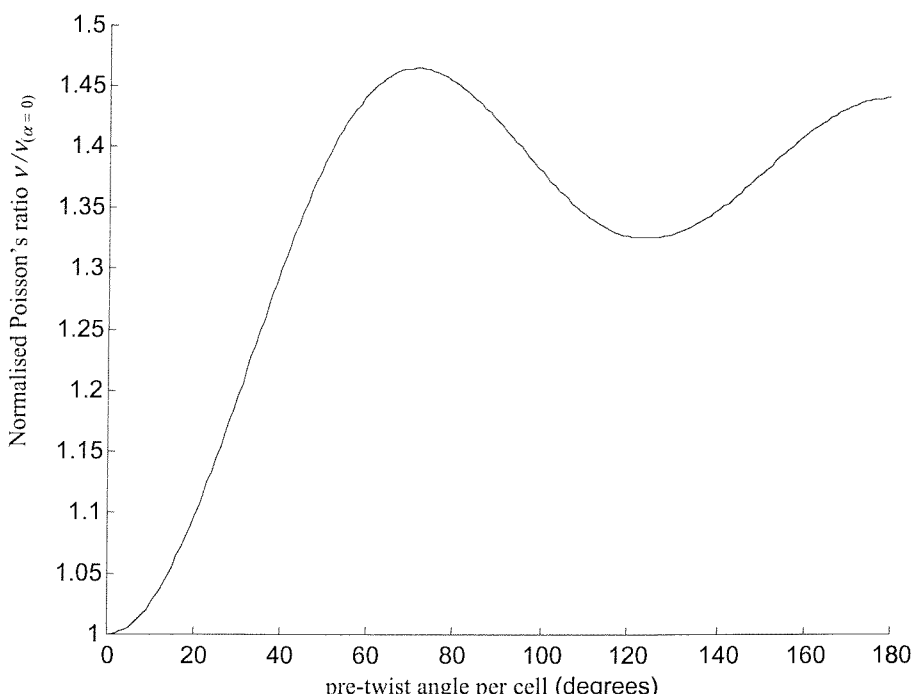


Figure 7.6. Variation of Poisson's ratio with pre-twist angle.

The variation in Poisson's ratio ν is shown in Figure 7.6; for zero pre-twist one has a value of $\nu = 0.26120$, and this increases throughout range A to give a maximum value of $\nu = 0.38246$ at $\alpha = 71^\circ$. Poisson's ratio contraction implies a decrease in length of the cross-sectional members. For the straight structure, if there were no diagonal members, then one would have $\nu = 0$; it is the presence of the diagonal bars which leads to compressive loads in these cross-sectional members, and their reduction in length. Over range A, the initially horizontal members, which have dominant stiffness, become

inclined to the x -axis, leading to increased compressive loads on the cross-sectional members, and hence increased contraction, and Poisson's ratio. Over range B, initially diagonal members become horizontal, leading to a reduction in the compressive loads in the cross-sectional members, and hence a reduction in Poisson's ratio to a local minimum, $\nu = 0.34613$, at 124° . Over range C, these members again become inclined to the x -axis, which leads to an increase in the cross-sectional contraction, and hence an increase to a local maximum, $\nu = 0.37595$, at 180° . The trend for the shear modulus G is shown in Figure 7.7, and is a direct consequence of the relationship of $G = E/2(1+\nu)$, in which E is treated as constant.

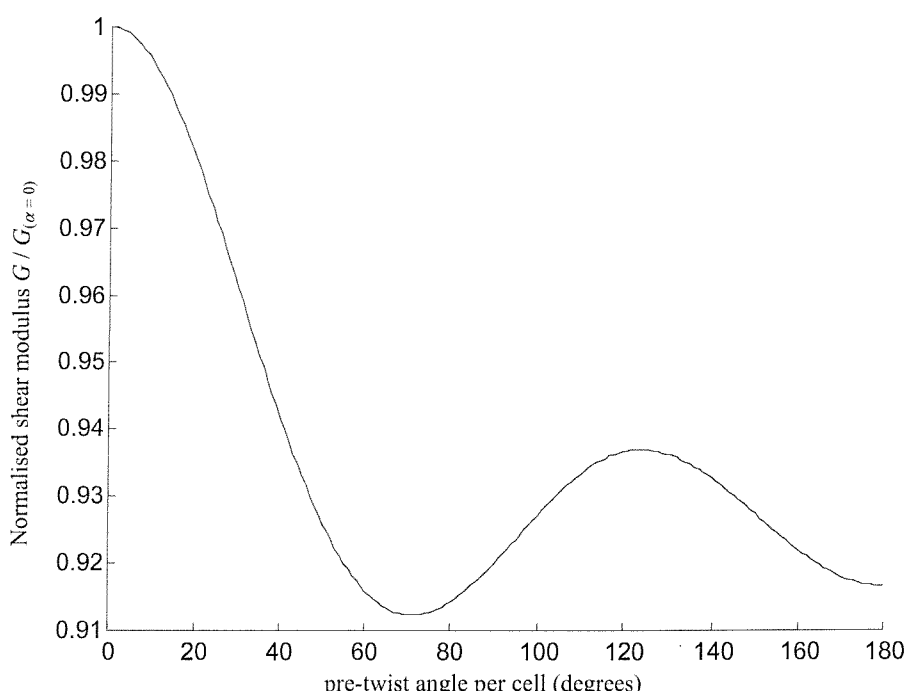


Figure 7.7. Variation of shear modulus with pre-twist angle.

Variation in the torsion constant, J , is shown in Figure 7.8; for the straight structure, $J = 8.2972 \times 10^{-7} \text{ m}^4$, and this increases over range A to a maximum of $J = 2.4868 \times 10^{-6} \text{ m}^4$ at $\alpha = 64^\circ$; this is almost exactly a threefold increase, and represents the largest sensitivity to pre-twist angle. Again, imagine a straight structure having no diagonal members: its torsional stiffness would be zero, as the cell would be a mechanism under torsional loading. Under torsion, it is the diagonal members that provide torsional stiffness, as they undergo tension or compression. As the pre-twist

angle increases, so the initially horizontal members become inclined, and start to withstand tension or compression during torsion. At $\alpha = 60^\circ$, all of the initially horizontal and diagonal members are inclined to the x -axis, leading to the maximum stiffness at 64° . Over range B, three (initially) diagonal members gradually shift to become parallel to the x -axis, and this leads to the decrease in torsional stiffness. Last, over range C, all these members shift away from being parallel to the x -axis, and hence the increase in the torsional stiffness.

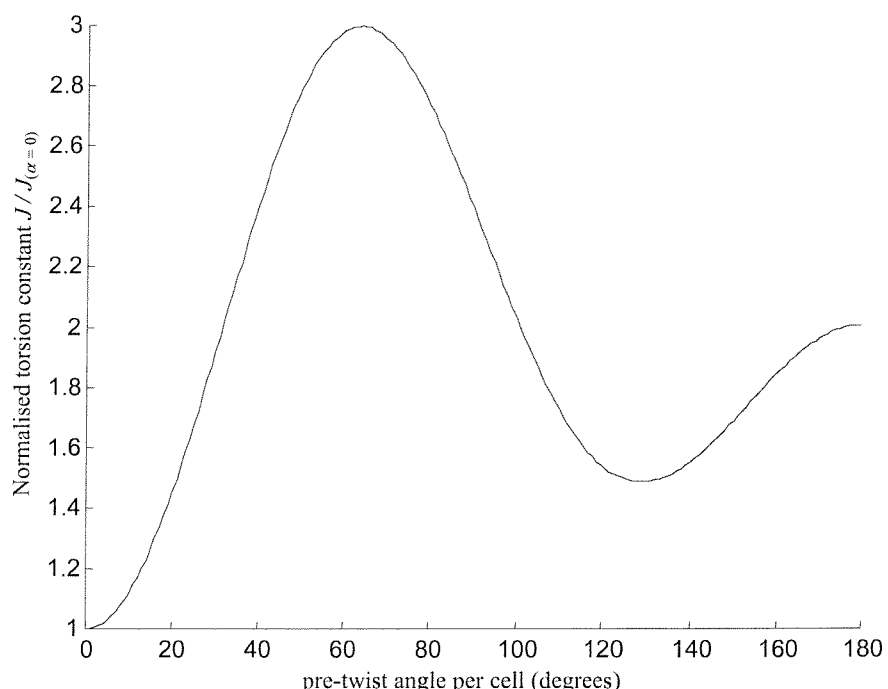


Figure 7.8. Variation of torsion constant with pre-twist angle.

Since Young's modulus E is constant, the axial stiffness EA varies in a manner identical to area A , Figure 7.9; however, both parameters within the torsional stiffness, GJ , vary with pre-twist angle, and their product is shown in Figure 7.10. These results show that the axial stiffness decreases while the torsional stiffness increases, with increased angle of pre-twist, when the latter is small, which agrees with previous results of [46]. Bearing in mind the relevant axis scales in Figures 7.7 and 7.8, the shear modulus G is much less sensitive to variations in the pre-twist angle α , than the torsion constant J , so it is the latter which dominates their conflicting trends in the torsional stiffness product GJ ; thus the trends in Figures 7.10 and 7.8 are near identical.

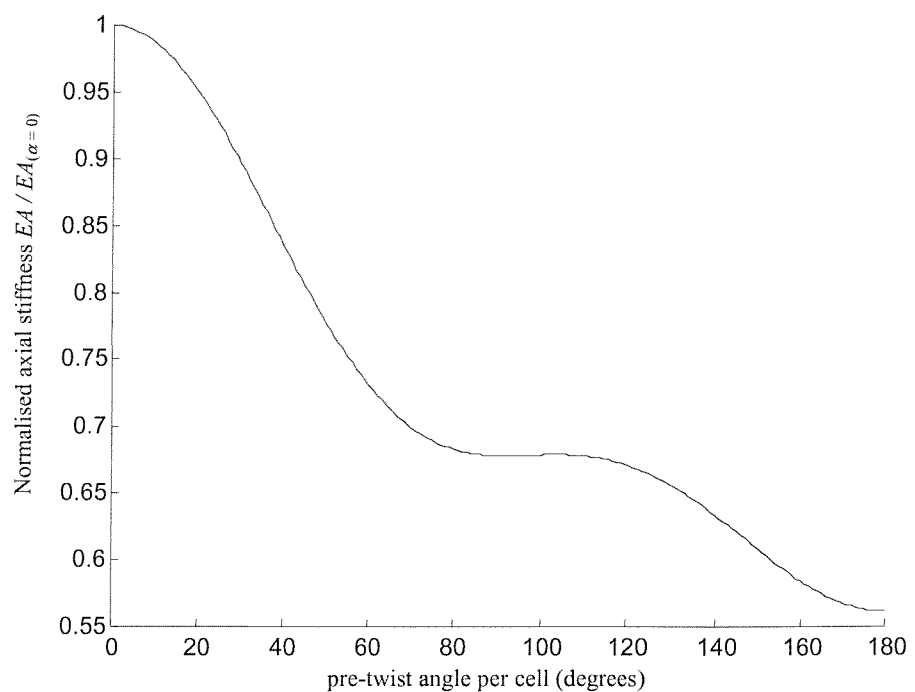


Figure 7.9. Variation of axial stiffness with pre-twist angle.

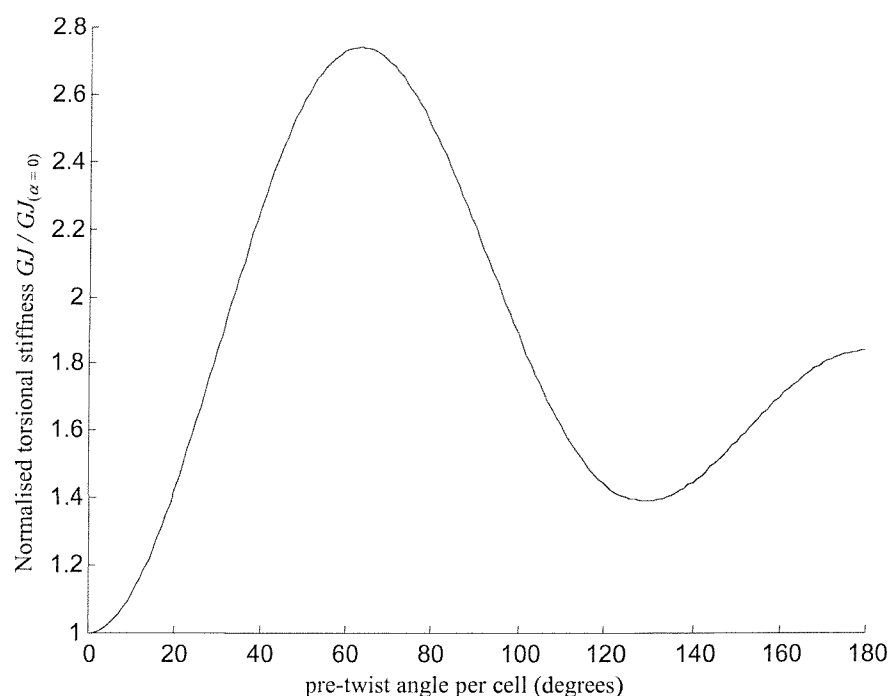


Figure 7.10. Variation of torsional stiffness with pre-twist angle.

In contrast, the characteristic of the axial stiffness product EA , which is the same as the equivalent cross-sectional area characteristic, Figure 7.9, does not show the same sensitivity, or indeed fluctuations, to pre-twist angle. Thus it is no surprise that torsional natural frequencies should be more sensitive to pre-twist angle than are the extensional frequencies.

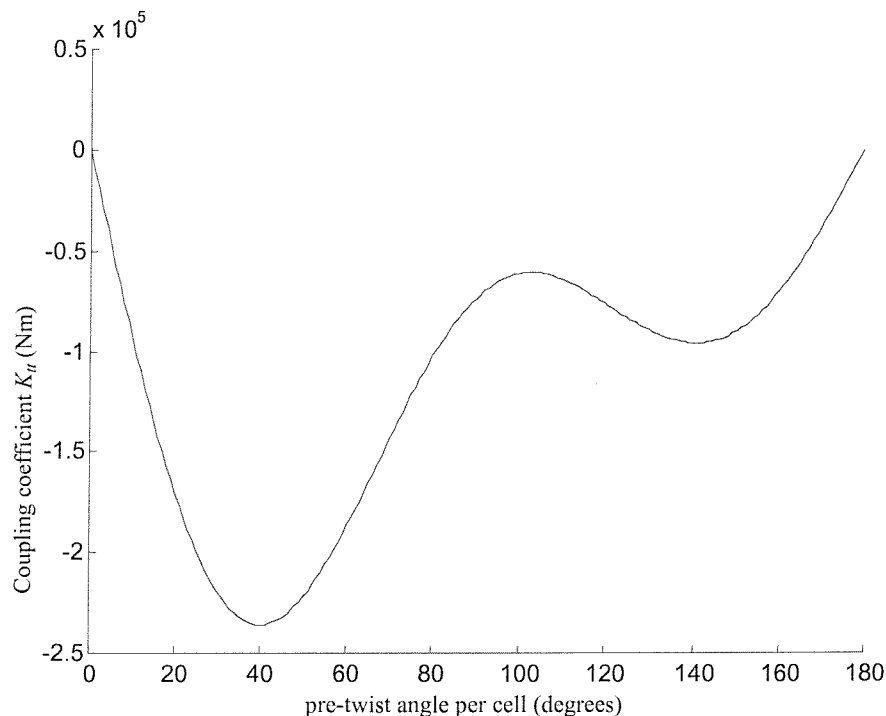


Figure 7.11. Variation of tension-torsion coupling coefficient with pre-twist angle.

Tension-torsion coupling is caused by asymmetry of the structure, and variation in the coefficient K_u is shown in Figure 7.11. The coefficient is zero for the straight structure, and decreases to a global minimum of $K_u = -2.3571 \times 10^5 \text{ Nm}$ at $\alpha = 40^\circ$, which represents the largest coupling between tension and torsion; in contrast to the other equivalent properties, this minimum does not occur close to a pre-twist angle of 60° or 120° , so discussion does not fall neatly into ranges A, B and C.

For small angles of pre-twist, the initially horizontal members become inclined to the x -axis; under tension they attempt to re-align themselves with the x -axis, resulting in rotation of the cross-section. In the absence of (initially) diagonal members in the faces of the cell, the cross-section would be free to rotate, and the cell would fully straighten

before becoming stiff; thus it is the relative stiffness' of these diagonals (compared to the horizontals) that controls the degree of rotation induced by the tensile force. Indeed, under tension, coupling is encouraged by axial stiffness (the horizontals) being greater than torsional stiffness (the diagonals). Equivalently, under a twisting moment, in the absence of the (initially) horizontal members, the cross-sections would be free to move apart (or closer together, according to the sense of the moment); again that elongation is controlled by the relative stiffness' of the horizontals and diagonals. Indeed, under a twisting moment, coupling is encouraged by the torsional stiffness (the diagonals) being greater than the axial stiffness (the horizontals). Additional to the above, as pre-twist angle increases, so (initially) horizontals become diagonals, and vice-versa, with further stiffness changes on account of the differing cross-sectional areas. So again one has many factors contributing to the overall characteristic.

7.4 VIBRATION ANALYSIS OVER THE RANGE 0° TO 180° .

The variation in natural frequency of the fundamental torsional and extensional modes, with pre-twist angle, is shown in Figures 7.12 and 7.13, respectively, for a ten-cell structure. First one notes that coupling has the effect of depressing the higher natural frequency of the predominantly extensional mode, while increasing the lower natural frequency of the predominantly torsional mode; coupling brings the frequencies closer together. For small angles, one can also see that the torsional frequencies are more affected than the extensional, which is consistent with Di Prima [47]. Indeed, the torsional frequencies are much more sensitive to angle of pre-twist over the entire range considered. The differences between the equivalent continuum predictions, and those provided by ANSYS, are shown in Figure 7.14, indicating that the errors are confined within the range of -1.5% to $+1.0\%$.

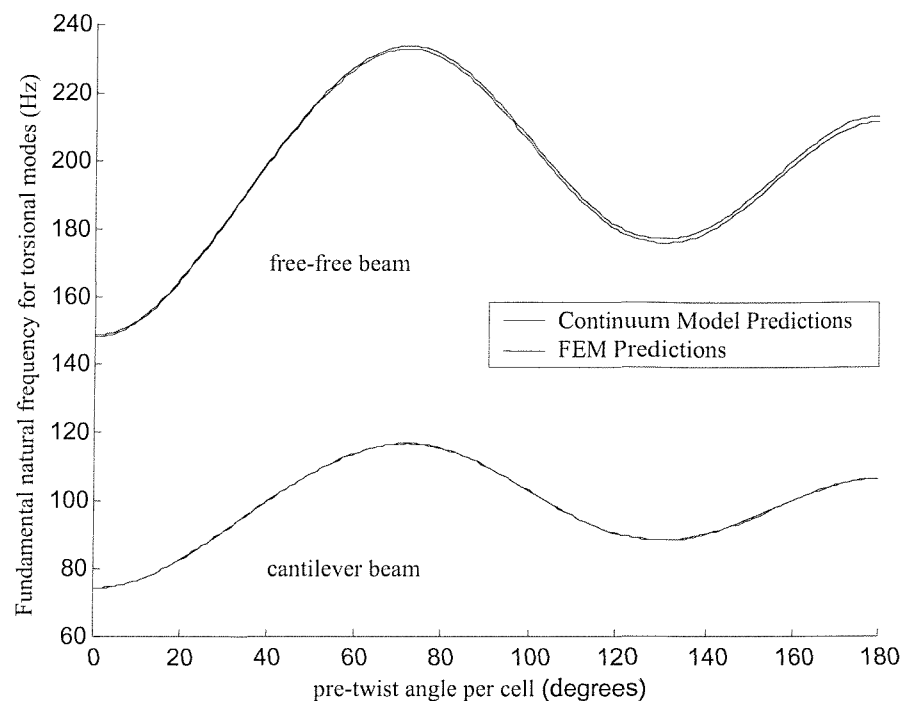


Figure 7.12. Variation of fundamental torsional natural frequency with pre-twist angle.

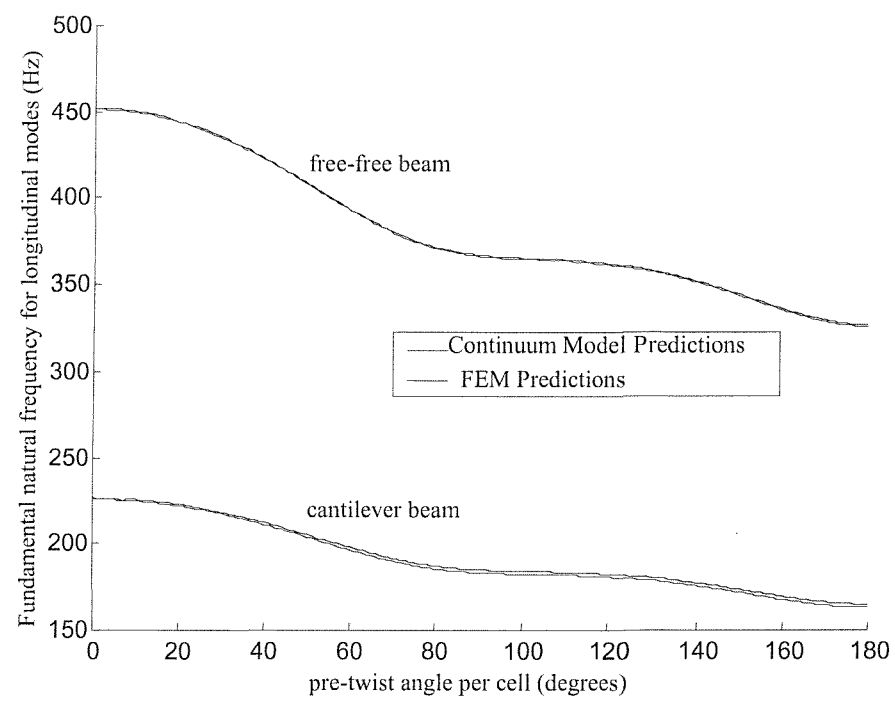


Figure 7.13. Variation of fundamental longitudinal natural frequency with pre-twist angle.

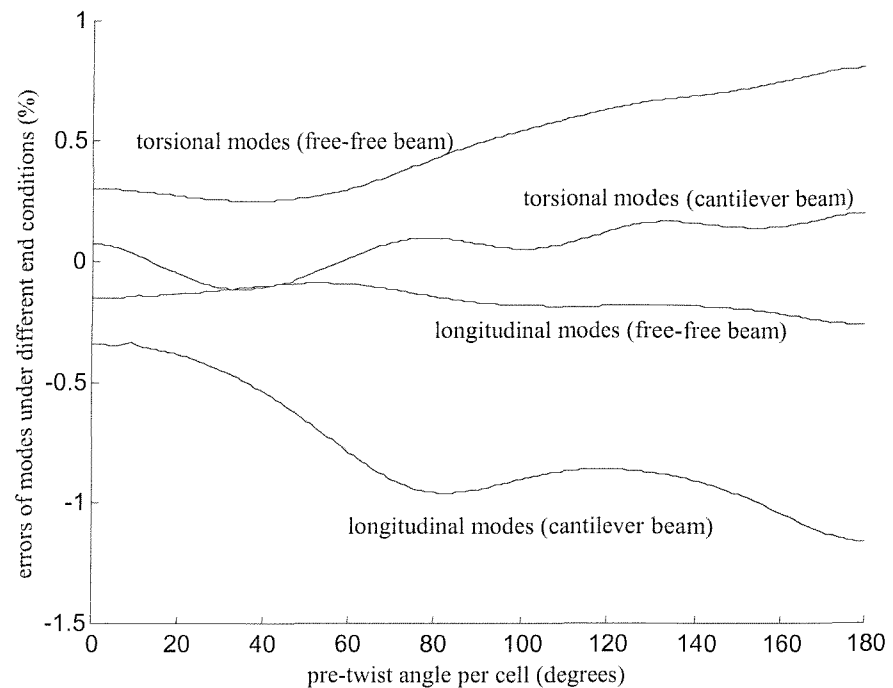


Figure 7.14. Errors of the fundamental torsional and longitudinal natural frequency with pre-twist angle:

$$\frac{\text{Present method} - \text{ANSYS}}{\text{ANSYS}} \times 100\%.$$

CHAPTER EIGHT

CONCLUSIONS AND RECOMMENDATIONS

The research presented in this thesis is largely concerned with the continuum modelling of repetitive beam-like structures; the main method employed is the eigenanalysis of a state variable transfer matrix \mathbf{G} , which can be derived by manipulation of the stiffness matrix \mathbf{K} of a single cell. Non-unity eigenvalues describe the rate of decay of the associated eigenvector, as anticipated by Saint-Venant's principle, while the multiple (possibly complex) unity eigenvalues pertain to the transmission of end loading, as in Saint-Venant's problem, together with the rigid body displacements and rotations.

The majority of the structures considered are treated as pin-jointed, as the Finite Element Analysis of such structures may be regarded as exact; in turn, the predictions of the methods developed here have been verified by comparison with these FE simulations. Justification is provided in Chapter 2, where the general theory of the state variable transfer matrix method is presented, and employed to analyse a 2-D rigid-jointed planar framework; both the Saint-Venant decay rates and the equivalent continuum beam properties are determined. Compared with the pin-jointed case examined in [10], a direct consequence of introducing a rotational degree of freedom for the rigid-jointed framework is a 50% increase in size of the transfer matrix and state vector, leading to three new pairs of decay eigenvalues, whose associated eigenvectors are characterised by comparatively large self-equilibrated nodal moments and shearing forces within the generalised force vector. Rigid-jointing has no effect on the multiplicity of the unity eigenvalues, which remains at six, and is fixed by the planar nature of the structure; it does have the effect of introducing small nodal moments – indeed just sufficient that the nodal rotation components should transmit with unity eigenvalue – and these moments are included in the calculation of the resultant bending moment for determination of the equivalent second moment of area. Comparison of the decay rates and equivalent *beam* properties of the two frameworks lead to the conclusion that rigid jointing does make the structure stiffer, but the increase is quite negligible. The treatment of rigid-jointed

structures as pin-jointed is thus justified, at least as far as determination of the equivalent continuum beam properties is concerned, and the assumption of pin-jointing is employed throughout the remainder of the thesis.

In Chapter 3, rather independently, an alternative analytical method is presented for determination of the equivalent continuum properties of the symmetric repetitive structure considered in Chapter 2, but now treated as pin-jointed. The method requires only knowledge of the stiffness matrix \mathbf{K} , and relies upon the ability to deduce the cell displacement vectors for tension, bending moment and shearing force, a process aided by the planar nature and symmetry of the structure. The tension displacement vector contains the Poisson's ratio as an unknown, and this is determined by a *once and for all* minimisation of strain energy. For less symmetric structure, and those involving torsion, deduction of the vector is slightly more complicated, but still quite straightforward. Extension of the process to two-dimensional, plate-like structure is also possible.

In Chapter 4, eigenanalysis is applied to a 3-D (space) asymmetric framework, which has seen practical use by *NASA* as a deployable boom, in connection with the International Space Station. Since a particular partition of the stiffness matrix \mathbf{K} is singular (when treated as pin-jointed), construction of the transfer matrix \mathbf{G} is impossible. Instead, a generalised eigenvalue problem is presented, which does not require inversion of the partitioned stiffness matrix and thus can be applied to repetitive structures of a more general character. The presence of zero decay eigenvalues implies that self-equilibrated loading does not penetrate into the structure at all, and that one can have loads and displacements on the left hand side of the cell which are quite unrelated with those on the right hand side – indeed this is precisely why the partition of \mathbf{K} is singular, and the conventional transfer matrix does not exist. The vectors associated with the multiple unity eigenvalues reveal some unexpected coupling between various displacement modes. First, tension is coupled with torsion, which is the known behaviour of pre-twisted structures. Second, bending is coupled with a shear deflection in the perpendicular plane. In order to understand the cause of this coupling, eigenanalysis of a simpler 2-D planar asymmetric framework, representing a single face of the 3-D *NASA* truss, shows a tension-shear coupling, which is sufficient to explain the

tension-torsion and bending-shear couplings of the 3-D *NASA* truss. The generalised coupled force-displacement equations for the tension-torsion and bending-shear couplings are provided which allows one to determine the equivalent continuum beam properties of the truss, which in turn also validates the static coupled equations assumed.

In Chapter 5, the dynamic continuum beam theories for coupled tension-torsion and bending-shear of the 3-D *NASA* truss are derived through the use of Hamilton's principle, and solved for a variety end conditions. The equivalent continuum properties employed are those found in Chapter 4, while the inertia properties were calculated by elementary means. The predicted natural frequencies are in fairly good agreement with those obtained from the FEM. For best agreement, the *lumped mass* matrix is employed for the flexural modes predictions, while the *consistent mass* matrix is used for the extensional and torsional modes predictions, within the FEM. This shows that the combined approach of the *periodic structure method* and *substitute continuum method*, two of Noor's classifications, can provide an efficient and accurate means for the prediction of the global dynamic behaviour of the repetitive structure.

In part motivated by the unexpected tension-torsion coupling of the asymmetric *NASA* truss, Chapter 6 presents an extension of the transfer matrix approach to pin-jointed structures having a pre-twisted form, which are known to possess such coupling. Employing a local coordinate system that rotates with the cross-section, allows one to construct an autonomous transfer matrix \mathbf{G}' , which is the same for each of the repeating cells; within global coordinates, the transfer matrix depends on the index of the cell. The existence of such an autonomous matrix forms part of Floquet theory, and the structural example presented, with its inherent spatial periodicity, is perhaps easier to visualise than systems possessing temporal periodicity, where this theory is more usually applied. Besides the non-unity eigenvalues that describe Saint-Venant decay, eight of the twelve unity eigenvalues which one expects for a 3-D beam-like framework become complex; the real and imaginary parts are the cosine and sine of the angle of pre-twist per cell, respectively, and occur as conjugates as they must.

The four real unity eigenvalues are associated with rigid body displacements in, and rotation about, the axial direction, together with tension and torsion; these are coupled within a 4×4 Jordan block, indicating the expected tension-torsion coupling. The equivalent continuum beam properties such as cross-sectional area, Poisson's ratio, torsion constant and the tension-torsion coupling coefficients, are determined through physical interpretation of the vectors; the resulting coupled equations are in agreement with existing theories which have been developed for continuum pre-twisted structures, such as a turbine blade. Much of the simplicity of this tension-torsion coupling can no doubt be attributed to the well-known fact that finite rotations do not commute; for tension-torsion coupling, however, this is not a problem, as the rotation during deformation either adds to, or subtracts from, the existing pre-twist of the structure, according to the sense of the applied loads.

For the eight complex unity eigenvalues, pertaining to the remaining transmission modes – transverse rigid body displacements, rotations, bending moments and shearing forces – a variety of strategies have been presented for determination of the eigen- and principal vectors, each of which leads to a different Jordan decomposition of the transfer matrix \mathbf{G}' . Those which lead to the simplest, standard Jordan canonical form, which has the repeating eigenvalue on the diagonal, and a unity on the super-diagonal, lead to complex vectors which are the most difficult to interpret. On the other hand, the simplest possible interpretation of the vectors is when the force and displacement components on *both* sides of the cell are expressed within a global coordinate system, and this leads to a block Jordan decomposition in which a real block replaces not only the complex unity eigenvalue on the leading diagonal, but also the customary real unity on the super-diagonal.

However, reconciliation of these bending moment and shearing force vectors with existing theories for bending/flexure of pre-twisted structures has proved frustrating. While the tension-torsion coupling model employed for the asymmetric 3-D *NASA* truss, Chapter 4, readily extends to the pre-twisted structure; the same cannot be said for the moment-shear coupling, as it leads to asymmetric coupling coefficients within the matrix constitutive relationship. This is not what one expects within the context of a linear

theory, being contrary to the reciprocal theorem. On the other hand, none of the known existing theories for the bending of pre-twisted structures makes allowance for the coupling of bending curvature with shear in a perpendicular plane, as found.

Reconciliation of these differences represents a major recommendation for further research – either construction of a continuum beam theory for bending of structures having pre-twisted form which can accommodate the presently observed coupling, or an alternative interpretation of the vectors for bending moment and shearing force which is in agreement with an existing theory. Or perhaps something in between: after all, the present eigenanalysis of an, albeit idealised, pin-jointed structure is probably the only exact elastic analysis of a structure having pre-twisted form, and deserves accommodation.

Bearing in mind the above dilemma, Chapter 7 concentrates on the tension-torsion coupling of a pin-jointed pre-twisted repetitive structure, for which the nature of the coupling appears to be unambiguous, and fully investigates the variation of the equivalent continuum beam properties over the range of 0° to 180° of pre-twist angle per cell. The variation of these stiffness properties can be largely understood from an appreciation of the changes in length of individual members with angle of pre-twist, together with their inclination to the axis of the rod. Just as in Chapter 4, these equivalent continuum properties, together with the mass and rotary moment of inertia per unit length, are then employed into suitably modified continuum dynamic beam theories for vibration analysis. For the specific case of pre-twist angle per cell of $\alpha = 22.5^\circ$, as considered in Chapter 6, natural frequencies under free-free and fixed-free end conditions are predicted for rods consisting of 10 and 30 repeating cells, and compared with FEM predictions. Not surprisingly, better agreement is found for the longer 30 cell case, when the maximum difference between the FEM predictions, and those according to the methods described in the present thesis are about 3% for the lowest 14 modes of vibration. For the shorter, 10 cell rod, the same accuracy is obtained for the lowest four or five modes of vibration.

In any vibration analysis, knowledge of the lowest, fundamental, frequency is of prime importance – damping tends to be smallest, so that amplitudes of forced vibration at resonance tend to be the largest. Moreover, if one seeks to avoid excitation of *any* resonance, so long as the highest frequency of excitation is lower than that of the lowest natural frequency, it is obviously lower than *all* natural frequencies. For coupled tension-torsion, these fundamental natural frequencies, again for free-free and fixed-free end conditions and for the more onerous, shorter, 10 cell structure, are compared with FE predictions over the range of 0° to 180° of pre-twist angle per cell. Differences in natural frequency prediction are less than $\pm 1.5\%$, which lends considerable support to the accuracy of the methods employed within this thesis.

The major new avenues for research, building on the work described in this thesis, are in the area of pre-twisted structures; the first challenge is a resolution the constitutive relationships describing coupled bending-shear, in particular those issues leading to asymmetry of the coupling coefficients. For tension-torsion coupling, this issue does not arise, and one can envisage a more in-depth study of this aspect of the elastic behaviour of pre-twisted structures, initially for pin-jointed structures *not* having the equilateral cross-section considered here, but for a range of more general cross-sections, for example a rectangle, or an isosceles triangle, and cross-sections for which the shear centre and centre of area (and mass) do not coincide, leading to tension-torsion-flexure coupling. Extension of these methods to continuum rods, rather than the discrete pin-jointed structures considered here, is possible using the super-element techniques described in [12]; initially these were employed as a procedure for determination of Saint-Venant decay rates for straight rods of arbitrary cross-section for which analytical solution is impossible – stiffness properties were not determined, as the most important properties of cross-sectional and second moment of area can be determined by familiar methods.

In the real world, the concept of a perfect periodic structure is an idealisation. The theory originated in the study of the behaviour of the constituent atoms of crystalline solids, which come closest to perfect periodicity; however, the existence of atomic isotopes introduces some disorder. In an engineering context, due to reasons such as

material variance, manufacturing tolerances, etc, many periodic structures can only be regarded as near-periodic. Near-periodic structures can be categorised into two major classes: *single disordered*, which contain only one element that is not identical to the others, and *disordered*, having many elements which deviate from the averaged element regarded as repeating. *Periodic structure methods* have been extended to analyse wave propagation in near-periodic structures, in which perturbation, deterministic and probabilistic, and other statistical approaches are incorporated, and have proven to be very successful, see [78] for a review.

Single disorder can be readily accommodated within the methods described in this thesis: a lack of fit, or the presence of a more flexible element, may be regarded as a local self-equilibrated load which will decay according to Saint-Venant's principle and the equivalent beam properties will be largely unchanged, so long as the deviation is not large. For general disorder, so long as the probability distributions are spatially invariant, one can reduce the analysis of the imperfect structure to an equivalent one for the ideal, [79].

Thus, the existence of disorder does not detract from the value of periodic structure theory – after all, if one were to analyse a complete, nominally periodic, structure, the location of any disorder is unlikely to be known in advance; manufacturing tolerances are always present, but less frequently modelled. Adequate quality control should ensure that elements having material defect and unacceptable dimensional tolerance are not present. Rather, it is more important that the possible consequences of disorder are taken into account. In dynamic analysis, disorder can produce the phenomenon of localisation, where the amplitude of one of the nominally identical elements, is significantly greater than the others; this is thought to be the cause of premature fatigue failure of turbine blades. Localisation also has implications for the design of systems for the control of large space structures, including vibration suppression, and shape and directional control: control schemes can become effective or unstable.

REFERENCES

1. R.A. Toupin 1965. *Archive for Rational Mechanics and Analysis*. **18**: 83-96. Saint-Venant's principle.
2. C.O. Horgan and J.K. Knowles 1983. *Advances in Applied Mechanics*. **23**: 179-269. Recent developments concerning Saint-Venant's principle.
3. C.O. Horgan 1989. *ASME Applied Mechanics Reviews*. **42**: 295-303. Recent developments concerning Saint-Venant's principle: an update.
4. C.O. Horgan 1996. *ASME Applied Mechanics Reviews*. **49**: 101-111. Recent developments concerning Saint-Venant's principle: a second update.
5. N.G. Stephen and M.Z. Wang 1992. *ASME Journal of Applied Mechanics*. **59**: 747-753. Decay rates for the hollow circular cylinder.
6. N.G. Stephen 1991. *Journal of Strain Analysis for Engineering Design*. **26**: 215-220. Decay rates for the compound circular cylinder.
7. N.G. Stephen and P.J. Wang 1996. *Journal of Strain Analysis for Engineering Design*. **31**: 231-234. Saint-Venant's principle and the anti-plane elastic wedge.
8. N.G. Stephen and P.J. Wang 1999. *International Journal of Solids and Structures*. **36**: 345-361. Saint-Venant's principle and the plane elastic wedge.
9. N.J. Hoff 1945. *Journal of Aeronautical Science*. **12**: 455-460. The applicability of Saint-Venant's principle to airplane structures.
10. N.G. Stephen and P.J. Wang 1996. *International Journal of Solids and Structures*. **33**: 79-97. On Saint-Venant's principle in pin-jointed frameworks.
11. N.G. Stephen 1999. *Journal of Sound and Vibration*. **227**: 1133-1142. On the vibration of one-dimensional periodic structures.
12. N.G. Stephen and P.J. Wang 1995. *Computers and Structures*. **58**: 1059-1066. Saint-Venant decay rates: a procedure for the prism of general cross-section.
13. <http://images.jsc.nasa.gov/images/pao/STS61B/10062569.jpg>
14. A.K. Noor 1988. *ASME Applied Mechanics Reviews*. **41**: 285-296. Continuum modelling for repetitive lattice structures.
15. J.D. Renton 1984. *AIAA Journal*. **22**: 273-280. The beam like behaviour of space trusses.

16. Y. Yong and Y.K. Lin 1989. *Journal of Sound and Vibration*. **129**: 98-118. Propagation of decaying waves in periodic and piecewise periodic structures of finite length.
17. Y. Yong and Y.K. Lin 1989. *AIAA Journal*. **28**: 1250-1258. Dynamics of complex truss-type space structures.
18. D.J. Mead 1994. *Journal of Sound and Vibration*. **171**: 695-702. Waves and modes in finite beams: application of the phase-closure principle.
19. D.J. Mead 1970. *Journal of Sound and Vibration*. **13**: 181-197. Free wave propagation in periodically-supported infinite beams.
20. D.J. Mead 1996. *Journal of Sound and Vibration*. **190**: 495-520. Wave propagation in continuous periodic structures: research contributions from Southampton.
21. W.X. Zhong and F.W. Williams 1995. *Journal of Sound and Vibration*. **181**: 485-501. On the direct solution of wave propagation for repetitive structures.
22. W.X. Zhong and F.W. Williams 1992. *Journal of Mechanical Engineering Science*. **206**: 371-379. Wave problems for repetitive structures and symplectic mathematics.
23. L. Meirovitch and R.C. Engels 1977. *AIAA Journal*. **15**: 167-174. Response of periodic structures by the z-transform method.
24. R.S. Langley 1996. *Proceeding of the Royal Society, Series A*. **452**: 1631-1648. A transfer matrix analysis of the energetics of structural wave motion and harmonic vibration.
25. W.X. Zhong and F.W. Williams 1993. *Computers and Structures*. **49**: 749-750. Physical interpretation of the symplectic orthogonality of a Hamiltonian or symplectic matrix.
26. A.K. Noor and C.M. Andersen 1979. *Computer Methods in Applied Mechanics and Engineering*. **20**: 53-70. Analysis of beam-like lattice trusses.
27. A.K. Noor, C.M. Andersen and W.H. Greece 1978. *AIAA Journal*. **16**: 1219-1228. Continuum models for beam- and plate-like lattice structures.
28. U. Lee 1990. *AIAA Journal*. **28**: 725-731. Dynamic continuum modelling of beamlike space structures using finite element matrices.

29. C.T. Sun and B.J. Kim 1985. In *Damage Mechanics and Continuum Modeling, ASCE Convention, Detroit, Michigan*: 57-71. Continuum modelling of periodic truss structures.
30. A. Rosen 1991. *ASME Applied Mechanics Reviews*. **44**: 483-515. Structural and dynamic behaviour of pretwisted rods and beams.
31. M. Ohtsuka 1975. *ASME Journal of Engineering for Power*. **97**: 180-187. Untwist of rotating blades.
32. C. Chen 1951. *Proceedings of the First US National Congress of Applied Mechanics*. 265-269. The effect of initial twist on the torsional rigidity of thin prismatical bars and tubular members.
33. A. Rosen and P. Friedmann 1979. *ASME Journal of Applied Mechanics*. **46**: 161-168. The nonlinear behaviour of elastic slender straight beams undergoing small strains and moderate rotations.
34. A. Rosen 1980. *ASME Journal of Applied Mechanics*. **47**: 389-392. The effect of initial twist on the torsional rigidity of beams-another point of view.
35. H. Okubo 1951. *Quarterly Journal of Mechanics and Applied Mathematics*. **9**: 263-272. The torsion and stretching of spiral rods (I).
36. H. Okubo 1953. *ASME Journal of Applied Mechanics*. **20**: 273-278. The torsion of spiral rods.
37. H. Okubo 1954. *Quarterly Journal of Mechanics and Applied Mathematics*. **11**: 488-495. The torsion and stretching of spiral rods (II).
38. S. Krenk 1983. *ASME Journal of Applied Mechanics*. **50**: 137-142. A linear theory for pretwisted elastic beams.
39. S. Krenk 1983. *International Journal of Solids and Structures*. **19**: 67-72. The torsion-extension coupling in pretwisted elastic beams.
40. J.N. Goodier and D.S. Griffin 1969. *International Journal of Solids and Structures*. **5**: 1231-1245. Elastic bending of pretwisted bars.
41. E. Pucci and A. Risitano 1996. *International Journal of Engineering Science*. **34**: 437-452. Bending of a pretwisted bar by terminal transverse load.
42. E. Guglielmino and G. Saccomandi 1996. *International Journal of Engineering Science*. **34**: 1285-1299. On the bending of pretwisted bars by a terminal transverse load.

43. A. N. Druz', N. A. Polyakov and Y. U. Ustinov 1996. *Journal of Applied Mathematics and Mechanics*. **60**: 657-664. Homogeneous solutions and Saint-Venant problems for a naturally twisted rod.
44. A. K. Rukhadze 1947. *Priklad. Mat. i Mekh.* **11**: 533-542. The deformation of naturally twisted beams. (In Russian)
45. L. D. Magomaev 1985. *Soviet Applied Mechanics*. **21**: 901-908. Certain problems of the theory of rectilinear, naturally twisted beams.
46. R.T. Shield 1982. *ASME Journal of Applied Mechanics*. **49**: 779-786. Extension and torsion of elastic bars with initial twists.
47. R.C. Di Prima 1959. *ASME Journal of Applied Mechanics*. **26**: 510-512. Coupled torsional and longitudinal vibrations of a thin bar.
48. J.P. Den Hartog 1952. *Advanced Strength of Materials*. New York, McGraw-Hill: 315-319.
49. J. Zickel 1954. *ASME Journal of Applied Mechanics*. **22**: 348-352. Bending of pretwisted beam.
50. J. Zickel 1956. *ASME Journal Applied Mechanics*. **23**: 165-175. Pretwisted beams and columns.
51. L. Maunder 1958. *ASME Journal of Applied Mechanics*. **25**: 261-266. The bending of pretwisted thin walled beams of symmetric star-shaped cross-sections.
52. B. Tabarrok and Y. Xiong 1989. *International Journal of Mechanical Sciences*. **31**: 179-192. On the buckling equations for spatial rods.
53. P. Vielsack 2000. *Engineering Structures*. **22**: 691-698. Lateral bending vibrations of a beam with small pretwist.
54. D. H. Hodges 1980. *ASME Journal of Applied Mechanics*. **47**: 393-397. Torsion of pretwisted beams due to axial loading, See also 1981 *ASME Journal of Applied Mechanics* **48**: 679-681.
55. J. K. Knowles and E. Reissner 1960. *Quarterly of Applied Mathematics*. **17**: 409-422. Torsion and extension of helicoidal shells.
56. J. R. Banerjee 2001. *International Journal of Solids and Structures*. **38**: 6703-6722. Free vibration analysis of a twisted beam using the dynamic stiffness method.

57. J. B. Kosmatka 1992. *ASME Journal of Applied Mechanics*. **59**: 146-152. On the behaviour of pretwisted beams with irregular cross-sections.

58. A.I. Martin 1957. *Aeronautical Quarterly*. **8**: 291-308. Approximation for the effect of twist on the vibration of a turbine blade.

59. A.S. Balhaddad and D. Onipede Jr 1998. *AIAA Journal*. **36**: 1524-1528. Three-dimensional free vibration of pretwisted beams.

60. B. Dawson, N.G. Ghosh and W. Carnegie 1971. *Journal of Mechanical Engineering Science*. **13**: 51-59. Effect of slenderness ratio on the natural frequencies of pre-twisted cantilever beams of uniform rectangular cross-section.

61. D.A. Steinman, W.L. Cleghorn, and B. Tabarrok 1995. *International Journal of Engineering Science*. **37**: 21-30. Exact solution for the free vibration of axially-loaded pretwisted rods.

62. D. Petersen 1982. *VERTICA: International Journal of Rotorcraft and Powered Lift Aircraft*. **6**: 311-325. Interaction of torsion and tension in beam theory.

63. E. Reissner and K. Washizu 1957. *Journal of the Japan Society of Aeronautical Engineers*. **5**: 330-335. On torsional vibrations of a beam with a small amount of pretwist.

64. K. Washizu 1964. *Journal of Mathematical Physics*. **43**: 111-116. Some considerations on the naturally curved and twisted slender beam.

65. L. Brillouin 1953. *Wave Propagation in Periodic Structures*. New York, Dover.

66. K. R. Meyer and G. R. Hall 1991. *Introduction to Hamiltonian Dynamic Systems and the N-Body Problem*. Applied Mathematical Sciences **90**, Berlin, Springer-Verlag.

67. R.C. Coates, M.G. Coutie and F.K. Kong 1980. *Structural Analysis*. Second ed. London, Thomas Nelson and Sons Ltd.

68. F.L. Stasa 1985. *Applied Finite Element Analysis for Engineering*. New York, Holt Rinehart and Winston.

69. J.S. Przemieniecki 1968. *Theory of Matrix Structural Analysis*. New York, McGraw-Hill.

70. W.G. Kelley and A.C. Peterson 2001. *Difference Equations*. Second Edition, Academic Press.

71. S.C. Wong and A.Y.T. Leung 1998. *Communications in Numerical Methods In Engineering*. **14**: 879-893. Determination of Jordan chains by extended matrices.
72. S.P. Timoshenko 1921. *Philosophical Magazine*. **41**: 744-746. On the correction for shear for the differential equation for transverse vibrations of prismatic bars.
73. I.S. Sokolnikoff 1956. *Mathematical Theory of Elasticity*. New York, McGraw-Hill.
74. R.D. Cook, D.S. Malkus and M.E. Plesha 1989. *Concepts and Applications of Finite Element Analysis*. New York, Wiley.
75. C.S. Desai and J.F. Abel 1972. *Introduction to the Finite Element Method*. New York, Van Nostrand Reinhold.
76. J. H. Ginsberg and J. Genin 1977. *Combined Statics and Dynamics*. New York, John Wiley.
77. K. Washizu 1975. *Variational Method In Elasticity and Plasticity*. Second ed. Pergamon Press Ltd.
78. S.S. Mester and H. Benaroya 1995. *Shock and Vibration*. **2**(1): 69-95. Periodic and Near-Periodic Structures.
79. E.G. Karpov, N.G. Stephen and W.K. Liu. *International Journal of Solids and Structures*. Initial Tension in Randomly Disordered Periodic Lattices. To be published.

BIBLIOGRAPHY

1. R. Abraham and J. E. Marsden 1978. *Foundations of Mechanics*. London, Benjamin Cummings.
2. M. C. Pease 1965. *Methods of Matrix Algebra*. London, Academic Press.
3. S.S. Rao 1995. *Mechanical Vibrations*. Third ed. Reading, Massachusetts, Addison-Wesley.
4. S.P. Timoshenko, D.H. Young and W. Weaver Jr 1974. *Vibration Problems in Engineering*. Fourth ed. New York, Wiley.
5. O.C. Zienkiewicz 1977. *The Finite Element Method*. Third ed. New York, McGraw-Hill.
6. U. Lee 1993. *International Journal of Solids and Structures*. **31**: 457-467. Equivalent continuum models of large plate-like lattice structures.
7. B. Tabarrok, Y. Xiong, D. Steinman and W.L. Cleghorn 1990. *International Journal of Solids and Structures*. **26**: 59-72. On buckling of pretwisted columns.
8. N.G. Stephen and P.J. Wang 2000. *Computers and Structures*. **78**: 603-605. On transfer matrix eigenanalysis of pin-jointed frameworks.
9. D.L. Dean and R.R. Advent 1975. In *Proceedings of the Second International Conference on Space Structures* (Univ. Surrey, Guildford, England). 7-16. State of the art of discrete field analysis of space structures.
10. A.C. Eringen 1966. *Journal of Mathematics and Mechanics*. **15**: 909-923. Linear theory of micro-polar elasticity.
11. C.T. Sun and T.Y. Yang 1973. *ASME Journal of Applied Mechanics*. **40**: 186-192. A continuum approach toward dynamics of gridworks.
12. K.I. Kanantani 1979. *International Journal of Engineering Science*. **17**: 409-418. A micro-polar continuum model for vibrating grid frameworks.
13. A.K. Noor and M.P. Nemeth 1980. *Computer Methods in Applied Mechanics and Engineering*. **21**: 249-263. Micro-polar beam models for lattice grids with rigid joints.
14. A.K. Noor and M.P. Nemeth 1980. *Computer Methods in Applied Mechanics and Engineering*. **25**: 35-59. Analysis of spatial beam-like lattices with rigid joints.

15. A.Y.T Leung and J.K.W Chang 1999. *Journal of Sound and Vibration*. **222**(4): 679-690. Null space solution of Jordan chains for derogatory eigenproblems.
16. W. W. Lin 1987. *Linear Algebra and Its Applications*. **96**: 157-180. A new method for computing the closed loop eigenvalue of a discrete-time algebraic Riccati equation.